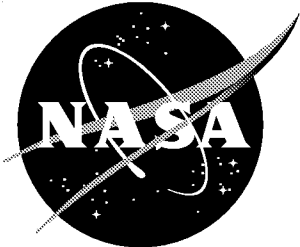


NASA/TM-1999-209513



Static Performance of a Fixed-Geometry Exhaust Nozzle Incorporating Porous Cavities for Shock-Boundary Layer Interaction Control

Scott C. Asbury and Craig A. Hunter
Langley Research Center, Hampton, Virginia

August 1999

The NASA STI Program Office ... in Profile

Since its founding, NASA has been dedicated to the advancement of aeronautics and space science. The NASA Scientific and Technical Information (STI) Program Office plays a key part in helping NASA maintain this important role.

The NASA STI Program Office is operated by Langley Research Center, the lead center for NASA's scientific and technical information. The NASA STI Program Office provides access to the NASA STI Database, the largest collection of aeronautical and space science STI in the world. The Program Office is also NASA's institutional mechanism for disseminating the results of its research and development activities. These results are published by NASA in the NASA STI Report Series, which includes the following report types:

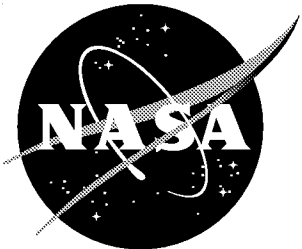
- **TECHNICAL PUBLICATION.** Reports of completed research or a major significant phase of research that present the results of NASA programs and include extensive data or theoretical analysis. Includes compilations of significant scientific and technical data and information deemed to be of continuing reference value. NASA counterpart of peer-reviewed formal professional papers, but having less stringent limitations on manuscript length and extent of graphic presentations.
- **TECHNICAL MEMORANDUM.** Scientific and technical findings that are preliminary or of specialized interest, e.g., quick release reports, working papers, and bibliographies that contain minimal annotation. Does not contain extensive analysis.
- **CONTRACTOR REPORT.** Scientific and technical findings by NASA-sponsored contractors and grantees.
- **CONFERENCE PUBLICATION.** Collected papers from scientific and technical conferences, symposia, seminars, or other meetings sponsored or co-sponsored by NASA.
- **SPECIAL PUBLICATION.** Scientific, technical, or historical information from NASA programs, projects, and missions, often concerned with subjects having substantial public interest.
- **TECHNICAL TRANSLATION.** English-language translations of foreign scientific and technical material pertinent to NASA's mission.

Specialized services that complement the STI Program Office's diverse offerings include creating custom thesauri, building customized databases, organizing and publishing research results ... even providing videos.

For more information about the NASA STI Program Office, see the following:

- Access the NASA STI Program Home Page at <http://www.sti.nasa.gov>
- E-mail your question via the Internet to help@sti.nasa.gov
- Fax your question to the NASA STI Help Desk at (301) 621-0134
- Phone the NASA STI Help Desk at (301) 621-0390
- Write to:
NASA STI Help Desk
NASA Center for AeroSpace Information
7121 Standard Drive
Hanover, MD 21076-1320

NASA/TM-1999-209513



Static Performance of a Fixed-Geometry Exhaust Nozzle Incorporating Porous Cavities for Shock-Boundary Layer Interaction Control

Scott C. Asbury and Craig A. Hunter
Langley Research Center, Hampton, Virginia

National Aeronautics and
Space Administration

Langley Research Center
Hampton, Virginia 23681-2199

August 1999

Available from:

NASA Center for AeroSpace Information (CASI)
7121 Standard Drive
Hanover, MD 21076-1320
(301) 621-0390

National Technical Information Service (NTIS)
5285 Port Royal Road
Springfield, VA 22161-2171
(703) 605-6000

Summary

An investigation was conducted in the model preparation area of the Langley 16-Foot Transonic Tunnel to determine the internal performance (nozzle thrust ratio) of a fixed-geometry exhaust nozzle incorporating porous cavities for shock-boundary layer interaction control. Testing was conducted at static conditions using a sub-scale, nonaxisymmetric, convergent-divergent nozzle model designed with interchangeable inserts in the upper and lower divergent flaps. The nozzle model had an expansion ratio (exit area/throat area) of 1.797 and a design nozzle pressure ratio of 8.78. Force, moment, and pressure measurements were taken and internal focusing schlieren flow visualization was obtained for one baseline (no porosity) and 27 porous configurations. An additional configuration with a porous upper divergent flap insert and a baseline lower divergent flap insert was tested to evaluate the potential of the porous nozzle concept to generate thrust vectoring. For the porous configurations, the effects of percent open porosity (10%, 20%, and 30%), hole diameter (0.025 in., 0.052 in., and 0.076 in.), and cavity depth (shallow, medium, and deep) on shock-boundary layer interaction control were determined. All tests were conducted with no external flow at nozzle pressure ratios from 1.25 to approximately 9.50.

Results indicate that baseline (no porosity) nozzle performance was dominated by unstable, shock-induced, boundary-layer separation at overexpanded (below the design nozzle pressure ratio) conditions, which came about through the natural tendency of overexpanded exhaust flow to satisfy conservation requirements by separating from the nozzle divergent flaps. Porous configurations were capable of controlling off-design separation in the nozzle by either alleviating separation or encouraging stable separation of the exhaust flow. Separation alleviation offers the potential for installed nozzle aeropropulsive (thrust-minus-drag) performance benefits by reducing drag at flight speeds, even though this may reduce nozzle thrust ratio at off-design conditions by as much as 3.2%.

Separation encouragement offers the potential for significant aeropropulsive performance improvements at low nozzle pressure ratio flight conditions by improving off-design nozzle thrust ratio as much as 1.4%.

The ability of the porous nozzle concept to alternately alleviate separation or encourage stable separation of exhaust flow through shock-boundary layer interaction control offers tremendous off-design performance benefits for fixed-geometry nozzle installations. By designing a fixed-geometry nozzle with porous divergent flaps, where percent open porosity of the flaps could be varied, shock-boundary layer interaction control would make it possible to improve off-design nozzle aeropropulsive performance across a wide operating range. In addition, the ability to encourage separation on one divergent flap while alleviating it on the other makes it possible to generate thrust vectoring using a fixed-geometry nozzle.

Introduction

Supersonic cruise transport aircraft and modern military aircraft with supersonic cruise or dash capabilities utilize variable-geometry exhaust nozzles to ensure efficient aeropropulsive (thrust-minus-drag) performance across a wide operating range. A variable-geometry nozzle functions by adjusting throat area and expansion ratio to provide the optimum nozzle configuration for each engine power setting and flight condition. Independent throat area A_t control is necessary to satisfy engine afterburning requirements, and separate control of the exit area A_e provides the proper nozzle expansion ratio A_e/A_t at each flight condition (ref. 1). For example, a typical fighter aircraft might have a low nozzle pressure ratio of about 3.0 at takeoff, requiring a nozzle expansion ratio of about 1.1 for optimum nozzle performance. During a supersonic dash to Mach 2.0, nozzle pressure ratio increases to approximately 10.0, and a nozzle expansion ratio of 1.9 is required for optimum nozzle performance. Figure 1 illustrates a typical variable-geometry nozzle at several operating conditions.

Nozzle geometry variation is typically achieved using actuators and movable nozzle flaps as shown in figure 2. While effective, these systems can be heavy, mechanically complex, and prone to fatigue through thermal, aerodynamic, and aeroacoustic loading. In addition, variable-geometry mechanisms are inherently difficult to integrate into fighter aircraft afterbodies and can be a primary cause of afterbody drag. Additional requirements such as multiaxis thrust vectoring (ref. 2), thrust reversing (ref. 3), low observability (ref. 4), and noise suppression (ref. 5) further complicate the propulsion-airframe integration of variable-geometry nozzle systems.

The capabilities of future high performance military aircraft will be critically dependent on the development of simple, lightweight exhaust systems that are aerodynamically efficient, compact, and low observable. Supersonic transport aircraft will rely heavily on efficient nozzle performance for extended cruise at high supersonic speeds where the ratio of lift to drag is low and fuel consumption is high. There is tremendous incentive to improve both military and transport aircraft performance by reducing the complexity of exhaust nozzles.

The desire for reduced weight and complexity in exhaust systems has led designers to consider reducing, or even eliminating, variable-geometry mechanisms in exhaust nozzles. The fundamental problem with this solution is that a fixed-geometry nozzle will only operate efficiently at the flight condition for which it is designed. When operated away from the design point (which may be common if a supersonic aircraft is expected to cruise subsonically, loiter, or divert to alternate airports), a fixed-geometry nozzle suffers large off-design performance penalties. For example, if the fighter aircraft mentioned previously were to operate with a fixed-geometry, 1.9 expansion ratio nozzle at the takeoff condition, a 20-percent loss in thrust ratio would result from nozzle overexpansion effects (ref. 1). Large performance penalties such as this would be unacceptable in most applications.

The successful utilization of fixed-geometry

nozzles in most aircraft applications will require improvements in off-design performance. At highly overexpanded conditions, exhaust flow separation results from the natural tendency of overexpanded exhaust flow to satisfy conservation requirements by separating from the nozzle divergent flaps through shock-boundary layer interaction. This increases off-design performance by allowing the nozzle to effectively “adjust” to a shorter nozzle with a lower expansion ratio. However, the stability of shock-induced, boundary layer separation is inherently unpredictable. Asymmetric, unsteady, or transient separation can have a detrimental impact on nozzle performance and may result in undesirable flow vectoring, pressure pulsations, and oscillatory flow patterns inside the nozzle. Therefore, the ability to stabilize separation inside a fixed-geometry nozzle through shock-boundary layer interaction control could be critical to efficient and practical off-design nozzle performance.

At forward flight speeds, however, external flow can aspirate the separated portion of the divergent flaps, causing increased drag (ref. 6). In some instances, separation alleviation may be necessary to ensure efficient aeropropulsive performance, even if losses in nozzle thrust ratio result from increased exhaust flow overexpansion. A detailed study (including wind tunnel tests with external flow) would be required to determine the conditions at which separation alleviation or separation encouragement is beneficial to nozzle aeropropulsive performance.

The objective of the research described in this report was to determine the effects on performance of adding porous cavities to the divergent flap surfaces of a fixed-geometry exhaust nozzle. Primary emphasis was placed on understanding the effects of porosity at highly overexpanded (off-design) conditions, particularly at nozzle pressure ratios between 2.0 and 3.0, where shock-boundary layer interaction control could provide significant nozzle aeropropulsive performance benefits.

Testing was conducted at static conditions

using a sub-scale, nonaxisymmetric, convergent-divergent (C-D) nozzle model designed with interchangeable divergent flap inserts. The nozzle model had an expansion ratio of 1.797 and a design nozzle pressure ratio of 8.78. Force, moment, and pressure measurements were taken and internal focusing schlieren flow visualization was obtained for one baseline (no porosity) and 27 porous configurations. An additional configuration with a porous upper divergent flap insert and a baseline lower divergent flap insert was tested to evaluate the potential of the porous nozzle concept to generate thrust vectoring. For the porous configurations, the effects of percent open porosity (10%, 20%, and 30%), hole diameter (0.025 in., 0.052 in., and 0.076 in.), and cavity depth (shallow, medium, and deep) on shock-boundary layer interaction control were determined. All tests were conducted with no external flow at nozzle pressure ratios from 1.25 to approximately 9.50.

Symbols

All forces and moments are referred to the model centerline (body axis). The model (balance) moment reference center was located at station 29.39. A discussion of the data reduction procedure, definitions of force and moment terms and propulsion relationships used herein can be found in reference 7. All pressures presented are absolute unless otherwise noted.

A_e	nozzle exit area, 7.758 in ²
A_t	nozzle throat area, 4.317 in ²
d	porous cavity hole diameter, in.
D	cavity depth, in.
F	measured thrust along body axis, positive in forward direction, lbf
F_i	ideal isentropic thrust, lbf
F/F_i	nozzle thrust ratio
$(F/F_i)_{\text{peak}}$	peak nozzle thrust ratio

g	acceleration due to gravity, 32.174 ft/sec ²
M	Mach number
NPR	nozzle pressure ratio, $p_{t,j}/p_a$
NPR_d	design nozzle pressure ratio (NPR for fully expanded flow at the nozzle exit)
p	local static pressure, psi
p_a	ambient pressure, psi
$p_{t,j}$	average jet-total pressure, psi
R_j	gas constant (for $\gamma=1.3997$), 1716 ft ² /sec ² ·°R
$T_{t,j}$	average jet-total temperature, °R
w_p	measured weight-flow rate, lbf/sec
x	linear dimension measured along model centerline from nozzle connect station (Sta. 41.13), positive downstream (see figs. 6 and 7), in.
x_t	distance between nozzle connect station (Sta. 41.13) and nozzle throat, measured along model centerline, positive downstream (see fig. 10), 2.275 in.
y	vertical distance measured from model centerline, positive upwards (see figs. 6 and 7), in.
z	lateral distance measured from model centerline, positive to right when looking upstream (see figs. 6 and 10), in.
α	nozzle divergence half angle (see fig. 7), 11.01 deg
β	oblique shock-wave inclination angle, measured from upstream flow direction, deg

γ	ratio of specific heats, 1.3997 for air
θ	angle of flow direction across an oblique shock wave, measured from upstream flow direction, deg

Subscripts:

1	conditions just upstream of a shock wave
2	conditions just downstream of a shock wave
<i>adj</i>	adjusted internal static pressure (baseline static pressure removed)

Abbreviations:

C-D	convergent-divergent
Hz	Hertz
NPAC	Nozzle Performance Analysis Code
R	radius, in.
Sta.	model station, in.

Apparatus and Procedures

Test Facility

This investigation was conducted in the model preparation area of the Langley 16-Foot Transonic Tunnel. Although this facility is normally used for setup and calibration of wind-tunnel models, it can also be used for nozzle internal performance testing at static (no external flow) conditions. Testing is conducted in a 10 x 29-foot chamber where a cold-flow ($T_{ij} \approx 540^{\circ}\text{R}$) jet from a single-engine propulsion simulation system exhausts to the atmosphere through an acoustically treated exhaust passage. A control room is adjacent to the test chamber, and offers access through a sound-proof door and observation window. The model preparation area shares a high-pressure air system with the 16-Foot Transonic Tunnel that includes valving, filters,

and a heat exchanger to provide a continuous flow of clean, dry air to the propulsion simulation system for jet-exhaust simulation. A complete description of the test facility is provided in reference 8.

Single-Engine Propulsion Simulation System

The single-engine propulsion simulation system used in this investigation is shown in detail in figure 3. High-pressure air supplied to the propulsion simulation system was varied from atmosphere up to about 140 psi total pressure in the instrumentation section at a constant stagnation temperature of approximately 540°R . As shown in figure 3(b), the high-pressure air was delivered by six air lines through a support strut into a annular high-pressure plenum. The air was then discharged radially into a low-pressure plenum through eight equally spaced, multiholed, sonic nozzles. This flow transfer system was designed to minimize any forces imposed by the transfer of axial momentum as the air passed from the non-metric high-pressure plenum to the metric (attached to the balance) low-pressure plenum. Two flexible metal bellows functioned as seals between the non-metric and metric portions of the model and compensated for axial forces caused by pressurization. The air then passed through a circular-to-rectangular transition section, a rectangular choke plate (primarily used for flow straightening), a rectangular instrumentation section, and then through the nozzle, which exhausted to atmospheric back pressure. The instrumentation section had a ratio of flow path width to height of 1.437 and was identical in geometry to the nozzle airflow entrance (nozzle connect station). All nozzle configurations tested were attached to the downstream end of instrumentation section at model station 41.13.

Nozzle Concept

A fixed-geometry, nonaxisymmetric, C-D nozzle was designed with symmetric pairs (upper and lower) of convergent and divergent flaps and flat (internally) sidewalls to contain the exhaust flow in the lateral direction. The nozzle geometry

was based on a previous design described in reference 9. In an effort to improve off-design nozzle performance across a wide operating range (through the use of shock-boundary layer interaction control), each nozzle divergent flap surface was modified with a porous cavity.

Porous cavities. Most research into porous cavity applications has been to study reduction of shock-induced, boundary-layer separation on transonic airfoils (refs. 10 and 11). Additional research has been performed using a porous cavity and vortex generators on wind tunnel bumps and in wind tunnel normal shock regions (refs. 12 and 13). Figure 4 illustrates the porous cavity concept for shock-boundary layer interaction control originally proposed at NASA Langley Research Center in 1979 (ref. 14). This concept consists of a porous cavity located in the shock-boundary layer interaction region. As shown in figure 4, high pressure downstream of the shock induces flow into the cavity, which exits into the low pressure region upstream of the shock, producing an upstream blowing/downstream suction flow. The porosity of the porous surface is typically kept low to minimize cavity flow and associated effects when a shock is not present over the porous region.

In terms of boundary-layer separation alleviation, the porous cavity functions in two distinct ways. First, the upstream blowing mechanism increases pressure communication across the shock and generates weak oblique waves ahead of the main shock; this extends the shock-boundary layer interaction region further upstream and causes a more gradual isentropic pressure rise, a weaker shock system, and a reduction in the tendency for exhaust flow separation to occur (ref. 12). Second, suction downstream of the shock suppresses boundary-layer separation by reducing possible flow separation regions and damping unsteady effects of the shock-boundary layer interaction (ref. 13).

Nozzle Models

The model used in this investigation was a sub-scale, nonaxisymmetric, C-D nozzle with an

expansion ratio A_e/A_t of 1.797 ($NPR_d=8.78$), a nominal throat area A_t of 4.317 in², and a constant flow path width of 3.990 in. The model was composed of upper and lower nozzle flap assemblies (each equipped with interchangeable divergent flap inserts) and two sidewall assemblies (each equipped with optical quality boro-silicate crown glass windows to permit internal focusing schlieren flow visualization). The model was designed with 28 pairs of interchangeable divergent flap inserts including one baseline (no porosity) and 27 porous configurations. A photograph, sketch, and geometric details of the nozzle model with baseline flap inserts installed are presented in figures 5, 6, and 7, respectively. Photographs of the porous flap inserts and a typical porous nozzle configuration are presented in figure 8.

Geometric details of the porous flap inserts are presented in figure 9. Each porous nozzle configuration was assembled by using pairs of porous flap inserts (one each installed in the upper and lower nozzle divergent flap), with the upper flap insert instrumented with static pressure taps. Geometric variations in the porous flap insert pairs included percent open porosity (10%, 20%, and 30%), hole diameter d (0.025 in., 0.052 in., and 0.076 in.), and cavity depth D (shallow, medium, and deep); this resulted in a 3x3x3 test matrix (27 configurations).

Instrumentation

Weight-flow rate of high-pressure air supplied to the nozzle was calculated from pressures and temperatures measured in a calibrated multiple-critical venturi system located upstream of the propulsion simulation system. This venturi system is the same airflow-measurement system used in the 16-Foot Transonic Tunnel, and is rated to be 99.9% accurate in weight-flow measurements. Forces and moments were measured by a six-component strain-gauge balance located on the centerline of the propulsion simulation system. Jet total pressure was measured at a fixed station in the instrumentation section with a four-probe rake through the upper surface and a three-probe rake through the corner

as shown in figure 3(b). Two iron-constantan thermocouples in the instrumentation section measured jet total temperature.

Static pressures were measured inside the nozzle for each configuration using 0.020-inch diameter static pressure orifices as shown in figure 10. There were six static pressure orifices in the nozzle convergent section and one orifice at the geometric throat (fig. 10(a)), located on the nozzle centerline ($z=0.000$ in.). The flap inserts were equipped with a row of centerline and sideline (0.400 inches from the sidewall) pressure orifices, each containing 21 static pressure orifices spaced 0.100 inches apart. Unique to the porous configurations were three static pressure orifices located on the floor of the porous cavity at $z=-0.200$ in. as shown in figure 10(c).

Individual pressure transducers were used to measure pressures in the air supply system, multiple-critical venturi, instrumentation section, and nozzle convergent section. The transducers were selected and sized to allow the highest accuracy over each required measurement range. Divergent flap pressures were measured by two electronically scanning pressure modules located in an acoustically shielded cabinet in the model preparation area test chamber.

Data Reduction

Each data point is the average steady-state value computed from 50 frames of data taken at a rate of 10 frames per second. All data were taken with ascending NPR. A detailed description of the procedures used for data reduction in this investigation can be found in reference 7.

Balance corrections. Each of the six measured balance components were initially corrected for model weight tares and isolated balance component interactions. Although the bellows arrangement in the air pressurization system was designed to minimize forces on the balance caused by pressurization, small bellows tares on the six-component balance still existed. These tares resulted from small pressure differences between the ends of the bellows when

air system internal velocities were high and from small differences in the spring constant of the forward and aft bellows when the bellows were pressurized. Bellows tares were determined by testing Stratford choke calibration nozzles with known performance over a range of expected internal pressure and external forces and moments. The resulting tares were then applied to the six-component balance data to obtain corrected balance measurements. Balance axial force obtained in this manner is a direct measurement of the nozzle thrust along the body axis, F . The procedure used for computing bellows tares is discussed in detail in reference 15.

Calculations. Jet total pressure was measured from four center rake and three corner rake total pressure probes located in the instrumentation section. Nozzle pressure ratio (NPR) is the average jet total pressure $p_{t,j}$ measured in the instrumentation section divided by ambient pressure p_a ; NPR was varied in this investigation from 1.25 to approximately 9.50. Jet total temperature $T_{t,j}$ was obtained from two total temperature probes located in the instrumentation section. The average jet total pressure and jet total temperature are computed as the arithmetic mean of the individual measurements.

Nozzle thrust ratio F/F_i is the ratio of measured thrust along the body axis F to the computed ideal isentropic thrust F_i . The measured weight-flow rate w_p , determined by the multiple-critical venturi system, is used to compute ideal isentropic thrust from the following equation:

$$F_i = w_p \sqrt{\frac{R_j T_{t,j}}{g^2} \frac{2\gamma}{\gamma - 1} \left[1 - \left(\frac{1}{NPR} \right)^{(\gamma-1)/\gamma} \right]}$$

Uncertainty Analysis

An uncertainty analysis of the results presented was performed based on a propagation of bias uncertainties of actual measurements through the data reduction equations. This analysis assumes that bias errors are dominant

over precision errors and is based on the method presented in reference 16. This method uses the first order terms in a Taylor series expansion of the data reduction equations to estimate the uncertainty contributions of each measurement. With this technique, the contribution of each measurement would be the measurement uncertainty multiplied by the derivative of the data reduction equation with respect to that measurement. The total uncertainty of the final calculated result is estimated as the root-sum-square of the individual contributions with 95-percent confidence.

The analysis accounted for the uncertainties of the following measurements; jet total pressure, jet total temperature, atmospheric pressure, venturi weight-flow rate, and balance axial force. The analysis also accounted for the beneficial effect of averaging multiple measurements of the same quantity, such as the total pressure in the instrumentation section. This type of analysis is typical of that used for experimental static test programs and is credited to the work presented in reference 17.

The results of the analysis for the range of test conditions indicate that the uncertainty of NPR and $p/p_{t,j}$ is approximately ± 0.28 percent of measured value. The uncertainty of F/F_i is approximately ± 0.004 and is essentially independent of NPR. Although some of the differences seen in the dataset are smaller than the thrust-ratio uncertainty of 0.004, relative comparisons between data points are still valid because the uncertainty analysis was based on the assumption that bias errors are dominant over precision errors. Bias errors are fixed errors and apply uniformly to all data points acquired with the same instrumentation and calibrations; therefore, they do not affect relative differences between data points.

Focusing Schlieren Flow Visualization

A focusing schlieren flow visualization system was used during this investigation to visualize the nozzle internal (through glass sidewalls) and external exhaust flowfield. An optical description

and schematic layout of the focusing schlieren system are presented in figure 11. The system was designed and built based on criterion reported in reference 18. The system is characterized by a 133 mm diameter field of view, sensitivity of 17 arcsec, resolution of 0.25 mm, depth of sharp focus of 4.6 mm, and depth of unsharp focus of 36 mm. The image was focused on the centerline of the nozzle.

The light source for the focusing schlieren system was a xenon strobe flash tube. A driving circuit picked up sync pulses generated by the recording video camera and triggered the flash at a rate of 30 Hz with pulses of 0.6 μ sec duration and 0.05 watt-sec power. A 720 x 480 pixel resolution color camera recorded video and a 70 mm still camera recorded stop-motion images.

The focusing schlieren system was assembled on a 44 x 66 inch table that mounted on a rigid platform equipped with casters and leveling screws. The platform was placed under the propulsion simulation system and jacked and leveled to the appropriate position. Flow visualization data were recorded simultaneously with other data acquisition.

Presentation of Results

A description of nozzle configurations tested is presented in table 1. Nozzle thrust ratio F/F_i and internal static pressure ratio $p/p_{t,j}$ data for nozzle configurations 1 to 28 are tabulated in table 2 and tables 3 to 30, respectively. During the discussion of results, comparisons of nozzle thrust ratio F/F_i are made in terms of percentage change from ideal ($F/F_i=1$) isentropic conditions. Graphical presentation of basic and summary data are presented in figures 12 to 59.

Results and Discussion

On-Design Performance

Baseline configuration. Nozzle thrust ratio F/F_i performance for the baseline (no porosity) configuration is presented as a function of nozzle pressure ratio (NPR) in figure 12. Peak thrust

ratio $(F/F_i)_{\text{peak}}$ for the baseline configuration is approximately 0.986 near the on-design condition ($\text{NPR}_d=8.78$), which is within the 0.985 to 0.990 range consistent with previous studies of nonaxisymmetric convergent-divergent nozzles (refs. 19 to 21). The approximate 1.4% loss in peak thrust ratio from ideal isentropic conditions at NPR_d can be attributed to exit flow angularity effects and friction drag inside the nozzle (ref. 22).

Porous configurations. When an exhaust nozzle is operating at the on-design condition, the flow is fully expanded and peak nozzle thrust ratio is produced. Therefore, the presence of porous cavities in the divergent section of the nozzle would most likely result in on-design performance penalties. In an actual aircraft application, it is envisioned that the porous nozzle concept could employ a simple mechanism (i.e., a sliding plate) capable of varying porosity or closing off the porous cavities altogether (if losses are severe enough) in order to maintain optimum nozzle performance.

Peak nozzle thrust ratio $(F/F_i)_{\text{peak}}$ performance for baseline and porous configurations, measured at $\text{NPR}=8.9$, is presented in table 31. All porous configurations had $(F/F_i)_{\text{peak}}$ near NPR_d that were slightly lower than the baseline value of 0.986, ranging from a low of 0.980 to a high of 0.984. To determine peak thrust ratio trends for the porous configurations, a “response plot” was generated for each cavity depth D by plotting $(F/F_i)_{\text{peak}}$ against hole diameter d and percent porosity in figure 13. While it is difficult to establish exact trends with the limited number of configurations tested, there is a general trend of $(F/F_i)_{\text{peak}}$ increasing with decreasing porosity and increasing hole diameter. Likely causes of this trend are surface roughness of the porous plates and porous cavity flow effects. The few configurations that seem to contradict this trend may be statistically insignificant as the differences in $(F/F_i)_{\text{peak}}$ and the general trend fall within the uncertainty of the data.

Effect of surface roughness. Surface roughness of the porous plates is dependent on

both percent porosity and hole diameter. For a fixed hole diameter, increasing porosity results in more holes and greater effective surface roughness. Likewise, for a fixed porosity, decreasing hole diameter also results in more holes and greater effective surface roughness. In either case, greater effective surface roughness will increase nozzle skin friction drag and decrease nozzle thrust ratio.

The effect of surface roughness on exhaust flow characteristics at $\text{NPR}=8.9$ for porous configurations with constant hole diameter and cavity depth is illustrated in the flow visualization photographs of figure 14. Compared to the baseline configuration at the same NPR (fig. 15), each porous configuration had substantially greater Mach wave radiation emanating from the divergent flaps. While such radiation is generally an isentropic mechanism, it does indicate that there were more surface disturbances, and hence an effectively rougher nozzle surface for the porous configurations. The comparison of flow visualization photographs in figure 14 shows a noticeable increase in wave radiation as porosity, and hence surface roughness, increased.

Effect of porous cavity flow. Porous cavity flow is also dependent on both percent porosity and hole diameter, since this effect is governed by the entrainment of flow into the cavities through the porous plates (ref. 23). A comparison of internal static pressure ratio distributions at $\text{NPR}=8.9$ for baseline and porous configurations with 20% porosity and a deep cavity is presented in figure 16. Nozzle internal static pressure ratio $p/p_{t,i}$ is plotted against the nondimensionalized pressure tap location relative to the nozzle throat, x/x_r . The porous configurations had static pressure ratio distributions nearly identical to the baseline configuration upstream and downstream of the nozzle porous region. Over the porous region, all three porous configurations had varying signs of cavity flows: expansion over the leading and trailing edges of the cavities (surface static pressure ratio decreasing more rapidly for porous configurations than the baseline configuration), an impingement flow recompression (increasing $p/p_{t,i}$) past the leading

expansion, and near constant pressures inside the cavities. Configuration 5 (fig. 16(a)), which had the smallest hole diameter, was characterized by little flow adjustment between leading and trailing expansion fans (surface pressures approached a near constant value in the porous region). This is an expected result of the porous cavities, which tend to equalize surface pressures across the porous region of the nozzle. The cavity pressures agreed well with surface pressures in this case, indicating that there was probably some combination of cavity flow and recirculation leading to near constant pressure in the cavities. Cavity flow entrainment decreased as hole diameter increased; this is indicated by a decrease in the difference between baseline and porous static pressure ratio distributions with increasing hole diameter in figure 16.

By subtracting baseline surface pressures from those of porous configurations with 20% porosity and a deep cavity, general pressure gradient effects of the nozzle geometry were eliminated (i.e., an effective flat plate scenario was created). The resulting adjusted static pressure ratio distributions ($p/p_{i,j}$)_{adj}, presented in figure 17, isolate the effects of the porous cavities and show no effect of hole diameter d on the pressure rise through the cavity floor impingement (i.e., cavity static pressure ratio distributions are constant with changing d). However, the pressure rise on the surface of the porous plate and the strength of cavity leading and trailing edge expansions decreased with increasing hole diameter, indicating that cavity flow decreased with increasing d . As a result, external flow over the porous region was less affected by the porous cavities at the higher hole diameters and the effects of porous cavity flow on $(F/F_i)_{peak}$ were smaller.

The fact that cavity flow decreased as hole diameter increased seems contradictory, since it would be expected that larger hole diameters would result in more cavity flow. However, it is important to note that, with a fixed porosity, increasing hole diameter results in fewer holes and a smaller distribution of open area (hole size relative to hole spacing). Given the fact that

nozzle boundary layer displacement thickness is approximately one order of magnitude less (ref. 24) than even the smallest hole diameter tested, it is unlikely that boundary layer/hole diameter scaling had any effect on cavity entrainment for the range of hole diameters tested; thus, an increase in the open area distribution resulted in increased cavity entrainment. This would not necessarily be the case for situations where the boundary layer displacement thickness and porous surface hole diameters were of the same order of magnitude.

Based on surface and cavity pressure data, a sketch of the flowfield over the porous region at $NPR=8.9$ was constructed as shown in figure 18. The streamline pattern in this sketch is one that could fit the pressure gradient measured for configuration 5 (fig. 17(a)), and suggests an effective change in the geometry of the nozzle divergent section due to the porous cavities. This flowfield shows strong resemblance to transitional-closed cavity flow, which is illustrated in figure 19 and discussed in detail in reference 23. In transitional-closed cavity flow, local flows over the front and rear of the cavities are similar to supersonic flows over rearward- and forward-facing steps, respectively, resulting in low pressures acting on the rearward-facing front step and high pressures acting on the forward-facing aft step. From the standpoint of nozzle performance, these cavity pressures act to generate an internal drag that reduces nozzle thrust ratio. As a result, the configurations with the most cavity flow (smaller hole diameter) had higher internal drag penalties and lower $(F/F_i)_{peak}$.

Effect of cavity depth. The general peak thrust ratio trend for both hole diameter and percent porosity comes about from their mutual dependence on determining both surface roughness and porous cavity flow effects. However, a comparison of the three response plots in figure 13 shows no clear trend associated with cavity depth at the on-design condition. A comparison of static pressure distributions at $NPR=8.9$ for baseline and porous configurations with 30% porosity and $d=0.025$ in. is presented in figure 20. All three cavity depths show similar

signs of cavity flow, however, notable differences emerge when plotted with the baseline pressure gradient removed. These plots are presented in figure 21, and show that as cavity depth decreased, flow over the porous region changed from transitional-closed cavity flow to closed cavity flow. Closed cavity flow is characterized by a "pressure plateau" (ref. 24) in the impingement region, as shown in figure 22. In general, closed cavity flow results in higher cavity drag levels, but in this investigation, an increase in thrust ratio (or a decrease in cavity drag) occurred with the onset of closed cavity flow. A comparison of static pressure ratio distributions in figure 21 shows little or no difference among the three cavity depths outside of the small plateau present in the shallow cavity configuration. This suggests that lower cavity drag at the shallow cavity depth was the result of the same pressures acting on smaller rearward and forward facing steps.

Off-Design Performance

Baseline configuration. As shown in figure 12, nozzle thrust ratio decreased as NPR decreased below NPR_d ; a result of exhaust flow overexpansion effects. Internal static pressure ratio distributions for the baseline configuration, presented in figure 23, are typical of convergent-divergent nozzle flow characteristics (ref. 25). For centerline pressures ($z=0.00$ in.), the first two curves at NPRs of 1.26 and 1.42 indicate choked ($p/p_{t,j} \leq 0.528$), internally overexpanded flow with a weak shock (noted by the significant increase in $p/p_{t,j}$ with x/x_t) present near the nozzle geometric throat ($x/x_t=1.00$). Flow downstream of the shock was subsonic ($p/p_{t,j} > 0.528$), remained attached to the divergent flap wall, and recovered to ambient pressure ($p/p_{t,j}=1/NPR$) in a smooth, continuous fashion. Flow visualization for the baseline configuration is shown in figure 24. At $NPR=1.4$ (fig. 24(a)), there was a weak, almost normal shock downstream of the throat with little or no lambda foot structure evident. This behavior is characteristic of a weak shock, with a flow Mach number of approximately 1.2 just upstream of the shock (M_t), and a thin boundary layer inside the nozzle. Flow Mach number inside the nozzle was

estimated from $p/p_{t,j}$ values using tables for compressible flow in reference 26.

As shown in figure 23, the discontinuous nature of the centerline static pressure ratio distribution at $NPR=1.6$ indicates that shock strength increased ($M_t \approx 1.4$), and the inflection point in the pressure recovery downstream of the shock at $x/x_t \approx 1.28$ indicates that flow separation occurred on the divergent flaps, though it was not severe. The pressure ratio distribution also indicates that the flow became subsonic downstream of $x/x_t \approx 1.55$ and flow reattachment to the flap is indicated by the smooth pressure recovery downstream of this point. By $NPR=1.8$, the upstream shock Mach number was $M_t \approx 1.5$, and shock-induced, boundary-layer separation began to dominate nozzle flow characteristics. At $NPR=1.8$, there are strong signs of a separation bubble, with minimal pressure recovery indicated by a relatively flat pressure distribution from the shock location at $x/x_t \approx 1.35$ to $x/x_t \approx 1.70$; however, full recovery to ambient pressure occurred over the remaining length of the nozzle. Flow visualization at $NPR=1.8$ in figure 24(b) shows the shock with a small lambda foot structure. The flow was also highly unstable; this phenomena was observed in the schlieren video recorded during the test and is indicated by the schlieren photograph, which captured an image of the shock in two positions over a 0.6 μ sec duration. Because the image was focused on the centerline of the nozzle with a depth of sharp focus of 4.6 mm, the dual-shock nature of this photo should not be attributed to an alignment problem.

An increase in pressure ratio to $NPR=2.0$ did not significantly change shock location or strength, but did result in fully detached, shock-induced separation with almost no pressure recovery downstream of the shock (fig. 23). Flow visualization at $NPR=2.0$, presented in figure 24(c), shows the shock with a pronounced lambda foot structure and a large separation region extending from the leading lambda foot downstream past the nozzle exit. The results discussed above indicate that the nozzle flow adjusted to exit conditions at $NPR=2.0$ simply by detaching from the divergent flaps, while

normalized pressure (and thus Mach number) upstream of the shock matched those of the previous NPR. This behavior indicates that the onset of fully detached flow separation at $NPR=2.0$ was not the result of a stronger shock-boundary layer interaction, but instead came about through the natural tendency of overexpanded exhaust flow in a fixed-geometry nozzle to conserve mass, momentum, and energy by detaching from the divergent flaps and "adjusting" to an effectively shorter nozzle with a lower expansion ratio.

As shown in figure 12, the onset of fully detached, shock-induced, boundary-layer separation at $NPR=2.0$ corresponds to a marked increase in nozzle thrust ratio. By providing an effectively lower nozzle expansion ratio, internal flow separation reduced overexpansion losses in the nozzle and increased nozzle thrust ratio. It should be noted that this beneficial effect may not exist at forward speeds where external flow could aspirate the separated portion of the divergent flaps, causing increased drag. As a result, the ability to alleviate separation inside a fixed-geometry nozzle may be beneficial to overall aeropropulsive performance at forward speeds, even if small losses in nozzle thrust ratio occur as a result of the separation alleviation process. The information required to make the tradeoff between allowing separation to occur or alleviating separation in the nozzle is beyond the scope of this investigation.

As shown in figure 23, fully-detached flow separation occurred for all subsequent internally overexpanded NPRs above 2.0. As NPR was increased beyond 2.0, the leading lambda foot progressed downstream in the nozzle. Figure 24(d) shows the shock at $NPR=2.4$ with a well defined lambda foot structure and fully detached flow separation. By $NPR=3.4$ (fig. 24(e)), the lambda foot structure had grown significantly, such that the main shock and trailing lambda foot were outside the nozzle. At this NPR, flow inside the nozzle past the separation point showed strong resemblance to externally overexpanded exhaust flow (ref. 25); the jet plume necked down from the separation point at the leading lambda foot to

the trailing lambda foot, and there was an expansion fan emanating from each trailing lambda foot. This behavior indicates that the separation point was behaving as if it were the nozzle exit, and flow past this point was externally overexpanded. Static pressure distributions in figure 23 indicate that the shock was positioned near the nozzle exit by $NPR=5.0$ and that the nozzle was shock free by $NPR=5.4$. At $NPR \geq 5.4$, all pressure distributions fell on the same curve, indicating that nozzle internal flow characteristics were independent of NPR beyond that point.

A comparison of sideline ($z=1.595$ in.) to centerline ($z=0.000$ in.) internal static pressure ratio distributions in figure 23 indicates noticeable differences at $NPR < 2.4$. Differences between sideline and centerline static pressure ratio distributions in both shock location and pressure recovery past the shock indicate that flow inside the nozzle was three-dimensional and that the shock was non-planar. Sideline data at NPRs of 1.26 and 1.42 show fully-detached flow separation and a shock location upstream of its centerline position. In addition, sideline pressure ratios near the nozzle exit are lower than centerline pressure ratios; this indicates that sideline flow was recompressing outside the nozzle.

The sideline location of the shock neared its centerline location at $NPR=1.6$, and sideline pressure ratio was approximately equal to centerline pressure ratio at the nozzle exit. At $NPR=1.8$, the shock moved downstream of its centerline location, and the pressure ratio at the exit was higher at the nozzle sideline. By $NPR=2.4$, centerline and sideline pressure ratios at the nozzle exit were equal and remained that way for all subsequent NPRs. The same was true for centerline and sideline shock locations at $NPR > 3.0$. Sideline pressure ratios show good agreement with centerline pressure ratios, indicating that flow was well behaved and two-dimensional at $NPR > 3.0$.

Porous configurations. Recall that exhaust flow separation often improves off-design thrust

ratio performance by allowing a nozzle to effectively “adjust” to a shorter nozzle with a lower expansion ratio. At forward flight speeds, however, external flow can aspirate the separated portion of the nozzle divergent flaps causing increased drag. In some instances, separation alleviation may be desirable for maximum aeropropulsive (thrust-minus-drag) performance.

Thrust ratio performance for baseline (no porosity) and all porous configurations, discussed in the Appendix, indicate that the presence of the porous cavity added the ability to control off-design separation in the nozzle, by either alleviating separation or encouraging stable separation of the exhaust flow. Data for selected configurations will be presented and used to discuss representative results for each category.

Separation alleviation. Porous configurations with low porosity and large hole diameter generally reduced off-design nozzle performance relative to the baseline (no porosity) configuration, indicating that these configurations were most effective at alleviating separation. To better understand the separation alleviation behavior of porous configurations with low porosity and large hole diameter, the performance of configuration 20 (10% porosity/0.076 in. hole diameter/deep cavity) is examined in detail. Configuration 20 was chosen because, based on low nozzle thrust ratio performance, it appeared to be most effective at alleviating flow separation in the nozzle across the widest NPR range.

As shown in figure 25, configuration 20 (10%/0.076/deep) had lower nozzle thrust ratio performance than the baseline configuration across the entire NPR range investigated. Static pressure ratio distributions for configuration 20, presented in figure 26, show the nozzle shock located in the porous region at NPRs from 1.81 to 3.41. A comparison of centerline, internal static pressure ratio distributions for configuration 20 and the baseline configuration, presented in figure 27, shows the porous cavity affected nozzle flow characteristics across the entire NPR range investigated.

At $NPR < 1.81$, the shock was located upstream of the porous region and F/F_i for configuration 20 was as much as 3.2% lower than the baseline configuration. The agreement between centerline and sideline static pressure ratio distributions at these NPRs in figure 26 indicates that flow in the nozzle was well behaved and two dimensional. There were also no large areas of separated flow in the nozzle at either the centerline or sideline location. Flow characteristics for configuration 20 are significantly different than the baseline configuration, which had fully-detached flow separation at the sideline and three-dimensional flow inside the nozzle. This indicates that the porous cavity was providing some subsonic separation alleviation in the divergent section of the nozzle.

A comparison of surface and cavity static pressure ratio distributions for configuration 20 at $NPR \leq 1.81$ is presented in figure 28. Relative to surface pressures, low pressure in the downstream end of the cavity and high pressure in the upstream end of the cavity suggests that there was upstream flow out of the cavity and downstream flow into the cavity, or upstream blowing/downstream suction. Therefore, an entrainment mechanism reduced separation by simply pulling the exhaust flow towards the divergent flaps along the downstream end of the porous cavity. Reduced separation in the nozzle at overexpanded conditions caused the reduction in F/F_i (relative to the baseline configuration) shown in figure 25.

A comparison of internal static pressure ratio distributions for the baseline configuration and configuration 20 is presented in figure 29. At $NPR = 1.80$, the shock was positioned at the leading edge of the porous region and significant differences in the static pressure ratio distribution between configuration 20 and the baseline configuration are evident (fig. 29(a)). At this NPR, compression through the shock was more gradual, the separated flow region in the nozzle was smaller, and recovery to ambient pressure began sooner for configuration 20 compared to the baseline configuration. However, it wasn’t until $NPR = 2.00$ that the shock was positioned

such that the full separation alleviation effect of the porous cavity was realized; differences in the static pressure ratio distributions (fig. 29(b)) show that the shock was positioned in the porous region and that fully-detached flow separation was alleviated. Focusing schlieren flow visualization at $NPR=2.0$ for configuration 20, presented in figure 30, shows oblique waves emanating from the porous cavity upstream of the shock. These waves intersected the main shock, which had a small lambda foot structure. When coupled with pressure data in figure 29(b), this observation suggests that the porous cavity was functioning as intended, by communicating the shock jump condition and its associated pressure rise upstream. Oblique waves ahead of the main shock helped to spread the shock pressure rise over a longer distance and downstream suction closed the separated region behind the shock. Compared to the baseline case, this resulted in a more gradual compression through the main shock, effectively alleviating separation and providing good downstream pressure recovery.

As shown in figure 31, configuration 20 continued to alleviate separation in the nozzle at NPR 's between 2.0 and 3.0, where the shock was located in the porous region of the nozzle. Flow visualization photographs at NPR s from 2.4 to 3.0, presented in figure 32, show oblique waves emanating from the porous cavity that reduced the severity of the main shock by communicating the shock-jump condition upstream. A comparison of surface and cavity internal static pressure distributions in figure 31, indicates that the blowing/suction mechanism was operating at NPR 's below 3.0. However, the blowing/suction mechanism ceased (indicated by downstream cavity pressures higher than surface pressures) at $NPR=3.0$ where the shock location had moved to the very downstream end of the porous cavity (fig. 31(d)). At this NPR , the porous cavity provided little apparent separation alleviation and the only significant difference in the static pressure ratio distributions between configuration 20 and the baseline configuration is a more gradual compression through the shock for the porous configuration (fig. 31(d)).

At $NPR>3.0$, the porous cavity provided little apparent separation alleviation; the only effect of the porous cavity on static pressure ratio distributions (fig. 27) were local areas of expansion and compression at the leading and trailing edges of the cavities. As shown in figure 33, static pressure ratio distributions in the porous region showed signs of transitional-closed cavity flow, discussed previously, at higher NPR s. This created an internal pressure drag inside the nozzle and caused the reduction in F/F_i (relative to the baseline configuration) at $NPR>3.0$. Static pressure ratio distributions for configuration 20 (fig. 26) show that the shock moved smoothly out of the nozzle with increasing NPR and the nozzle was internally shock free at $NPR>5.42$.

Separation encouragement. Porous configurations with high porosity and small hole diameter generally increased off-design performance, indicating that they were most effective at encouraging separation. To better understand the separation encouragement behavior of porous configurations, the performance of configuration 7 (20% porosity/0.025 in. hole diameter/shallow cavity) is examined in detail. Configuration 7 was chosen because, based on improved nozzle thrust ratio performance, it appeared to be the most effective at encouraging flow separation in the nozzle across the widest NPR range.

As shown in figure 34, configuration 7 (20%/0.025/Shallow) had nozzle thrust ratio performance as much as 1.4% higher than the baseline configuration over an extended NPR range between 2.0 and 4.4. Nozzle internal static pressure ratio distributions for configuration 7, presented in figure 35, show the nozzle shock located over the porous region at NPR s from 1.80 to 4.21. A comparison of centerline, internal static pressure ratio distributions for configuration 7 and the baseline configuration, presented in figure 36, shows that the porous cavity affected static pressure ratio distributions in the nozzle across the entire operating range. For $NPR\leq 1.60$, the shock for configuration 7 was positioned further upstream and was stronger than the baseline configuration. Relative to configuration

20 (fig. 25), low NPR thrust ratio for configuration 7 (fig. 34) was higher and closer to baseline levels.

A comparison of surface and cavity internal static pressure ratio distributions for configuration 7 at NPRs from 1.25 to 1.80, presented in figure 37, shows low pressure in the downstream end of the cavity and high pressure in the upstream end of the cavity, or upstream blowing/downstream suction. While this result is similar to that of configuration 20, a surprising result is the indication of possible flow separation for configuration 7 from $x/x_f \approx 1.30$ to $x/x_f \approx 1.50$ at these NPR values. This result was surprising, since it was expected that configurations with high porosity would have the strongest blowing/suction mechanism, the largest amount of cavity flow, and better separation alleviation. This result indicates that increased cavity flow at the higher porosities actually encouraged the flow to separate from the divergent flaps, which reduced the effective nozzle expansion ratio. Reduced exhaust flow overexpansion for configuration 7 resulted in nozzle thrust ratio performance, relative to configuration 20, that was higher and closer to baseline levels.

At $\text{NPR}=1.80$, the shock moved to the beginning of the porous cavity and remained fixed at that location until $\text{NPR}=3.00$ (fig. 35). As shown in figure 36(b), compression through the shock became more and more gradual as NPR increased and downstream pressure recovery flattened out considerably. Flow visualization photographs for configuration 7, presented in figure 38, show that as NPR increased, the leading branch of the lambda foot remained at the start of the porous cavity while the main portion of the shock moved downstream. In each case, flow separated past the leading lambda foot, and by $\text{NPR}=2.6$ (fig. 38(c)), flow inside the nozzle resembled externally overexpanded flow; the bifurcation point of the lambda foot was near the nozzle centerline and the internal shock system took the form of the first shock cell downstream of the exit of a highly overexpanded nozzle. There was an expansion fan past each trailing lambda foot and an external shock cell was visible

within the field of view of the schlieren system, downstream of the physical nozzle exit.

These results indicate that configuration 7 did not alleviate separation, but instead “encouraged” flow separation (compare shock/separation locations on configuration 7 with those on the baseline configuration in figure 36), resulting in a drastic change in the effective nozzle geometry. This is especially evident in nozzle thrust ratio data presented in figure 34, which showed a steady increase in F/F_i over the baseline value as NPR increased from 2.0 to 2.6, at which point configuration 7 had a thrust ratio of 0.927, 1.4% higher than the baseline value. The reasons for such behavior are not immediately evident, but it is obvious that with a fixed leading lambda foot, onset shock-boundary layer interaction conditions were virtually the same at NPRs from 2.0 to 2.6. In addition, nozzle geometry up to the shock location for configuration 7 was the same as the baseline configuration, indicating that conditions downstream of the shock drove the shock-boundary layer interaction.

Surface and cavity internal static pressure ratio distributions, compared at NPRs from 2.00 to 3.00 in figure 39, show that pressure distributions were nearly constant across the porous region of the nozzle. This suggests that the porous cavity vented the nozzle flap to a constant pressure, and encouraged the natural tendency of the exhaust flow to separate from the divergent flaps. This fixed the “effective” nozzle exit at the most upstream ventilated point, stabilized internal flow separation, lowered the effective expansion ratio of the nozzle, and improved nozzle performance. Since configuration 7 differed from configuration 20 by having a smaller hole diameter but higher porosity, this upstream ventilation mechanism could be attributed to increased cavity flow. Combined with the behavior observed at lower NPR values, this suggests that there was a point (i.e., porosity, hole diameter) at which the blowing/suction mechanism of the porous cavity became too strong, disturbed nozzle flow, and set up a large recirculation region on the nozzle divergent flap.

An increase in NPR to 3.00 eliminated the strong compression that occurred at the beginning of the porous region at NPR's from 1.80 to 2.60 and moved the leading lambda foot downstream in the nozzle. In fact, the pressure distribution in figure 36(c) at $NPR=3.00$ indicates that the nozzle flow partially expanded (decreasing $p/p_{t,i}$) until encountering a weak shock at a point midway along the porous region of the nozzle. The flow visualization photograph at $NPR=3.0$ (fig. 38(d)) shows what appears to be a weak leading lambda foot midway along the porous cavity followed by a separated flow region. By increasing NPR from 2.60 to 3.00, the ventilation mechanism of the porous cavity was overcome and the separated region moved downstream in the nozzle. As separation diminished in the nozzle, overexpansion losses increased and thrust ratio began to decrease back towards the baseline level (fig. 34).

The comparison of static pressure ratio distributions for configuration 7 and the baseline configuration in figure 36 indicate that the porous cavity continued to encourage flow separation in the nozzle at NPRs greater than 3.00. As was the case for configuration 20, static pressure ratio distributions in the porous region showed signs of transitional-closed cavity flow, discussed previously. Losses in F/F_i above $NPR=3.00$ are the result of separation encouragement and internal pressure drag generated by transitional-closed cavity flow. Static pressure ratio distributions for configuration 7 (fig. 35) show that the shock moved smoothly out of the nozzle with increasing NPR and the nozzle was internally shock free at $NPRs>5.40$.

Effect of porosity. The effect of porosity at constant hole diameter and cavity depth is evaluated by comparing data for configurations 20, 23, and 26 (10%, 20%, and 30% porosity, respectively). The effect of porosity on nozzle thrust ratio performance for configurations 20, 23, and 26 is presented in figure 40. Configurations 20 and 23 had nozzle thrust ratios of $F/F_i=0.888$ and $F/F_i=0.909$ at $NPR=2.60$, lower than the baseline value of $F/F_i=0.913$. Configuration 26 had a nozzle thrust ratio of $F/F_i=0.919$, higher

than the baseline. This indicates separation alleviation at 10% and 20% porosity, but a switch to separation encouragement at 30% porosity.

Nozzle internal static pressure ratio distributions for configurations 23 and 26 are presented in figures 41 and 42, respectively. When compared to static pressure ratio distributions for configuration 20 (fig. 26), it is apparent that the amount of separated flow in the divergent section of the nozzle increased with increasing porosity. A comparison of internal static pressure ratio distributions for configurations 20, 23, and 26 at $NPR=2.60$, presented in figure 43, shows significant differences in the location of the porous cavity blowing/suction suction mechanism shock boundary (i.e., the point where the mechanism switches from upstream blowing to downstream suction) between configurations, such that the ability of the porous cavity to extend the shock-boundary layer interaction region upstream is affected. At 20% porosity (configuration 23), there was less distance upstream of the shock over which the blowing mechanism could provide pressure communication across the shock. A comparison of flow visualization photographs at $NPR=2.6$ between configurations 20 (fig. 32(b)) and 23 (fig. 44(a)) shows a noticeable decrease in oblique wave radiation upstream of the main shock and the formation of an external shock cell(s) with increasing porosity. At 30% porosity (configuration 26), all porous cavity blowing/suction occurred downstream of the nozzle shock (fig. 43). As a result, the blowing/suction mechanism at 30% porosity could no longer communicate the shock-jump condition and shock-induced, boundary layer separation occurred in the nozzle as shown in figure 44(b). Apparently, there was enough cavity entrainment for this configuration (e.g., the blowing/suction mechanism was strong enough) to disturb nozzle flow and set up a recirculation region on the nozzle divergent flap, thus encouraging flow separation inside the nozzle.

Effect of hole diameter. The effect of hole diameter at constant porosity and cavity depth is evaluated by comparing data for configurations

20 and 11 (0.076 in. and 0.052 in. hole diameter, respectively). The effect of hole diameter on nozzle thrust ratio performance for configurations 20 and 11 is presented in figure 45. Configurations 20 and 11 had nozzle thrust ratios of $F/F_i=0.888$ and $F/F_i=0.894$ at $NPR=2.60$, lower than the baseline value of $F/F_i=0.913$. This suggests an increase in separation with decreasing hole diameter.

Nozzle internal static pressure ratio distributions for configuration 11 are presented in figure 46. When compared to static pressure ratio distributions for configuration 20 (fig. 26), it is apparent that the amount of separated flow in the divergent section of the nozzle increased with decreasing hole diameter. A comparison of internal static pressure ratio distributions for configurations 20 and 11 at $NPR=2.60$, presented in figure 47, also indicates a shift in the location of the blowing/suction mechanism shock boundary with decreasing hole diameter, such that there was less distance upstream of the main shock over which the shock-jump condition could be communicated by the blowing mechanism. A comparison of flow visualization photographs between configurations 20 (fig. 32(b)) and 11 (fig. 48) shows that both of these configurations generated oblique compression waves upstream of the main shock, though the spacing of these waves was closer at the lower hole diameter as a result of closer hole spacing. However, an external shock cell formed downstream of the main shock when hole diameter was increased. This result is the same as that observed for increasing porosity, which indicates the blowing suction mechanism became less effective at reducing shock severity as hole diameter decreased. Recall that reducing hole diameter results in a greater “distribution” of open area (hole size relative to hole spacing) and increased cavity entrainment. Therefore, the increase in flow separation between configurations 20 and 11 can be attributed to increased cavity entrainment as a result decreasing hole diameter.

Effect of cavity depth. Porosity and hole diameter each had a significant effect on off-design performance. As was the case for on-

design performance, the interaction between porosity and hole diameter comes about from their mutual dependence on determining cavity flow effects. The effect of cavity depth at constant porosity and hole diameter is evaluated by comparing data for configurations 20, 21, and 22 (deep, medium, and shallow cavity depths, respectively). As shown in figure 49, there are only small effects of cavity depth on nozzle thrust ratio performance. Nozzle internal static pressure ratio distributions for configurations 21 and 22, presented in figures 50 and 51, respectively, indicate that both configurations provided effective separation alleviation. A comparison of internal static pressure ratio distributions for configurations 20, 21, and 22 at $NPR=2.60$, presented in figure 52, indicates slightly less pressure communication upstream of the shock via the blowing/suction mechanism with decreasing cavity depth, but a more gradual compression through the shock. Focusing schlieren flow visualization in figure 53 shows attached flow downstream of the shock for configurations 21 (fig. 53(a)) and 22 (fig. 53(b)), but the flow appears to be slightly more turbulent for configuration 22.

Shock-Boundary Layer Interaction

Baseline configuration. Focusing schlieren flow visualization for the baseline configuration at $NPR=3.0$, presented in figure 54, shows the shock with a large, well defined lambda foot structure and fully detached, shock-induced boundary layer separation beginning at the leading branch of the lambda foot and extending downstream. Shock angle measurements were made from figure 54, and were used in conjunction with oblique shock theory (ref. 26) in an effort to better describe the shock-boundary layer interaction as shown by the sketch in figure 55.

Upstream of the leading lambda foot, flow was assumed to be locally parallel to the nozzle divergent flap and M_1 was calculated from $p/p_{t,j}$ values to be approximately 1.8. Flow decelerated across the leading lambda foot which, with an inclination angle β of approximately 52° from the

nozzle divergent flap, resulted in a downstream Mach number M_2 of approximately 1.2. Using oblique shock theory, the flow turning angle θ across the leading lambda foot was calculated to be 15° . The strength of leading lambda foot approached the severity of a normal shock and was strong enough to completely detach nozzle flow from the divergent flaps. From the new flow direction, the trailing branch of the lambda foot had an inclination angle of $\beta=63^\circ$. For $M \approx 1.2$ approaching this shock, the corresponding flow turning angle of the trailing lambda foot was calculated to be $\theta=3^\circ$. This satisfied flow turning requirements of the fully detached flow separation region and resulted in nearly axial flow downstream of the trailing lambda foot.

In this shock-boundary layer interaction, it is apparent that the nozzle flap was steep enough and the remaining length of the nozzle past the flow separation point was short enough that reattachment would not occur, since the given shock structure resulted in nearly axial flow in the nozzle. As a result, the free shear layer generated in the flow separation process became the actual exit shear layer of the nozzle and the flow separation point behaved as if it were the nozzle exit.

Porous configurations. Configuration 20 (10%/0.076/Deep) is used in the shock-boundary layer interaction discussion, since this configuration alleviated off-design flow separation in the nozzle across a wide NPR range. Not surprisingly, configuration 20 had shock-boundary layer interaction characteristics that were significantly different from that of the baseline configuration. The flow visualization photograph at $NPR=2.6$ for configuration 20 (fig. 32(c)) shows a large lambda foot structure and three oblique waves upstream of the shock. The fact that these waves did not show up in pressure ratio distributions plotted in figure 26 indicates that they were weak, and upstream blowing from the porous cavity did not greatly disturb the flow. Downstream of the shock system, flow was turbulent, but appeared to be attached.

Shock angle measurements were made from

figure 32(c) and were used in conjunction with oblique shock theory (ref. 26) in an effort to better describe the shock-boundary layer interaction as shown in figure 56. Upstream of the leading lambda foot, flow was parallel to the divergent flap and M_1 was approximately 1.8. Flow decelerated across the leading lambda foot which, with $\beta=45^\circ$ from the nozzle divergent flap, resulted in a downstream Mach number of $M_2 \approx 1.4$, and a flow turning angle of $\theta=10.7^\circ$. In contrast, the leading lambda foot in the baseline case (fig. 41) had a steeper flow inclination angle of $\beta=52^\circ$, a much lower downstream Mach number of $M_2 \approx 1.2$, and a flow turning angle of $\theta=15^\circ$. From the new flow direction indicated in figure 56, the trailing lambda foot for configuration 20 had an inclination angle of $\beta=60^\circ$, which was close to the $\beta=63^\circ$ flow turning angle of the baseline configuration. However, configuration 20 had a higher Mach number of approximately 1.5 approaching the trailing lambda foot shock and the flow turning angle through the trailing lambda foot was $\theta=9^\circ$, much higher than the $\theta=3^\circ$ flow turning angle of the baseline configuration. This result indicates that flow exited the shock-boundary layer interaction region for configuration at an off-axis angle of about 9° , or only 2° off the divergent nozzle flap angle. This is in sharp contrast to the baseline case, in which flow left the trailing lambda foot in a nearly axial direction (about 8° off the nozzle flap angle, see figure 55).

These results substantiate previous findings for the baseline case, namely, that the leading lambda foot sets up the shock-boundary layer interaction. For both configuration 20 and the baseline configuration, the trailing lambda foot had nearly the same flow inclination angle and approximately the same turning potential; however, in the baseline case the leading lambda foot was stronger and steeper, and separated flow past this point could not reattach upon turning through the trailing lambda foot. This resulted in complete separation of the nozzle flow from the divergent flaps. In contrast, the leading compression was weaker in configuration 20, such that the trailing lambda foot turned the separated flow back towards the nozzle flap,

causing flow reattachment to the divergent flap. Combined with flow visualization, this confirms that the blowing/suction mechanism of the porous cavity spread the shock pressure jump over a longer distance, reduced the strength of the leading lambda foot, and resulted in reduced separation in the nozzle.

Active Flow Control

Porous configurations that alleviate shock-induced, boundary-layer separation provide the potential to improve aeropropulsive performance of installed exhaust nozzles by reducing drag on nozzle divergent flaps with little or no on-design performance penalties. Configurations that encourage separation have the potential to improve off-design nozzle thrust ratio at static, low NPR, low Mach number flight conditions such as takeoff and landing. Together, the ability to either alleviate or encourage flow separation inside fixed-geometry exhaust nozzles offers tremendous potential to actively control nozzle flows and improve performance. By designing a fixed-geometry nozzle with porous divergent flaps, where percent open porosity of the flaps could be varied, the porous nozzle concept can also produce thrust vectoring as depicted in figure 57. In this application, sliding plates control the porosity and encourage separation on the upper divergent flap, while alleviating separation on the lower flap. A flow visualization photograph obtained at $NPR=2.0$ and presented in figure 58 shows the results of testing a configuration with a baseline lower flap and a porous cavity that encouraged separation (10%/0.025/Deep) installed on the upper flap. This photo clearly shows the thrust vectoring capability of the porous nozzle concept, which generated approximately 11° of pitch vectoring through shock-boundary layer interaction control.

Conclusions

An investigation was conducted in the model preparation area of the Langley 16-Foot Transonic Tunnel to determine the internal performance (nozzle thrust ratio) of a fixed-geometry exhaust nozzle incorporating porous

cavities for shock-boundary layer interaction control. Testing was conducted at static conditions using a sub-scale, nonaxisymmetric, convergent-divergent nozzle model designed with interchangeable divergent flap inserts. The nozzle model had an expansion ratio (exit area/throat area) of 1.80 and a design nozzle pressure ratio of 8.78. Force, moment, and pressure measurements were taken and internal focusing schlieren flow visualization was obtained for one baseline (no porosity) and 27 porous configurations. An additional configuration with a porous, upper divergent flap insert and a baseline, lower divergent flap insert was tested to evaluate the potential of the porous nozzle concept to generate thrust vectoring. For the porous configurations, the effects of percent open porosity (10%, 20%, and 30%), hole diameter (0.025 in., 0.052 in., and 0.076 in.), and cavity depth (shallow, medium, and deep) on shock-boundary layer interaction control were determined. All tests were conducted with no external flow at nozzle pressure ratios from 1.25 to approximately 9.50. The results of this investigation indicate the following conclusions:

1. Off-design performance for the baseline configuration was dominated by the effects of fully detached, shock-induced boundary layer separation. This separation came about through the natural tendency of overexpanded exhaust flow in a fixed-geometry nozzle to conserve mass, momentum, and energy by detaching from the divergent flaps and "adjusting" to an effectively shorter nozzle with a lower expansion ratio. By providing a lower effective expansion ratio, flow separation reduced overexpansion losses in the nozzle and increased static thrust ratio.
2. The porous nozzle concept demonstrated the ability to control off-design separation in the nozzle by either alleviating or encouraging separation of the exhaust flow. Separation alleviation offers the potential for installed nozzle performance benefits by reducing drag at forward flight speeds, even though it may reduce off-design static thrust ratio by as much as 3.2%. Encouraging stable separation

of the exhaust flow provides significant performance improvements at static, low NPR conditions by improving off-design (overexpanded) static thrust ratio by as much as 1.4%.

3. The ability to alternately alleviate or encourage stable flow separation through active flow control offers tremendous off-design performance benefits for fixed-geometry nozzle installations. By designing a fixed-geometry nozzle with porous divergent flaps, where percent open porosity of the flaps could be varied using sliding plates, active flow control would make it possible to improve nozzle performance across a wide operating and also generate thrust vectoring.

NASA Langley Research Center
Hampton, Virginia 23681-0001
May 17, 1999

Appendix

Individual comparisons of nozzle thrust ratio performance between the baseline (no porosity) and porous configurations, presented in figure 59, are used to establish the shock-boundary layer interaction control characteristics of the porous nozzle concept. Recall that exhaust flow separation often improves off-design thrust ratio performance by allowing a nozzle to effectively "adjust" to a shorter nozzle with a lower expansion ratio. Therefore, porous configurations that generally reduced off-design nozzle performance relative to the baseline configuration were effectively alleviating flow separation in the divergent section of the nozzle. Configurations that alleviated separation generally had low porosity and large hole diameter as shown in table 32. Conversely, configurations that generally increased off-design nozzle performance relative to the baseline configuration were effectively encouraging flow separation in the divergent section of the nozzle. Configurations that encouraged separation generally had high porosity and/or small hole diameter as shown in table 33.

References

1. Stitt, Leonard E.: Exhaust Nozzles for Propulsion Systems With Emphasis on Supersonic Cruise Aircraft. NASA RP-1235, May 1990.
2. Berrier, Bobby L.; and Re, Richard, J.: A Review of Thrust Vectoring Schemes for Fighter Aircraft. AIAA-78-1023, July 1978.
3. Yetter, Jeffrey A.: Why Do Airlines Want and Use Thrust Reversers? NASA TM-109158, January 1995.
4. Asbury, Scott C.; and Carlson, John R.: Transonic Aeropropulsive Performance of Advanced Exhaust Nozzles Designed for Reduced Radar Cross-Section Signatures. NASA TP-3505, April 1995.
5. Gilkey, S. C.; Hines, R.W.: A Joint Propulsion Perspective of the Next Generation Supersonic Transport. AIAA-91-3330, September 1991.
6. Berrier, Bobby L.; and Re, Richard J.: Investigation of Convergent-Divergent Nozzles Applicable to Reduced-Power Supersonic Cruise Aircraft. NASA TP-1766, 1980.
7. Mercer, Charles E.; Berrier, Bobby L.; Capone, Francis J.; and Grayston, Alan M.: Data Reduction Formulas for the 16-Foot Transonic Tunnel—NASA Langley Research Center. Revision 2. NASA TM-107646, 1992.
8. Staff of the Propulsion Aerodynamics Branch: A User's Guide to the Langley 16-Foot Transonic Tunnel Complex, Revision 1. NASA TM-102750, 1990. (Supersedes NASA TM-83186, compiled by Kathryn H. Peddrew, 1981.)
9. Berrier, Bobby L.; and Re, Richard J.: Effects of Several Geometric Parameters on the Static Internal Performance of Three Nonaxisymmetric Nozzle Concepts. NASA TP-1468, 1979.
10. Nagamatsu, H.T.; Trilling, T.W.; and Bossard, J.A.: Passive Drag Reduction on a Complete NACA 0012 Airfoil at Transonic Mach Numbers. AIAA-87-12 63, June 1987.

11. Bauer, S.X.S.; and Hernandez, G.: Reduction of Cross-Flow Shock-Induced Separation with a Porous Cavity at Supersonic Speeds. AIAA-88-2567, June 1988.
12. McCormick, D.C.: Shock-Boundary Layer Interaction Control with Low-Profile Vortex Generators and Porous Cavity. AIAA-92-0064, January 1992.
13. Raghunathan, S.: Passive Shockwave Boundary Layer Control Experiments on a Circular Arc Model. AIAA-86-0285, January 1986.
14. Raghunathan, S.: Passive Control of Shock-Boundary Layer Interaction. Progress in Aerospace Sciences, vol. 25, 1988.
15. Capone, F.J.; Konarski, M.; Stevens, H.L.; and Willard, C.M.: Static Performance of Vectoring/Reversing Non-Axisymmetric Nozzles. AIAA-77-840, July 1977.
16. Coleman, Hugh W.; and Steele, W. Glenn, Jr.: Experimentation and Uncertainty Analysis for Engineers. John Wiley & Sons, 1989.
17. Wing, David J.; Mills, Charles T.L.; and Mason, Mary L.: Static Investigation of a Multiaxis Thrust-Vectoring Nozzle With Variable Internal Contouring Ability. NASA TP-3628, 1997.
18. Weinstein, L.M.: An Improved Large-Field Focusing Schlieren System. AIAA-91-0567, January 1991.
19. Capone, F.J.; Konarski, M.; Stevens, H.L.; and Willard, C.M.: Static Performance of Vectoring/Reversing Non-Axisymmetric Nozzles. AIAA-77-840, July 1977.
20. Re, Richard J.; and Leavitt, Laurence D.: Static Internal Performance Including Thrust Vectoring and Thrust Reversing of Two-Dimensional Convergent-Divergent Nozzles. NASA TP-2253, 1984.
21. Taylor, John G.: Static Investigation of a Two-Dimensional Convergent Divergent Exhaust Nozzle With Multiaxis Thrust Vectoring Capability. NASA TP-2973, 1990.
22. Hunter, Craig A.: An Approximate Theoretical Method for Modeling the Static Thrust Performance of Nonaxisymmetric Two-Dimensional Convergent-Divergent Nozzles. NASA CR-195050, 1995.
23. Stallings, R.L., Jr.; and Wilcox, F.J., Jr.: Experimental Cavity Pressure Distributions at Supersonic Speeds. NASA TP-2683, 1987.
24. Hunter, Craig A.: A Experimental Analysis of Passive Shock-Boundary Layer Interaction Control for Improving the Off-Design Performance of Jet Exhaust Nozzles. M.S. Thesis, The George Washington University, 1993.
25. Liepmann, Hans Wolfgang; and Roshko, Anatol: Elements of Gasdynamics. John Wiley & Sons, Inc., 1957.
26. Staff of NASA Ames Research Center: Equations, Tables, and Charts for Compressible Flow. NASA TR-1135, 1953.

Table 1. Description of Nozzle Configurations

Configuration No.	Flap Inserts	Porosity, %	Hole Dia., in.	Cavity Depth, in.
1	Baseline	0	0	0
2	Porous	10	0.025	0.219
3	Porous	10	0.025	0.119
4	Porous	10	0.025	0.072
5	Porous	20	0.025	0.219
6	Porous	20	0.025	0.119
7	Porous	20	0.025	0.072
8	Porous	30	0.025	0.219
9	Porous	30	0.025	0.119
10	Porous	30	0.025	0.072
11	Porous	10	0.052	0.187
12	Porous	10	0.052	0.087
13	Porous	10	0.052	0.040
14	Porous	20	0.052	0.187
15	Porous	20	0.052	0.087
16	Porous	20	0.052	0.040
17	Porous	30	0.052	0.187
18	Porous	30	0.052	0.087
19	Porous	30	0.052	0.040
20	Porous	10	0.076	0.187
21	Porous	10	0.076	0.087
22	Porous	10	0.076	0.040
23	Porous	20	0.076	0.187
24	Porous	20	0.076	0.087
25	Porous	20	0.076	0.040
26	Porous	30	0.076	0.187
27	Porous	30	0.076	0.087
28	Porous	30	0.076	0.040
29	Porous (Upper)/Baseline (Lower)	10/0	0.025/0	0.219/0

Table 2. Nozzle Thrust Ratio Performance

(a) Configurations 1 to 7

Configuration 1 (Baseline)		Configuration 2		Configuration 3		Configuration 4		Configuration 5		Configuration 6		Configuration 7	
NPR	F/F_i	NPR	F/F_i	NPR	F/F_i	NPR	F/F_i	NPR	F/F_i	NPR	F/F_i	NPR	F/F_i
1.26	0.869	1.25	0.877	1.25	0.856	1.25	0.856	1.25	0.830	1.25	0.853	1.25	0.851
1.40	0.832	1.40	0.826	1.40	0.824	1.40	0.827	1.41	0.806	1.40	0.823	1.40	0.821
1.61	0.837	1.60	0.817	1.60	0.820	1.60	0.823	1.61	0.809	1.60	0.820	1.60	0.820
1.81	0.830	1.80	0.825	1.81	0.825	1.80	0.830	1.81	0.819	1.80	0.829	1.80	0.829
2.01	0.865	2.00	0.861	2.01	0.859	2.00	0.862	2.01	0.853	2.00	0.860	2.00	0.864
2.21	0.882	2.20	0.896	2.21	0.891	2.20	0.894	2.21	0.885	2.20	0.891	2.20	0.895
2.41	0.904	2.40	0.915	2.41	0.909	2.40	0.913	2.41	0.901	2.40	0.909	2.40	0.914
2.61	0.913	3.01	0.939	2.61	0.922	2.60	0.925	2.61	0.913	2.60	0.922	2.60	0.927
3.01	0.924	3.41	0.947	3.01	0.934	3.00	0.936	3.01	0.913	3.00	0.933	3.00	0.937
3.41	0.935	3.81	0.954	3.41	0.941	3.40	0.943	3.41	0.933	3.40	0.940	3.40	0.944
3.82	0.944	4.21	0.953	3.81	0.946	3.80	0.948	3.81	0.945	3.80	0.949	3.79	0.951
4.22	0.951	4.61	0.958	4.22	0.949	4.20	0.951	4.22	0.953	4.20	0.955	4.21	0.953
4.62	0.959	5.01	0.964	4.61	0.955	4.60	0.957	4.62	0.955	4.60	0.956	4.59	0.957
5.02	0.965	5.42	0.969	5.02	0.961	5.00	0.963	5.02	0.959	5.00	0.959	5.00	0.961
5.42	0.971	6.22	0.976	5.42	0.967	5.40	0.968	5.42	0.964	5.40	0.964	5.40	0.966
5.82	0.975	7.03	0.980	6.22	0.974	6.20	0.976	6.23	0.972	6.20	0.971	6.19	0.973
6.23	0.979	8.03	0.983	7.03	0.979	7.00	0.980	7.03	0.976	7.00	0.976	7.00	0.978
7.03	0.983	8.94	0.984	8.03	0.982	8.00	0.983	8.03	0.979	8.00	0.979	7.99	0.981
8.04	0.986	9.51	0.983	8.94	0.983	8.90	0.984	8.94	0.980	8.90	0.980	8.90	0.981
8.94	0.986			9.55	0.983	9.51	0.983	9.55	0.980	9.50	0.980	9.50	0.981
9.54	0.986												

Table 2. Continued
 (b) Configurations 8 to 14

Configuration 8		Configuration 9		Configuration 10		Configuration 11		Configuration 12		Configuration 13		Configuration 14	
NPR	F/F_i	NPR	F/F_i	NPR	F/F_i	NPR	F/F_i	NPR	F/F_i	NPR	F/F_i	NPR	F/F_i
1.25	0.832	1.25	0.847	1.25	0.850	1.26	0.842	1.26	0.842	1.25	0.871	1.26	0.840
1.40	0.811	1.40	0.814	1.40	0.815	1.41	0.815	1.41	0.815	1.40	0.830	1.41	0.808
1.61	0.826	1.60	0.817	1.60	0.816	1.61	0.814	1.61	0.814	1.59	0.825	1.61	0.810
1.80	0.838	1.80	0.826	1.80	0.822	1.81	0.821	1.81	0.821	1.79	0.826	1.81	0.822
2.01	0.850	2.00	0.853	2.00	0.858	2.01	0.847	2.01	0.847	2.00	0.849	2.01	0.860
2.21	0.885	2.20	0.888	2.20	0.888	2.21	0.875	2.21	0.875	2.19	0.876	2.21	0.886
2.41	0.899	2.40	0.906	2.40	0.911	2.41	0.890	2.41	0.890	2.40	0.889	2.41	0.907
2.61	0.900	2.60	0.919	2.60	0.923	2.61	0.894	2.61	0.894	2.59	0.898	2.61	0.917
3.01	0.906	3.00	0.916	3.00	0.923	3.01	0.910	3.01	0.910	3.00	0.911	3.01	0.920
3.41	0.927	3.40	0.930	3.39	0.933	3.42	0.927	3.42	0.927	3.39	0.929	3.41	0.933
3.82	0.939	3.80	0.940	3.80	0.943	3.81	0.935	3.81	0.935	3.80	0.938	3.82	0.935
4.21	0.946	4.20	0.947	4.20	0.948	4.22	0.945	4.22	0.945	4.19	0.947	4.22	0.944
4.62	0.952	4.60	0.953	4.60	0.956	4.62	0.953	4.62	0.953	4.60	0.955	4.62	0.952
5.02	0.958	5.00	0.959	5.00	0.961	5.02	0.960	5.02	0.960	5.00	0.962	5.02	0.960
5.42	0.964	5.40	0.964	5.39	0.966	5.42	0.966	5.42	0.966	5.39	0.971	5.42	0.965
6.22	0.972	6.20	0.971	6.20	0.973	6.23	0.975	6.23	0.975	6.20	0.977	6.23	0.974
7.03	0.976	6.99	0.976	7.00	0.978	7.03	0.980	7.03	0.980	6.99	0.981	7.03	0.978
8.03	0.979	7.99	0.979	8.00	0.980	8.03	0.983	8.03	0.983	7.99	0.983	8.03	0.981
8.94	0.980	8.92	0.980	8.90	0.982	8.96	0.983	8.96	0.983	8.89	0.983	8.94	0.982
9.53	0.980	9.38	0.992	9.49	0.981	9.54	0.983	9.54	0.983	9.50	0.983	9.54	0.983

Table 2. Continued

(c) Configurations 15 to 21

Configuration 15		Configuration 16		Configuration 17		Configuration 18		Configuration 19		Configuration 20		Configuration 21	
NPR	F/F_i												
1.24	0.857	1.25	0.848	1.25	0.839	1.25	0.850	1.25	0.833	1.26	0.841	1.25	0.852
1.39	0.824	1.40	0.815	1.40	0.823	1.40	0.819	1.40	0.807	1.40	0.808	1.40	0.827
1.59	0.821	1.59	0.808	1.60	0.827	1.60	0.819	1.60	0.809	1.61	0.805	1.60	0.823
1.80	0.830	1.80	0.818	1.80	0.834	1.80	0.827	1.80	0.818	1.81	0.815	1.80	0.829
1.99	0.864	2.00	0.853	2.00	0.858	2.00	0.863	2.00	0.855	2.01	0.837	2.00	0.847
2.19	0.893	2.20	0.886	2.20	0.894	2.20	0.889	2.20	0.887	2.21	0.863	2.19	0.874
2.39	0.911	2.40	0.905	2.41	0.910	2.40	0.909	2.40	0.907	2.41	0.877	2.39	0.884
2.60	0.924	2.60	0.916	2.61	0.924	2.60	0.922	2.60	0.920	2.61	0.888	2.60	0.894
2.99	0.923	3.00	0.917	3.01	0.935	3.00	0.930	3.00	0.928	3.01	0.905	2.99	0.910
3.39	0.935	3.40	0.930	3.41	0.942	3.40	0.935	3.40	0.935	3.41	0.921	3.40	0.925
3.79	0.939	3.80	0.935	3.81	0.950	3.80	0.944	3.80	0.946	3.81	0.933	3.80	0.936
4.19	0.947	4.20	0.945	4.21	0.950	4.20	0.946	4.20	0.948	4.21	0.945	4.19	0.946
4.59	0.955	4.60	0.954	4.62	0.955	4.60	0.952	4.60	0.953	4.62	0.953	4.59	0.955
4.99	0.961	5.00	0.961	5.01	0.961	5.00	0.958	5.00	0.960	5.02	0.961	4.99	0.961
5.39	0.966	5.39	0.966	5.42	0.966	5.40	0.965	5.40	0.965	5.42	0.967	5.39	0.968
6.19	0.974	6.20	0.974	6.22	0.974	6.20	0.973	6.20	0.973	6.22	0.975	6.20	0.976
6.99	0.979	7.00	0.979	7.02	0.978	7.00	0.977	7.00	0.979	7.03	0.980	7.00	0.981
7.99	0.982	8.00	0.982	8.03	0.981	8.00	0.980	8.00	0.981	8.03	0.983	7.99	0.983
8.90	0.983	8.90	0.982	8.94	0.981	8.91	0.981	8.90	0.981	8.94	0.983	8.90	0.984
9.55	0.983	9.50	0.983	9.55	0.982	9.50	0.981	9.50	0.981	9.53	0.984	9.50	0.984

Table 2. Concluded
(d) Configurations 22 to 28

Configuration 22		Configuration 23		Configuration 24		Configuration 25		Configuration 26		Configuration 27		Configuration 28	
NPR	<i>F/F_i</i>												
1.25	0.855	1.25	0.846	1.25	0.856	1.25	0.854	1.25	0.829	1.25	0.851	1.25	0.845
1.40	0.823	1.40	0.816	1.40	0.826	1.40	0.817	1.40	0.805	1.40	0.823	1.40	0.813
1.60	0.818	1.60	0.811	1.60	0.821	1.60	0.809	1.60	0.808	1.60	0.818	1.60	0.808
1.80	0.822	1.81	0.822	1.80	0.829	1.80	0.819	1.80	0.818	1.80	0.826	1.80	0.820
2.00	0.845	2.01	0.856	2.00	0.856	2.00	0.848	2.00	0.851	2.00	0.857	2.00	0.853
2.20	0.867	2.21	0.885	2.20	0.888	2.20	0.881	2.21	0.885	2.20	0.886	2.20	0.881
2.40	0.880	2.41	0.902	2.40	0.903	2.40	0.899	2.41	0.905	2.40	0.904	2.40	0.902
2.60	0.891	2.61	0.909	2.60	0.911	2.60	0.907	2.61	0.919	2.60	0.919	2.60	0.915
3.00	0.906	3.01	0.908	3.00	0.908	3.00	0.907	3.01	0.918	2.99	0.913	3.00	0.916
3.40	0.922	3.41	0.921	3.40	0.921	3.40	0.921	3.41	0.931	3.40	0.927	3.40	0.929
3.80	0.933	3.81	0.931	3.80	0.930	3.80	0.931	3.81	0.934	3.80	0.933	3.80	0.934
4.20	0.944	4.21	0.942	4.20	0.942	4.20	0.942	4.21	0.944	4.20	0.942	4.20	0.944
4.60	0.953	4.61	0.952	4.60	0.952	4.60	0.952	4.62	0.953	4.60	0.951	4.60	0.952
5.00	0.961	5.02	0.960	5.00	0.959	5.00	0.960	5.02	0.962	5.00	0.958	5.00	0.959
5.40	0.966	5.42	0.966	5.40	0.965	5.40	0.966	5.42	0.968	5.40	0.964	5.40	0.966
6.20	0.975	6.26	0.974	6.20	0.974	6.20	0.974	6.22	0.973	6.20	0.972	6.20	0.974
6.99	0.980	7.02	0.979	6.99	0.978	7.00	0.979	7.03	0.978	7.00	0.978	7.00	0.978
8.00	0.982	8.03	0.982	8.00	0.981	8.00	0.982	8.03	0.980	8.00	0.981	8.00	0.981
8.90	0.983	8.95	0.982	8.90	0.982	8.90	0.983	8.94	0.980	8.90	0.982	8.90	0.981
9.49	0.983	9.31	0.983	9.50	0.982	9.49	0.982	9.54	0.980	9.50	0.982	9.51	0.982

Table 3. Nozzle Internal Static Pressure Ratios for the Baseline Configuration

(a) Convergent Flap, $z = 0.000$ $p/p_{t,j}$ at x/x_f of

NPR	0.330	0.440	0.550	0.659	0.769	0.890	1.000
1.26	0.959	0.946	0.930	0.903	0.856	0.681	0.448
1.40	0.958	0.945	0.927	0.899	0.850	0.671	0.391
1.61	0.957	0.943	0.927	0.899	0.849	0.670	0.369
1.81	0.958	0.943	0.928	0.899	0.850	0.670	0.369
2.01	0.958	0.942	0.927	0.899	0.849	0.670	0.368
2.21	0.958	0.943	0.929	0.899	0.850	0.670	0.368
2.41	0.958	0.942	0.928	0.899	0.850	0.670	0.368
2.61	0.959	0.943	0.929	0.900	0.851	0.670	0.368
3.01	0.959	0.943	0.929	0.900	0.851	0.670	0.368
3.41	0.959	0.943	0.929	0.900	0.851	0.671	0.369
3.82	0.959	0.943	0.929	0.900	0.850	0.671	0.369
4.22	0.959	0.943	0.929	0.899	0.850	0.671	0.369
4.62	0.959	0.942	0.929	0.899	0.850	0.671	0.369
5.02	0.959	0.942	0.928	0.899	0.850	0.671	0.368
5.42	0.958	0.942	0.928	0.899	0.849	0.670	0.368
5.82	0.958	0.941	0.928	0.898	0.848	0.670	0.367
6.23	0.957	0.941	0.927	0.898	0.848	0.669	0.366
7.03	0.957	0.940	0.926	0.897	0.847	0.669	0.365
8.04	0.956	0.940	0.925	0.896	0.846	0.668	0.364
8.94	0.956	0.939	0.924	0.895	0.845	0.668	0.362
9.54	0.956	0.939	0.924	0.895	0.845	0.668	0.362

(b) Divergent Flap, $z = 0.000$ $p/p_{t,j}$ at x/x_f of

NPR	1.111	1.154	1.198	1.241	1.284	1.327	1.370	1.413	1.456	1.500	1.543	1.586	1.629	1.672	1.715	1.758	1.802	1.845	1.888	1.931	1.974
1.26	0.600	0.641	0.670	0.687	0.704	0.716	0.729	0.737	0.746	0.753	0.760	0.765	0.770	0.774	0.778	0.781	0.783	0.786	0.788	0.790	0.792
1.40	0.447	0.495	0.528	0.546	0.566	0.581	0.596	0.610	0.624	0.635	0.648	0.657	0.666	0.673	0.680	0.686	0.691	0.696	0.700	0.703	0.706
1.61	0.274	0.281	0.294	0.321	0.441	0.468	0.482	0.492	0.503	0.516	0.533	0.546	0.562	0.578	0.593	0.605	0.614	0.622	0.626	0.628	0.627
1.81	0.277	0.285	0.295	0.283	0.277	0.286	0.407	0.433	0.439	0.441	0.444	0.445	0.450	0.455	0.463	0.472	0.483	0.496	0.509	0.523	0.537
2.01	0.278	0.283	0.292	0.282	0.275	0.281	0.413	0.438	0.447	0.451	0.455	0.454	0.456	0.457	0.457	0.459	0.461	0.464	0.468	0.469	0.462
2.21	0.280	0.288	0.293	0.284	0.277	0.263	0.251	0.340	0.402	0.413	0.418	0.420	0.421	0.422	0.422	0.423	0.424	0.425	0.428	0.429	0.420
2.41	0.282	0.285	0.291	0.284	0.276	0.262	0.250	0.234	0.228	0.361	0.382	0.386	0.389	0.391	0.392	0.392	0.392	0.392	0.395	0.395	0.388
2.61	0.282	0.290	0.293	0.286	0.277	0.264	0.252	0.236	0.223	0.209	0.314	0.351	0.359	0.363	0.364	0.365	0.366	0.367	0.368	0.367	0.361
3.01	0.283	0.291	0.293	0.286	0.276	0.264	0.252	0.237	0.224	0.209	0.198	0.183	0.175	0.288	0.305	0.311	0.313	0.315	0.316	0.318	0.313
3.41	0.285	0.291	0.291	0.286	0.276	0.264	0.252	0.237	0.224	0.210	0.198	0.184	0.171	0.159	0.149	0.245	0.267	0.273	0.277	0.279	0.279
3.82	0.284	0.291	0.289	0.286	0.276	0.265	0.253	0.238	0.225	0.210	0.198	0.185	0.172	0.160	0.150	0.139	0.132	0.221	0.240	0.247	0.252
4.22	0.284	0.290	0.289	0.286	0.276	0.265	0.253	0.238	0.225	0.211	0.198	0.185	0.172	0.160	0.150	0.139	0.131	0.123	0.145	0.213	0.225
4.62	0.283	0.290	0.288	0.286	0.275	0.265	0.253	0.238	0.225	0.211	0.198	0.185	0.173	0.161	0.151	0.140	0.131	0.123	0.115	0.115	0.198
5.02	0.283	0.290	0.288	0.285	0.275	0.265	0.253	0.239	0.226	0.212	0.198	0.186	0.173	0.161	0.151	0.141	0.132	0.124	0.116	0.110	0.159
5.42	0.283	0.289	0.288	0.285	0.275	0.265	0.253	0.238	0.226	0.212	0.199	0.187	0.174	0.162	0.152	0.141	0.133	0.124	0.117	0.110	0.107
5.82	0.282	0.289	0.287	0.285	0.275	0.265	0.253	0.239	0.226	0.212	0.199	0.187	0.174	0.162	0.152	0.141	0.133	0.125	0.117	0.110	0.104
6.23	0.281	0.288	0.287	0.284	0.274	0.265	0.253	0.239	0.226	0.213	0.199	0.187	0.174	0.163	0.153	0.142	0.133	0.125	0.118	0.111	0.104
7.03	0.280	0.287	0.286	0.283	0.273	0.264	0.252	0.239	0.226	0.213	0.199	0.188	0.175	0.163	0.153	0.142	0.134	0.126	0.118	0.111	0.105
8.04	0.279	0.285	0.285	0.282	0.272	0.264	0.252	0.238	0.226	0.213	0.200	0.188	0.175	0.164	0.154	0.143	0.135	0.127	0.119	0.112	0.106
8.94	0.278	0.284	0.284	0.282	0.272	0.263	0.252	0.238	0.226	0.214	0.200	0.188	0.176	0.165	0.155	0.144	0.135	0.127	0.119	0.112	0.106
9.54	0.277	0.283	0.283	0.281	0.271	0.263	0.251	0.238	0.226	0.214	0.200	0.189	0.176	0.165	0.155	0.144	0.136	0.128	0.120	0.113	0.106

Table 3. Concluded

(c) Divergent Flap, $z = 1.595$ $p/p_{t,j}$ at x/x_f of

NPR	1.111	1.154	1.198	1.241	1.284	1.327	1.370	1.413	1.456	1.500	1.543	1.586	1.629	1.672	1.715	1.758	1.802	1.845	1.888	1.931	1.974
1.26	0.721	0.738	0.743	0.747	0.748	0.748	0.749	0.749	0.749	0.751	0.752	0.753	0.754	0.756	0.757	0.759	0.759	0.762	0.761	0.762	0.759
1.40	0.566	0.628	0.647	0.658	0.660	0.660	0.660	0.658	0.657	0.658	0.657	0.659	0.658	0.660	0.661	0.662	0.662	0.664	0.664	0.665	0.664
1.61	0.282	0.295	0.328	0.404	0.461	0.504	0.526	0.536	0.545	0.555	0.564	0.578	0.587	0.596	0.603	0.610	0.612	0.617	0.617	0.620	0.620
1.81	0.280	0.288	0.291	0.292	0.289	0.283	0.276	0.344	0.435	0.486	0.515	0.531	0.535	0.538	0.541	0.544	0.546	0.550	0.551	0.553	0.553
2.01	0.278	0.285	0.289	0.288	0.281	0.269	0.256	0.245	0.342	0.398	0.415	0.433	0.449	0.464	0.474	0.484	0.487	0.491	0.493	0.496	0.498
2.21	0.280	0.287	0.291	0.290	0.283	0.270	0.256	0.242	0.239	0.346	0.379	0.387	0.392	0.399	0.405	0.411	0.416	0.422	0.427	0.434	0.439
2.41	0.278	0.286	0.291	0.289	0.281	0.268	0.253	0.238	0.226	0.236	0.355	0.372	0.376	0.379	0.381	0.384	0.384	0.388	0.391	0.395	0.392
2.61	0.280	0.290	0.294	0.291	0.283	0.269	0.254	0.238	0.225	0.212	0.222	0.340	0.353	0.358	0.359	0.361	0.362	0.364	0.365	0.366	0.360
3.01	0.283	0.294	0.295	0.290	0.282	0.269	0.254	0.238	0.224	0.210	0.197	0.185	0.174	0.239	0.294	0.302	0.303	0.304	0.304	0.308	0.314
3.41	0.286	0.295	0.295	0.289	0.282	0.269	0.254	0.238	0.225	0.210	0.197	0.185	0.172	0.162	0.153	0.202	0.260	0.270	0.273	0.277	0.278
3.82	0.286	0.295	0.295	0.289	0.282	0.269	0.255	0.239	0.225	0.211	0.197	0.185	0.172	0.161	0.152	0.142	0.134	0.190	0.234	0.244	0.251
4.22	0.286	0.295	0.295	0.289	0.282	0.269	0.255	0.239	0.226	0.211	0.198	0.185	0.173	0.162	0.152	0.142	0.134	0.127	0.121	0.204	0.224
4.62	0.285	0.295	0.295	0.288	0.281	0.270	0.255	0.240	0.226	0.212	0.198	0.186	0.174	0.162	0.152	0.143	0.134	0.127	0.120	0.115	0.194
5.02	0.285	0.294	0.295	0.288	0.281	0.270	0.255	0.240	0.226	0.212	0.199	0.186	0.174	0.163	0.152	0.143	0.134	0.127	0.120	0.114	0.144
5.42	0.285	0.294	0.295	0.287	0.281	0.270	0.256	0.240	0.226	0.212	0.199	0.187	0.174	0.163	0.153	0.143	0.134	0.127	0.120	0.114	0.110
5.82	0.284	0.293	0.295	0.287	0.280	0.270	0.256	0.240	0.227	0.212	0.199	0.187	0.175	0.163	0.153	0.143	0.135	0.127	0.120	0.113	0.108
6.23	0.283	0.293	0.294	0.286	0.280	0.269	0.256	0.240	0.227	0.213	0.200	0.188	0.175	0.164	0.154	0.144	0.135	0.127	0.120	0.113	0.107
7.03	0.282	0.291	0.293	0.285	0.278	0.268	0.255	0.240	0.227	0.213	0.200	0.188	0.176	0.165	0.155	0.145	0.136	0.128	0.120	0.113	0.107
8.04	0.280	0.290	0.292	0.284	0.277	0.268	0.256	0.241	0.227	0.213	0.201	0.189	0.177	0.166	0.156	0.146	0.136	0.128	0.121	0.114	0.107
8.94	0.279	0.288	0.292	0.284	0.276	0.267	0.255	0.241	0.227	0.213	0.201	0.189	0.178	0.166	0.156	0.146	0.137	0.129	0.121	0.114	0.108
9.54	0.278	0.288	0.292	0.283	0.275	0.268	0.256	0.241	0.227	0.213	0.201	0.190	0.178	0.166	0.156	0.146	0.137	0.129	0.121	0.115	0.108

Table 4. Nozzle Internal Static Pressure Ratios for Configuration 2

Convergent Flap, $z = 0.000$

$p/p_{t,j}$ at x/x_t of								
NPR	0.330	0.440	0.550	0.659	0.769	0.890	1.000	
1.25	0.961	0.950	0.930	0.903	0.858	0.684	0.463	
1.40	0.959	0.947	0.928	0.900	0.852	0.673	0.396	
1.60	0.959	0.945	0.929	0.899	0.852	0.672	0.369	
1.80	0.959	0.945	0.929	0.899	0.852	0.672	0.369	
2.00	0.959	0.945	0.929	0.899	0.852	0.671	0.368	
2.20	0.959	0.945	0.929	0.899	0.851	0.671	0.368	
2.40	0.959	0.945	0.929	0.899	0.852	0.671	0.367	
3.01	0.959	0.944	0.930	0.900	0.852	0.671	0.368	
3.41	0.959	0.944	0.930	0.900	0.852	0.671	0.368	
3.81	0.959	0.944	0.930	0.899	0.851	0.671	0.368	
4.21	0.959	0.943	0.929	0.899	0.851	0.671	0.368	
4.61	0.959	0.943	0.929	0.899	0.850	0.671	0.368	
5.01	0.958	0.943	0.928	0.899	0.850	0.670	0.368	
5.42	0.958	0.943	0.928	0.898	0.849	0.670	0.367	
6.22	0.957	0.942	0.927	0.898	0.848	0.669	0.366	
7.03	0.957	0.941	0.926	0.897	0.847	0.669	0.364	
8.03	0.956	0.940	0.925	0.896	0.846	0.668	0.363	
8.94	0.956	0.940	0.924	0.895	0.846	0.668	0.361	
9.51	0.956	0.939	0.924	0.895	0.845	0.668	0.361	

Divergent Flap, $z = 0.000$

$p/p_{t,j}$ at x/x_t of																			
NPR	1.111	1.154	1.198	1.241	1.327	1.370	1.413	1.456	1.500	1.543	1.586	1.629	1.672	1.758	1.802	1.845	1.888	1.931	1.974
1.25	0.615	0.652	0.684	0.696	0.722	0.726	0.731	0.736	0.743	0.748	0.755	0.762	0.769	0.779	0.782	0.785	0.789	0.789	0.792
1.40	0.484	0.509	0.539	0.545	0.579	0.587	0.597	0.604	0.612	0.620	0.630	0.639	0.650	0.668	0.677	0.683	0.691	0.695	0.701
1.60	0.269	0.280	0.318	0.319	0.482	0.497	0.508	0.513	0.520	0.526	0.537	0.550	0.565	0.593	0.602	0.609	0.616	0.618	0.620
1.80	0.270	0.281	0.309	0.290	0.405	0.425	0.435	0.440	0.442	0.442	0.445	0.450	0.457	0.477	0.487	0.497	0.511	0.521	0.529
2.00	0.271	0.282	0.306	0.290	0.390	0.410	0.421	0.426	0.430	0.431	0.434	0.435	0.438	0.447	0.452	0.458	0.466	0.469	0.461
2.20	0.274	0.283	0.304	0.289	0.357	0.380	0.395	0.400	0.405	0.407	0.409	0.410	0.412	0.416	0.419	0.423	0.429	0.430	0.422
2.40	0.275	0.283	0.299	0.289	0.318	0.329	0.344	0.361	0.369	0.372	0.374	0.376	0.378	0.383	0.387	0.392	0.396	0.390	0.390
3.01	0.277	0.285	0.286	0.283	0.266	0.270	0.260	0.249	0.246	0.252	0.274	0.291	0.296	0.309	0.313	0.315	0.318	0.315	0.315
3.41	0.278	0.286	0.282	0.284	0.244	0.249	0.243	0.234	0.231	0.228	0.216	0.217	0.248	0.266	0.269	0.273	0.278	0.280	0.283
3.81	0.278	0.285	0.278	0.284	0.235	0.244	0.239	0.230	0.221	0.215	0.206	0.200	0.202	0.232	0.238	0.240	0.243	0.247	0.253
4.21	0.278	0.285	0.277	0.284	0.234	0.243	0.239	0.230	0.220	0.213	0.203	0.199	0.196	0.136	0.129	0.154	0.203	0.217	0.226
4.61	0.278	0.285	0.277	0.284	0.234	0.243	0.239	0.231	0.221	0.214	0.204	0.199	0.197	0.137	0.129	0.124	0.116	0.173	0.203
5.01	0.277	0.285	0.277	0.284	0.234	0.244	0.240	0.231	0.221	0.214	0.205	0.200	0.198	0.137	0.130	0.124	0.116	0.109	0.177
5.42	0.277	0.284	0.277	0.284	0.234	0.244	0.240	0.232	0.222	0.214	0.205	0.200	0.198	0.138	0.131	0.125	0.117	0.109	0.138
6.22	0.276	0.283	0.276	0.283	0.234	0.244	0.241	0.232	0.223	0.215	0.206	0.201	0.198	0.139	0.132	0.126	0.118	0.110	0.103
7.03	0.274	0.282	0.275	0.282	0.234	0.244	0.241	0.233	0.223	0.216	0.207	0.201	0.198	0.140	0.133	0.127	0.119	0.111	0.103
8.03	0.273	0.281	0.274	0.282	0.233	0.244	0.241	0.233	0.224	0.217	0.208	0.202	0.199	0.141	0.134	0.128	0.120	0.112	0.104
8.94	0.272	0.280	0.274	0.281	0.233	0.244	0.241	0.233	0.224	0.217	0.208	0.202	0.199	0.142	0.135	0.129	0.120	0.113	0.105
9.51	0.271	0.279	0.274	0.281	0.233	0.244	0.241	0.233	0.225	0.218	0.208	0.202	0.199	0.142	0.135	0.129	0.121	0.113	0.105

 $p/p_{t,j}$ at x/x_t of**Cavity, $z = -0.200$**

$p/p_{t,j}$ at x/x_t of								
NPR	1.456	1.543	1.629					
1.25	0.747	0.679	0.747					
1.40	0.619	0.565	0.620					
1.60	0.523	0.484	0.524					
1.80	0.435	0.395	0.436					
2.00	0.420	0.376	0.421					
2.20	0.397	0.361	0.399					
2.40	0.360	0.329	0.363					
3.01	0.272	0.252	0.273					
3.41	0.239	0.220	0.239					
3.81	0.222	0.198	0.222					
4.21	0.218	0.201	0.219					
4.61	0.219	0.204	0.219					
5.01	0.219	0.204	0.220					
5.42	0.219	0.206	0.220					
6.22	0.220	0.210	0.221					
7.03	0.220	0.213	0.222					
8.03	0.221	0.212	0.222					
8.94	0.221	0.212	0.222					
9.51	0.221	0.214	0.222					

 $p/p_{t,j}$ at x/x_t of

$p/p_{t,j}$ at x/x_t of																			
NPR	1.111	1.154	1.198	1.241	1.327	1.370	1.413	1.456	1.500	1.543	1.586	1.629	1.672	1.758	1.802	1.845	1.888	1.931	1.974
1.25	0.720	0.739	0.746	0.747	0.751	0.752	0.753	0.755	0.756	0.759	0.759	0.761	0.760	0.763	0.765	0.765	0.764	0.762	
1.40	0.469	0.510	0.539	0.561	0.598	0.605	0.610	0.617	0.627	0.634	0.647	0.656	0.669	0.686	0.693	0.698	0.702	0.703	0.706
1.60	0.267	0.320	0.411	0.435	0.509	0.516	0.520	0.522	0.528	0.534	0.548	0.560	0.579	0.606	0.617	0.620	0.620	0.619	
1.80	0.261	0.289	0.312	0.308	0.399	0.417	0.425	0.429	0.434	0.438	0.450	0.461	0.480	0.516	0.530	0.547	0.549	0.551	
2.00	0.260	0.290	0.310	0.303	0.387	0.407	0.416	0.420	0.422	0.424	0.425	0.424	0.428	0.439	0.447	0.455	0.464	0.473	0.480
2.20	0.261	0.290	0.307	0.303	0.362	0.384	0.396	0.401	0.405	0.405	0.408	0.405	0.405	0.408	0.414	0.418	0.424	0.429	0.423
2.40	0.264	0.291	0.300	0.300	0.320	0.333	0.348	0.362	0.371	0.372	0.374	0.372	0.373	0.377	0.382	0.386	0.391	0.395	0.389
3.01	0.278	0.2																	

Table 5. Nozzle Internal Static Pressure Ratios for Configuration 3

Convergent Flap, $z = 0.000$

$p/p_{t,j}$ at x/x_t of							$p/p_{t,j}$ at x/x_t of																				
NPR	0.330	0.440	0.550	0.659	0.769	0.890	1.000	NPR	1.111	1.154	1.198	1.241	1.327	1.370	1.413	1.456	1.500	1.543	1.586	1.629	1.672	1.758	1.802	1.845	1.888	1.931	1.974
1.25	0.961	0.947	0.930	0.903	0.857	0.683	0.456	1.25	0.608	0.647	0.680	0.694	0.718	0.721	0.726	0.729	0.735	0.741	0.749	0.756	0.764	0.775	0.779	0.782	0.784	0.786	0.787
1.40	0.959	0.944	0.927	0.899	0.850	0.672	0.397	1.40	0.483	0.510	0.540	0.548	0.582	0.589	0.598	0.604	0.613	0.621	0.631	0.641	0.652	0.671	0.679	0.685	0.691	0.696	0.699
1.60	0.959	0.943	0.926	0.898	0.850	0.671	0.369	1.60	0.267	0.278	0.309	0.334	0.494	0.503	0.511	0.514	0.519	0.527	0.537	0.550	0.566	0.595	0.605	0.612	0.615	0.618	0.617
1.81	0.958	0.943	0.928	0.898	0.850	0.671	0.368	1.81	0.268	0.280	0.301	0.278	0.414	0.428	0.433	0.434	0.436	0.437	0.439	0.445	0.451	0.472	0.485	0.495	0.508	0.520	0.528
2.01	0.959	0.943	0.928	0.898	0.851	0.671	0.368	2.01	0.270	0.281	0.299	0.280	0.402	0.418	0.423	0.425	0.428	0.430	0.431	0.432	0.434	0.441	0.447	0.453	0.459	0.463	0.453
2.21	0.958	0.943	0.928	0.898	0.851	0.671	0.368	2.21	0.273	0.282	0.298	0.280	0.371	0.392	0.403	0.405	0.408	0.411	0.412	0.414	0.415	0.418	0.422	0.424	0.428	0.426	0.418
2.41	0.959	0.942	0.928	0.898	0.851	0.670	0.367	2.41	0.274	0.282	0.296	0.327	0.336	0.352	0.365	0.370	0.371	0.373	0.375	0.376	0.383	0.386	0.388	0.392	0.395	0.387	
2.61	0.959	0.943	0.928	0.898	0.850	0.671	0.367	2.61	0.275	0.283	0.293	0.282	0.304	0.304	0.299	0.313	0.334	0.338	0.341	0.343	0.346	0.357	0.360	0.361	0.363	0.366	0.360
3.01	0.959	0.942	0.928	0.898	0.850	0.671	0.368	3.01	0.276	0.285	0.285	0.284	0.263	0.267	0.258	0.247	0.242	0.246	0.269	0.288	0.291	0.305	0.310	0.314	0.316	0.318	0.314
3.41	0.959	0.943	0.928	0.898	0.851	0.671	0.368	3.41	0.277	0.286	0.282	0.286	0.240	0.246	0.240	0.230	0.227	0.223	0.213	0.211	0.234	0.267	0.268	0.271	0.275	0.279	0.283
3.81	0.959	0.942	0.928	0.898	0.850	0.671	0.368	3.81	0.277	0.285	0.278	0.286	0.233	0.240	0.236	0.227	0.218	0.211	0.200	0.198	0.200	0.212	0.231	0.237	0.240	0.242	0.243
4.22	0.959	0.942	0.927	0.898	0.850	0.671	0.368	4.22	0.277	0.285	0.278	0.286	0.232	0.240	0.237	0.228	0.218	0.211	0.200	0.198	0.199	0.137	0.133	0.146	0.199	0.212	0.222
4.61	0.959	0.942	0.928	0.897	0.850	0.671	0.368	4.61	0.277	0.285	0.278	0.287	0.232	0.240	0.237	0.229	0.219	0.211	0.201	0.198	0.200	0.138	0.133	0.120	0.114	0.172	0.201
5.02	0.959	0.942	0.927	0.897	0.850	0.670	0.367	5.02	0.276	0.285	0.278	0.287	0.232	0.241	0.238	0.229	0.219	0.212	0.202	0.198	0.200	0.140	0.134	0.120	0.114	0.108	0.177
5.42	0.958	0.941	0.927	0.897	0.849	0.670	0.366	5.42	0.276	0.284	0.277	0.286	0.232	0.241	0.238	0.229	0.220	0.212	0.202	0.199	0.201	0.140	0.135	0.121	0.115	0.109	0.135
6.22	0.957	0.941	0.926	0.896	0.848	0.669	0.365	6.22	0.275	0.283	0.277	0.286	0.232	0.241	0.238	0.230	0.221	0.213	0.203	0.199	0.202	0.142	0.136	0.122	0.116	0.110	0.102
7.03	0.957	0.941	0.926	0.895	0.847	0.669	0.364	7.03	0.274	0.283	0.277	0.285	0.232	0.242	0.239	0.231	0.221	0.214	0.204	0.200	0.202	0.143	0.137	0.123	0.117	0.111	0.103
8.03	0.957	0.940	0.925	0.895	0.846	0.668	0.362	8.03	0.272	0.281	0.276	0.284	0.232	0.242	0.239	0.231	0.222	0.215	0.205	0.200	0.202	0.144	0.138	0.123	0.118	0.112	0.104
8.94	0.956	0.940	0.924	0.894	0.845	0.667	0.361	8.94	0.271	0.280	0.275	0.284	0.232	0.242	0.239	0.232	0.223	0.216	0.205	0.200	0.203	0.145	0.138	0.124	0.118	0.112	0.104
9.55	0.956	0.939	0.923	0.893	0.845	0.667	0.360	9.55	0.270	0.280	0.275	0.283	0.231	0.242	0.239	0.232	0.223	0.216	0.206	0.201	0.203	0.146	0.139	0.124	0.119	0.113	0.105

Cavity, $z = -0.200$

$p/p_{t,j}$ at x/x_t of							$p/p_{t,j}$ at x/x_t of																
NPR	1.456	1.543	1.629	NPR	1.111	1.154	1.198	1.241	1.327	1.370	1.413	1.456	1.500	1.543	1.586	1.629	1.672	1.758	1.802	1.845	1.888	1.931	1.974
1.25	0.738	0.670	0.740	1.25	0.666	0.691	0.702	0.708	0.729	0.729	0.732	0.735	0.739	0.745	0.752	0.759	0.768	0.780	0.783	0.784	0.786	0.789	0.789
1.40	0.619	0.557	0.621	1.40	0.473	0.528	0.559	0.584	0.617	0.620	0.625	0.630	0.638	0.646	0.656	0.666	0.678	0.695	0.700	0.701	0.703	0.703	
1.60	0.528	0.479	0.530	1.60	0.269	0.332	0.430	0.451	0.520	0.524	0.527	0.527	0.533	0.542	0.556	0.570	0.587	0.613	0.617	0.619	0.619	0.618	
1.81	0.435	0.392	0.437	1.81	0.266	0.279	0.315	0.308	0.402	0.416	0.425	0.431	0.436	0.443	0.456	0.470	0.492	0.528	0.537	0.542	0.546	0.548	0.548
2.01	0.426	0.376	0.429	2.01	0.266	0.282	0.309	0.305	0.390	0.409	0.418	0.421	0.423	0.424	0.425	0.428	0.437	0.443	0.451	0.459	0.470	0.478	
2.21	0.405	0.363	0.408	2.21	0.266	0.284	0.305	0.304	0.368	0.389	0.400	0.404	0.407	0.408	0.409	0.407	0.406	0.408	0.410	0.414	0.418	0.425	0.422
2.41	0.366	0.339	0.370	2.41	0.267	0.288	0.298	0.299	0.323	0.339	0.356	0.366	0.372	0.374	0.376	0.375	0.377	0.380	0.384	0.388	0.393	0.386	
2.61	0.330	0.306	0.334	2.61	0.269	0.290	0.291	0.290	0.301	0.303	0.308	0.321	0.335	0.342	0.345	0.345	0.347	0.353	0.358	0.361	0.364	0.358	
3.01	0.269	0.246	0.270	3.01	0.278	0.291	0.283	0.288	0.267	0.263	0.256	0.249	0.243	0.251	0.269	0.286	0.294	0.307	0.310	0.313	0.315	0.318	0.314
3.41	0.234	0.213	0.233	3.41	0.281	0.292	0.282	0.288	0.254	0.248	0.238	0.228	0.229	0.217	0.215	0.220	0.239	0.264	0.270	0.272	0.278	0.279	
3.81	0.216	0.196	0.217	3.81	0.281	0.292	0.281	0.288	0.251	0.243	0.234	0.224	0.216	0.214	0.201	0.196	0.197	0.209	0.227	0.234	0.240	0.245	0.250
4.22	0.216	0.196	0.216	4.22	0.281	0.292	0.281	0.288	0.251	0.243	0.234	0.224	0.216	0.213	0.199	0.193	0.194	0.147	0.137	0.123	0.171	0.211	0.227
4.61	0.216	0.197	0.217	4.61	0.281	0.292	0.281	0.288	0.252	0.244	0.235	0.225	0.217	0.215	0.198	0.192	0.194	0.147	0.139	0.120	0.117	0.139	0.199
5.02	0.216	0.200	0.217	5.02	0.281	0.292	0.281	0.288	0.252	0.244	0.235	0.225	0.217	0.215	0.199								

Table 6. Nozzle Internal Static Pressure Ratios for Configuration 4

Convergent Flap, $z = 0.000$

$p/p_{t,j}$ at x/x_t of							$p/p_{t,j}$ at x/x_t of																				
NPR	0.330	0.440	0.550	0.659	0.769	0.890	1.000	NPR	1.111	1.154	1.198	1.241	1.327	1.370	1.413	1.456	1.500	1.543	1.586	1.629	1.672	1.758	1.802	1.845	1.888	1.931	1.974
1.25	0.960	0.948	0.928	0.903	0.857	0.683	0.455	1.25	0.630	0.670	0.701	0.714	0.734	0.740	0.747	0.751	0.753	0.761	0.766	0.773	0.780	0.789	0.793	0.795	0.798	0.799	0.800
1.40	0.957	0.944	0.926	0.898	0.851	0.671	0.401	1.40	0.500	0.526	0.554	0.563	0.595	0.603	0.614	0.623	0.628	0.639	0.648	0.658	0.667	0.685	0.693	0.699	0.704	0.709	0.711
1.60	0.957	0.943	0.926	0.897	0.850	0.670	0.368	1.60	0.280	0.291	0.322	0.360	0.503	0.512	0.521	0.526	0.529	0.539	0.549	0.563	0.577	0.603	0.613	0.620	0.625	0.627	0.626
1.80	0.957	0.942	0.926	0.897	0.849	0.670	0.367	1.80	0.278	0.289	0.309	0.287	0.426	0.441	0.448	0.449	0.448	0.452	0.455	0.462	0.468	0.487	0.498	0.508	0.519	0.530	0.536
2.00	0.957	0.942	0.926	0.898	0.850	0.670	0.367	2.00	0.279	0.289	0.306	0.287	0.411	0.428	0.436	0.439	0.440	0.444	0.445	0.447	0.449	0.457	0.462	0.466	0.473	0.476	0.465
2.20	0.957	0.942	0.927	0.898	0.850	0.670	0.367	2.20	0.280	0.290	0.304	0.287	0.379	0.403	0.413	0.416	0.416	0.420	0.421	0.424	0.424	0.427	0.431	0.432	0.437	0.437	0.426
2.40	0.957	0.942	0.927	0.898	0.850	0.670	0.367	2.40	0.280	0.289	0.301	0.286	0.323	0.347	0.367	0.376	0.378	0.382	0.384	0.386	0.388	0.393	0.395	0.396	0.400	0.403	0.393
2.60	0.957	0.942	0.927	0.899	0.850	0.670	0.367	2.60	0.280	0.289	0.298	0.287	0.298	0.309	0.312	0.329	0.342	0.348	0.350	0.354	0.356	0.365	0.368	0.370	0.373	0.366	
3.00	0.958	0.942	0.928	0.899	0.850	0.671	0.367	3.00	0.280	0.290	0.289	0.289	0.263	0.268	0.260	0.249	0.245	0.255	0.276	0.295	0.302	0.316	0.320	0.322	0.323	0.325	0.320
3.40	0.958	0.942	0.928	0.899	0.850	0.671	0.367	3.40	0.280	0.289	0.285	0.289	0.245	0.248	0.243	0.235	0.230	0.224	0.211	0.216	0.243	0.275	0.278	0.279	0.282	0.284	0.287
3.80	0.958	0.942	0.928	0.899	0.850	0.671	0.368	3.80	0.279	0.288	0.281	0.289	0.238	0.243	0.240	0.232	0.219	0.213	0.203	0.197	0.199	0.224	0.237	0.244	0.246	0.247	0.250
4.20	0.958	0.942	0.928	0.899	0.850	0.671	0.367	4.20	0.279	0.288	0.280	0.289	0.238	0.243	0.239	0.232	0.218	0.212	0.203	0.196	0.196	0.144	0.138	0.137	0.201	0.221	0.230
4.60	0.958	0.942	0.928	0.899	0.849	0.671	0.367	4.60	0.278	0.287	0.279	0.289	0.237	0.243	0.239	0.232	0.219	0.212	0.203	0.196	0.196	0.145	0.138	0.123	0.116	0.171	0.205
5.00	0.958	0.941	0.928	0.899	0.849	0.671	0.366	5.00	0.277	0.286	0.279	0.288	0.237	0.243	0.240	0.232	0.219	0.212	0.203	0.196	0.196	0.145	0.138	0.123	0.116	0.110	0.178
5.40	0.958	0.941	0.927	0.899	0.849	0.670	0.366	5.40	0.276	0.286	0.278	0.288	0.237	0.243	0.239	0.232	0.219	0.213	0.204	0.196	0.196	0.146	0.139	0.123	0.116	0.110	0.147
6.20	0.957	0.941	0.926	0.898	0.847	0.669	0.364	6.20	0.275	0.284	0.277	0.287	0.236	0.243	0.239	0.232	0.219	0.213	0.204	0.196	0.196	0.147	0.139	0.124	0.117	0.111	0.104
7.00	0.957	0.940	0.926	0.897	0.846	0.669	0.363	7.00	0.273	0.283	0.276	0.286	0.235	0.243	0.239	0.232	0.220	0.214	0.204	0.196	0.196	0.147	0.140	0.124	0.117	0.111	0.104
8.00	0.957	0.940	0.925	0.896	0.846	0.668	0.362	8.00	0.272	0.281	0.275	0.284	0.234	0.242	0.239	0.232	0.220	0.214	0.205	0.196	0.196	0.148	0.140	0.124	0.118	0.112	0.104
8.90	0.956	0.940	0.924	0.896	0.845	0.667	0.360	8.90	0.270	0.280	0.274	0.283	0.234	0.242	0.239	0.232	0.220	0.214	0.205	0.195	0.196	0.148	0.141	0.125	0.118	0.112	0.105
9.51	0.956	0.939	0.924	0.895	0.844	0.667	0.360	9.51	0.269	0.279	0.274	0.283	0.233	0.241	0.239	0.232	0.220	0.215	0.205	0.196	0.196	0.149	0.141	0.125	0.118	0.112	0.105

Cavity, $z = -0.200$

$p/p_{t,j}$ at x/x_t of							$p/p_{t,j}$ at x/x_t of																
NPR	1.456	1.543	1.629	NPR	1.111	1.154	1.198	1.241	1.327	1.370	1.413	1.456	1.500	1.543	1.586	1.629	1.672	1.758	1.802	1.845	1.888	1.931	1.974
1.25	0.754	0.708	0.758	1.25	0.686	0.709	0.719	0.728	0.747	0.746	0.750	0.750	0.756	0.763	0.769	0.774	0.780	0.798	0.797	0.799	0.802	0.801	0.804
1.40	0.632	0.576	0.638	1.40	0.489	0.544	0.573	0.602	0.633	0.634	0.640	0.644	0.654	0.663	0.673	0.681	0.691	0.713	0.713	0.714	0.716	0.715	0.717
1.60	0.535	0.492	0.541	1.60	0.284	0.358	0.444	0.466	0.529	0.532	0.535	0.534	0.540	0.549	0.562	0.575	0.591	0.622	0.625	0.629	0.631	0.628	0.629
1.80	0.447	0.410	0.452	1.80	0.277	0.290	0.326	0.317	0.418	0.429	0.438	0.442	0.448	0.455	0.468	0.482	0.502	0.544	0.548	0.553	0.557	0.557	0.558
2.00	0.436	0.407	0.442	2.00	0.275	0.289	0.317	0.314	0.397	0.414	0.424	0.427	0.430	0.431	0.433	0.434	0.436	0.451	0.455	0.464	0.472	0.481	0.491
2.20	0.414	0.380	0.420	2.20	0.275	0.291	0.313	0.313	0.378	0.397	0.408	0.411	0.415	0.417	0.417	0.417	0.417	0.451	0.453	0.458	0.462	0.463	0.462
2.40	0.373	0.342	0.381	2.40	0.274	0.293	0.306	0.309	0.334	0.347	0.363	0.372	0.378	0.381	0.383	0.383	0.385	0.390	0.395	0.399	0.394		
2.60	0.335	0.307	0.344	2.60	0.275	0.295	0.301	0.300	0.308	0.312	0.314	0.325	0.342	0.349	0.353	0.353	0.361	0.361	0.365	0.368	0.370	0.365	
3.00	0.272	0.238	0.274	3.00	0.282	0.296	0.290	0.294	0.274	0.268	0.261	0.255	0.248	0.254	0.268	0.289	0.299	0.314	0.315	0.319	0.321	0.323	0.321
3.40	0.236	0.208	0.237	3.40	0.285	0.295	0.288	0.292	0.259	0.253	0.244	0.232	0.228	0.226	0.218	0.220	0.239	0.273	0.276	0.278	0.281	0.283	0.285
3.80	0.219	0.192	0.220	3.80	0.284	0.295	0.287	0.291	0.256	0.249	0.239	0.227	0.219	0.211	0.211	0.200	0.200	0.225	0.236	0.243	0.248	0.252	0.255
4.20	0.218	0.190	0.218	4.20	0.284	0.294	0.286	0.291	0.256	0.248	0.238	0.227	0.218	0.210	0.208	0.199	0.195	0.154	0.142	0.123	0.187	0.216	0.229
4.60	0.218	0.193	0.218	4.60	0.283	0.294	0.286	0.290	0.255	0.248	0.238	0.227	0.218	0.210	0.208	0.199	0.195	0.151	0.145	0.121	0.120	0.152	0.205
5.00	0.218	0.198	0.218	5.00	0.283	0.293	0.286	0.289	0.255	0.248													

Table 8. Nozzle Internal Static Pressure Ratios for Configuration 6

Convergent Flap, $z = 0.000$

$p/p_{t,j}$ at x/x_t of							
NPR	0.330	0.440	0.550	0.659	0.769	0.890	1.000
1.25	0.960	0.947	0.929	0.903	0.858	0.684	0.457
1.40	0.957	0.944	0.926	0.898	0.851	0.671	0.396
1.60	0.957	0.943	0.926	0.897	0.849	0.669	0.369
1.80	0.958	0.943	0.927	0.898	0.850	0.670	0.368
2.00	0.957	0.943	0.927	0.898	0.849	0.670	0.367
2.20	0.958	0.943	0.927	0.898	0.850	0.670	0.367
2.40	0.958	0.943	0.927	0.898	0.850	0.670	0.368
2.60	0.958	0.942	0.928	0.898	0.850	0.670	0.367
3.00	0.958	0.942	0.927	0.898	0.850	0.670	0.368
3.40	0.958	0.942	0.928	0.898	0.850	0.671	0.368
3.80	0.958	0.942	0.928	0.898	0.850	0.671	0.368
4.20	0.958	0.942	0.928	0.898	0.849	0.670	0.368
4.60	0.958	0.942	0.928	0.898	0.849	0.671	0.368
5.00	0.958	0.942	0.927	0.898	0.849	0.670	0.367
5.40	0.958	0.942	0.927	0.898	0.848	0.670	0.367
6.20	0.957	0.941	0.926	0.897	0.847	0.669	0.365
7.00	0.957	0.941	0.925	0.896	0.847	0.669	0.364
8.00	0.956	0.940	0.925	0.895	0.846	0.668	0.363
8.90	0.956	0.940	0.924	0.895	0.845	0.668	0.361
9.50	0.956	0.939	0.923	0.895	0.845	0.668	0.361

Divergent Flap, $z = 0.000$

$p/p_{t,j}$ at x/x_t of																			
NPR	1.111	1.154	1.198	1.241	1.327	1.370	1.413	1.456	1.500	1.543	1.586	1.629	1.672	1.758	1.802	1.845	1.888	1.931	1.974
1.25	0.629	0.669	0.701	0.715	0.735	0.737	0.737	0.740	0.742	0.745	0.751	0.760	0.769	0.784	0.785	0.791	0.792	0.794	0.796
1.40	0.483	0.517	0.553	0.567	0.600	0.605	0.609	0.614	0.619	0.627	0.637	0.648	0.661	0.682	0.687	0.694	0.699	0.704	0.707
1.60	0.274	0.288	0.337	0.416	0.514	0.519	0.522	0.525	0.529	0.534	0.542	0.556	0.574	0.603	0.608	0.614	0.617	0.619	0.620
1.80	0.274	0.285	0.308	0.283	0.416	0.417	0.420	0.423	0.423	0.423	0.427	0.436	0.448	0.479	0.491	0.506	0.518	0.530	0.541
2.00	0.275	0.286	0.306	0.283	0.400	0.404	0.410	0.412	0.412	0.411	0.411	0.414	0.418	0.434	0.442	0.450	0.459	0.468	0.470
2.20	0.277	0.286	0.304	0.284	0.393	0.400	0.403	0.402	0.401	0.401	0.401	0.403	0.410	0.414	0.418	0.424	0.429	0.435	0.439
2.40	0.277	0.286	0.303	0.285	0.358	0.356	0.359	0.367	0.370	0.369	0.367	0.368	0.377	0.382	0.386	0.391	0.396	0.399	0.405
2.60	0.277	0.286	0.301	0.286	0.329	0.325	0.323	0.327	0.334	0.339	0.339	0.338	0.349	0.356	0.359	0.362	0.367	0.365	0.365
3.00	0.278	0.287	0.295	0.289	0.269	0.271	0.269	0.265	0.263	0.265	0.272	0.283	0.288	0.303	0.308	0.313	0.316	0.320	0.318
3.40	0.279	0.287	0.291	0.290	0.245	0.248	0.244	0.241	0.238	0.237	0.235	0.239	0.248	0.267	0.268	0.271	0.274	0.279	0.284
3.80	0.278	0.286	0.288	0.290	0.236	0.238	0.236	0.231	0.226	0.223	0.224	0.223	0.239	0.243	0.245	0.247	0.253		
4.20	0.277	0.285	0.287	0.290	0.233	0.234	0.234	0.227	0.220	0.215	0.215	0.216	0.211	0.198	0.214	0.221	0.223	0.225	0.228
4.60	0.277	0.285	0.287	0.290	0.232	0.234	0.233	0.227	0.220	0.215	0.213	0.214	0.209	0.139	0.135	0.136	0.183	0.196	0.205
5.00	0.276	0.285	0.286	0.290	0.232	0.234	0.233	0.227	0.220	0.215	0.213	0.214	0.209	0.139	0.135	0.122	0.115	0.147	0.188
5.40	0.276	0.284	0.286	0.292	0.232	0.234	0.234	0.227	0.221	0.215	0.213	0.214	0.209	0.140	0.135	0.122	0.115	0.109	0.162
6.20	0.275	0.283	0.285	0.288	0.231	0.234	0.234	0.227	0.221	0.216	0.214	0.214	0.210	0.141	0.136	0.123	0.116	0.109	0.103
7.00	0.273	0.282	0.284	0.287	0.231	0.234	0.234	0.228	0.221	0.216	0.214	0.214	0.210	0.142	0.137	0.123	0.117	0.110	0.103
8.00	0.272	0.280	0.283	0.287	0.230	0.233	0.234	0.228	0.222	0.217	0.215	0.215	0.211	0.143	0.139	0.125	0.118	0.111	0.104
8.90	0.271	0.279	0.282	0.286	0.230	0.233	0.234	0.228	0.222	0.217	0.215	0.215	0.211	0.144	0.139	0.125	0.118	0.111	0.104
9.50	0.270	0.278	0.282	0.285	0.230	0.233	0.234	0.228	0.222	0.217	0.215	0.215	0.211	0.144	0.139	0.125	0.118	0.111	0.104

Cavity, $z = -0.200$

$p/p_{t,j}$ at x/x_t of																			
NPR	1.111	1.154	1.198	1.241	1.327	1.370	1.413	1.456	1.500	1.543	1.586	1.629	1.672	1.758	1.802	1.845	1.888	1.931	1.974
1.25	0.684	0.706	0.715	0.728	0.744	0.744	0.742	0.743	0.744	0.749	0.754	0.759	0.772	0.790	0.792	0.795	0.795	0.796	0.797
1.40	0.485	0.539	0.573	0.604	0.633	0.635	0.634	0.634	0.636	0.643	0.653	0.662	0.679	0.705	0.707	0.709	0.709	0.710	0.710
1.60	0.300	0.372	0.451	0.515	0.553	0.554	0.553	0.553	0.552	0.555	0.558	0.562	0.573	0.596	0.601	0.606	0.605	0.606	0.607
1.80	0.272	0.286	0.299	0.310	0.424	0.426	0.425	0.426	0.428	0.433	0.446	0.460	0.487	0.541	0.549	0.554	0.555	0.556	0.554
2.00	0.271	0.286	0.297	0.297	0.396	0.400	0.402	0.406	0.407	0.408	0.410	0.409	0.414	0.432	0.443	0.456	0.467	0.478	0.489
2.20	0.270	0.288	0.297	0.294	0.384	0.391	0.396	0.401	0.402	0.404	0.400	0.400	0.403	0.404	0.408	0.411	0.418	0.425	
2.40	0.271	0.291	0.296	0.292	0.350	0.355	0.358	0.365	0.369	0.370	0.372	0.369	0.370	0.375	0.378	0.385	0.390		
2.60	0.273	0.293	0.296	0.291	0.319	0.324	0.323	0.327	0.334	0.339	0.342	0.339	0.339	0.341	0.342	0.347	0.352	0.360	0.361
3.00	0.280	0.294	0.295	0.289	0.271	0.269	0.266	0.267	0.265	0.269	0.275	0.283	0.289	0.298	0.302	0.309	0.313	0.318	0.316
3.40	0.282	0.293	0.295	0.288	0.257	0.253	0.245	0.239	0.233	0.235	0.240	0.242	0.249	0.266	0.265	0.267	0.272	0.278	0.282
3.80	0.282	0.293	0.294	0.287	0.253	0.246	0.238	0.230	0.224	0.222	0.225	0.226	0.237	0.240	0.240	0.239	0.244	0.250	
4.20	0.282	0.293	0.294	0.287	0.252	0.243	0.234	0.225	0.219	0.216	0.212	0.216	0.214	0.193	0.209	0.214	0.216	0.219	0.225
4.60	0.281	0.292	0.294	0.287	0.251	0.242	0.233	0.224	0.219	0.215	0.210	0.212	0.214	0.144	0.138	0.123	0.167	0.200	0.213
5.00	0.281	0.292	0.294	0.286	0.251	0.242	0.234	0.225	0.219	0.216	0.210	0.213	0.212	0.145	0.138	0.121	0.117	0.121	0.151
5.40	0.281	0.292	0.293	0.286	0.252	0.242	0.234	0.225	0.219	0.216	0.210	0.213	0.213	0.145	0.139	0.121	0.117	0.112	0.151
6.20	0.281	0.291	0.293	0.285	0.252	0.242	0.234	0.225	0.219	0.216	0.209	0.213	0.213	0.145	0.140	0.121	0.117	0.112	0.107
7.00	0.278	0.290	0.292	0.285															

Table 10. Nozzle Internal Static Pressure Ratios for Configuration 8

Convergent Flap, $z = 0.000$

$p/p_{t,j}$ at x/x_t of							
NPR	0.330	0.440	0.550	0.659	0.769	0.890	1.000
1.25	0.960	0.948	0.929	0.904	0.857	0.689	0.494
1.40	0.957	0.944	0.926	0.899	0.851	0.672	0.396
1.61	0.958	0.944	0.926	0.897	0.849	0.671	0.370
1.80	0.959	0.944	0.927	0.899	0.850	0.671	0.370
2.01	0.959	0.944	0.927	0.899	0.851	0.671	0.369
2.21	0.959	0.944	0.928	0.899	0.851	0.671	0.368
2.41	0.959	0.943	0.928	0.899	0.851	0.671	0.368
2.61	0.959	0.943	0.928	0.899	0.851	0.671	0.368
3.01	0.959	0.943	0.928	0.899	0.851	0.671	0.368
3.41	0.959	0.943	0.928	0.900	0.851	0.671	0.368
3.82	0.959	0.943	0.928	0.899	0.850	0.671	0.368
4.21	0.959	0.943	0.928	0.899	0.850	0.671	0.368
4.62	0.959	0.943	0.928	0.899	0.850	0.671	0.368
5.02	0.959	0.942	0.928	0.899	0.850	0.671	0.367
5.42	0.958	0.942	0.927	0.898	0.849	0.670	0.367
6.22	0.957	0.941	0.926	0.897	0.848	0.669	0.365
7.03	0.957	0.941	0.926	0.897	0.847	0.669	0.364
8.03	0.957	0.941	0.925	0.896	0.846	0.668	0.362
8.94	0.956	0.940	0.924	0.895	0.845	0.668	0.361
9.53	0.956	0.939	0.923	0.893	0.845	0.667	0.360

Divergent Flap, $z = 0.000$

$p/p_{t,j}$ at x/x_t of																			
NPR	1.111	1.154	1.198	1.241	1.327	1.370	1.413	1.456	1.500	1.543	1.586	1.629	1.672	1.758	1.802	1.845	1.888	1.931	1.974
1.25	0.608	0.641	0.669	0.684	0.713	0.715	0.716	0.718	0.720	0.725	0.731	0.739	0.749	0.769	0.773	0.778	0.780	0.783	0.786
1.40	0.467	0.504	0.538	0.552	0.588	0.590	0.591	0.592	0.593	0.598	0.605	0.617	0.635	0.669	0.676	0.685	0.690	0.696	0.700
1.61	0.275	0.297	0.380	0.446	0.519	0.523	0.522	0.525	0.527	0.534	0.552	0.589	0.595	0.603	0.606	0.610	0.612		
1.80	0.268	0.280	0.301	0.279	0.396	0.392	0.386	0.384	0.386	0.390	0.396	0.406	0.425	0.493	0.513	0.532	0.544	0.552	0.553
2.01	0.271	0.281	0.296	0.279	0.339	0.337	0.331	0.329	0.330	0.334	0.339	0.346	0.355	0.394	0.410	0.428	0.444	0.461	0.477
2.21	0.273	0.283	0.298	0.281	0.372	0.369	0.367	0.369	0.372	0.376	0.378	0.380	0.400	0.405	0.412	0.418	0.425	0.418	
2.41	0.275	0.283	0.296	0.281	0.336	0.334	0.329	0.326	0.328	0.333	0.339	0.344	0.352	0.373	0.377	0.381	0.386	0.391	0.384
2.61	0.275	0.284	0.287	0.282	0.270	0.273	0.270	0.266	0.263	0.255	0.255	0.261	0.289	0.339	0.348	0.355	0.359	0.364	0.366
3.01	0.276	0.286	0.284	0.283	0.237	0.235	0.236	0.234	0.233	0.230	0.231	0.227	0.228	0.280	0.291	0.299	0.306	0.313	0.319
3.41	0.277	0.286	0.282	0.284	0.231	0.228	0.229	0.228	0.225	0.226	0.227	0.223	0.247	0.258	0.264	0.267	0.271	0.276	
3.82	0.277	0.286	0.279	0.284	0.229	0.225	0.224	0.224	0.220	0.220	0.222	0.223	0.220	0.194	0.224	0.234	0.241	0.245	
4.21	0.277	0.286	0.278	0.284	0.228	0.224	0.223	0.224	0.219	0.219	0.220	0.221	0.220	0.143	0.135	0.131	0.189	0.212	0.224
4.62	0.276	0.285	0.278	0.284	0.228	0.224	0.224	0.224	0.219	0.219	0.221	0.222	0.220	0.143	0.135	0.117	0.114	0.168	0.201
5.02	0.276	0.285	0.278	0.284	0.229	0.224	0.224	0.225	0.220	0.220	0.221	0.221	0.221	0.144	0.137	0.118	0.114	0.108	0.179
5.42	0.276	0.285	0.278	0.284	0.229	0.225	0.225	0.225	0.220	0.220	0.222	0.222	0.221	0.145	0.138	0.119	0.115	0.108	0.132
6.22	0.275	0.284	0.277	0.283	0.229	0.225	0.226	0.226	0.221	0.221	0.222	0.222	0.223	0.146	0.139	0.119	0.116	0.109	0.101
7.03	0.273	0.283	0.277	0.283	0.229	0.226	0.226	0.226	0.221	0.222	0.223	0.222	0.223	0.147	0.141	0.120	0.117	0.110	0.101
8.03	0.272	0.282	0.276	0.282	0.228	0.226	0.227	0.227	0.222	0.222	0.223	0.222	0.224	0.148	0.142	0.121	0.118	0.111	0.102
8.94	0.271	0.280	0.276	0.281	0.228	0.226	0.227	0.227	0.223	0.223	0.224	0.224	0.223	0.149	0.143	0.122	0.118	0.112	0.103
9.53	0.270	0.280	0.275	0.281	0.228	0.226	0.227	0.227	0.223	0.223	0.224	0.224	0.223	0.149	0.144	0.122	0.119	0.112	0.103

Cavity, $z = -0.200$

$p/p_{t,j}$ at x/x_t of																							
NPR	1.456	1.543	1.629	NPR	1.111	1.154	1.198	1.241	1.327	1.370	1.413	1.456	1.500	1.543	1.586	1.629	1.672	1.758	1.802	1.845	1.888	1.931	1.974
1.25	0.680	0.701	0.711	1.25	0.680	0.701	0.711	0.718	0.731	0.730	0.730	0.734	0.736	0.740	0.742	0.752	0.765	0.767	0.772	0.772	0.773	0.772	
1.40	0.459	0.504	0.531	1.40	0.459	0.504	0.531	0.551	0.586	0.590	0.591	0.592	0.594	0.599	0.607	0.618	0.637	0.670	0.678	0.688	0.692	0.698	0.702
1.61	0.295	0.391	0.449	1.61	0.295	0.391	0.449	0.475	0.539	0.532	0.534	0.533	0.534	0.535	0.537	0.538	0.544	0.557	0.562	0.573	0.580	0.587	0.595
1.80	0.262	0.285	0.334	1.80	0.262	0.285	0.334	0.315	0.371	0.382	0.382	0.383	0.386	0.388	0.395	0.405	0.433	0.500	0.516	0.532	0.541	0.546	0.549
2.01	0.263	0.287	0.309	2.01	0.263	0.287	0.309	0.304	0.327	0.330	0.329	0.329	0.330	0.332	0.337	0.346	0.357	0.401	0.418	0.436	0.453	0.469	0.482
2.21	0.264	0.289	0.326	2.21	0.264	0.289	0.326	0.310	0.353	0.362	0.365	0.367	0.372	0.378	0.381	0.378	0.382	0.395	0.401	0.409	0.417	0.424	0.420
2.41	0.266	0.291	0.310	2.41	0.266	0.291	0.310	0.305	0.325	0.328	0.327	0.328	0.329	0.334	0.348	0.348	0.352	0.366	0.370	0.377	0.383	0.389	0.384
2.61	0.270	0.291	0.287	2.61	0.270	0.291	0.287	0.276	0.271	0.268	0.269	0.268	0.262	0.265	0.273	0.274	0.294	0.330	0.340	0.349	0.356	0.363	0.366
3.01	0.279	0.292	0.284	3.01	0.279	0.292	0.284	0.284	0.258	0.238	0.231	0.232	0.234	0.233	0.235	0.231	0.234	0.264	0.278	0.290	0.299	0.307	0.316
3.41	0.281	0.292	0.284	3.41	0.281	0.292	0.284	0.284	0.257	0.234	0.226	0.226	0.227	0.226	0.229	0.228	0.230	0.250	0.254	0.257	0.261	0.267	0.272
3.82	0.281	0.293	0.283	3.82	0.281	0.293	0.283	0.284	0.255	0.231	0.222	0.222	0.221	0.222	0.223	0.219	0.218	0.227	0.232	0.235	0.239	0.243	
4.21	0.281	0.293	0.284	4.21	0.281	0.293	0.284	0.284	0.255	0.231	0.221	0.220	0.220	0.219	0.219	0.221	0.214	0.153	0.188	0.203	0.207	0.211	0.217
4.62	0.281	0.293	0.284	4.62	0.281	0.293	0.284	0.284	0.255	0.231	0.222	0.220	0.219	0.220	0.222	0.222	0.215	0.139	0.130	0.137	0.169	0.190	0.204
5.02	0.281	0.293	0.283	5.02	0.281	0.293	0.283	0.283	0.256	0													

Table 12. Nozzle Internal Static Pressure Ratios for Configuration 10

Convergent Flap, $z = 0.000$

$p/p_{I,j}$ at x/x_f of							$p/p_{I,j}$ at x/x_f of																				
NPR	0.330	0.440	0.550	0.659	0.769	0.890	1.000	NPR	1.111	1.154	1.198	1.241	1.327	1.370	1.413	1.456	1.500	1.543	1.586	1.629	1.672	1.758	1.802	1.845	1.888	1.931	1.974
1.25	0.960	0.948	0.931	0.904	0.858	0.685	0.463	1.25	0.639	0.676	0.707	0.721	0.741	0.740	0.743	0.744	0.750	0.756	0.763	0.771	0.784	0.789	0.792	0.795	0.797	0.798	
1.40	0.958	0.945	0.927	0.899	0.851	0.672	0.411	1.40	0.510	0.536	0.566	0.577	0.607	0.609	0.614	0.618	0.623	0.633	0.642	0.650	0.660	0.679	0.689	0.695	0.700	0.706	0.708
1.60	0.958	0.944	0.927	0.898	0.850	0.670	0.368	1.60	0.277	0.293	0.373	0.456	0.521	0.521	0.525	0.523	0.530	0.538	0.549	0.564	0.593	0.604	0.611	0.616	0.621	0.623	
1.80	0.958	0.943	0.928	0.899	0.850	0.670	0.368	1.80	0.277	0.287	0.316	0.293	0.430	0.431	0.435	0.437	0.436	0.439	0.440	0.447	0.454	0.480	0.494	0.506	0.518	0.530	0.540
2.00	0.959	0.944	0.929	0.900	0.851	0.670	0.367	2.00	0.277	0.288	0.312	0.292	0.411	0.413	0.417	0.418	0.419	0.422	0.422	0.424	0.427	0.441	0.449	0.457	0.466	0.474	0.472
2.20	0.959	0.943	0.929	0.899	0.851	0.670	0.367	2.20	0.278	0.287	0.309	0.291	0.397	0.398	0.401	0.403	0.403	0.405	0.405	0.406	0.407	0.413	0.419	0.424	0.430	0.435	0.429
2.40	0.958	0.943	0.929	0.899	0.850	0.670	0.367	2.40	0.278	0.287	0.305	0.291	0.368	0.366	0.367	0.369	0.371	0.375	0.377	0.379	0.380	0.386	0.389	0.391	0.397	0.400	0.392
2.60	0.958	0.943	0.929	0.899	0.851	0.670	0.366	2.60	0.279	0.287	0.301	0.290	0.337	0.335	0.332	0.331	0.333	0.338	0.344	0.350	0.354	0.363	0.366	0.369	0.369	0.362	
3.00	0.959	0.943	0.929	0.899	0.850	0.670	0.367	3.00	0.279	0.288	0.289	0.285	0.260	0.264	0.265	0.261	0.257	0.255	0.254	0.262	0.278	0.300	0.305	0.311	0.317	0.321	0.322
3.39	0.958	0.943	0.929	0.899	0.850	0.670	0.367	3.39	0.279	0.288	0.285	0.285	0.238	0.235	0.239	0.230	0.229	0.231	0.231	0.231	0.233	0.265	0.272	0.275	0.277	0.278	0.283
3.80	0.959	0.942	0.929	0.899	0.849	0.670	0.367	3.80	0.279	0.287	0.281	0.284	0.233	0.229	0.234	0.224	0.217	0.218	0.217	0.221	0.220	0.205	0.233	0.242	0.246	0.247	0.250
4.20	0.958	0.942	0.928	0.899	0.849	0.670	0.367	4.20	0.278	0.286	0.280	0.284	0.232	0.228	0.234	0.223	0.216	0.216	0.214	0.218	0.218	0.146	0.138	0.142	0.196	0.213	0.223
4.60	0.958	0.942	0.927	0.898	0.848	0.669	0.366	4.60	0.276	0.285	0.278	0.282	0.231	0.228	0.233	0.223	0.216	0.216	0.214	0.218	0.218	0.146	0.138	0.117	0.171	0.202	
5.00	0.958	0.941	0.927	0.899	0.848	0.669	0.366	5.00	0.276	0.285	0.278	0.283	0.231	0.228	0.233	0.224	0.216	0.216	0.214	0.218	0.218	0.146	0.139	0.118	0.117	0.111	0.180
5.39	0.957	0.941	0.927	0.898	0.848	0.669	0.365	5.39	0.275	0.284	0.278	0.282	0.231	0.228	0.234	0.224	0.216	0.216	0.214	0.217	0.218	0.146	0.140	0.118	0.117	0.110	0.133
6.20	0.957	0.940	0.926	0.897	0.846	0.668	0.364	6.20	0.273	0.282	0.276	0.281	0.230	0.228	0.234	0.224	0.217	0.217	0.215	0.218	0.218	0.147	0.141	0.118	0.117	0.111	0.103
7.00	0.956	0.940	0.925	0.896	0.845	0.667	0.362	7.00	0.272	0.281	0.276	0.280	0.230	0.228	0.234	0.224	0.217	0.217	0.215	0.218	0.218	0.147	0.142	0.119	0.118	0.112	0.103
8.00	0.956	0.939	0.924	0.895	0.844	0.667	0.361	8.00	0.270	0.280	0.274	0.279	0.229	0.228	0.233	0.224	0.217	0.217	0.215	0.218	0.218	0.147	0.143	0.119	0.118	0.112	0.104
8.90	0.956	0.939	0.924	0.895	0.844	0.666	0.360	8.90	0.269	0.278	0.274	0.278	0.229	0.228	0.233	0.224	0.218	0.218	0.215	0.218	0.219	0.148	0.144	0.119	0.119	0.112	0.104
9.49	0.955	0.939	0.923	0.895	0.843	0.666	0.359	9.49	0.268	0.278	0.273	0.277	0.229	0.227	0.233	0.223	0.218	0.218	0.215	0.218	0.219	0.148	0.145	0.119	0.119	0.113	0.104

Table 14. Nozzle Internal Static Pressure Ratios for Configuration 12

Convergent Flap, $z = 0.000$

$p/p_{t,j}$ at x/x_t of							
NPR	0.330	0.440	0.550	0.659	0.769	0.890	1.000
1.26	0.959	0.945	0.928	0.901	0.856	0.683	0.453
1.41	0.957	0.943	0.925	0.898	0.851	0.671	0.394
1.61	0.957	0.942	0.925	0.896	0.849	0.670	0.369
1.81	0.957	0.942	0.926	0.896	0.849	0.671	0.369
2.01	0.957	0.942	0.926	0.896	0.849	0.670	0.368
2.21	0.958	0.942	0.926	0.897	0.850	0.671	0.368
2.41	0.958	0.942	0.927	0.897	0.850	0.670	0.368
2.61	0.958	0.942	0.927	0.897	0.850	0.670	0.368
3.01	0.958	0.942	0.927	0.897	0.850	0.671	0.368
3.42	0.958	0.942	0.927	0.897	0.850	0.671	0.368
3.81	0.958	0.942	0.927	0.897	0.850	0.671	0.369
4.22	0.958	0.942	0.927	0.897	0.850	0.671	0.368
4.62	0.958	0.942	0.927	0.897	0.849	0.671	0.368
5.02	0.958	0.942	0.927	0.897	0.849	0.671	0.367
5.42	0.958	0.941	0.927	0.896	0.849	0.670	0.366
6.23	0.958	0.941	0.926	0.896	0.848	0.669	0.365
7.03	0.957	0.940	0.925	0.895	0.847	0.669	0.364
8.03	0.956	0.940	0.924	0.894	0.846	0.668	0.362
8.96	0.956	0.939	0.924	0.894	0.845	0.668	0.361
9.54	0.956	0.939	0.923	0.893	0.844	0.667	0.360

Divergent Flap, $z = 0.000$

$p/p_{t,j}$ at x/x_t of																			
NPR	1.111	1.154	1.198	1.241	1.327	1.370	1.413	1.456	1.500	1.543	1.586	1.629	1.672	1.758	1.802	1.845	1.888	1.931	1.974
1.26	0.604	0.645	0.680	0.692	0.710	0.720	0.727	0.728	0.736	0.740	0.750	0.756	0.760	0.775	0.778	0.780	0.781	0.784	0.785
1.41	0.474	0.503	0.536	0.546	0.580	0.590	0.599	0.604	0.613	0.620	0.631	0.642	0.650	0.671	0.679	0.683	0.689	0.695	0.698
1.61	0.267	0.277	0.308	0.319	0.469	0.491	0.506	0.513	0.519	0.527	0.541	0.557	0.571	0.604	0.612	0.616	0.619	0.620	0.617
1.81	0.268	0.279	0.304	0.282	0.387	0.399	0.415	0.422	0.427	0.431	0.438	0.447	0.457	0.481	0.493	0.503	0.515	0.525	0.534
2.01	0.270	0.280	0.302	0.283	0.349	0.359	0.384	0.395	0.405	0.411	0.418	0.425	0.430	0.442	0.448	0.454	0.462	0.467	0.462
2.21	0.273	0.282	0.300	0.284	0.307	0.307	0.348	0.362	0.374	0.383	0.395	0.404	0.408	0.416	0.420	0.428	0.430	0.432	0.425
2.41	0.274	0.282	0.298	0.284	0.288	0.260	0.287	0.299	0.312	0.326	0.343	0.358	0.367	0.383	0.388	0.390	0.394	0.396	0.390
2.61	0.275	0.283	0.296	0.284	0.274	0.253	0.252	0.239	0.233	0.273	0.305	0.317	0.324	0.353	0.358	0.361	0.363	0.365	0.359
3.01	0.276	0.285	0.293	0.284	0.243	0.253	0.239	0.231	0.213	0.209	0.194	0.190	0.239	0.293	0.302	0.307	0.311	0.315	0.313
3.42	0.277	0.286	0.290	0.284	0.233	0.254	0.235	0.224	0.212	0.205	0.194	0.174	0.188	0.232	0.248	0.260	0.268	0.274	0.275
3.81	0.277	0.286	0.287	0.285	0.233	0.255	0.236	0.225	0.212	0.205	0.195	0.174	0.185	0.138	0.133	0.174	0.214	0.232	0.245
4.22	0.277	0.285	0.287	0.285	0.233	0.255	0.236	0.226	0.213	0.206	0.196	0.179	0.185	0.139	0.132	0.115	0.145	0.197	0.215
4.62	0.277	0.285	0.286	0.285	0.233	0.256	0.237	0.227	0.213	0.206	0.197	0.180	0.185	0.140	0.133	0.115	0.112	0.153	0.194
5.02	0.276	0.285	0.286	0.285	0.233	0.256	0.237	0.228	0.214	0.207	0.198	0.180	0.186	0.141	0.133	0.116	0.112	0.107	0.173
5.42	0.276	0.285	0.286	0.285	0.233	0.256	0.237	0.228	0.214	0.207	0.199	0.181	0.186	0.142	0.134	0.117	0.113	0.107	0.141
6.23	0.275	0.284	0.285	0.284	0.233	0.256	0.238	0.229	0.215	0.208	0.200	0.182	0.187	0.143	0.135	0.117	0.114	0.109	0.102
7.03	0.274	0.283	0.285	0.284	0.233	0.256	0.238	0.229	0.215	0.209	0.201	0.183	0.187	0.144	0.136	0.118	0.115	0.110	0.103
8.03	0.272	0.282	0.284	0.283	0.232	0.256	0.238	0.230	0.216	0.209	0.201	0.184	0.187	0.146	0.137	0.119	0.116	0.110	0.103
8.96	0.271	0.281	0.283	0.282	0.232	0.256	0.238	0.230	0.217	0.210	0.202	0.185	0.188	0.146	0.138	0.120	0.116	0.111	0.104
9.54	0.271	0.280	0.283	0.282	0.232	0.255	0.238	0.230	0.217	0.210	0.202	0.185	0.188	0.147	0.139	0.120	0.117	0.112	0.105

Cavity, $z = -0.200$

$p/p_{t,j}$ at x/x_t of						
NPR	1.456	1.543	1.629	1.769	1.890	1.974
1.26	0.738	0.675	0.740	0.703	0.712	0.727
1.41	0.619	0.553	0.623	0.555	0.588	0.616
1.61	0.528	0.480	0.534	0.321	0.418	0.453
1.81	0.429	0.380	0.433	0.267	0.314	0.304
2.01	0.395	0.358	0.402	0.307	0.298	0.338
2.21	0.372	0.341	0.381	0.305	0.297	0.325
2.41	0.328	0.297	0.333	0.268	0.284	0.307
2.61	0.288	0.248	0.286	0.270	0.290	0.286
3.01	0.237	0.213	0.236	0.279	0.292	0.278
3.42	0.220	0.189	0.219	0.282	0.292	0.277
3.81	0.219	0.198	0.216	0.277	0.289	0.251
4.22	0.219	0.194	0.218	0.277	0.289	0.251
4.62	0.219	0.196	0.219	0.277	0.289	0.251
5.02	0.220	0.205	0.219	0.281	0.292	0.277
5.42	0.220	0.203	0.220	0.277	0.288	0.251
6.23	0.221	0.204	0.220	0.280	0.291	0.251
7.03	0.221	0.208	0.221	0.279	0.287	0.251
8.03	0.221	0.210	0.221	0.277	0.286	0.251
8.96	0.222	0.209	0.221	0.276	0.285	0.251
9.54	0.222	0.212	0.222	0.276	0.285	0.251

Divergent Flap, $z = 1.595$

$p/p_{t,j}$ at x/x_t of																			
NPR	1.111	1.154	1.198	1.241	1.327	1.370	1.413	1.456	1.500	1.543	1.586	1.629	1.672	1.758	1.802	1.845	1.888	1.931	1.974
1.26	0.667	0.692	0.703	0.712	0.727	0.726	0.733	0.734	0.740	0.745	0.756	0.758	0.764	0.781	0.782	0.784	0.785	0.787	
1.41	0.466	0.523	0.555	0.588	0.616	0.618	0.627	0.632	0.641	0.647	0.664	0.667	0.673	0.699	0.700	0.702	0.707	0.701	
1.61	0.270	0.321	0.418	0.453	0.519	0.519	0.528	0.526	0.532	0.539	0.557	0.567	0.577	0.611	0.616	0.618	0.619	0.618	
1.81	0.267	0.279	0.314	0.304	0.384	0.378	0.403	0.412	0.425	0.441	0.468	0.483	0.497	0.549	0.552	0.551	0.553	0.548	
2.01	0.267	0.281	0.307	0.298	0.338	0.323	0.359	0.368	0.382	0.395	0.406	0.412	0.420	0.445	0.454	0.463	0.471	0.480	
2.21	0.268	0.284																	

Table 15. Nozzle Internal Static Pressure Ratios for Configuration 13

Convergent Flap, $z = 0.000$

$p/p_{t,j}$ at x/x_t of							
NPR	0.330	0.440	0.550	0.659	0.769	0.890	1.000
1.25	0.960	0.948	0.928	0.901	0.857	0.684	0.452
1.40	0.957	0.944	0.925	0.897	0.849	0.671	0.399
1.59	0.959	0.945	0.927	0.899	0.850	0.672	0.368
1.79	0.957	0.942	0.925	0.897	0.850	0.670	0.367
2.00	0.957	0.942	0.925	0.897	0.850	0.670	0.366
2.19	0.957	0.942	0.926	0.898	0.849	0.671	0.367
2.40	0.958	0.942	0.927	0.899	0.850	0.671	0.367
2.59	0.957	0.942	0.927	0.899	0.850	0.671	0.366
3.00	0.958	0.941	0.927	0.898	0.849	0.670	0.367
3.39	0.958	0.942	0.927	0.899	0.850	0.671	0.367
3.80	0.958	0.941	0.927	0.899	0.850	0.671	0.368
4.19	0.958	0.942	0.928	0.899	0.849	0.671	0.367
4.60	0.958	0.942	0.927	0.899	0.849	0.671	0.367
5.00	0.958	0.941	0.927	0.899	0.849	0.670	0.366
5.39	0.957	0.940	0.927	0.898	0.847	0.669	0.366
6.20	0.957	0.940	0.926	0.898	0.846	0.669	0.364
6.99	0.957	0.940	0.925	0.897	0.845	0.668	0.363
7.99	0.957	0.939	0.925	0.896	0.845	0.667	0.362
8.89	0.956	0.939	0.924	0.896	0.844	0.667	0.360
9.50	0.956	0.939	0.924	0.895	0.844	0.666	0.360

Divergent Flap, $z = 0.000$

$p/p_{t,j}$ at x/x_t of																			
NPR	1.111	1.154	1.198	1.241	1.327	1.370	1.413	1.456	1.500	1.543	1.586	1.629	1.672	1.758	1.802	1.845	1.888	1.931	1.974
1.25	0.623	0.665	0.698	0.711	0.726	0.735	0.742	0.743	0.750	0.757	0.766	0.770	0.776	0.788	0.789	0.793	0.793	0.796	0.797
1.40	0.489	0.519	0.551	0.562	0.594	0.602	0.611	0.619	0.628	0.638	0.648	0.656	0.665	0.684	0.690	0.697	0.701	0.706	0.710
1.59	0.275	0.286	0.318	0.358	0.492	0.509	0.519	0.525	0.533	0.546	0.558	0.572	0.586	0.615	0.622	0.628	0.630	0.631	0.629
1.79	0.274	0.286	0.310	0.291	0.410	0.422	0.432	0.440	0.446	0.451	0.454	0.461	0.469	0.489	0.499	0.510	0.520	0.531	0.539
2.00	0.274	0.287	0.306	0.289	0.375	0.388	0.404	0.416	0.424	0.432	0.436	0.439	0.444	0.452	0.457	0.464	0.468	0.472	0.465
2.19	0.276	0.288	0.304	0.289	0.320	0.329	0.366	0.384	0.394	0.404	0.413	0.418	0.422	0.427	0.430	0.433	0.436	0.436	0.429
2.40	0.277	0.287	0.301	0.288	0.292	0.264	0.288	0.310	0.322	0.337	0.355	0.370	0.379	0.391	0.394	0.396	0.399	0.400	0.394
2.59	0.277	0.288	0.298	0.287	0.279	0.257	0.257	0.245	0.239	0.280	0.316	0.326	0.333	0.359	0.364	0.366	0.368	0.370	0.365
3.00	0.278	0.288	0.294	0.287	0.248	0.255	0.241	0.235	0.215	0.213	0.197	0.196	0.241	0.297	0.306	0.312	0.315	0.319	0.317
3.39	0.279	0.288	0.291	0.286	0.238	0.256	0.238	0.229	0.213	0.208	0.197	0.180	0.188	0.227	0.249	0.264	0.272	0.279	0.281
3.80	0.278	0.287	0.288	0.286	0.237	0.256	0.238	0.228	0.213	0.208	0.197	0.180	0.184	0.142	0.135	0.171	0.222	0.239	0.250
4.19	0.278	0.287	0.287	0.286	0.237	0.256	0.239	0.228	0.213	0.208	0.198	0.180	0.184	0.142	0.135	0.116	0.136	0.199	0.220
4.60	0.277	0.286	0.286	0.285	0.237	0.256	0.239	0.229	0.214	0.208	0.198	0.181	0.184	0.142	0.135	0.116	0.113	0.151	0.197
5.00	0.276	0.286	0.285	0.285	0.237	0.256	0.239	0.229	0.214	0.208	0.199	0.181	0.185	0.143	0.136	0.117	0.114	0.109	0.175
5.39	0.274	0.284	0.284	0.284	0.236	0.255	0.238	0.229	0.214	0.208	0.198	0.181	0.184	0.143	0.136	0.117	0.114	0.109	0.143
6.20	0.273	0.283	0.283	0.283	0.236	0.255	0.238	0.229	0.214	0.208	0.199	0.182	0.184	0.144	0.137	0.117	0.115	0.109	0.103
6.99	0.272	0.282	0.282	0.282	0.235	0.254	0.238	0.231	0.214	0.209	0.200	0.182	0.184	0.145	0.138	0.118	0.115	0.110	0.104
7.99	0.271	0.280	0.281	0.281	0.235	0.254	0.238	0.231	0.215	0.210	0.200	0.182	0.183	0.146	0.139	0.118	0.116	0.110	0.104
8.89	0.269	0.279	0.280	0.280	0.234	0.254	0.238	0.231	0.215	0.210	0.200	0.182	0.183	0.146	0.139	0.119	0.116	0.111	0.105
9.50	0.269	0.279	0.279	0.280	0.234	0.254	0.238	0.231	0.215	0.210	0.200	0.183	0.183	0.147	0.140	0.119	0.116	0.111	0.105

Cavity, $z = -0.200$

$p/p_{t,j}$ at x/x_t of																						
NPR	1.456	1.543	1.629	1.111	1.154	1.198	1.241	1.327	1.370	1.413	1.456	1.500	1.543	1.586	1.629	1.672	1.758	1.802	1.845	1.888	1.931	1.974
1.25	0.684	0.706	0.714	0.728	0.737	0.740	0.748	0.748	0.755	0.761	0.772	0.774	0.778	0.792	0.792	0.796	0.796	0.798	0.799			
1.40	0.482	0.538	0.571	0.605	0.626	0.632	0.639	0.647	0.655	0.661	0.680	0.682	0.686	0.708	0.707	0.710	0.711	0.712				
1.59	0.284	0.354	0.432	0.487	0.535	0.534	0.539	0.533	0.542	0.553	0.569	0.580	0.590	0.620	0.623	0.628	0.629	0.628	0.628	0.628	0.628	
1.79	0.274	0.288	0.305	0.314	0.402	0.398	0.422	0.427	0.439	0.453	0.485	0.495	0.504	0.550	0.551	0.556	0.557	0.557	0.557	0.557	0.556	
2.00	0.273	0.288	0.300	0.299	0.353	0.340	0.373	0.384	0.401	0.413	0.424	0.427	0.433	0.453	0.459	0.469	0.477	0.485	0.493			
2.19	0.273	0.289	0.300	0.297	0.337	0.314	0.353	0.371	0.386	0.398	0.409	0.412	0.415	0.419	0.421	0.425	0.429	0.434	0.430			
2.40	0.273	0.292	0.299	0.295	0.311	0.272	0.286	0.283	0.302	0.332	0.355	0.365	0.373	0.383	0.385	0.390	0.394	0.399	0.395			
2.59	0.274	0.294	0.298	0.294	0.290	0.263	0.264	0.251	0.236	0.258	0.260	0.287	0.315	0.355	0.362	0.368	0.376	0.381	0.379			
3.00	0.281	0.295	0.296	0.291	0.257	0.258	0.243	0.237	0.217	0.218	0.202	0.198	0.239	0.284	0.293	0.300	0.306	0.314	0.323			
3.39	0.284	0.295	0.295	0.291	0.249	0.258	0.240	0.229	0.213	0.208	0.201	0.186	0.202	0.219	0.245	0.255	0.263	0.273	0.280			
3.80	0.283	0.294	0.294	0.290	0.249	0.258	0.240	0.228	0.213	0.207	0.200	0.187	0.198	0.145	0.164	0.205	0.223	0.234	0.246			
4.19	0.283	0.294	0.294	0.289	0.248	0.257	0.240	0.228	0.214	0.207	0.200	0.187	0.196	0.137	0.132	0.129	0.135	0.190	0.225			
4.60	0.282	0.293	0.293	0.289	0.248	0.257	0.240	0.228	0.214	0.207	0.200	0.188	0.195	0.137	0.132	0.127	0.124	0.121	0.193			
5.00	0.282	0.293	0.293	0.289	0.247	0.257	0.240	0.228	0.214	0.208	0.200	0.188	0.195	0.137	0.132	0.127	0.123	0.117	0.160			
5.39	0.280	0.292	0.292	0.287	0.246	0.256	0.239	0.228	0.214	0.208	0.200	0.188	0.195	0.137	0.132	0.126	0.123	0.117	0.118			
6.20	0.279	0.291	0.291</																			

Table 16. Nozzle Internal Static Pressure Ratios for Configuration 14

Convergent Flap, $z = 0.000$

$p/p_{t,j}$ at x/x_t of							
NPR	0.330	0.440	0.550	0.659	0.769	0.890	1.000
1.26	0.957	0.945	0.927	0.901	0.855	0.682	0.471
1.41	0.957	0.942	0.925	0.898	0.849	0.670	0.408
1.61	0.956	0.942	0.926	0.897	0.849	0.670	0.369
1.81	0.957	0.942	0.926	0.897	0.849	0.670	0.368
2.01	0.957	0.942	0.926	0.898	0.850	0.670	0.368
2.21	0.958	0.943	0.927	0.899	0.850	0.670	0.367
2.41	0.958	0.943	0.927	0.898	0.851	0.670	0.368
2.61	0.958	0.943	0.928	0.899	0.851	0.670	0.367
3.01	0.958	0.943	0.928	0.899	0.851	0.670	0.367
3.41	0.959	0.943	0.928	0.899	0.851	0.671	0.368
3.82	0.958	0.943	0.928	0.899	0.851	0.671	0.368
4.22	0.958	0.943	0.928	0.899	0.850	0.671	0.368
4.62	0.958	0.942	0.928	0.899	0.850	0.671	0.368
5.02	0.958	0.942	0.928	0.899	0.850	0.670	0.367
5.42	0.958	0.942	0.927	0.898	0.849	0.670	0.367
6.23	0.957	0.941	0.926	0.898	0.848	0.669	0.365
7.03	0.957	0.941	0.926	0.897	0.847	0.669	0.364
8.03	0.956	0.940	0.925	0.896	0.846	0.668	0.362
8.94	0.956	0.940	0.924	0.895	0.845	0.668	0.361
9.54	0.956	0.939	0.923	0.895	0.845	0.668	0.360

Divergent Flap, $z = 0.000$

$p/p_{t,j}$ at x/x_t of																			
NPR	1.111	1.154	1.198	1.241	1.327	1.370	1.413	1.456	1.500	1.543	1.586	1.629	1.672	1.758	1.802	1.845	1.888	1.931	1.974
1.26	0.610	0.645	0.677	0.691	0.713	0.719	0.721	0.725	0.730	0.735	0.742	0.749	0.758	0.772	0.776	0.780	0.783	0.785	0.788
1.41	0.501	0.526	0.554	0.563	0.592	0.598	0.603	0.606	0.611	0.617	0.624	0.631	0.641	0.660	0.668	0.674	0.681	0.687	0.691
1.61	0.269	0.279	0.312	0.374	0.496	0.504	0.507	0.509	0.513	0.516	0.524	0.537	0.556	0.592	0.602	0.610	0.614	0.616	0.617
1.81	0.269	0.280	0.303	0.283	0.393	0.409	0.416	0.418	0.419	0.420	0.427	0.435	0.446	0.476	0.489	0.500	0.512	0.524	0.533
2.01	0.271	0.282	0.302	0.284	0.402	0.415	0.423	0.427	0.429	0.431	0.433	0.436	0.439	0.451	0.456	0.461	0.468	0.472	0.464
2.21	0.273	0.283	0.300	0.284	0.363	0.383	0.390	0.396	0.399	0.400	0.402	0.404	0.414	0.419	0.423	0.427	0.432	0.423	0.424
2.41	0.274	0.283	0.298	0.284	0.311	0.341	0.347	0.355	0.364	0.368	0.370	0.372	0.374	0.383	0.386	0.388	0.392	0.396	0.389
2.61	0.275	0.284	0.296	0.284	0.283	0.290	0.283	0.297	0.308	0.321	0.332	0.338	0.343	0.357	0.360	0.361	0.364	0.366	0.361
3.01	0.276	0.286	0.291	0.284	0.253	0.251	0.245	0.234	0.229	0.218	0.217	0.227	0.265	0.305	0.311	0.314	0.317	0.318	0.319
3.41	0.278	0.286	0.288	0.284	0.245	0.248	0.236	0.226	0.219	0.207	0.205	0.192	0.204	0.255	0.267	0.273	0.276	0.279	0.283
3.82	0.277	0.286	0.285	0.284	0.244	0.247	0.235	0.225	0.216	0.204	0.204	0.189	0.196	0.144	0.175	0.213	0.222	0.234	0.245
4.22	0.277	0.286	0.285	0.284	0.244	0.248	0.235	0.226	0.217	0.204	0.205	0.189	0.196	0.143	0.124	0.190	0.205	0.218	0.218
4.62	0.277	0.285	0.284	0.284	0.244	0.248	0.236	0.227	0.218	0.205	0.205	0.190	0.196	0.144	0.130	0.119	0.114	0.171	0.196
5.02	0.277	0.285	0.284	0.284	0.244	0.248	0.236	0.227	0.218	0.205	0.206	0.191	0.197	0.144	0.131	0.120	0.114	0.108	0.176
5.42	0.276	0.285	0.284	0.284	0.243	0.248	0.237	0.228	0.218	0.206	0.206	0.191	0.197	0.145	0.132	0.120	0.115	0.108	0.141
6.23	0.275	0.284	0.283	0.283	0.243	0.248	0.237	0.229	0.219	0.207	0.207	0.192	0.198	0.146	0.134	0.121	0.116	0.109	0.102
7.03	0.274	0.283	0.282	0.283	0.243	0.248	0.238	0.229	0.220	0.208	0.208	0.193	0.198	0.147	0.135	0.122	0.116	0.110	0.103
8.03	0.273	0.281	0.282	0.282	0.242	0.248	0.238	0.229	0.221	0.208	0.209	0.194	0.199	0.149	0.136	0.123	0.117	0.111	0.103
8.94	0.271	0.280	0.281	0.281	0.242	0.248	0.238	0.230	0.221	0.209	0.209	0.194	0.199	0.150	0.137	0.123	0.118	0.111	0.104
9.54	0.271	0.280	0.281	0.281	0.241	0.248	0.239	0.230	0.221	0.209	0.209	0.195	0.199	0.150	0.138	0.124	0.118	0.111	0.104

Divergent Flap, $z = 1.595$

$p/p_{t,j}$ at x/x_t of																			
NPR	1.111	1.154	1.198	1.241	1.327	1.370	1.413	1.456	1.500	1.543	1.586	1.629	1.672	1.758	1.802	1.845	1.888	1.931	1.974
1.26	0.695	0.719	0.724	0.735	0.738	0.739	0.741	0.741	0.745	0.746	0.749	0.751	0.756	0.762	0.765	0.765	0.767	0.767	0.765
1.41	0.492	0.530	0.552	0.576	0.601	0.608	0.610	0.613	0.620	0.624	0.635	0.641	0.657	0.678	0.684	0.688	0.692	0.696	0.697
1.61	0.274	0.322	0.403	0.446	0.518	0.523	0.523	0.529	0.532	0.545	0.552	0.577	0.611	0.615	0.615	0.616	0.616	0.615	0.615
1.81	0.261	0.289	0.314	0.310	0.385	0.410	0.412	0.418	0.421	0.425	0.437	0.451	0.481	0.535	0.546	0.550	0.553	0.553	0.550
2.01	0.260	0.290	0.314	0.309	0.392	0.416	0.422	0.427	0.431	0.431	0.433	0.434	0.438	0.449	0.455	0.461	0.466	0.473	0.471
2.21	0.261	0.291	0.310	0.312	0.360	0.384	0.390	0.398	0.405	0.407	0.409	0.409	0.410	0.415	0.419	0.424	0.428	0.431	0.421
2.41	0.264	0.291	0.307	0.307	0.324	0.337	0.341	0.351	0.360	0.368	0.375	0.376	0.383	0.386	0.389	0.393	0.395	0.397	0.387
2.61	0.269	0.291	0.304	0.296	0.298	0.290	0.290	0.296	0.304	0.314	0.325	0.343	0.355	0.359	0.361	0.363	0.366	0.361	0.361
3.01	0.279	0.292	0.299	0.287	0.257	0.252	0.247	0.233	0.236	0.224	0.224	0.227	0.253	0.298	0.305	0.309	0.311	0.315	0.318
3.41	0.281	0.292	0.298	0.286	0.245	0.248	0.235	0.224	0.219	0.207	0.212	0.198	0.211	0.248	0.258	0.267	0.274	0.278	0.282
3.82	0.281	0.292	0.297	0.286	0.242	0.248	0.233	0.224	0.215	0.203	0.207	0.198	0.197	0.160	0.173	0.211	0.231	0.240	0.247
4.22	0.281	0.292	0.297	0.286	0.242	0.248	0.233	0.224	0.215	0.203	0.207	0.199	0.197	0.149	0.142	0.140	0.187	0.213	0.225
4.62	0.281	0.292	0.297	0.286	0.243	0.248	0.233	0.225	0.216	0.204	0.208	0.199	0.197	0.149	0.141	0.113	0.117	0.129	0.194
5.02	0.280	0.292	0.297	0.286	0.243	0.249	0.234	0.225	0.216	0.204	0.208	0.200	0.198	0.149	0.142	0.114	0.115	0.112	0.151
5.42	0.280	0.291	0.297	0.286	0.243	0.249	0.234	0.225	0.216	0.205	0.208	0.200	0.198	0.149	0.143	0.114	0.115	0.111	0.113
6.23	0.279	0.290	0.29																

Table 19. Nozzle Internal Static Pressure Ratios for Configuration 17

Convergent Flap, $z = 0.000$ **Divergent Flap, $z = 0.000$** $p/p_{t,j}$ at x/x_f of

NPR	0.330	0.440	0.550	0.659	0.769	0.890	1.000	NPR	1.111	1.154	1.198	1.241	1.327	1.370	1.413	1.456	1.500	1.543	1.586	1.629	1.672	1.758	1.802	1.845	1.888	1.931	1.974
1.25	0.960	0.950	0.931	0.903	0.858	0.687	0.477	1.25	0.609	0.645	0.672	0.687	0.713	0.717	0.718	0.723	0.726	0.730	0.737	0.747	0.758	0.775	0.778	0.783	0.786	0.787	0.790
1.40	0.959	0.947	0.928	0.899	0.852	0.672	0.398	1.40	0.478	0.513	0.546	0.557	0.591	0.597	0.599	0.604	0.608	0.613	0.623	0.634	0.648	0.673	0.681	0.688	0.694	0.699	0.702
1.60	0.958	0.946	0.929	0.898	0.851	0.670	0.369	1.60	0.271	0.292	0.360	0.388	0.508	0.517	0.519	0.521	0.522	0.525	0.532	0.546	0.568	0.599	0.606	0.611	0.613	0.615	0.617
1.80	0.959	0.945	0.928	0.899	0.851	0.670	0.368	1.80	0.270	0.284	0.331	0.275	0.386	0.406	0.407	0.410	0.411	0.417	0.425	0.432	0.444	0.478	0.492	0.505	0.518	0.529	0.540
2.00	0.959	0.944	0.929	0.899	0.851	0.670	0.368	2.00	0.272	0.284	0.323	0.280	0.343	0.369	0.371	0.377	0.381	0.386	0.389	0.392	0.399	0.419	0.429	0.438	0.449	0.461	0.465
2.20	0.959	0.944	0.929	0.899	0.851	0.670	0.367	2.20	0.274	0.284	0.325	0.278	0.353	0.377	0.379	0.383	0.385	0.390	0.395	0.399	0.402	0.410	0.415	0.419	0.425	0.428	0.430
2.41	0.959	0.944	0.929	0.899	0.852	0.670	0.367	2.41	0.275	0.284	0.312	0.289	0.307	0.329	0.331	0.337	0.342	0.347	0.352	0.357	0.361	0.372	0.375	0.379	0.384	0.389	0.381
2.61	0.959	0.944	0.929	0.899	0.852	0.670	0.367	2.61	0.276	0.285	0.304	0.292	0.290	0.302	0.303	0.311	0.315	0.321	0.326	0.333	0.339	0.352	0.355	0.357	0.360	0.362	0.354
3.01	0.959	0.944	0.929	0.900	0.852	0.671	0.368	3.01	0.277	0.286	0.285	0.283	0.261	0.260	0.251	0.251	0.242	0.249	0.260	0.272	0.284	0.305	0.308	0.310	0.313	0.316	0.318
3.41	0.960	0.944	0.930	0.900	0.852	0.671	0.368	3.41	0.278	0.286	0.278	0.283	0.245	0.248	0.240	0.230	0.219	0.219	0.216	0.216	0.238	0.267	0.271	0.273	0.274	0.275	0.281
3.81	0.959	0.944	0.929	0.900	0.851	0.671	0.369	3.81	0.277	0.286	0.273	0.283	0.240	0.245	0.238	0.224	0.216	0.211	0.205	0.201	0.214	0.229	0.239	0.243	0.244	0.246	0.251
4.21	0.959	0.943	0.929	0.899	0.851	0.671	0.368	4.21	0.277	0.286	0.272	0.283	0.238	0.245	0.238	0.223	0.216	0.210	0.202	0.198	0.209	0.143	0.128	0.121	0.189	0.216	0.227
4.62	0.959	0.943	0.929	0.899	0.851	0.671	0.367	4.62	0.277	0.285	0.272	0.283	0.238	0.245	0.238	0.223	0.216	0.211	0.202	0.198	0.209	0.144	0.128	0.119	0.113	0.159	0.196
5.01	0.959	0.943	0.928	0.899	0.850	0.670	0.367	5.01	0.276	0.285	0.272	0.283	0.238	0.246	0.239	0.224	0.216	0.211	0.203	0.199	0.209	0.145	0.129	0.120	0.114	0.110	0.177
5.42	0.958	0.942	0.927	0.898	0.849	0.670	0.366	5.42	0.276	0.285	0.271	0.283	0.238	0.246	0.239	0.224	0.217	0.211	0.203	0.199	0.209	0.146	0.130	0.120	0.114	0.108	0.156
6.22	0.958	0.941	0.927	0.897	0.848	0.669	0.365	6.22	0.275	0.284	0.271	0.282	0.238	0.246	0.240	0.225	0.218	0.213	0.204	0.199	0.210	0.147	0.132	0.121	0.115	0.109	0.102
7.02	0.957	0.941	0.926	0.897	0.847	0.669	0.364	7.02	0.274	0.283	0.270	0.281	0.238	0.246	0.240	0.225	0.218	0.213	0.204	0.200	0.210	0.148	0.133	0.122	0.116	0.110	0.102
8.03	0.956	0.940	0.925	0.896	0.846	0.668	0.362	8.03	0.272	0.281	0.270	0.280	0.237	0.246	0.240	0.226	0.219	0.214	0.204	0.200	0.210	0.149	0.134	0.122	0.117	0.110	0.103
8.94	0.956	0.940	0.924	0.895	0.845	0.668	0.361	8.94	0.271	0.280	0.269	0.280	0.237	0.246	0.240	0.226	0.219	0.215	0.205	0.200	0.210	0.150	0.135	0.123	0.118	0.111	0.103
9.55	0.956	0.939	0.923	0.895	0.845	0.667	0.360	9.55	0.270	0.280	0.269	0.279	0.236	0.246	0.240	0.226	0.219	0.215	0.205	0.200	0.211	0.151	0.135	0.123	0.118	0.111	0.104

Table 20. Nozzle Internal Static Pressure Ratios for Configuration 18

Convergent Flap, $z = 0.000$

$p/p_{t,j}$ at x/x_t of							$p/p_{t,j}$ at x/x_t of																				
NPR	0.330	0.440	0.550	0.659	0.769	0.890	1.000	NPR	1.111	1.154	1.198	1.241	1.327	1.370	1.413	1.456	1.500	1.543	1.586	1.629	1.672	1.758	1.802	1.845	1.888	1.931	1.974
1.25	0.959	0.947	0.928	0.904	0.857	0.684	0.462	1.25	0.629	0.668	0.697	0.712	0.731	0.733	0.734	0.734	0.737	0.740	0.747	0.755	0.766	0.781	0.785	0.788	0.791	0.792	0.794
1.40	0.957	0.944	0.926	0.899	0.851	0.671	0.403	1.40	0.493	0.524	0.555	0.566	0.597	0.600	0.604	0.609	0.615	0.623	0.633	0.643	0.654	0.676	0.685	0.690	0.696	0.701	0.705
1.60	0.957	0.943	0.926	0.897	0.850	0.669	0.370	1.60	0.276	0.294	0.354	0.386	0.505	0.510	0.514	0.513	0.517	0.521	0.533	0.549	0.569	0.601	0.610	0.615	0.618	0.620	0.621
1.80	0.958	0.942	0.926	0.898	0.849	0.669	0.369	1.80	0.275	0.286	0.331	0.281	0.406	0.417	0.422	0.425	0.425	0.426	0.430	0.439	0.450	0.479	0.493	0.504	0.516	0.528	0.537
2.00	0.958	0.942	0.926	0.898	0.850	0.670	0.369	2.00	0.276	0.286	0.330	0.281	0.401	0.412	0.418	0.421	0.425	0.428	0.431	0.434	0.437	0.449	0.455	0.461	0.468	0.472	0.467
2.20	0.958	0.942	0.927	0.898	0.850	0.670	0.369	2.20	0.278	0.285	0.325	0.282	0.374	0.386	0.392	0.397	0.400	0.401	0.401	0.401	0.409	0.415	0.420	0.426	0.431	0.427	
2.40	0.958	0.942	0.928	0.899	0.850	0.670	0.368	2.40	0.278	0.286	0.317	0.286	0.339	0.354	0.357	0.363	0.367	0.369	0.369	0.369	0.379	0.385	0.389	0.394	0.399	0.394	
2.60	0.958	0.942	0.928	0.899	0.851	0.670	0.368	2.60	0.278	0.286	0.308	0.292	0.307	0.321	0.322	0.327	0.332	0.337	0.340	0.341	0.343	0.356	0.361	0.362	0.365	0.369	0.362
3.00	0.959	0.942	0.928	0.900	0.850	0.671	0.369	3.00	0.279	0.287	0.288	0.285	0.263	0.262	0.253	0.250	0.243	0.250	0.263	0.274	0.287	0.306	0.310	0.313	0.316	0.319	0.320
3.40	0.959	0.942	0.928	0.899	0.851	0.671	0.369	3.40	0.279	0.287	0.281	0.284	0.246	0.248	0.242	0.231	0.220	0.219	0.215	0.214	0.236	0.268	0.272	0.273	0.275	0.279	0.284
3.80	0.959	0.942	0.928	0.900	0.850	0.671	0.369	3.80	0.278	0.286	0.276	0.284	0.241	0.245	0.240	0.225	0.216	0.210	0.202	0.199	0.209	0.229	0.239	0.243	0.244	0.247	0.253
4.20	0.959	0.942	0.928	0.900	0.850	0.671	0.369	4.20	0.278	0.286	0.276	0.284	0.240	0.245	0.240	0.224	0.216	0.210	0.200	0.195	0.207	0.144	0.129	0.123	0.194	0.218	0.228
4.60	0.959	0.942	0.928	0.899	0.850	0.671	0.369	4.60	0.277	0.285	0.275	0.284	0.240	0.245	0.240	0.225	0.217	0.210	0.200	0.196	0.207	0.145	0.129	0.121	0.115	0.166	0.199
5.00	0.958	0.942	0.928	0.899	0.849	0.671	0.368	5.00	0.276	0.285	0.274	0.283	0.240	0.245	0.240	0.225	0.217	0.210	0.201	0.196	0.207	0.145	0.130	0.121	0.115	0.111	0.179
5.40	0.958	0.942	0.927	0.898	0.848	0.670	0.367	5.40	0.276	0.284	0.274	0.283	0.240	0.245	0.240	0.225	0.217	0.210	0.201	0.196	0.207	0.146	0.130	0.122	0.116	0.109	0.154
6.20	0.957	0.941	0.926	0.897	0.847	0.669	0.365	6.20	0.274	0.283	0.273	0.282	0.239	0.245	0.241	0.226	0.218	0.211	0.201	0.196	0.206	0.147	0.131	0.122	0.117	0.110	0.103
7.00	0.957	0.940	0.925	0.897	0.846	0.668	0.363	7.00	0.273	0.282	0.272	0.281	0.239	0.245	0.240	0.226	0.218	0.212	0.202	0.197	0.206	0.148	0.132	0.122	0.117	0.111	0.103
8.00	0.956	0.940	0.925	0.896	0.845	0.668	0.362	8.00	0.271	0.281	0.271	0.280	0.239	0.245	0.240	0.227	0.218	0.213	0.202	0.197	0.206	0.148	0.133	0.123	0.118	0.111	0.103
8.91	0.956	0.939	0.924	0.895	0.845	0.667	0.361	8.91	0.270	0.279	0.270	0.279	0.238	0.245	0.241	0.227	0.219	0.213	0.202	0.197	0.206	0.149	0.134	0.123	0.118	0.112	0.104
9.50	0.956	0.939	0.923	0.895	0.844	0.667	0.360	9.50	0.270	0.279	0.270	0.279	0.238	0.245	0.240	0.227	0.219	0.214	0.202	0.198	0.206	0.149	0.134	0.124	0.119	0.112	0.104

44

Cavity, $z = -0.200$

$p/p_{t,j}$ at x/x_t of							$p/p_{t,j}$ at x/x_t of																	
NPR	1.456	1.543	1.629	NPR	1.111	1.154	1.198	1.241	1.327	1.370	1.413	1.456	1.500	1.543	1.586	1.629	1.672	1.758	1.802	1.845	1.888	1.931	1.974	
1.25	0.740	0.684	0.746	1.25	0.682	0.704	0.715	0.727	0.743	0.741	0.742	0.741	0.744	0.747	0.752	0.760	0.770	0.791	0.792	0.793	0.795	0.796	0.795	
1.40	0.614	0.544	0.629	1.40	0.488	0.540	0.572	0.603	0.634	0.631	0.632	0.631	0.633	0.640	0.648	0.662	0.678	0.706	0.708	0.709	0.710	0.709		
1.60	0.524	0.473	0.530	1.60	0.284	0.351	0.431	0.484	0.540	0.538	0.536	0.533	0.537	0.543	0.553	0.570	0.608	0.615	0.619	0.622	0.623	0.621		
1.80	0.426	0.386	0.433	1.80	0.268	0.287	0.307	0.312	0.422	0.425	0.422	0.426	0.427	0.432	0.443	0.459	0.485	0.546	0.554	0.558	0.558	0.554		
2.00	0.417	0.379	0.429	2.00	0.268	0.289	0.302	0.303	0.400	0.411	0.413	0.416	0.418	0.417	0.418	0.417	0.420	0.437	0.447	0.458	0.467	0.478	0.486	
2.20	0.395	0.371	0.404	2.20	0.268	0.291	0.302	0.302	0.379	0.394	0.398	0.404	0.407	0.404	0.405	0.402	0.404	0.413	0.417	0.422	0.427	0.433	0.425	
2.40	0.362	0.336	0.370	2.40	0.269	0.292	0.299	0.299	0.339	0.356	0.360	0.367	0.374	0.374	0.374	0.371	0.381	0.384	0.388	0.393	0.398	0.390		
2.60	0.329	0.295	0.337	2.60	0.271	0.294	0.297	0.295	0.305	0.314	0.321	0.326	0.335	0.340	0.343	0.341	0.346	0.350	0.360	0.365	0.361			
3.00	0.261	0.242	0.264	3.00	0.281	0.294	0.291	0.272	0.256	0.253	0.250	0.244	0.251	0.260	0.270	0.283	0.302	0.305	0.309	0.313	0.317	0.320		
3.40	0.233	0.208	0.232	3.40	0.283	0.293	0.290	0.263	0.248	0.239	0.226	0.222	0.221	0.211	0.206	0.205	0.210	0.220	0.232	0.236	0.241	0.247	0.252	
3.80	0.223	0.198	0.219	3.80	0.283	0.293	0.289	0.290	0.260	0.246	0.236	0.222	0.217	0.211	0.206	0.205	0.210	0.220	0.232	0.236	0.241	0.247	0.252	
4.20	0.221	0.192	0.216	4.20	0.282	0.293	0.289	0.260	0.246	0.235	0.222	0.215	0.208	0.203	0.202	0.203	0.204	0.201	0.204	0.204	0.204	0.198	0.213	0.226
4.60	0.221	0.201	0.217	4.60	0.282	0.292	0.289	0.289	0.260	0.246	0.235	0.222	0.215	0.207	0.201	0.204	0.201	0.204	0.201	0.204	0.201	0.193	0.201	0.201
5.00	0.221	0.202	0.217	5.00	0.282	0.292	0.289	0.289	0.260	0.246	0.235	0.222	0.216	0.20										

Table 31. Measured Peak Thrust Ratio at NPR=8.9 for Baseline and Porous Configurations

Configuration	Porosity, %	Hole Dia., in.	Cavity Depth, in.	$(F/F_i)_{\text{peak}}$
1	0	0.000	0.000	0.986
2	10	0.025	0.219	0.984
3	10	0.025	0.119	0.983
4	10	0.025	0.072	0.984
5	20	0.025	0.219	0.980
6	20	0.025	0.119	0.980
7	20	0.025	0.072	0.981
8	30	0.025	0.219	0.980
9	30	0.025	0.119	0.980
10	30	0.025	0.072	0.982
11	10	0.052	0.187	0.984
12	10	0.052	0.087	0.983
13	10	0.052	0.040	0.983
14	20	0.052	0.187	0.982
15	20	0.052	0.087	0.983
16	20	0.052	0.040	0.982
17	30	0.052	0.187	0.981
18	30	0.052	0.087	0.981
19	30	0.052	0.040	0.981
20	10	0.076	0.187	0.983
21	10	0.076	0.087	0.984
22	10	0.076	0.040	0.983
23	20	0.076	0.187	0.982
24	20	0.076	0.087	0.982
25	20	0.076	0.040	0.983
26	30	0.076	0.187	0.980
27	30	0.076	0.087	0.982
28	30	0.076	0.040	0.981

Table 32. Porous Configurations that Alleviated Separation

Configuration	Porosity, %	Hole Dia., in.	Cavity Depth, in.	$(F/F_i)_{\text{peak}}$
11	10	0.052	0.187	0.984
12	10	0.052	0.087	0.983
13	10	0.052	0.040	0.983
20	10	0.076	0.187	0.983
21	10	0.076	0.087	0.984
22	10	0.076	0.040	0.983

Table 33. Porous Configurations that Encouraged Separation

Configuration	Porosity, %	Hole Dia., in.	Cavity Depth, in.	$(F/F_i)_{\text{peak}}$
2	10	0.025	0.219	0.984
3	10	0.025	0.119	0.983
4	10	0.025	0.072	0.984
6	20	0.025	0.119	0.980
7	20	0.025	0.072	0.981
10	30	0.025	0.072	0.982
15	20	0.052	0.087	0.983
17	30	0.052	0.187	0.981
18	30	0.052	0.087	0.981
19	30	0.052	0.040	0.981

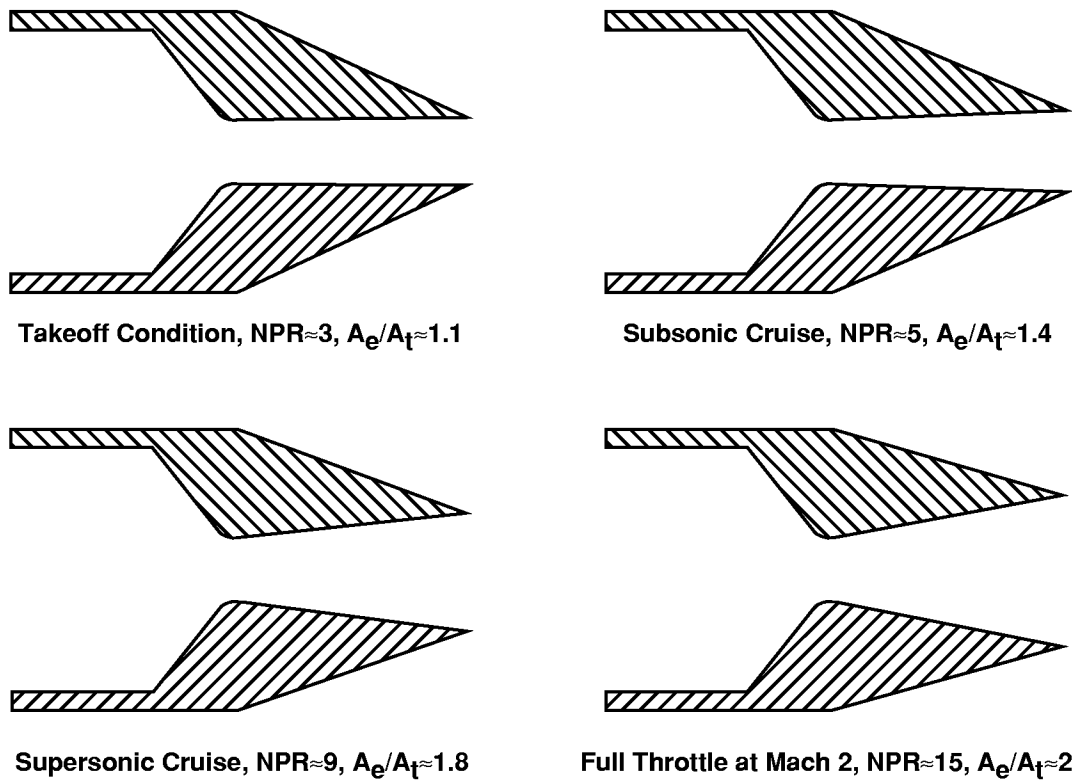


Figure 1. Sketch showing a typical variable geometry nozzle at several operating conditions.

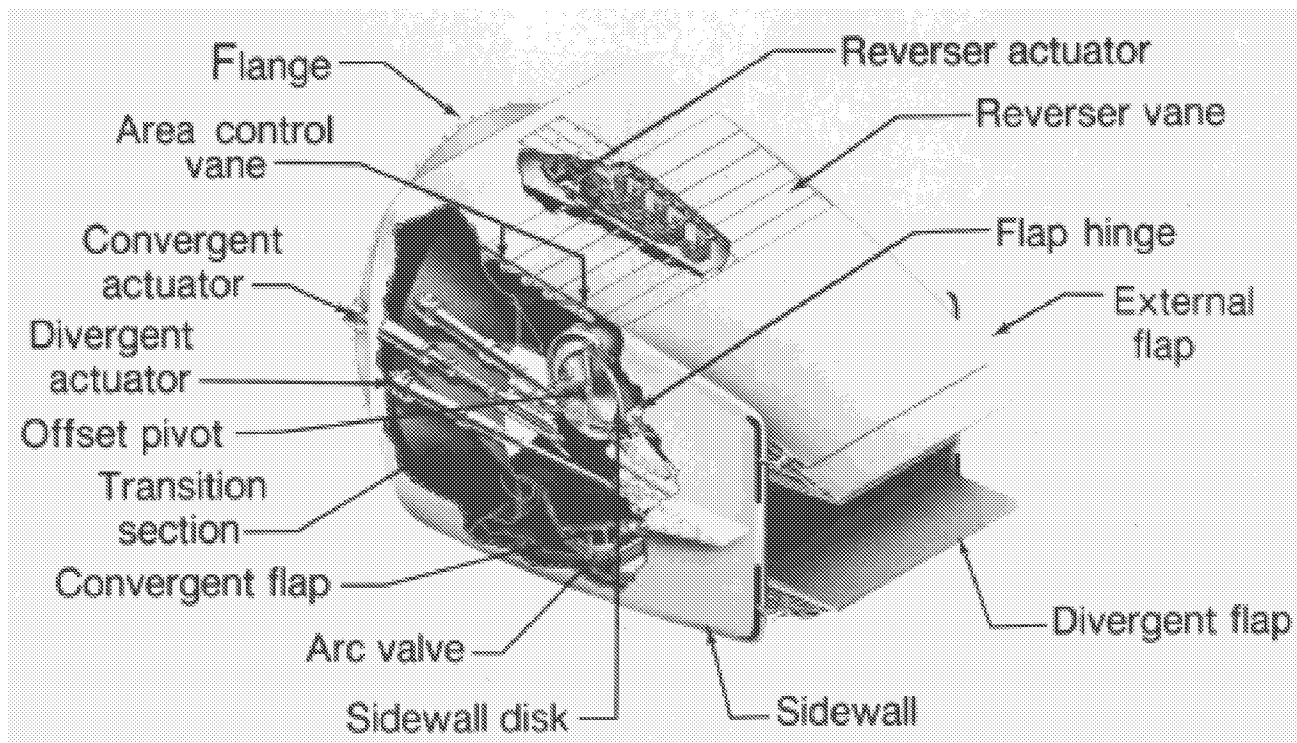
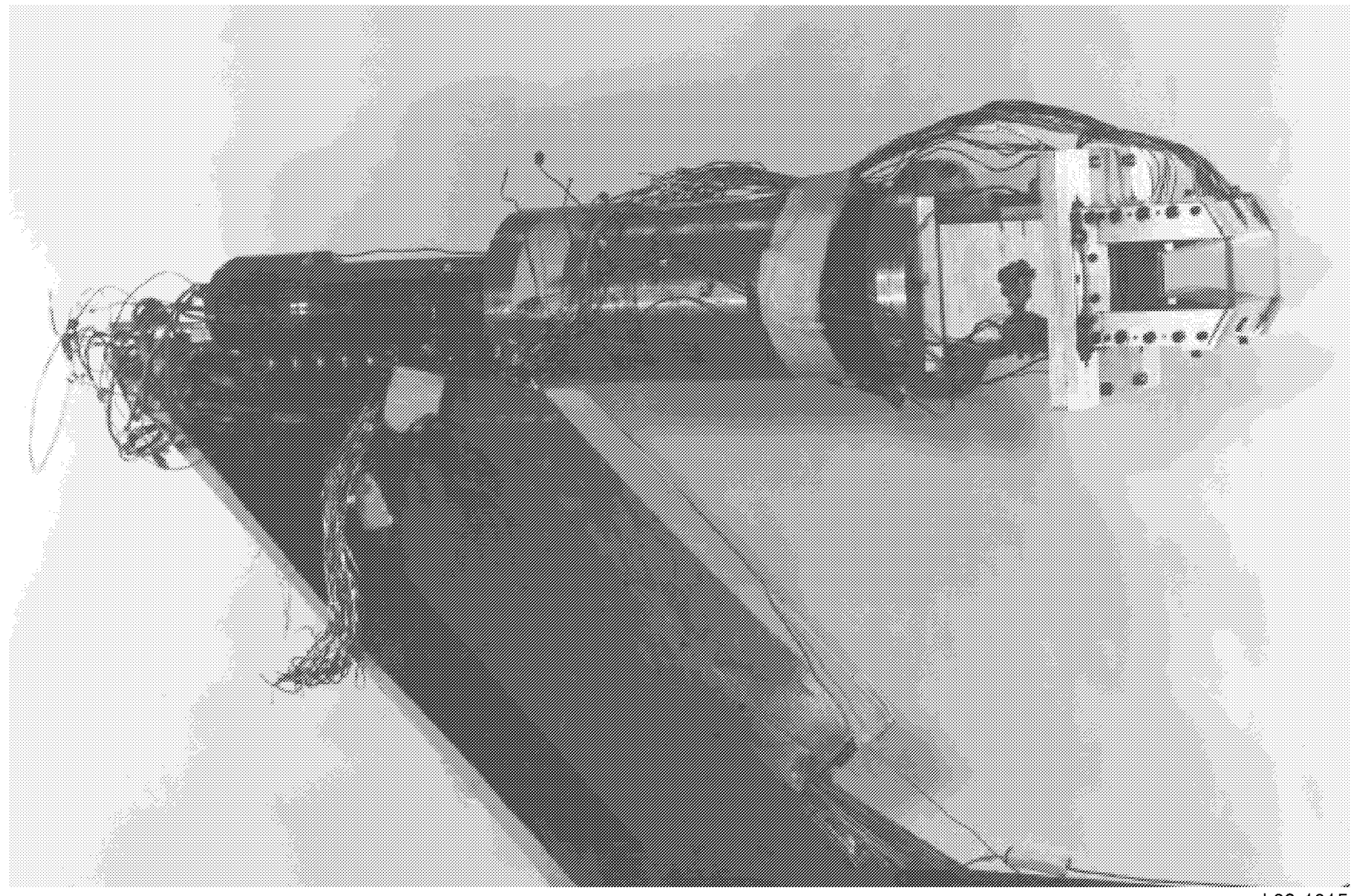


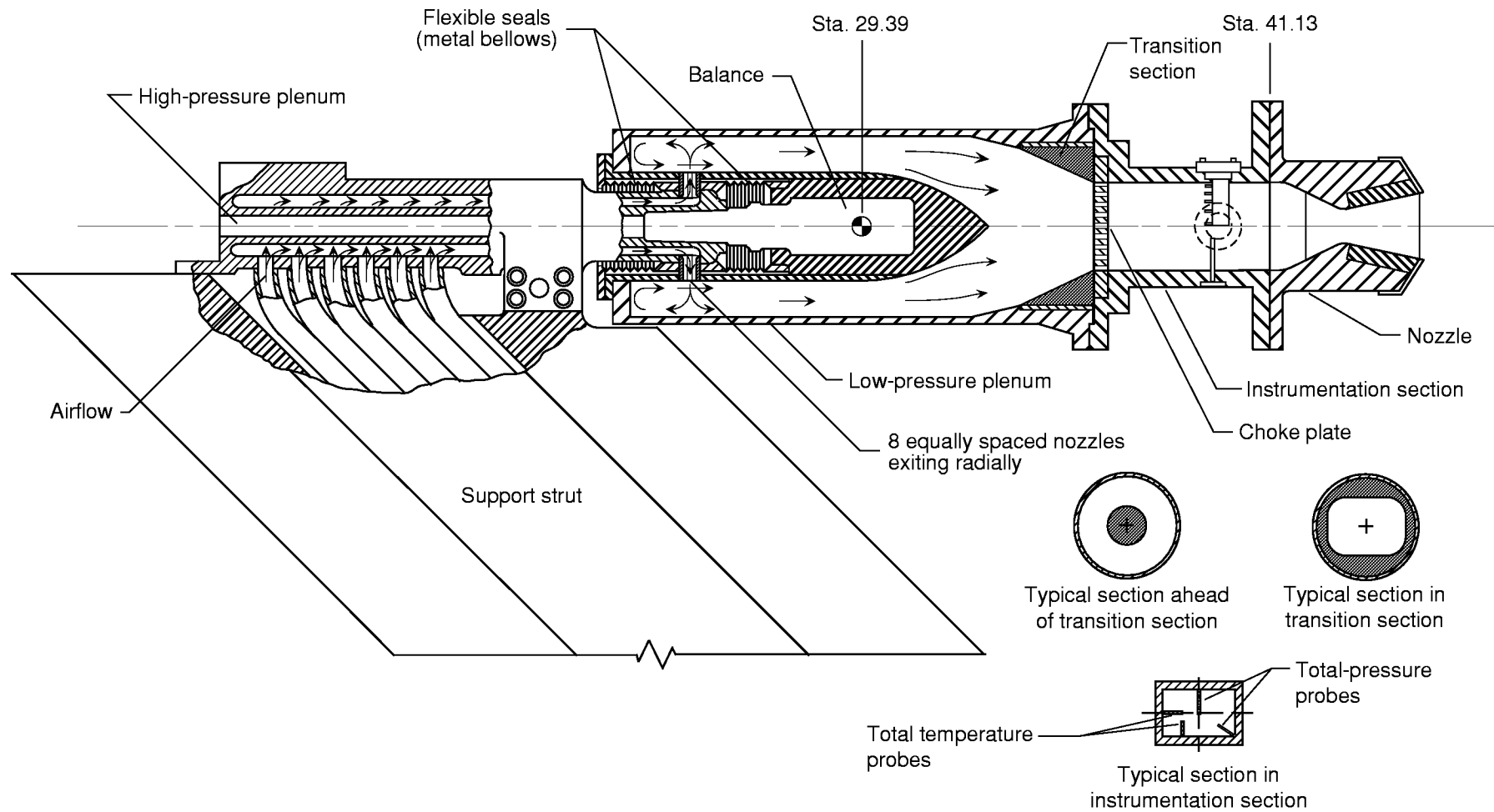
Figure 2. Sketch showing a typical variable geometry nonaxisymmetric exhaust nozzle.



L93-1015

(a) Photograph of the propulsion simulation system with a typical nozzle configuration installed.

Figure 3. Details of the single-engine propulsion simulation system.



(b) Sketch of the propulsion simulation system. Station number are in inches.

Figure 3. Concluded.

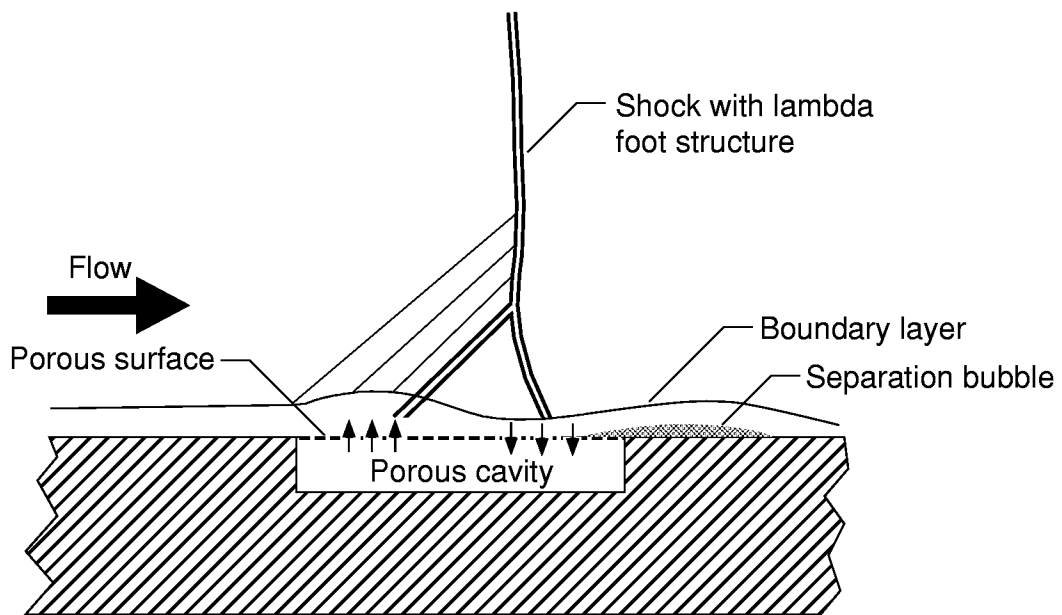


Figure 4. Sketch showing the porous cavity concept for shock-boundary layer interaction control.

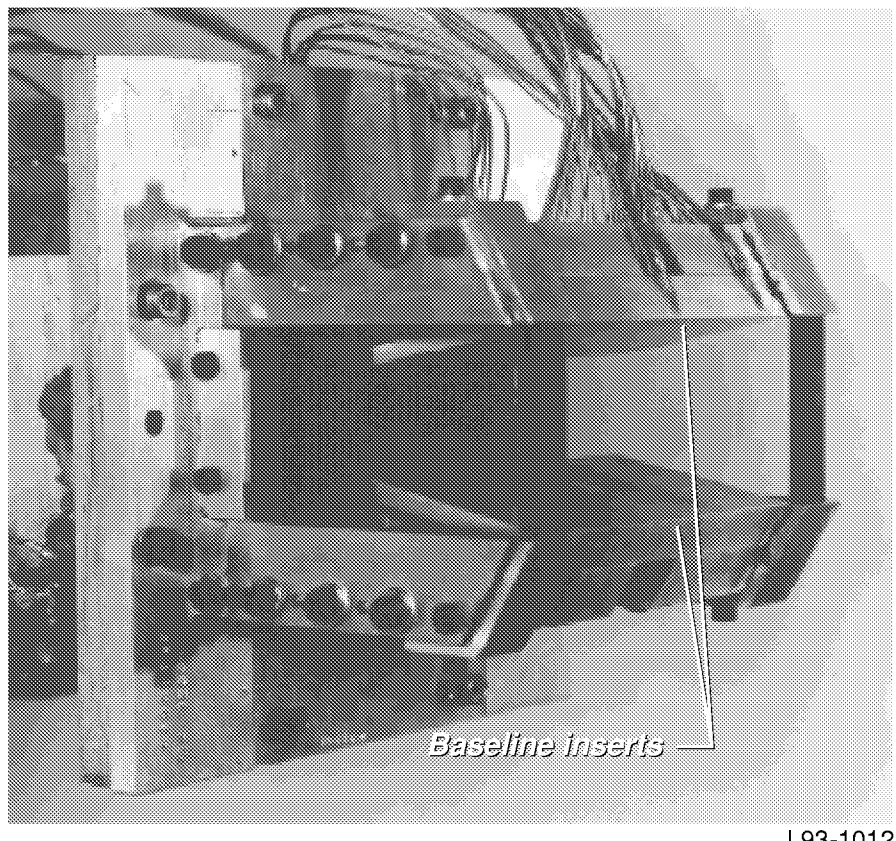
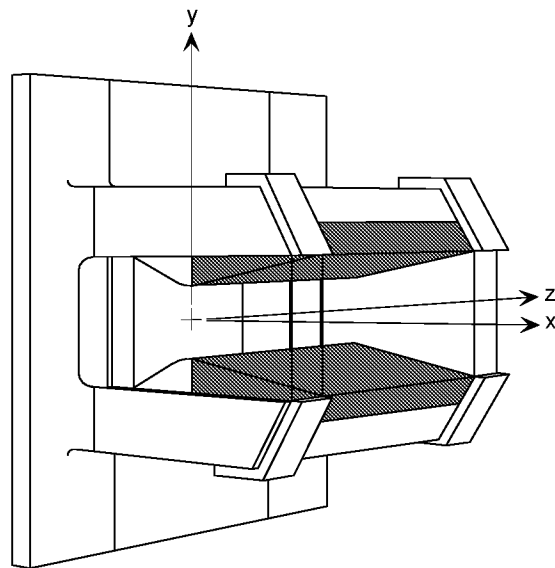
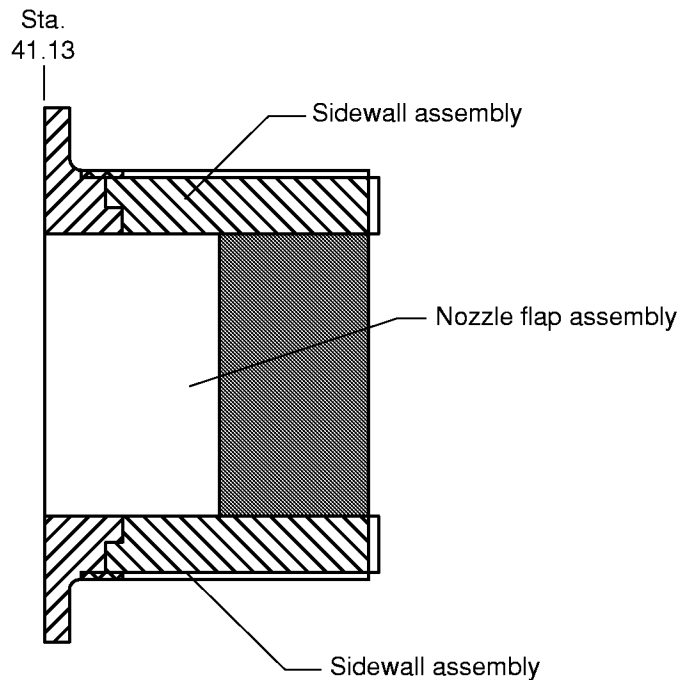


Figure 5. Photograph of the static test model with baseline flap inserts installed.

Section B-B

3-Quarter View



Section A-A

End View (looking upstream)

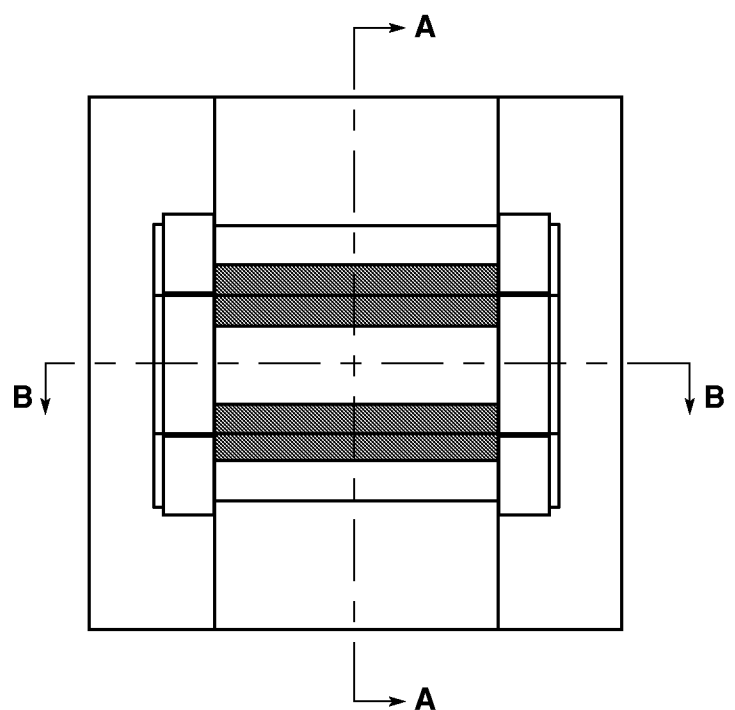
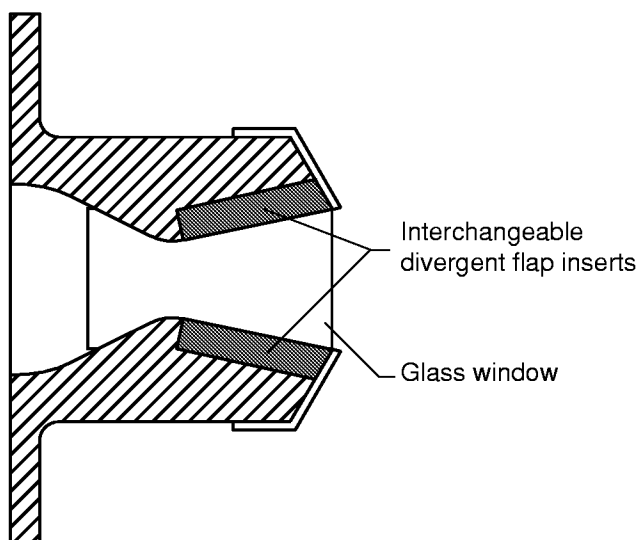
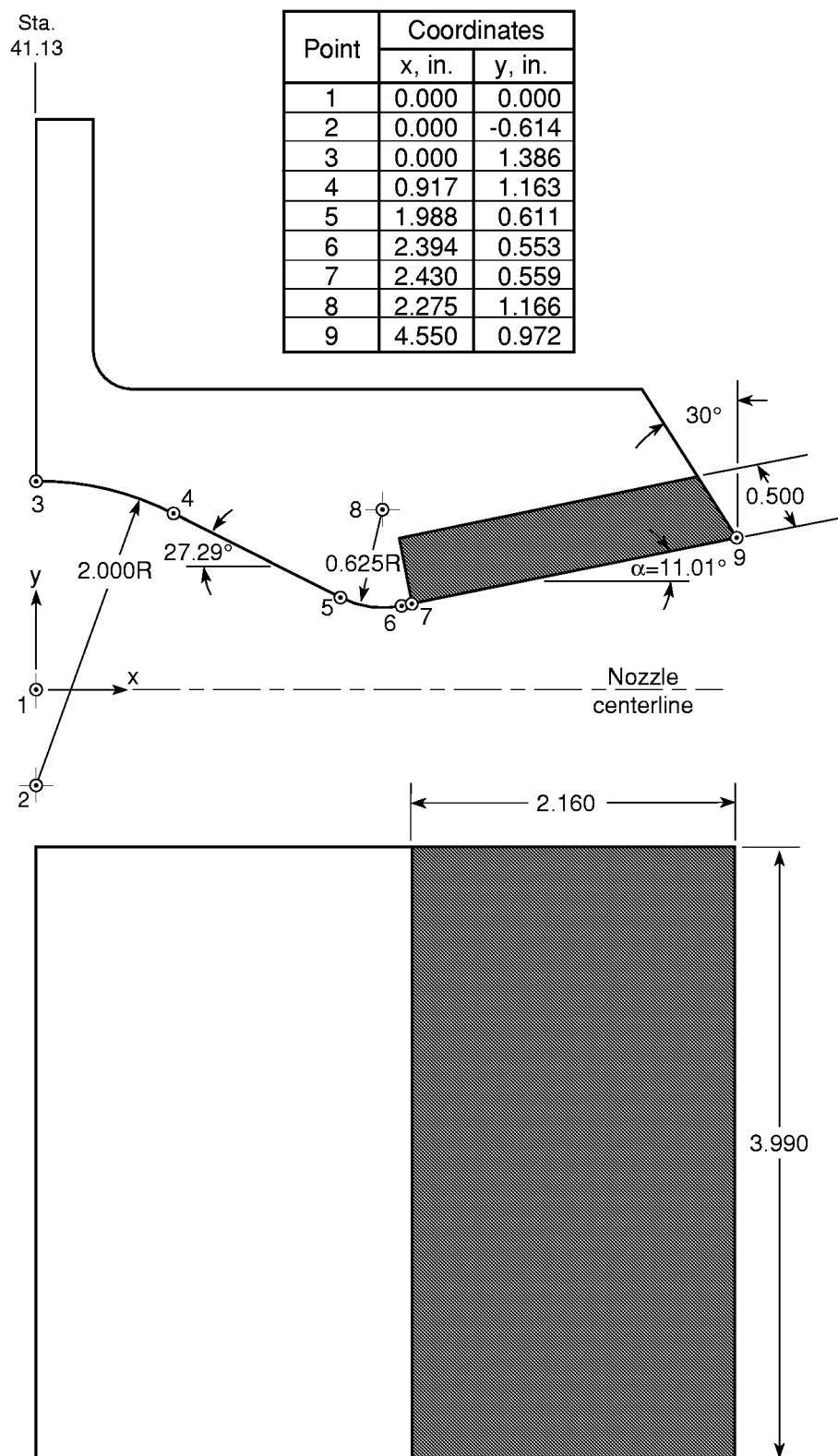
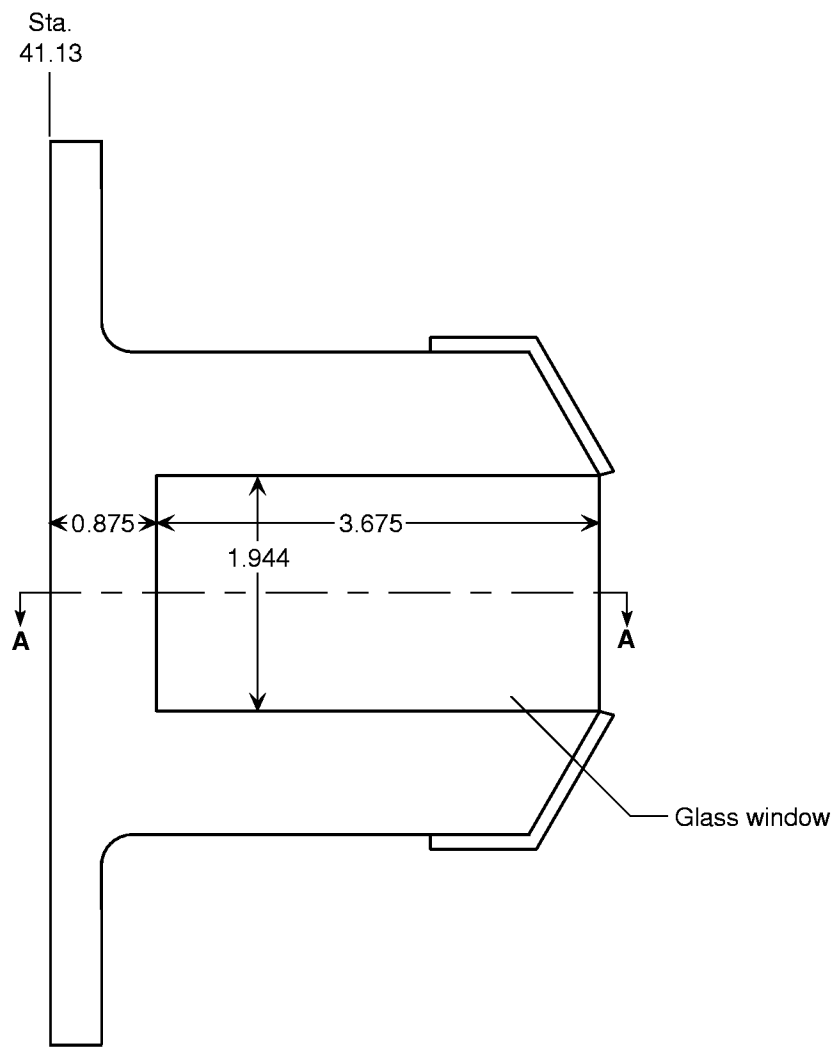


Figure 6. Sketch of nozzle model with baseline flap inserts (shaded) installed.

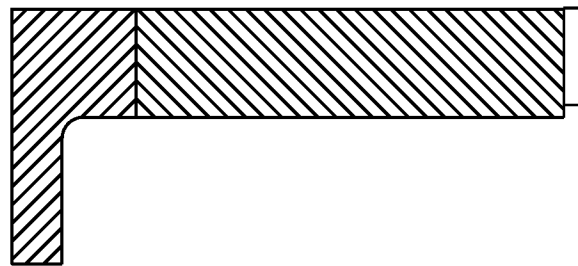


(a) Nozzle flap assembly.

Figure 7. Sketch showing nozzle geometric details. Dimensions are in inches.

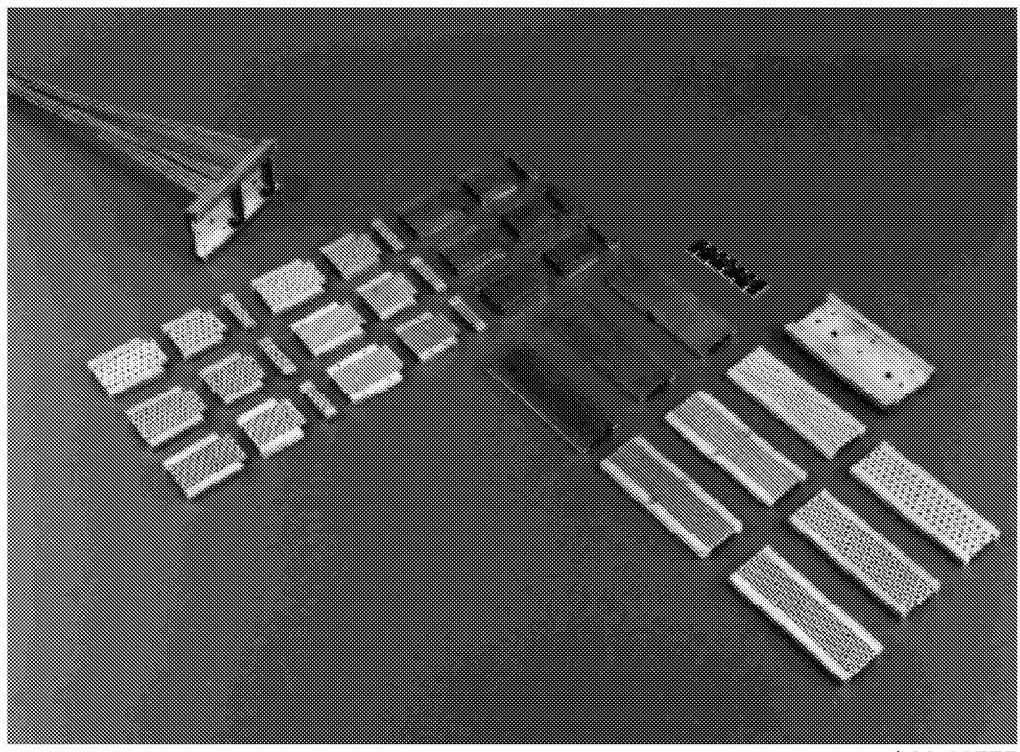


Section A-A



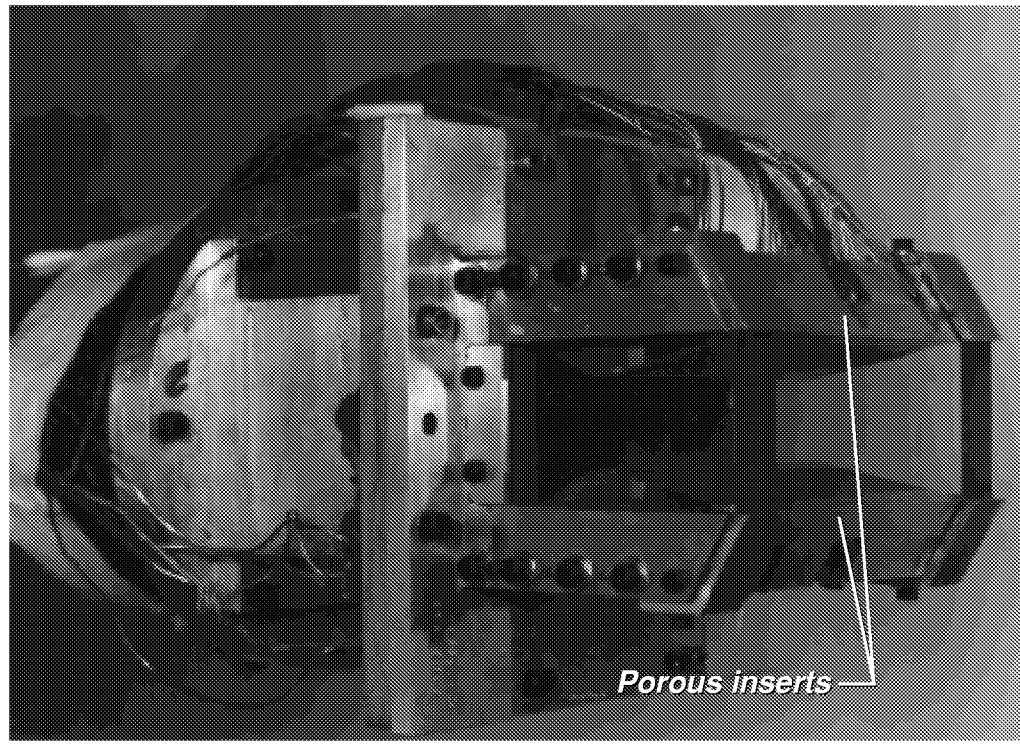
(b) Sidewall assembly.

Figure 7. Concluded.



L92-08775

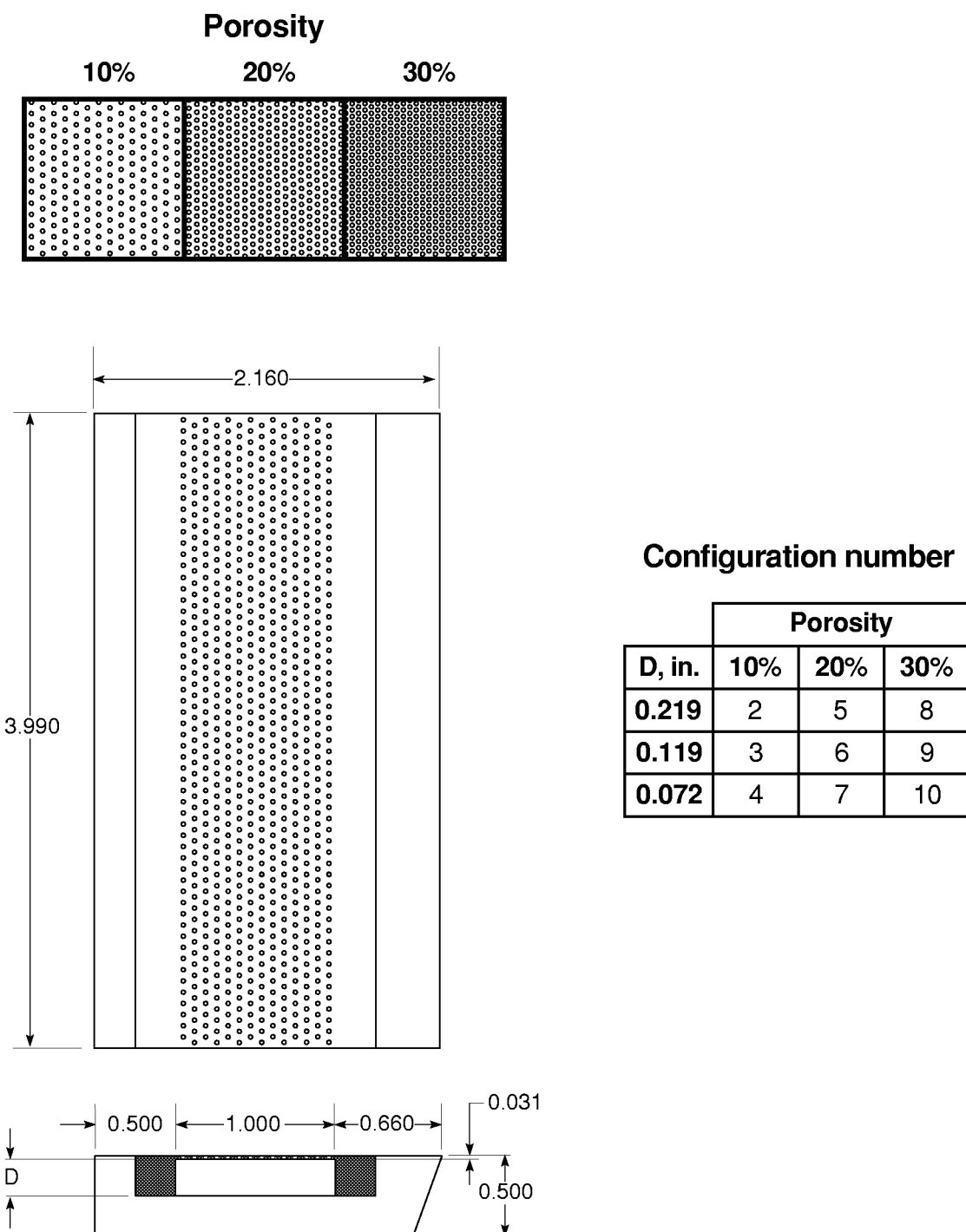
(a) Photograph of porous flap inserts.



L93-1013

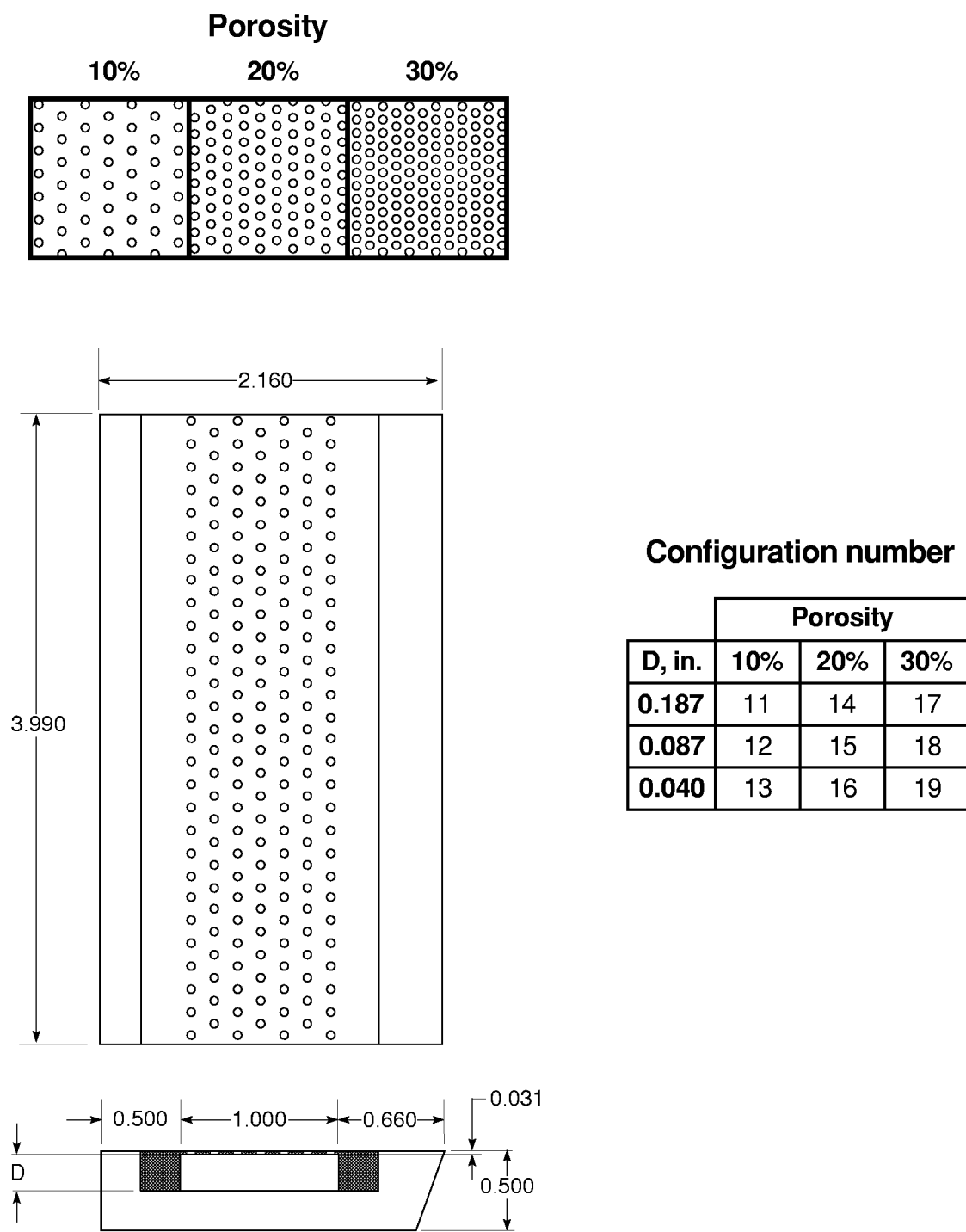
(b) Photograph of the static test model with porous flap inserts installed.

Figure 8. Details of porous flap inserts.



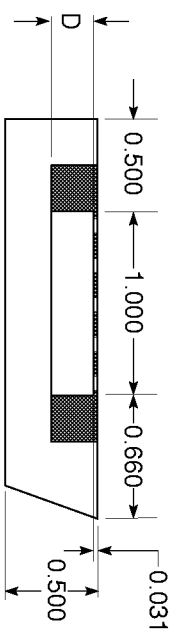
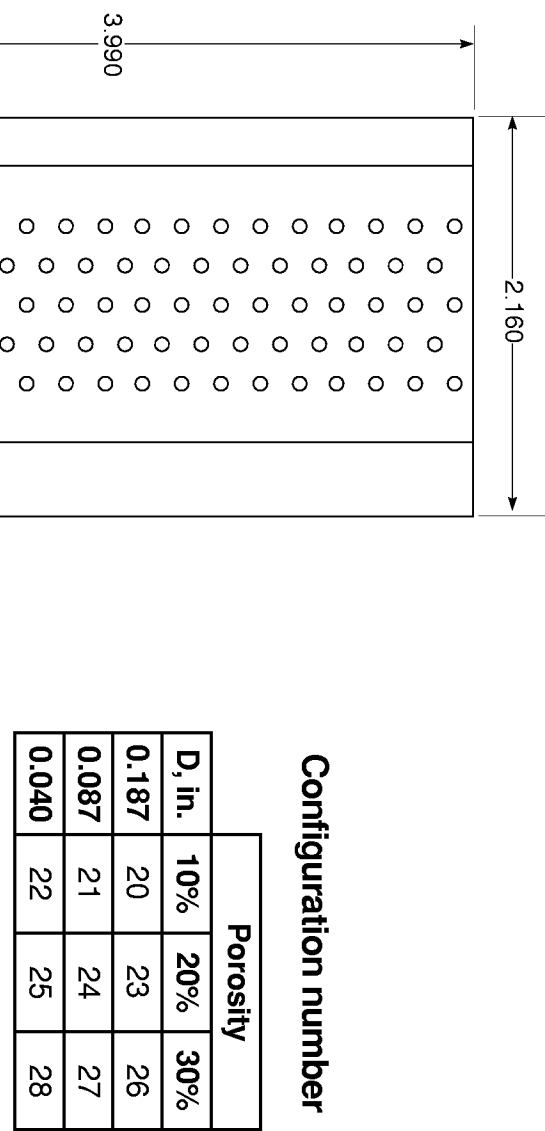
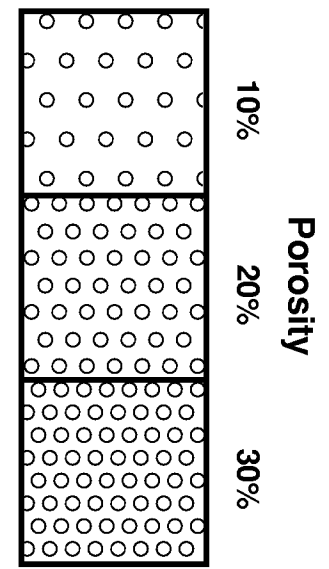
(a) The 0.025 in. hole diameter porous flap inserts.

Figure 9. Details of porous flap inserts. Dimensions are in inches.



(b) The 0.052 in. hole diameter porous flap inserts.

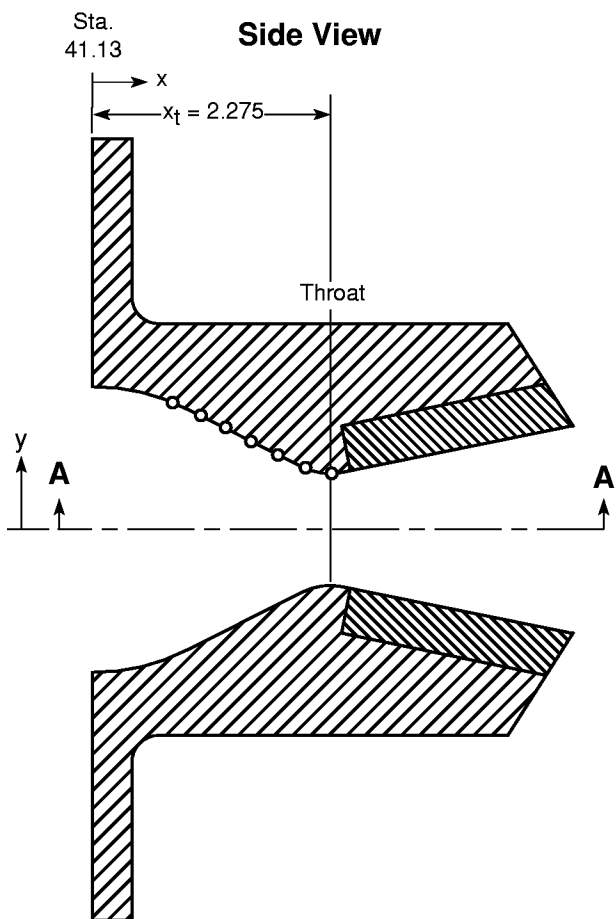
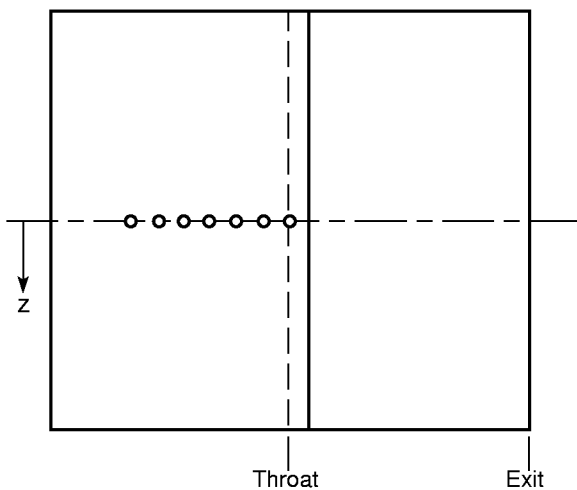
Figure 9. Continued.



(c) The 0.076 in. hole diameter porous flap inserts.

Figure 9. Concluded.

View A-A



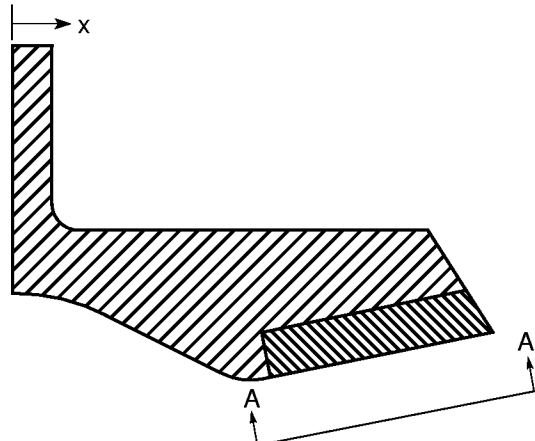
Static Pressure Orifice Locations	
x, in.	x/x_t
0.750	0.330
1.000	0.440
1.250	0.550
1.500	0.659
1.750	0.769
2.025	0.890
2.275	1.000

● Denotes static pressure orifice location

(a) Nozzle flap assembly static pressure taps.

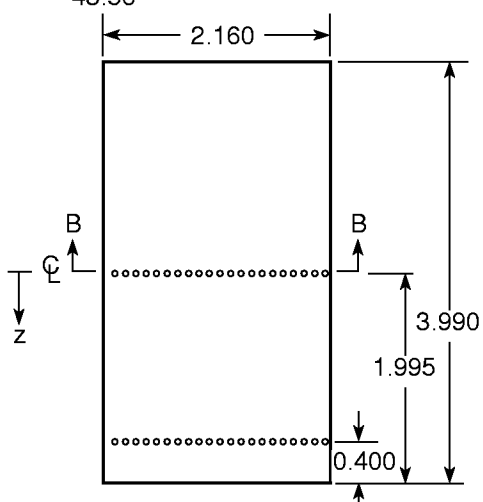
Figure 10. Nozzle static pressure orifice locations. Dimensions are in inches.

Sta.
41.13



View A-A

Sta.
43.56



Static Pressure Orifice Locations

$z = 0.000 \text{ in.}$		$z = 1.595 \text{ in.}$	
$x, \text{ in.}$	x/x_t	$x, \text{ in.}$	x/x_t
2.528	1.111	2.528	1.111
2.626	1.154	2.626	1.154
2.724	1.198	2.724	1.198
2.823	1.241	2.823	1.241
2.921	1.284	2.921	1.284
3.019	1.327	3.019	1.327
3.117	1.370	3.117	1.370
3.215	1.413	3.215	1.413
3.313	1.456	3.313	1.456
3.412	1.500	3.412	1.500
3.510	1.543	3.510	1.543
3.608	1.586	3.608	1.586
3.706	1.629	3.706	1.629
3.804	1.672	3.804	1.672
3.902	1.715	3.902	1.715
4.001	1.758	4.001	1.758
4.099	1.802	4.099	1.802
4.197	1.845	4.197	1.845
4.295	1.888	4.295	1.888
4.393	1.931	4.393	1.931
4.491	1.974	4.491	1.974

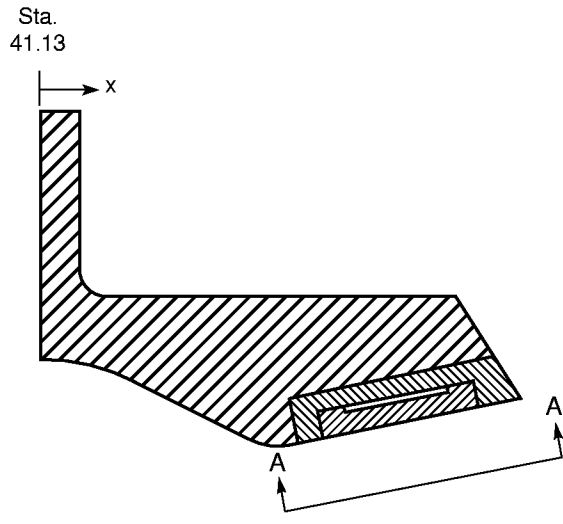
● Denotes static pressure orifice location

Section B-B

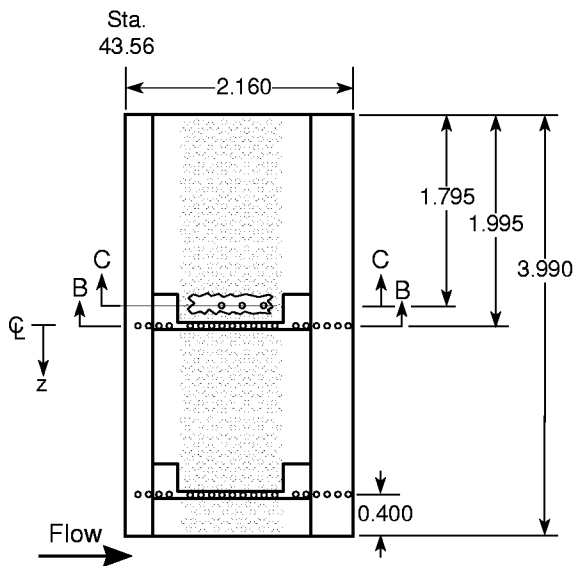


(b) Baseline flap insert static pressure taps.

Figure 10. Continued.



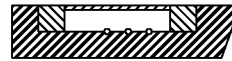
View A-A



Section B-B

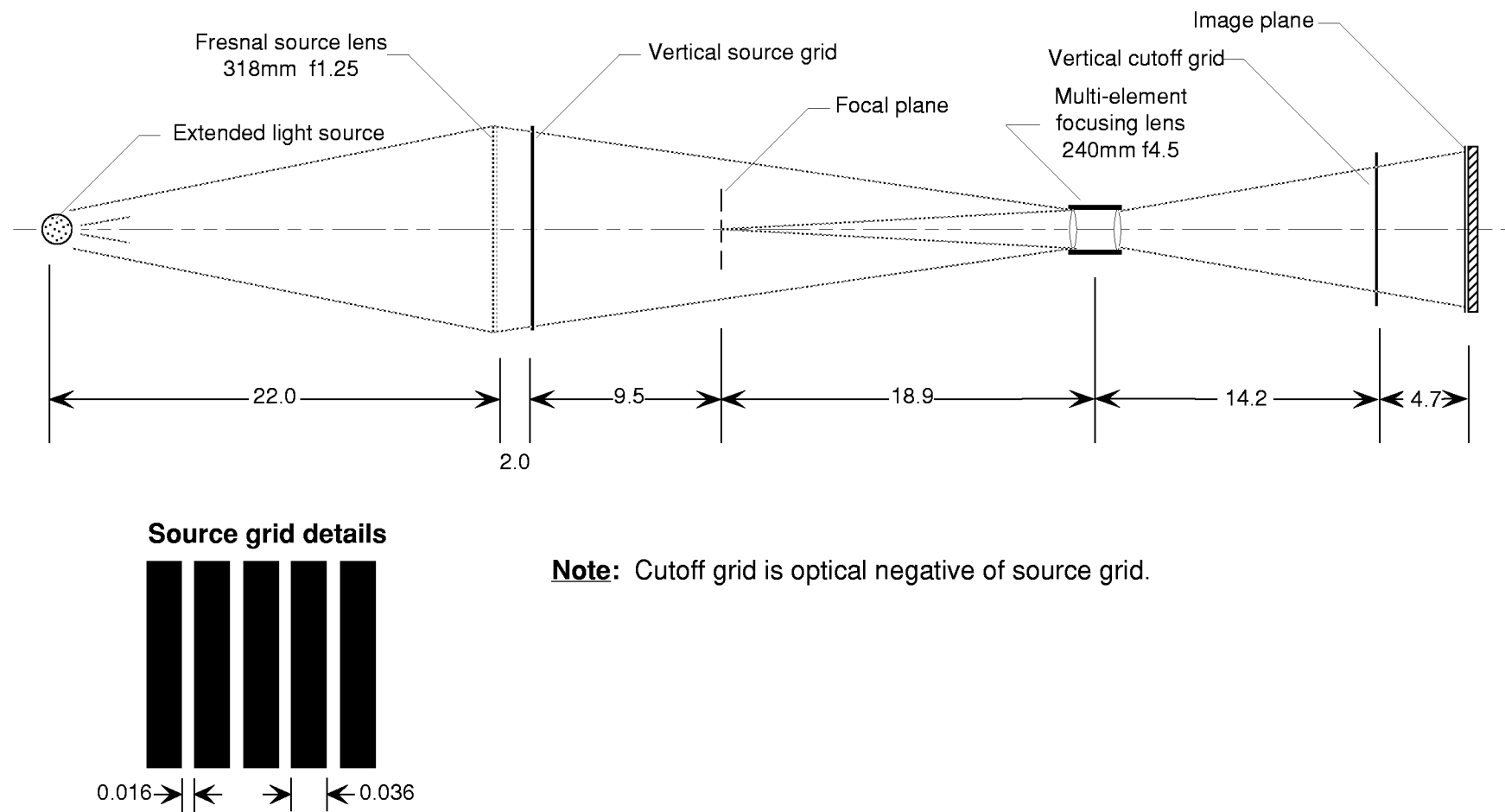


Section C-C



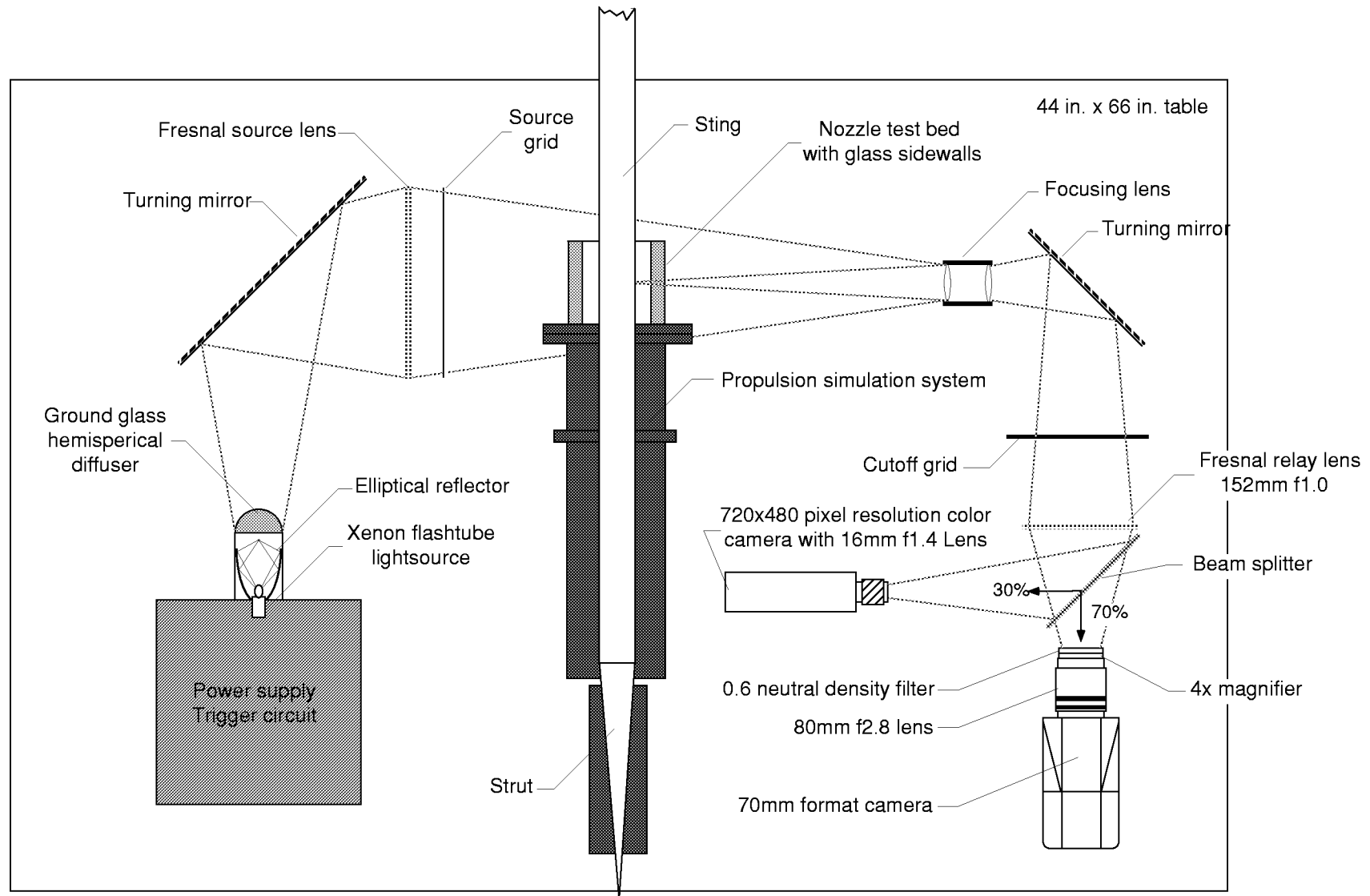
(c) Porous flap inserts static pressure taps.

Figure 10. Concluded.



(a) Optical description.

Figure 11. Optical description and schematic layout of focusing schlieren flow visualization system. Dimensions are in inches.



(b) Schematic layout.

Figure 11. Concluded.

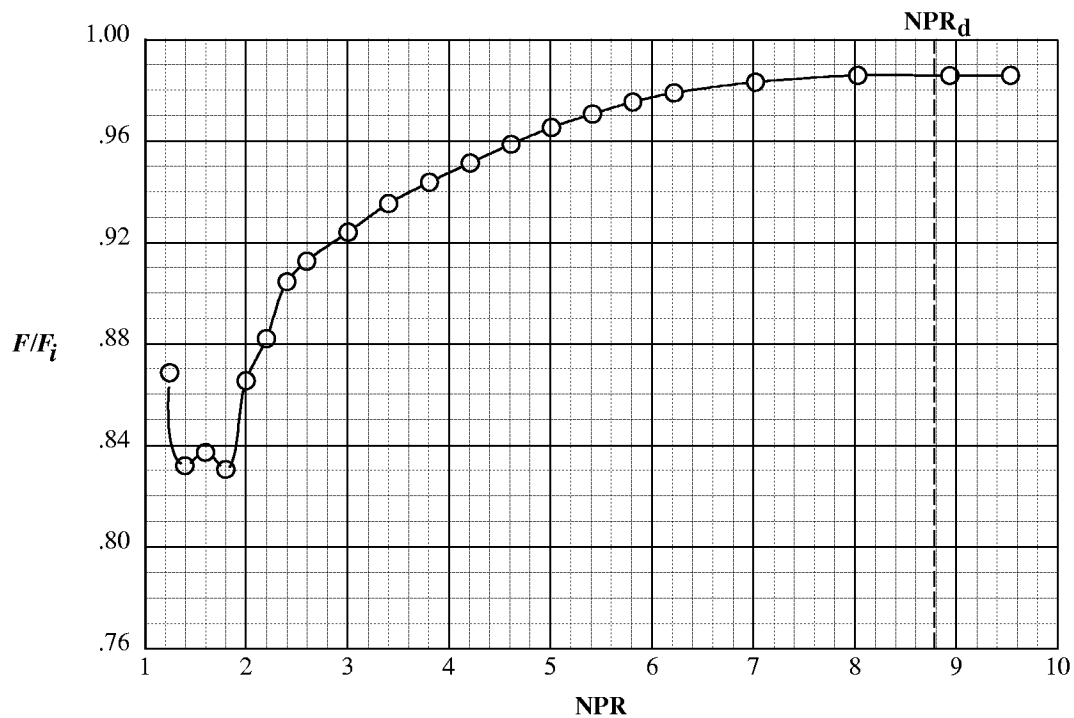
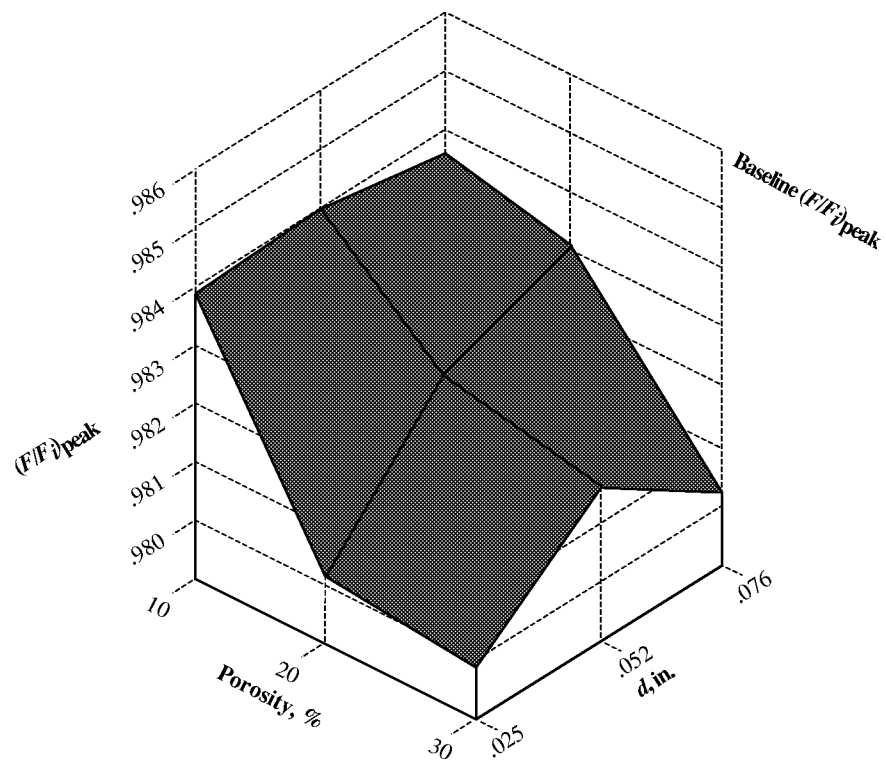
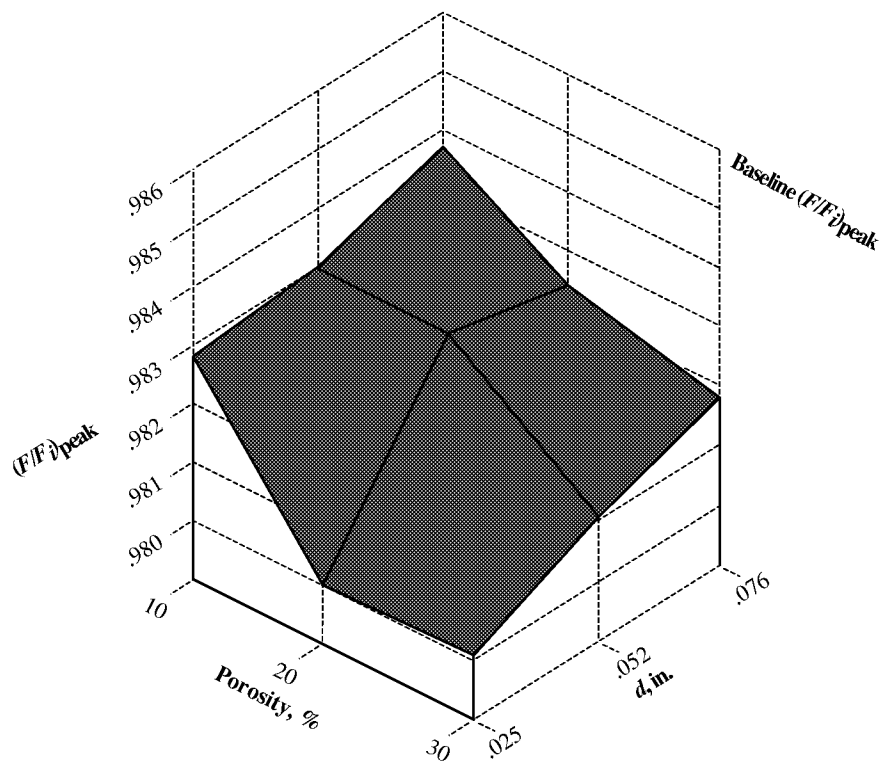


Figure 12. Nozzle thrust ratio performance for the baseline configuration.

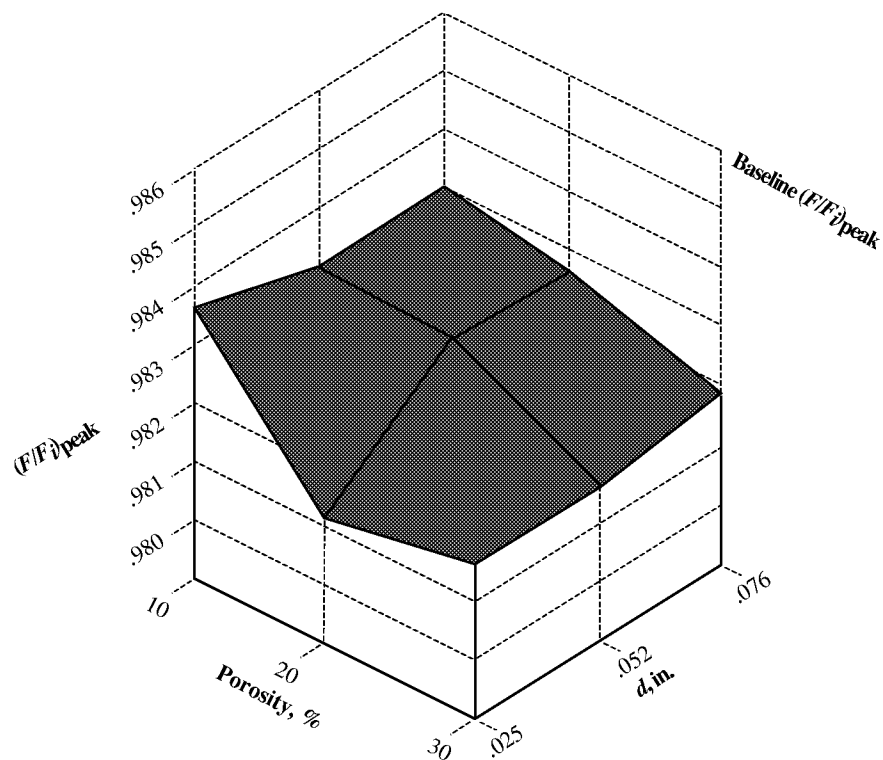


(a) Deep cavity.

Figure 13. Effect of percent porosity and hole diameter on peak thrust ratio of porous configurations.



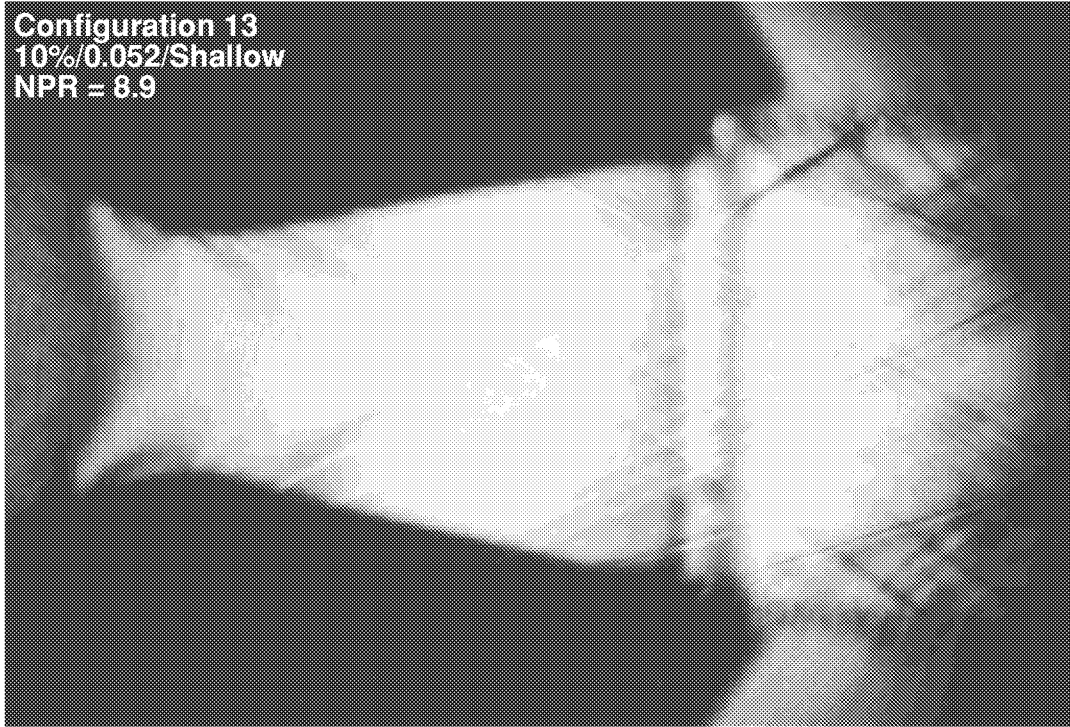
(b) Medium cavity.



(c) Shallow cavity.

Figure 13. Concluded.

Configuration 13
10%/0.052/Shallow
NPR = 8.9



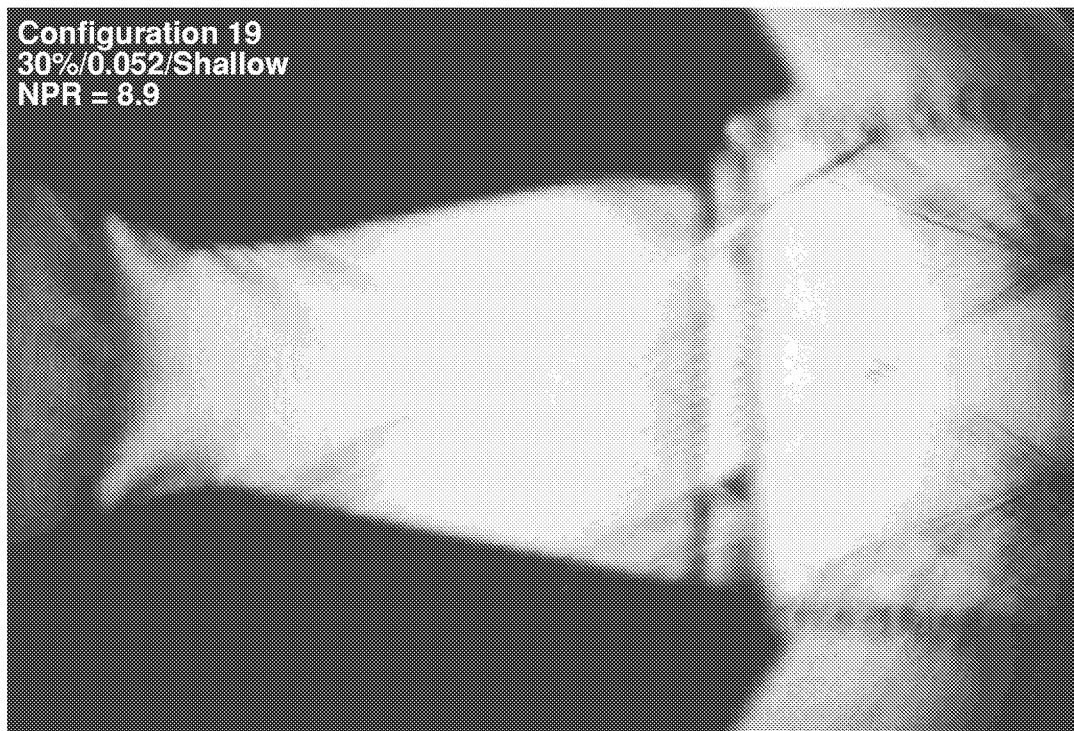
(a) 10% porosity.

Configuration 16
20%/0.052/Shallow
NPR = 8.9



(b) 20% porosity.

Figure 14. Focusing schlieren flow visualization at NPR = 8.9 for porous configurations with 0.052 in. hole diameter and a shallow cavity.



(c) 30% porosity.

Figure 14. Concluded.

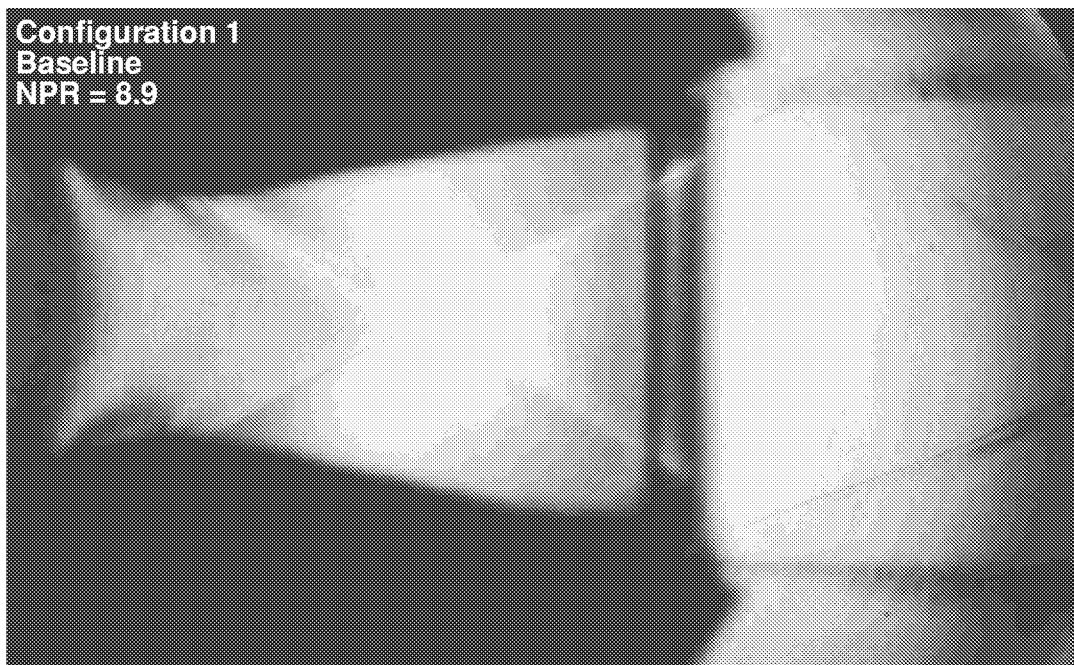
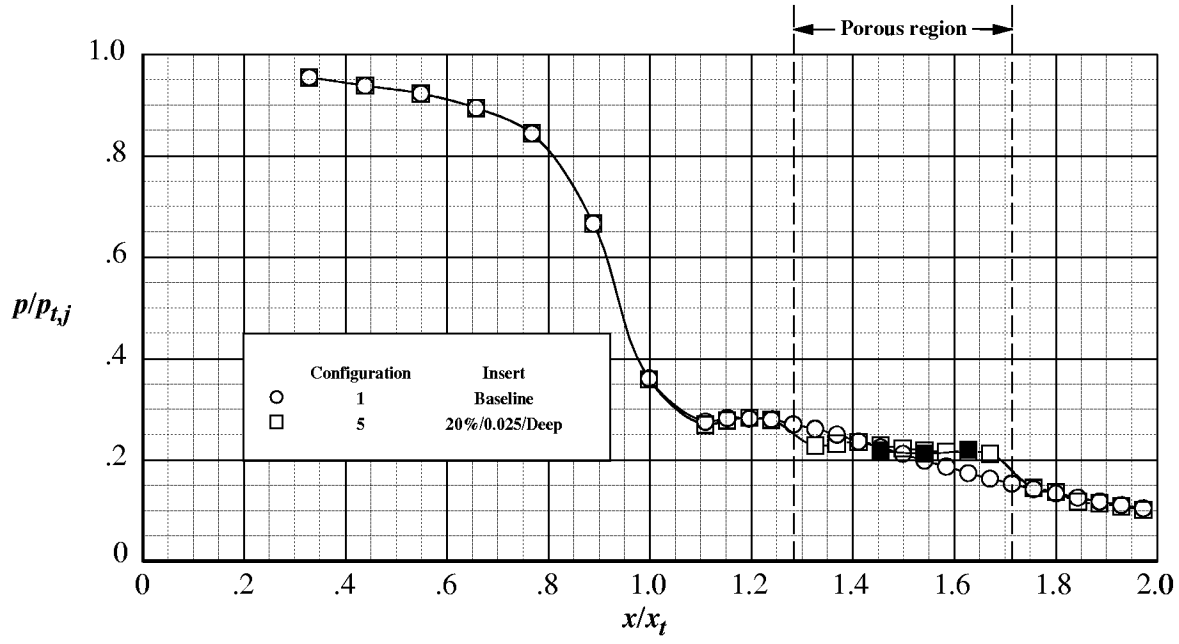
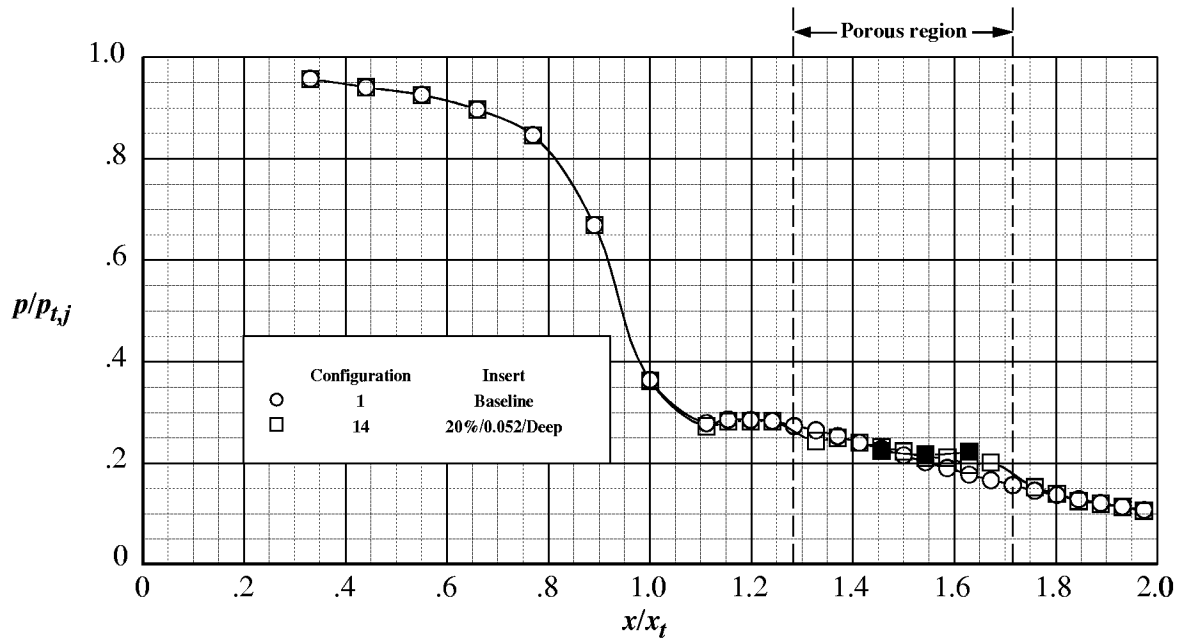


Figure 15. Focusing schlieren flow visualization at NPR = 8.9 for the baseline configuration.

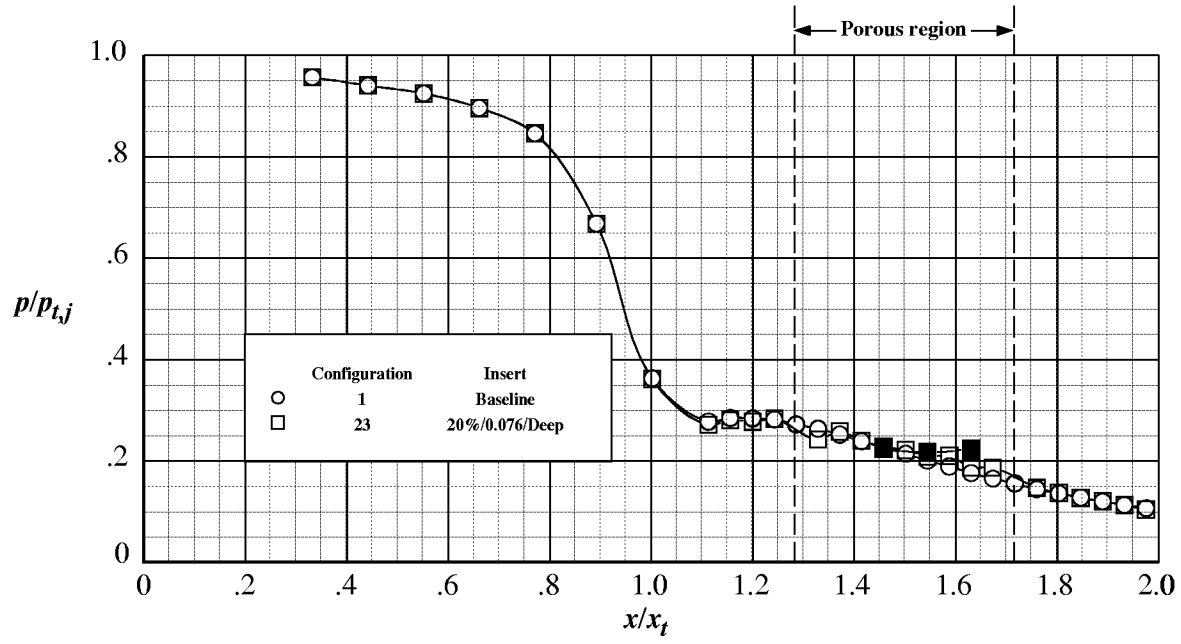


(a) $d = 0.025$ in.



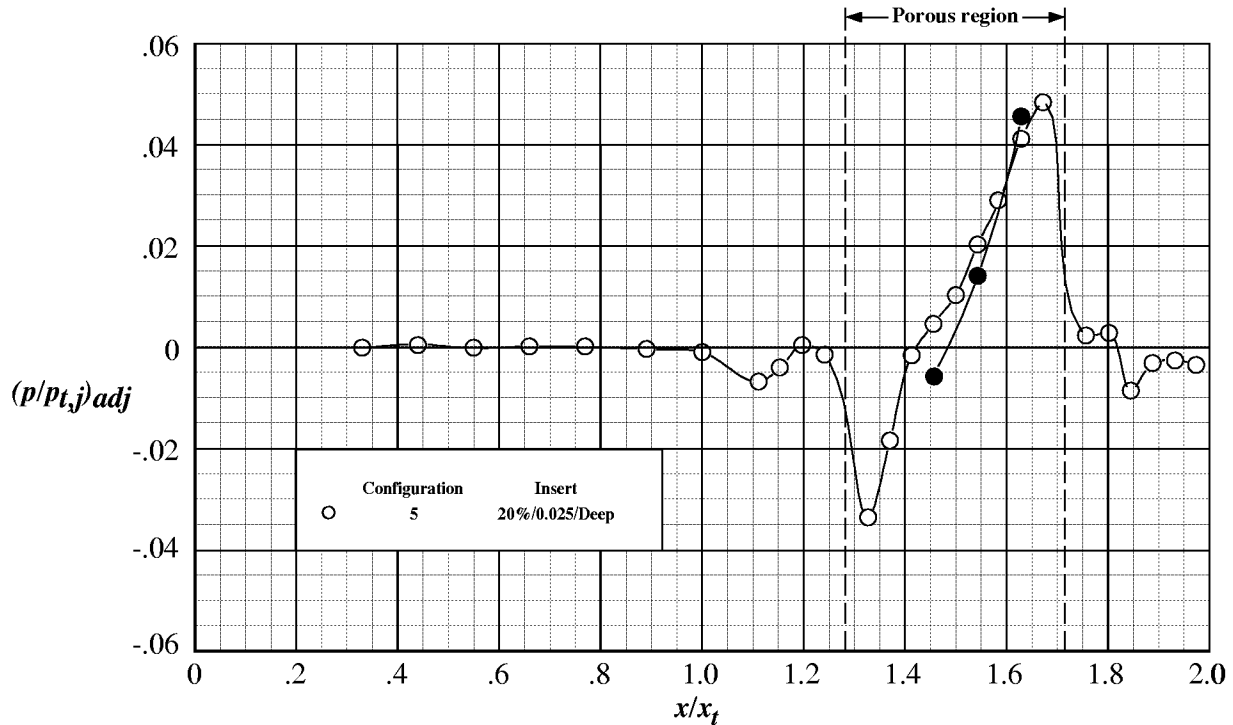
(b) $d = 0.052$ in.

Figure 16. Comparison of internal static pressure ratio distributions at NPR = 8.9 for baseline and porous configurations with 20% porosity and a deep cavity. Open symbols denote centerline (surface) pressures; solid symbols denote cavity pressures.



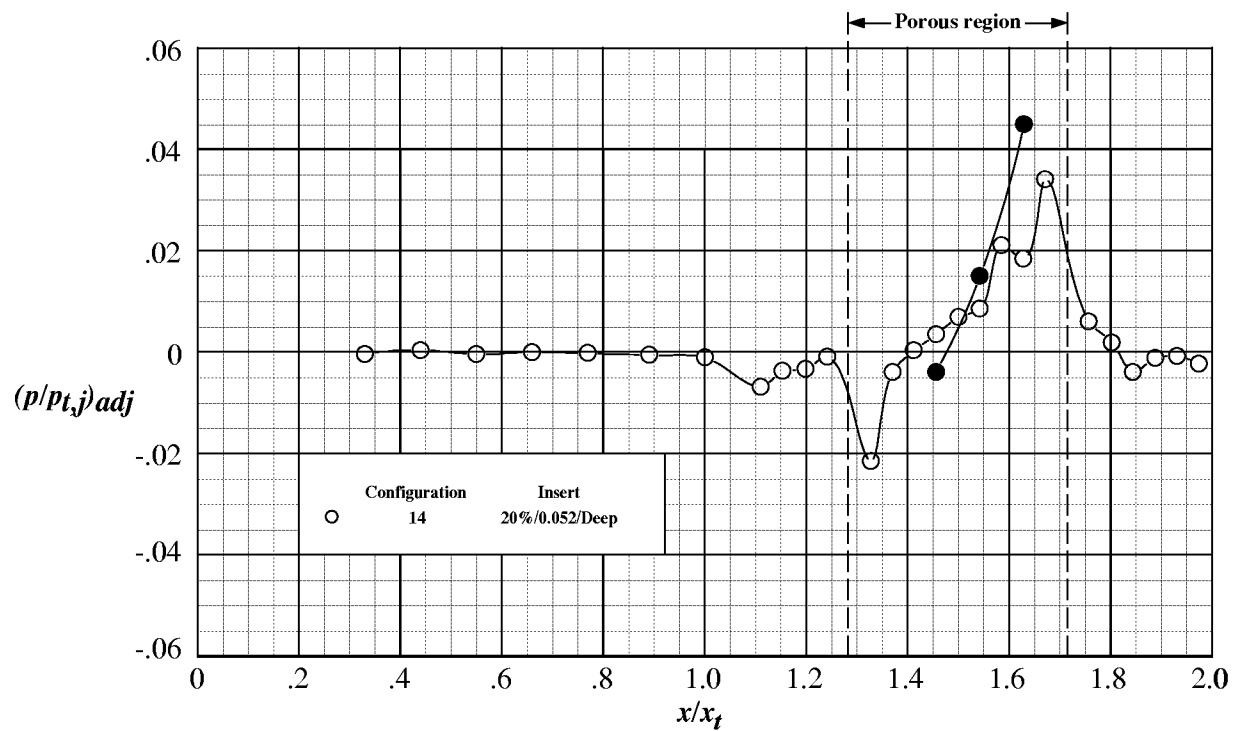
(c) $d = 0.076$ in.

Figure 16. Concluded.

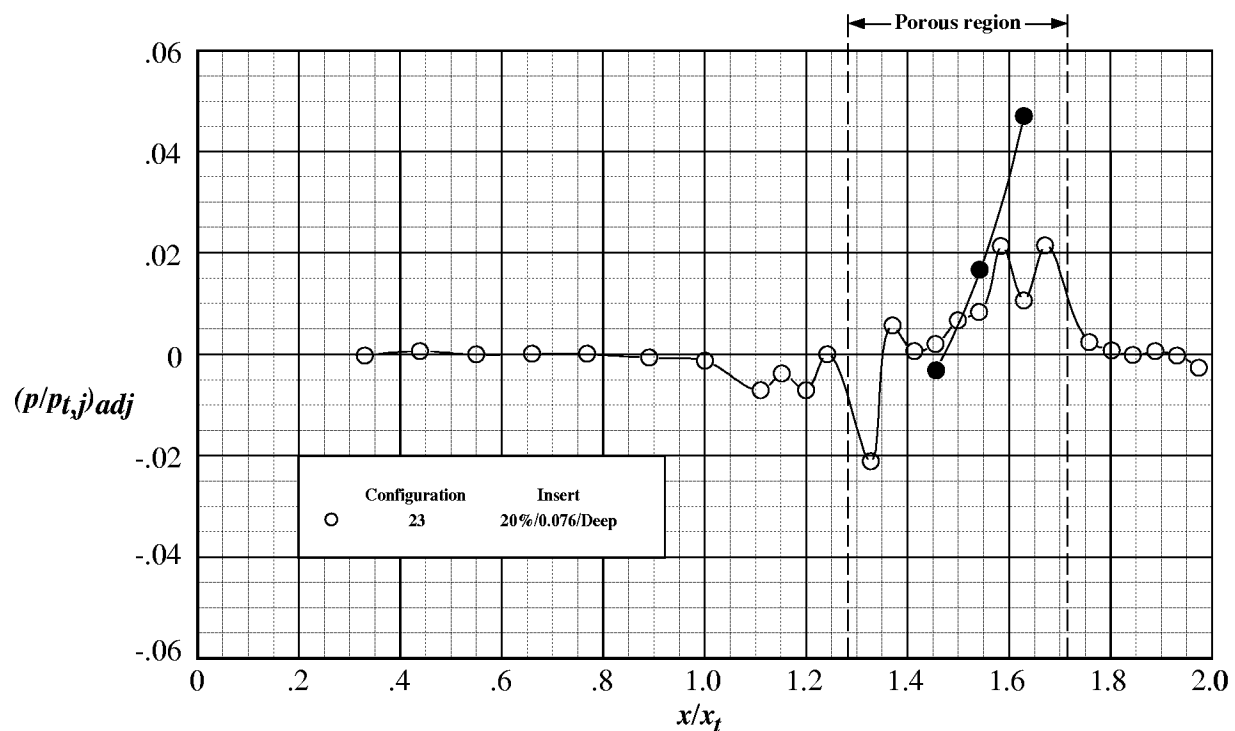


(a) $d = 0.025$ in.

Figure 17. Adjusted internal static pressure ratio distributions at NPR = 8.9 for porous configurations with 20% porosity and a deep cavity. Open symbols denote centerline (surface) pressures; solid symbols denote cavity pressures.



(b) $d = 0.052$ in.



(c) $d = 0.076$ in.

Figure 17. Concluded.

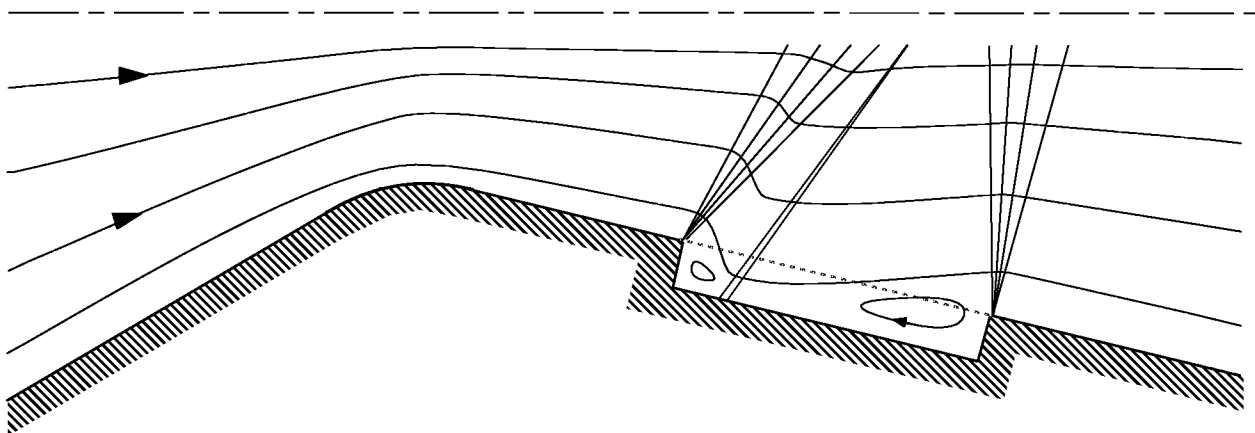


Figure 18. Sketch showing supersonic porous cavity flowfield at $NPR = 8.9$.

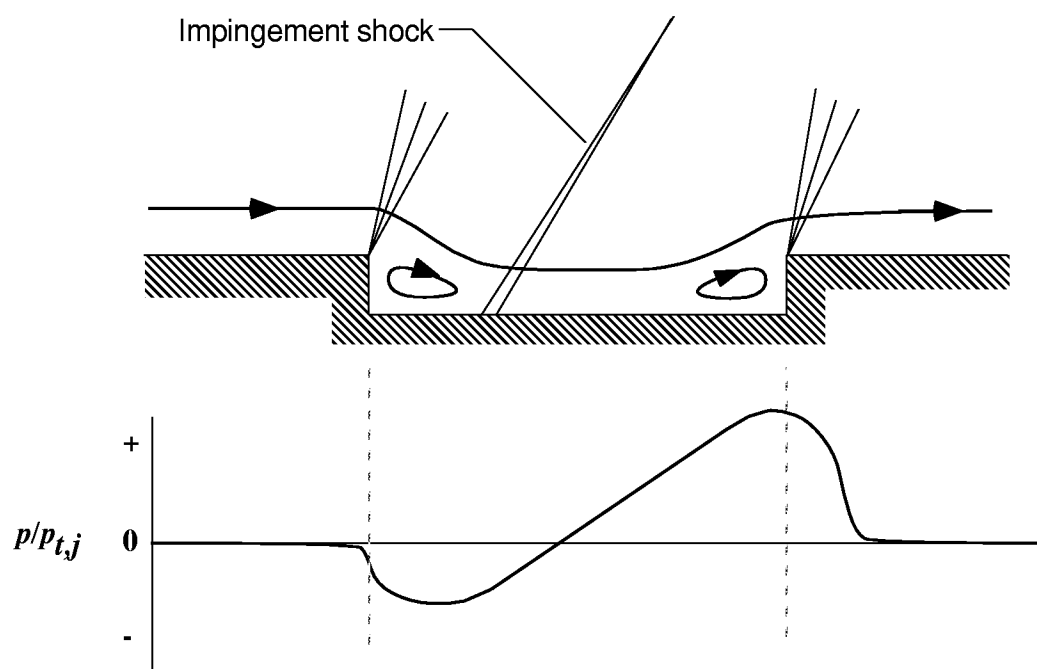
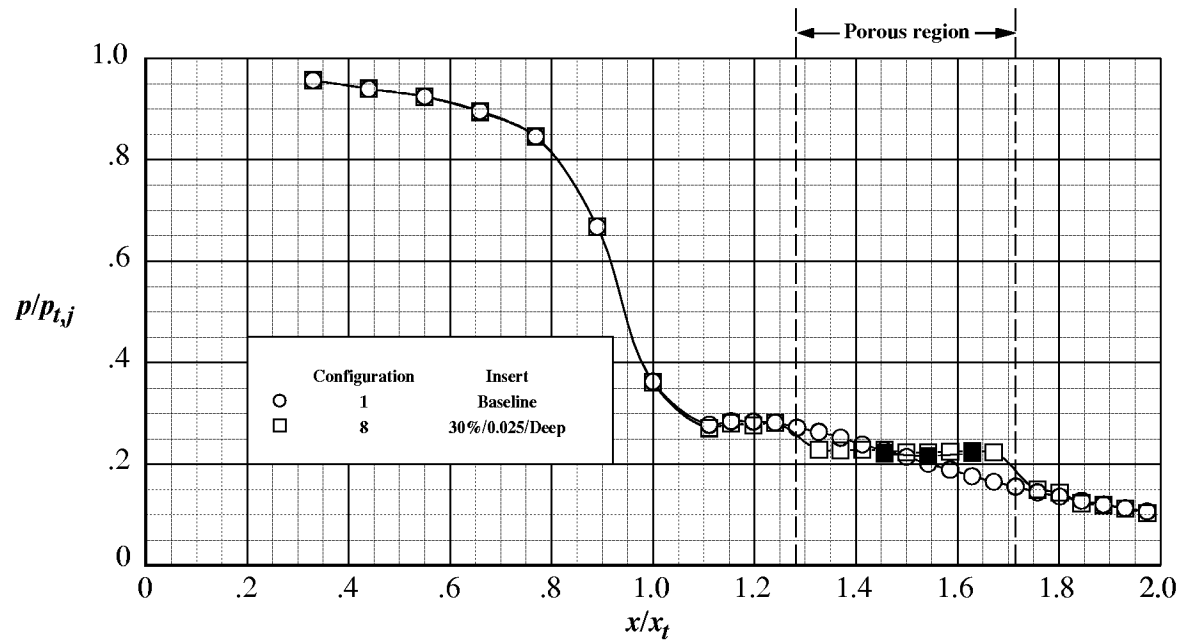
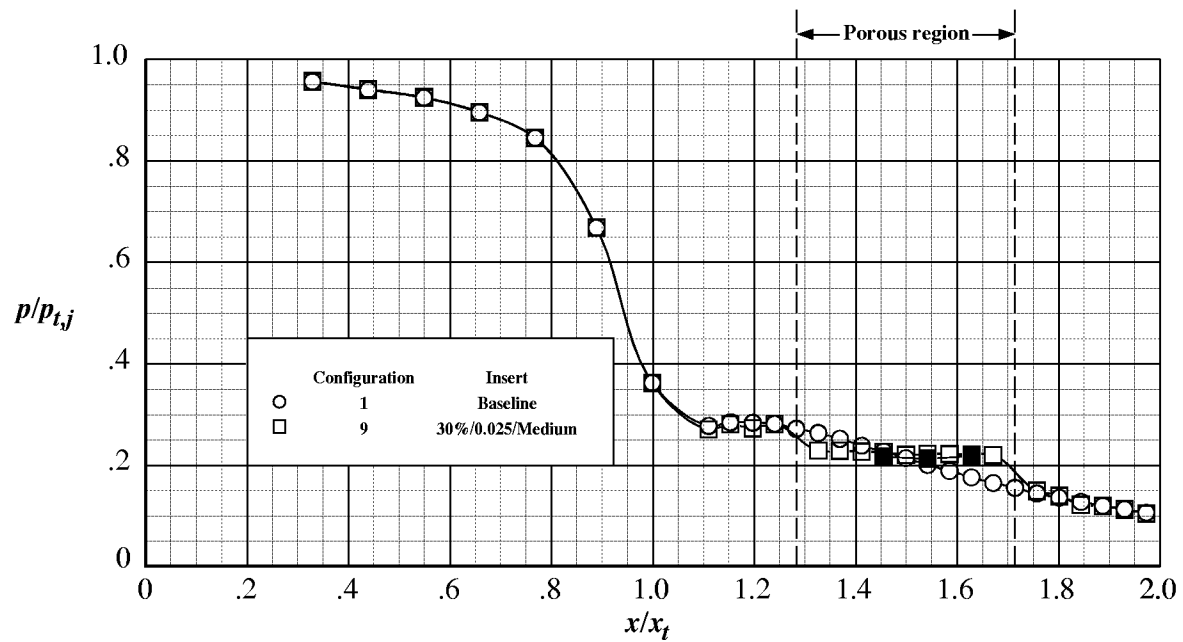


Figure 19. Sketch showing transitional-closed cavity flow.

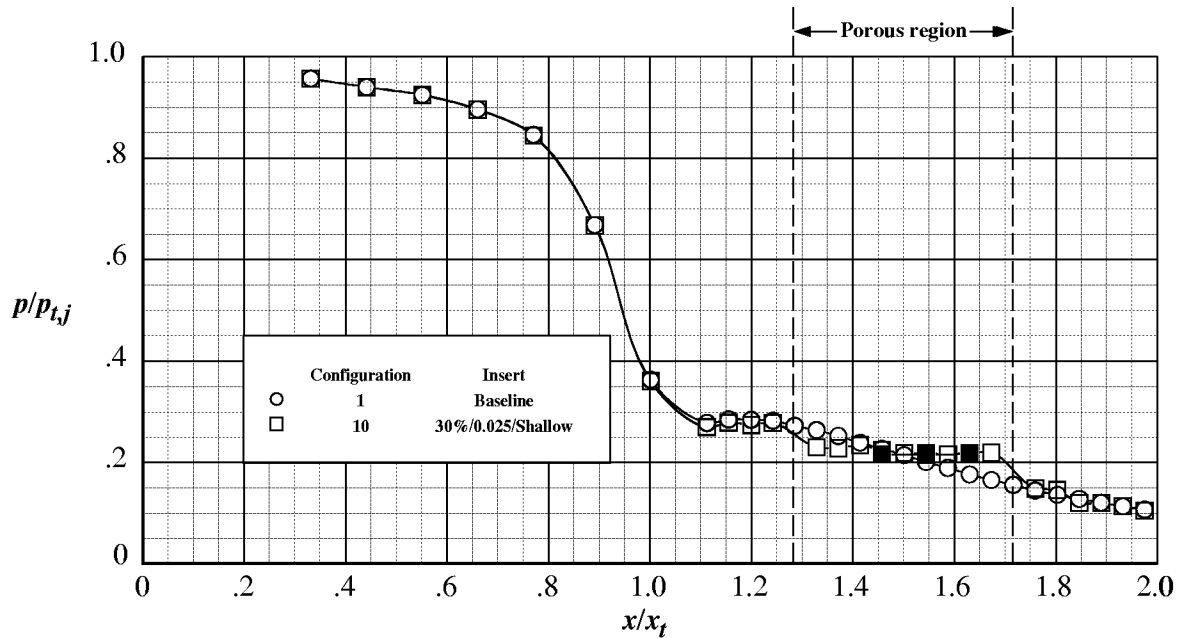


(a) Deep cavity.



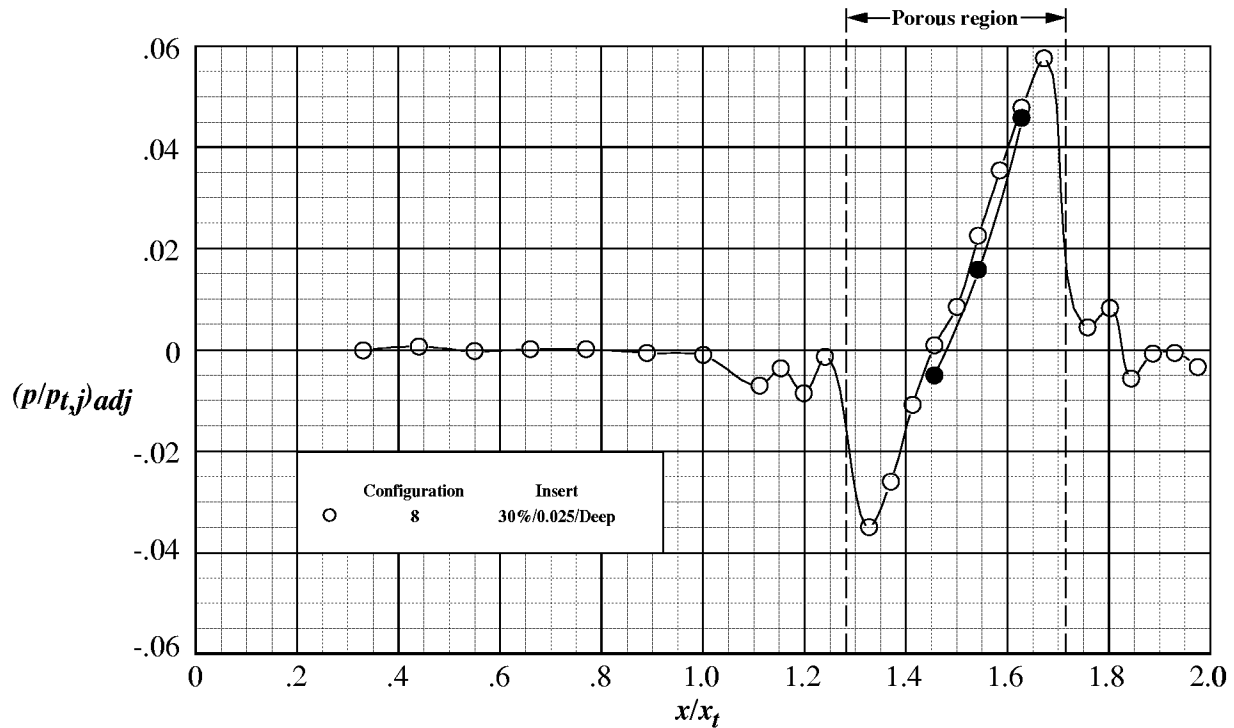
(b) Medium cavity.

Figure 20. Comparison of internal static pressure ratio distributions at $\text{NPR} = 8.9$ for baseline and porous configurations with 30% porosity and $d = 0.025$ in. Open symbols denote centerline(surface) pressures; solid symbols denote cavity pressures.



(c) Shallow cavity.

Figure 20. Concluded.

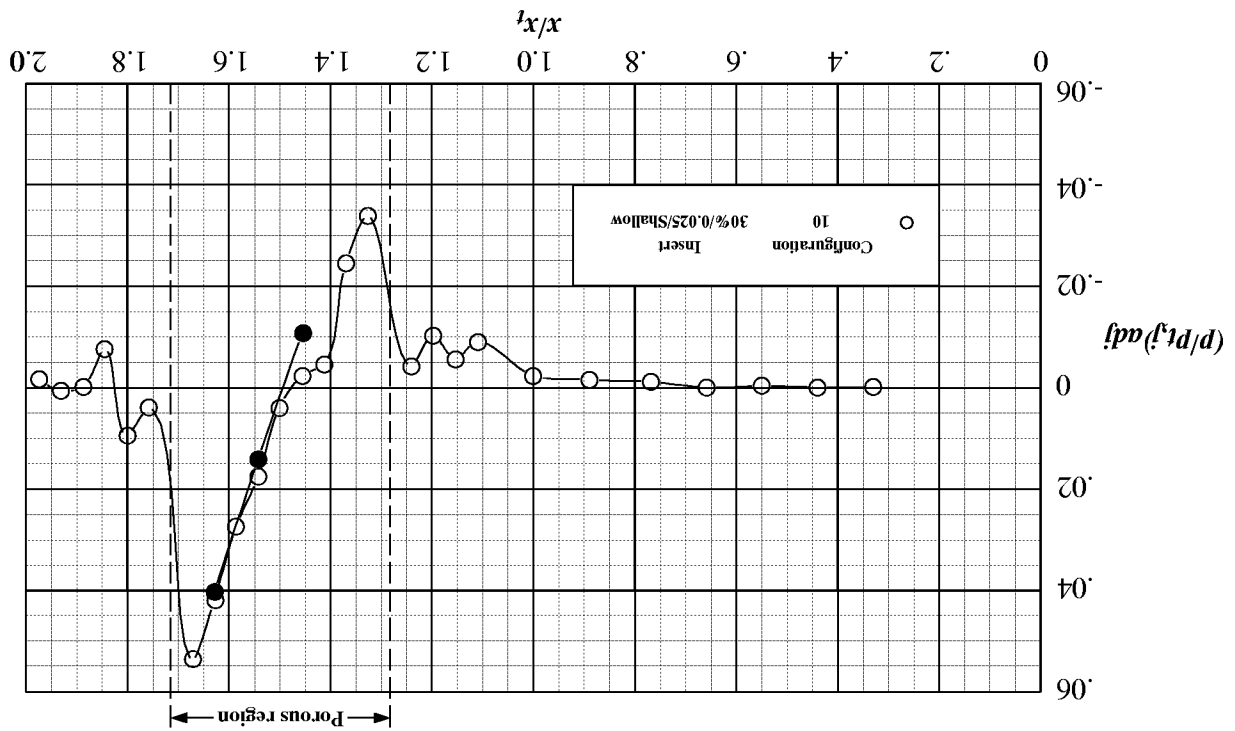


(a) Deep cavity.

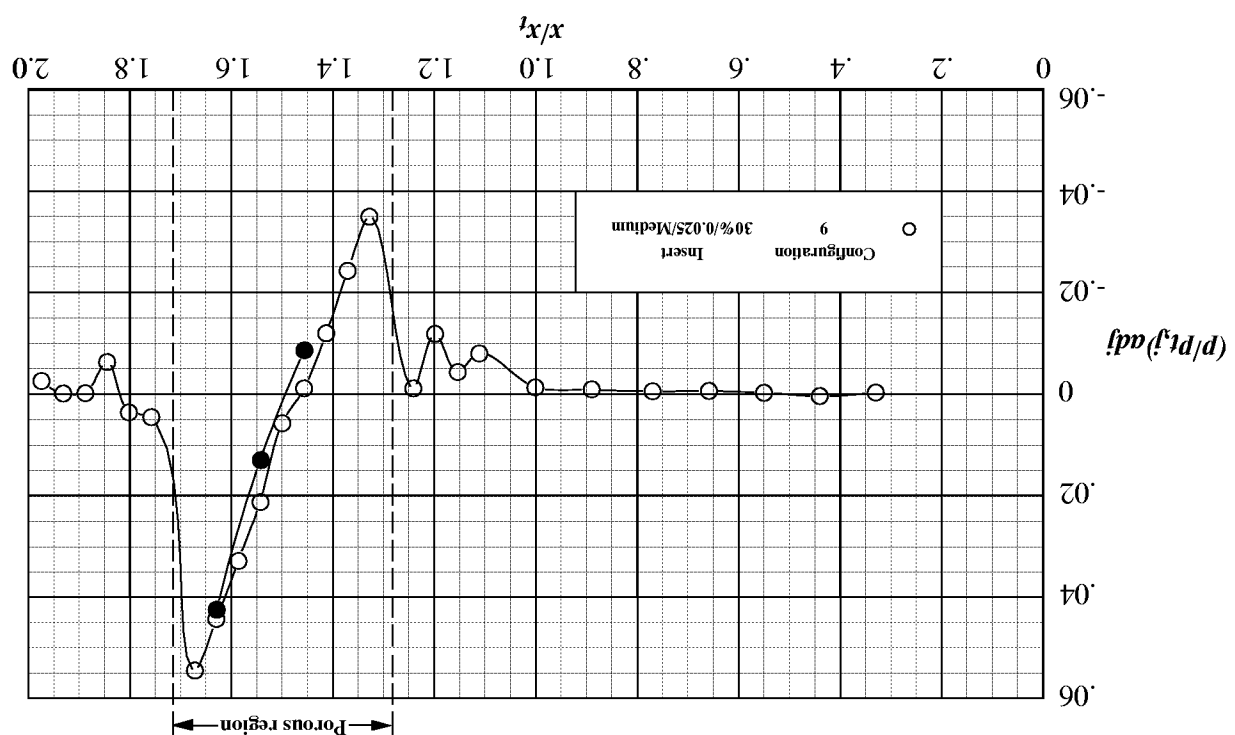
Figure 21. Adjusted internal static pressure ratio distributions at NPR = 8.9 for porous configurations with 30% porosity and $d = 0.025$ in. Open symbols denote centerline(surface) pressures; solid symbols denote cavity pressures.

Figure 21. Concluded.

(c) Shallow cavity.



(b) Medium cavity.



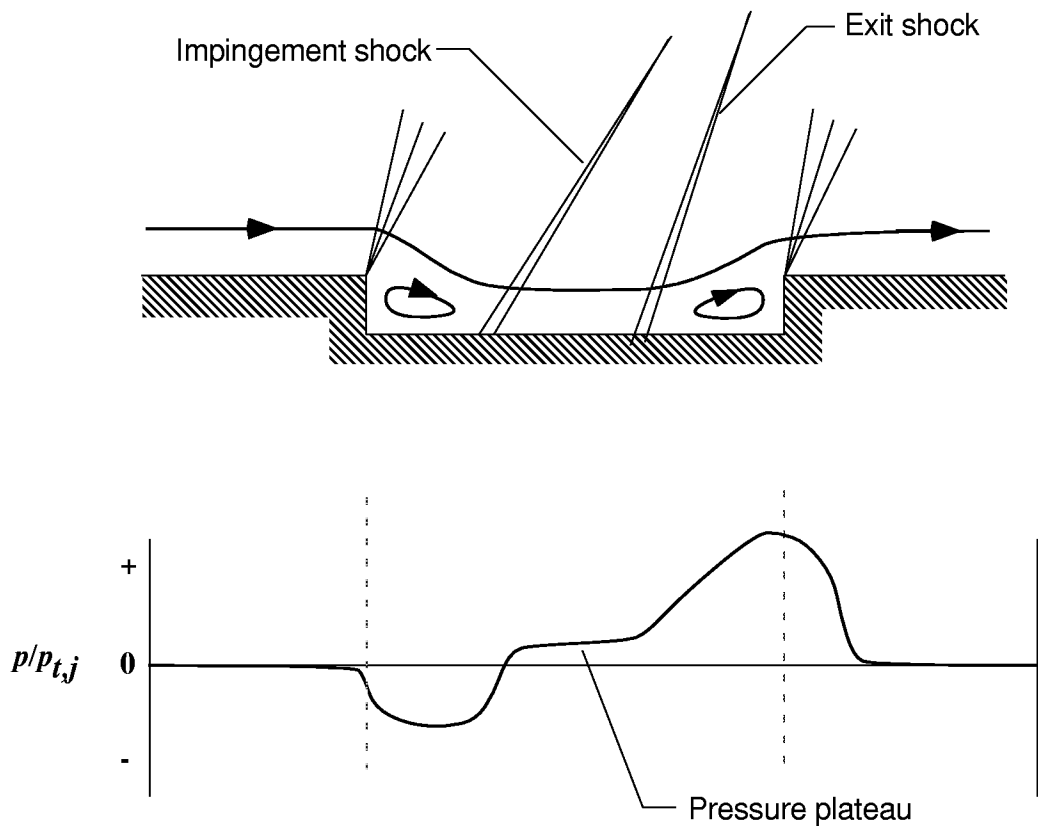


Figure 22. Sketch showing closed cavity flow.

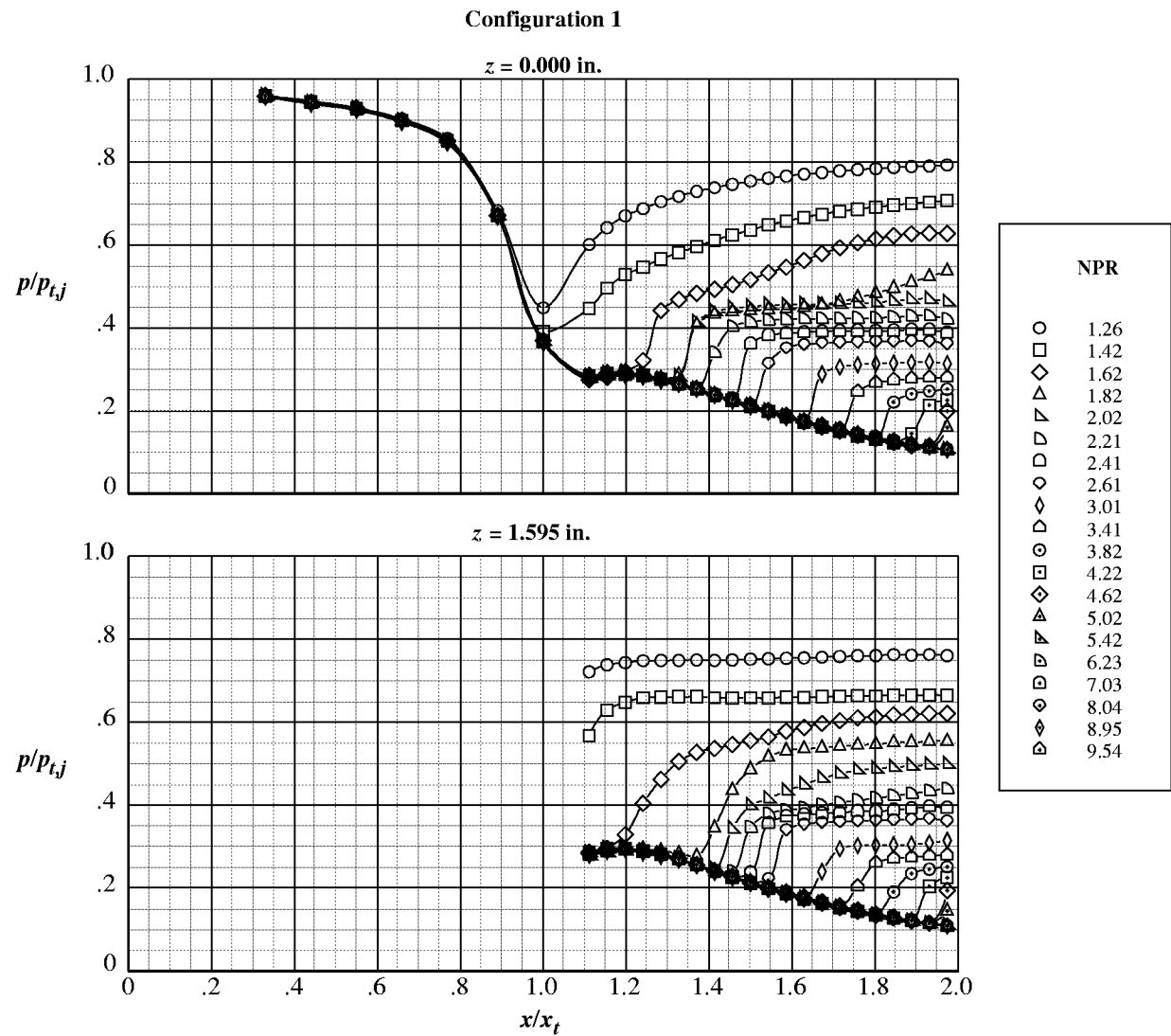
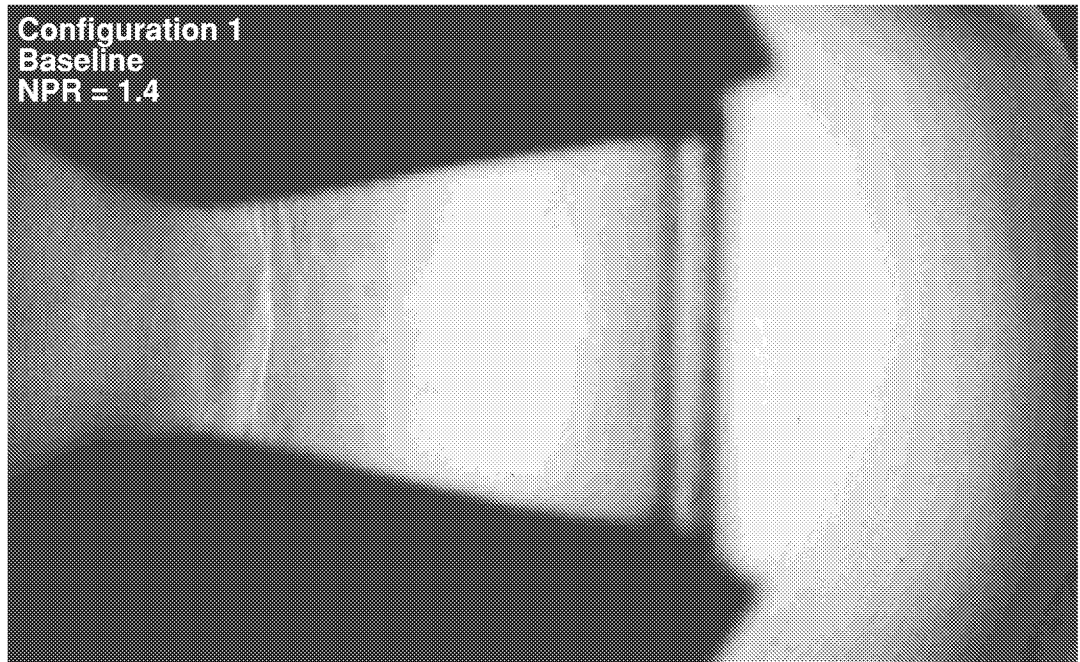


Figure 23. Internal static pressure ratio distributions for the baseline configuration.



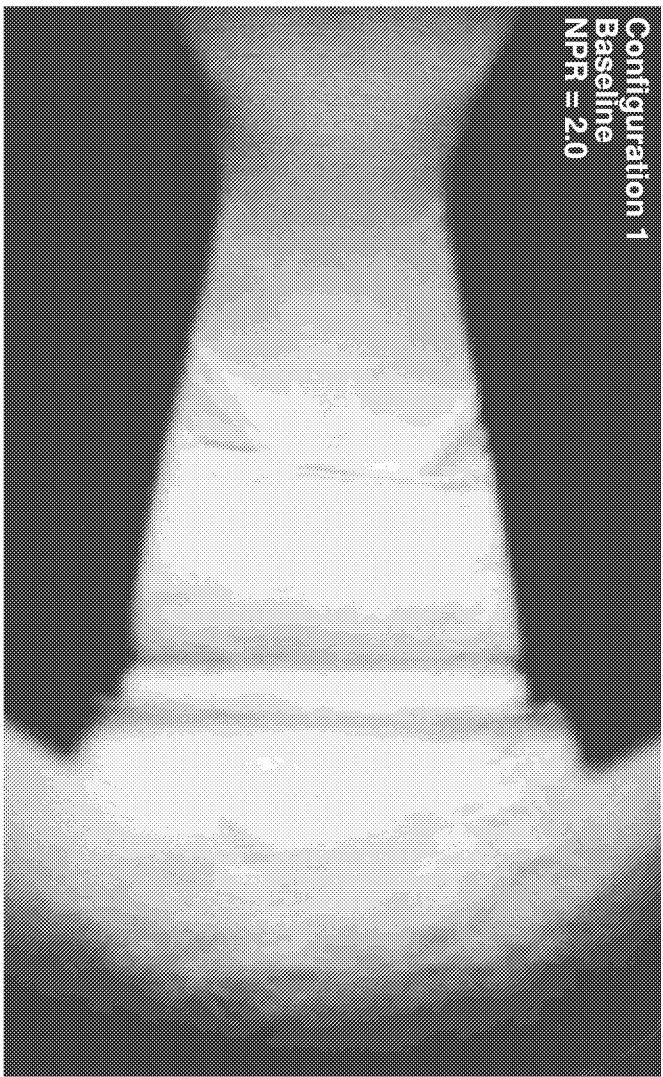
(a) $\text{NPR} = 1.4$.



(b) $\text{NPR} = 1.8$.

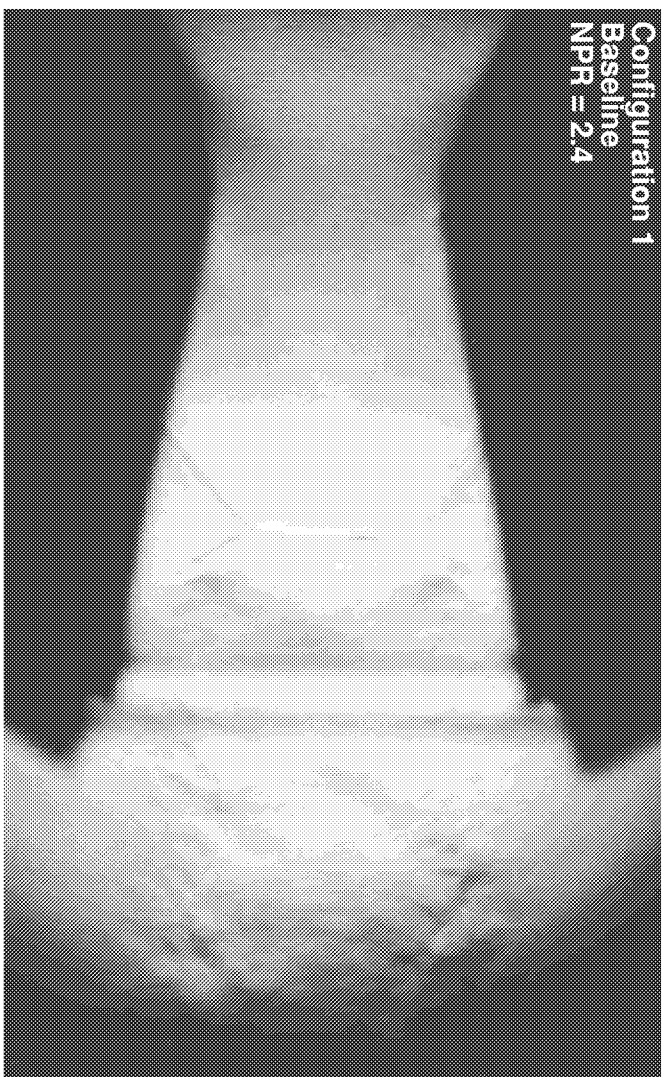
Figure 24. Focusing schlieren flow visualization for the baseline configuration.

Configuration 1
Baseline
NPR = 2.0



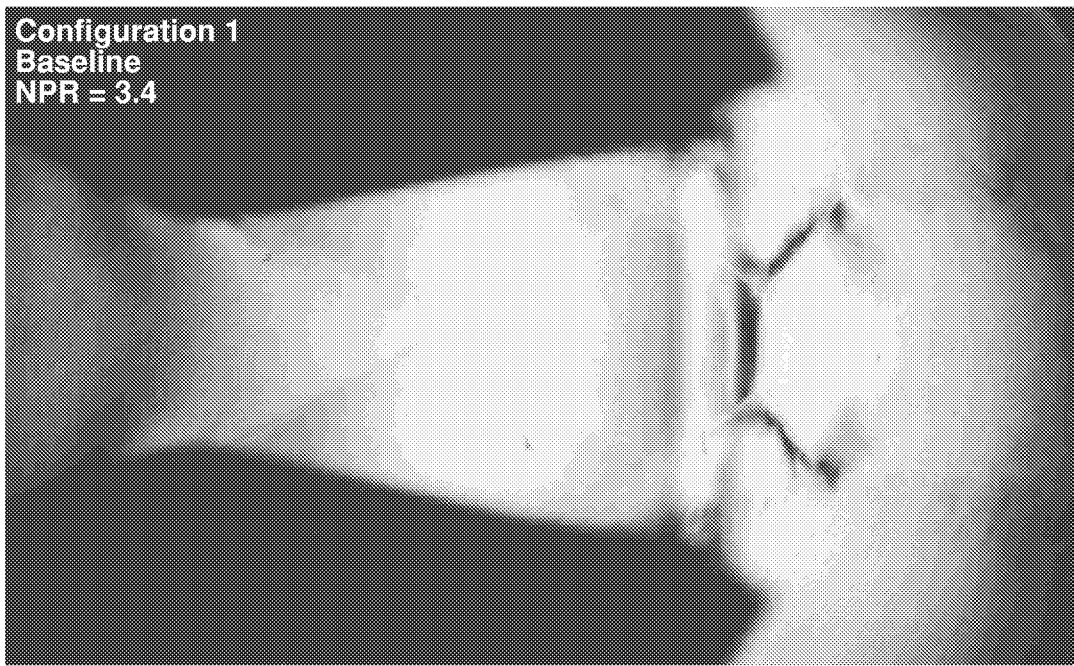
(c) NPR = 2.0.

Configuration 1
Baseline
NPR = 2.4



(d) NPR = 2.4.

Figure 24. Continued.



(e) $\text{NPR} = 3.4$.

Figure 24. Concluded.

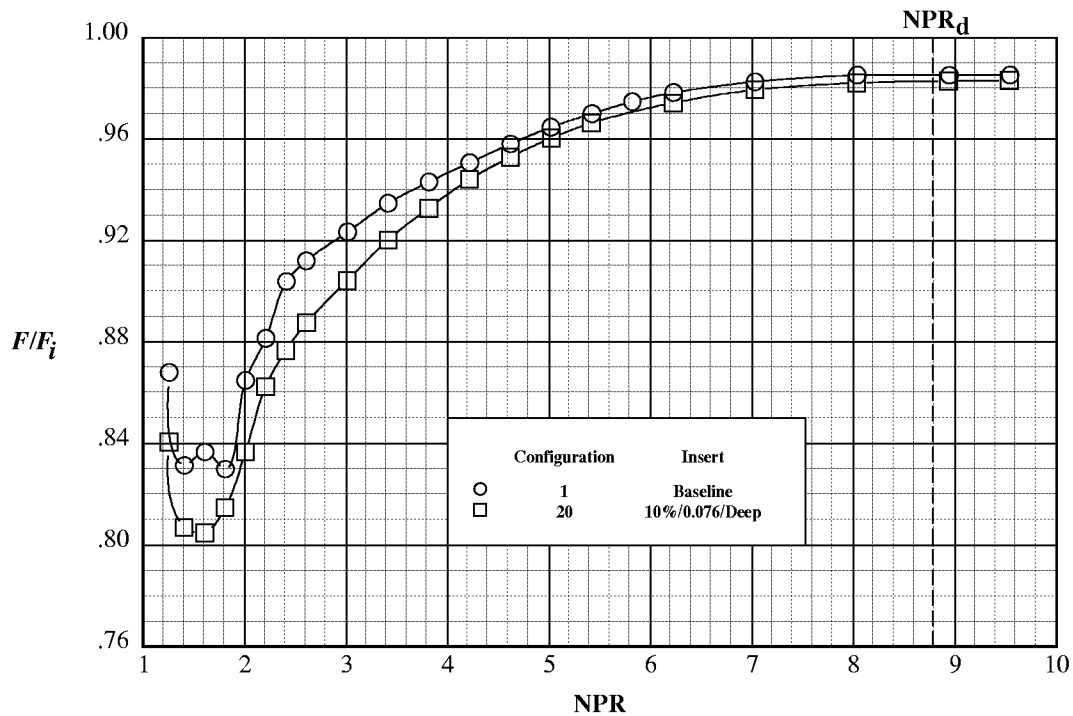


Figure 25. Comparison of nozzle thrust ratio performance for the baseline configuration and porous configuration 20.

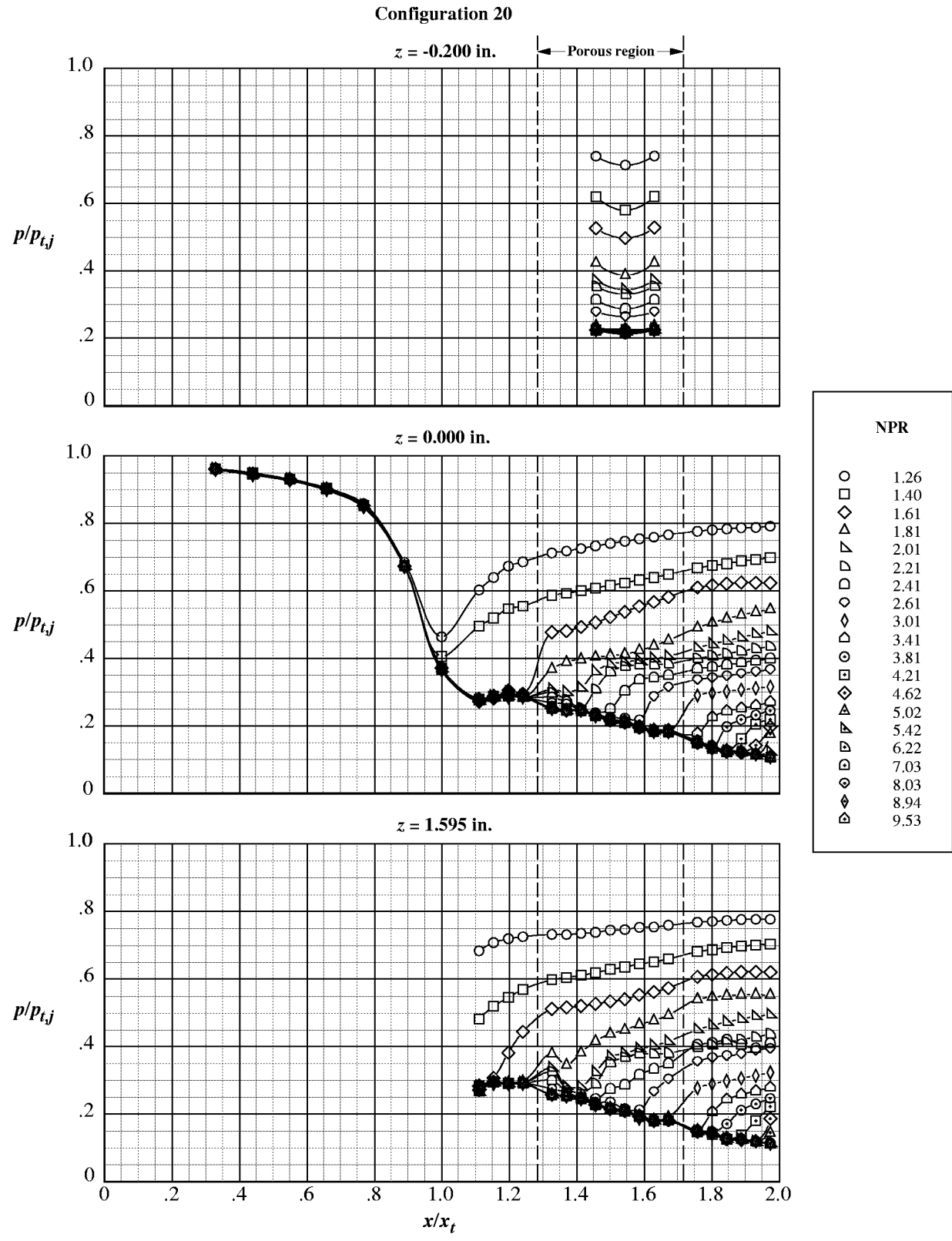
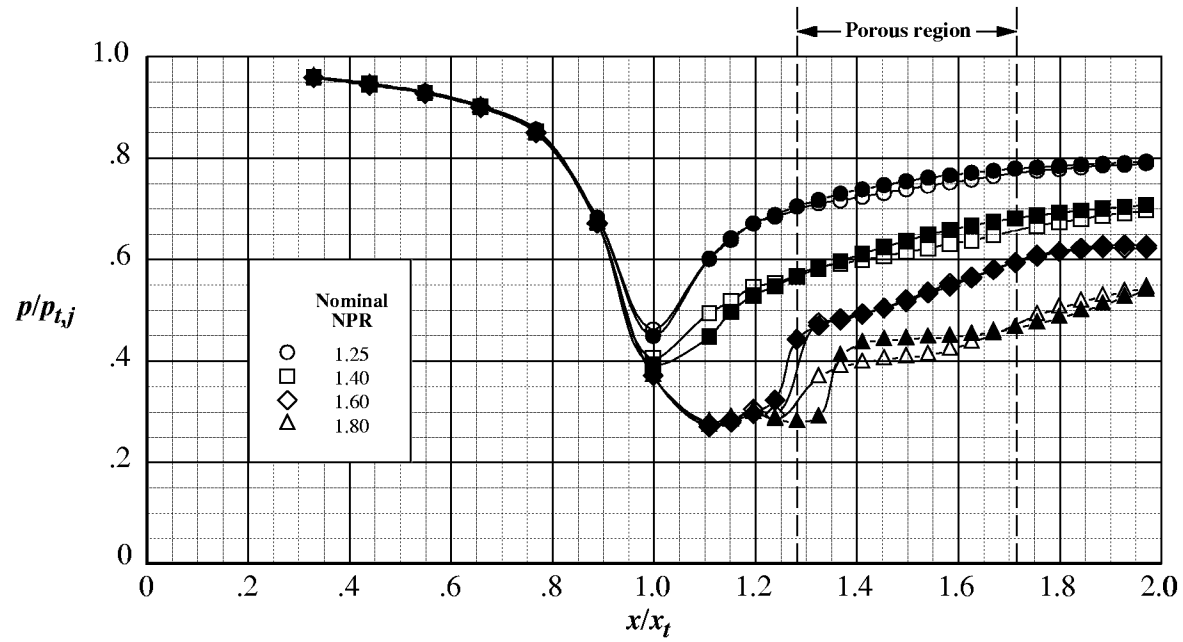
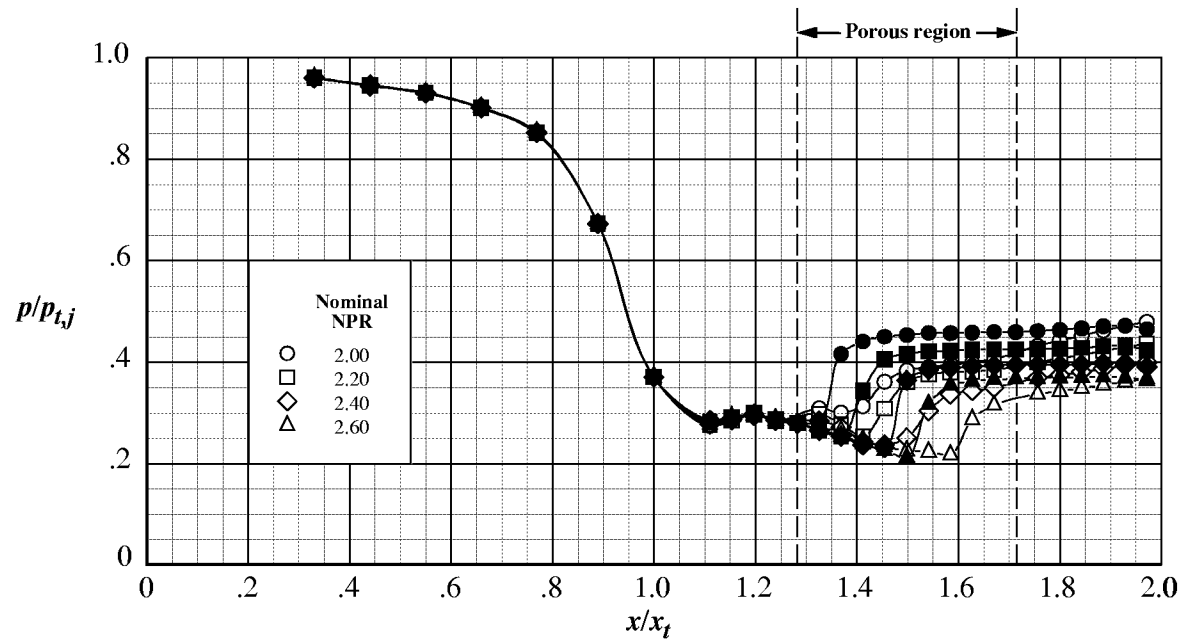


Figure 26. Internal static pressure ratio distributions for porous configuration 20.

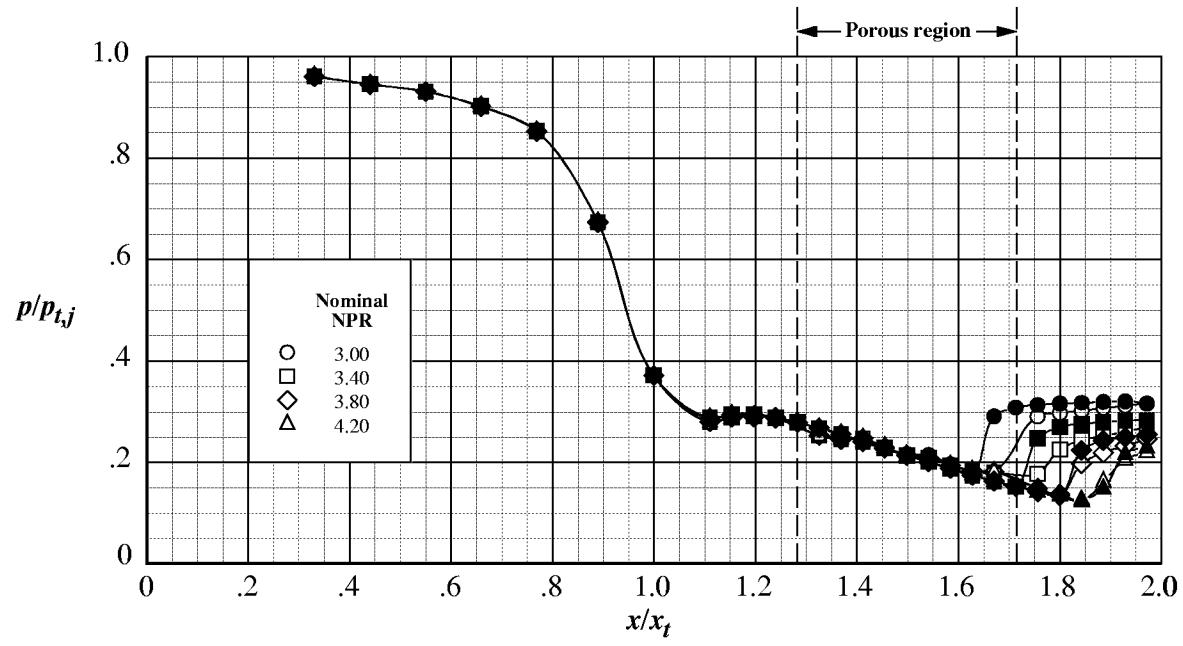


(a) Nominal NPRs from 1.25 to 1.80.

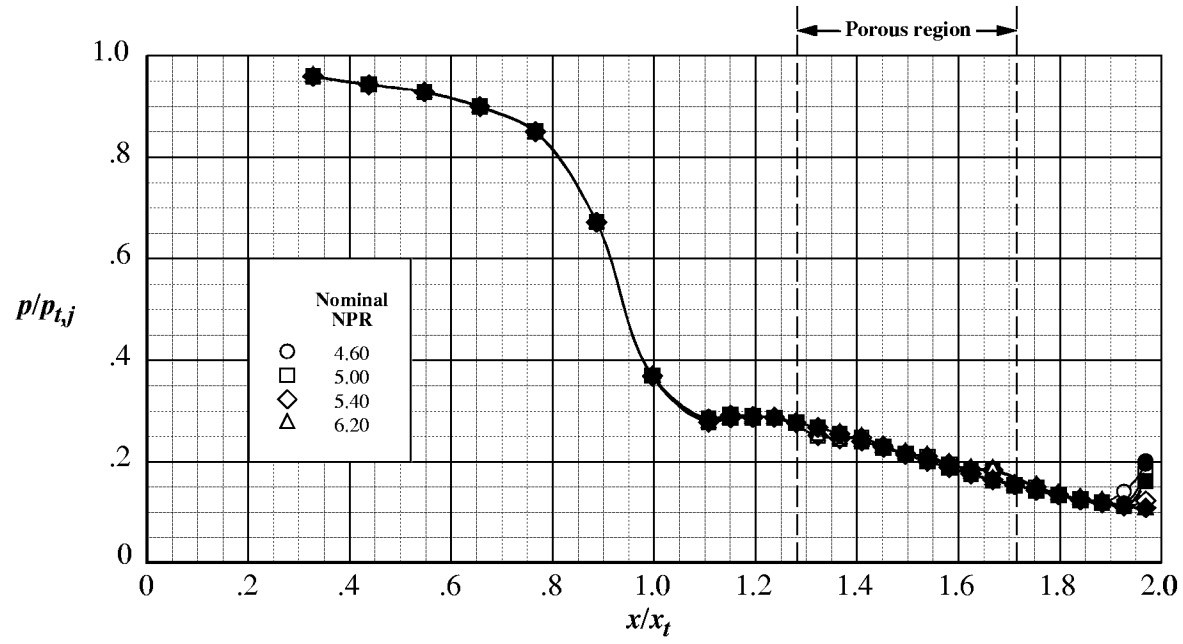


(b) Nominal NPRs from 2.00 to 2.60.

Figure 27. Comparison of centerline, internal static pressure ratio distributions between porous configuration 20 (open symbols) and the baseline configuration (solid symbols).

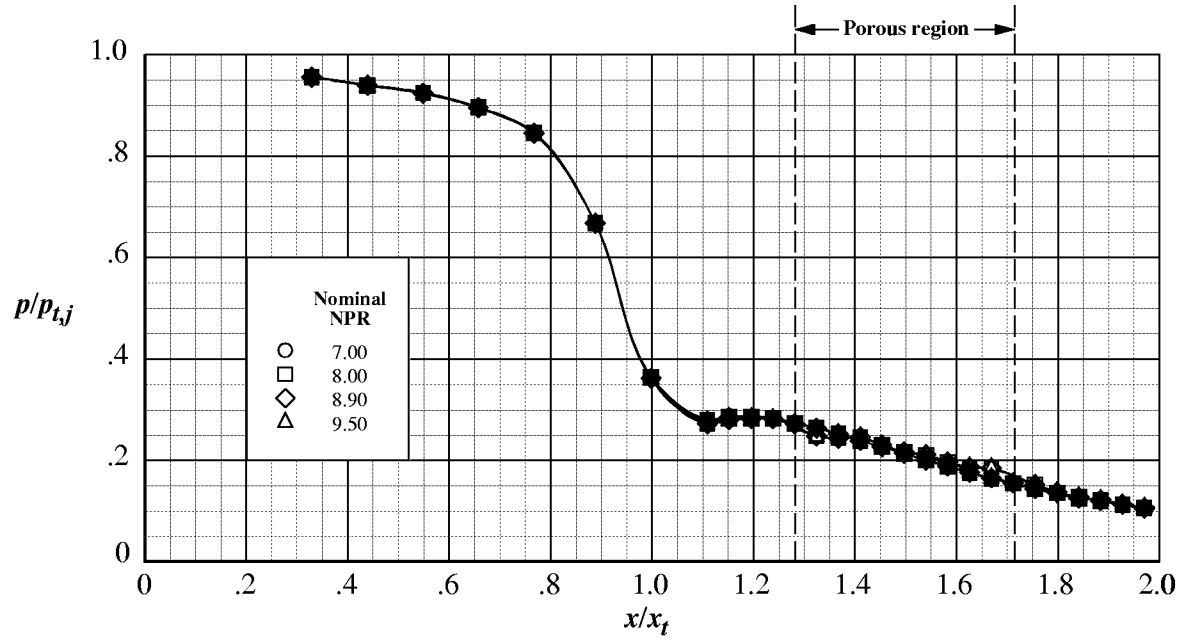


(c) Nominal NPRs from 3.00 to 4.20.



(d) Nominal NPRs from 4.60 to 6.20.

Figure 27. Continued.



(e) Nominal NPRs from 7.00 to 9.50.

Figure 27. Concluded.

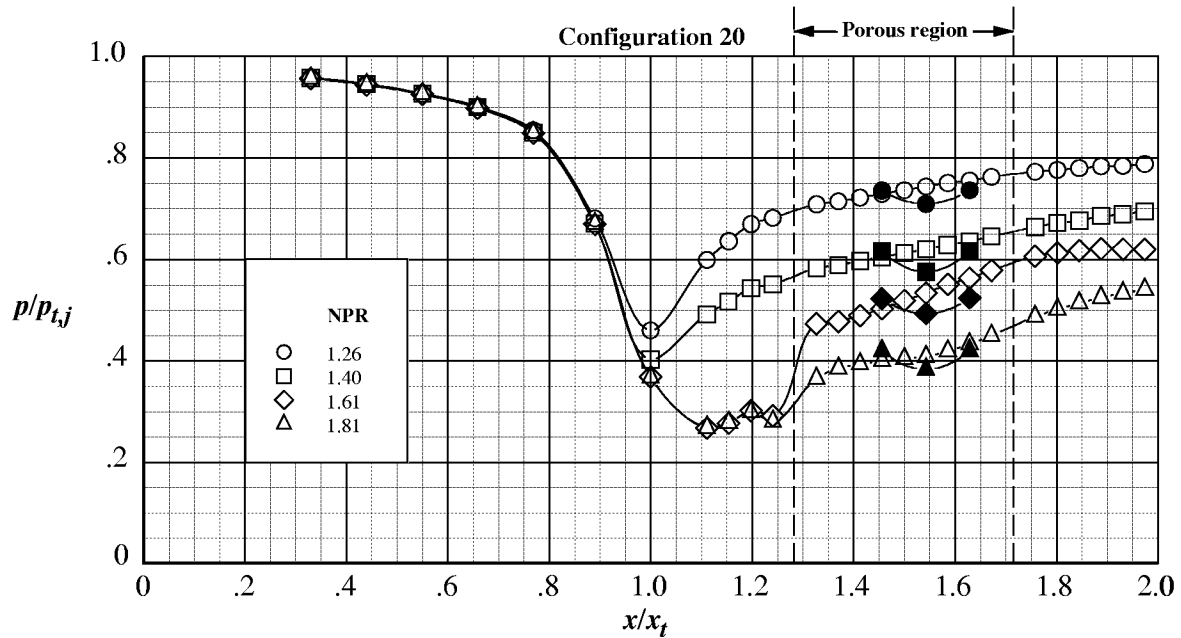
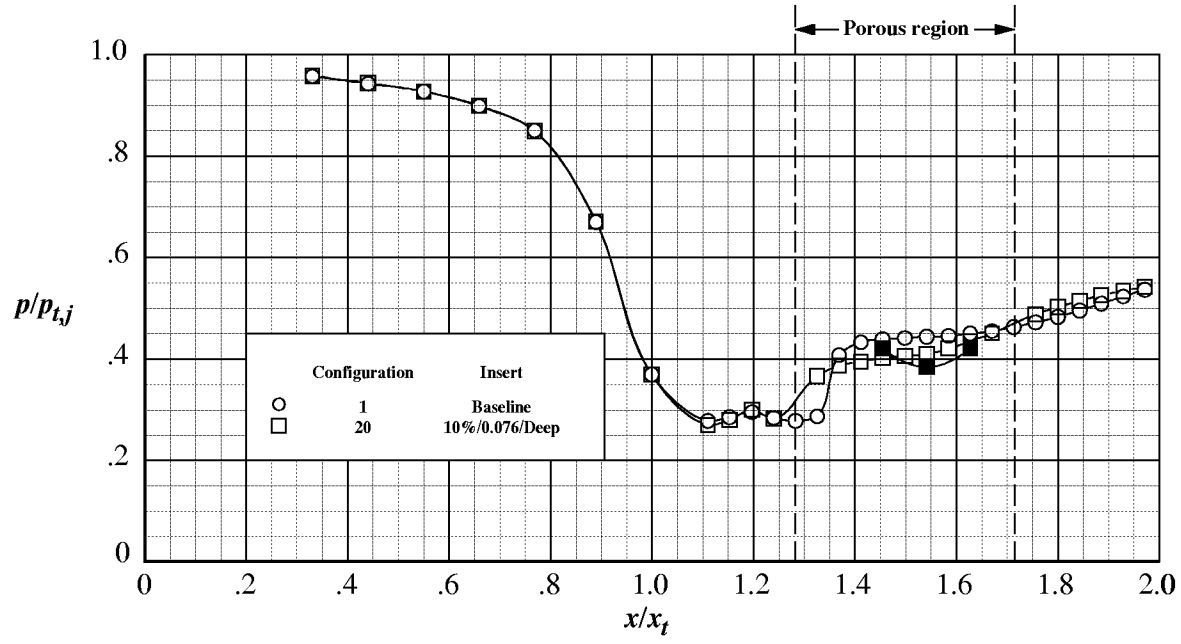
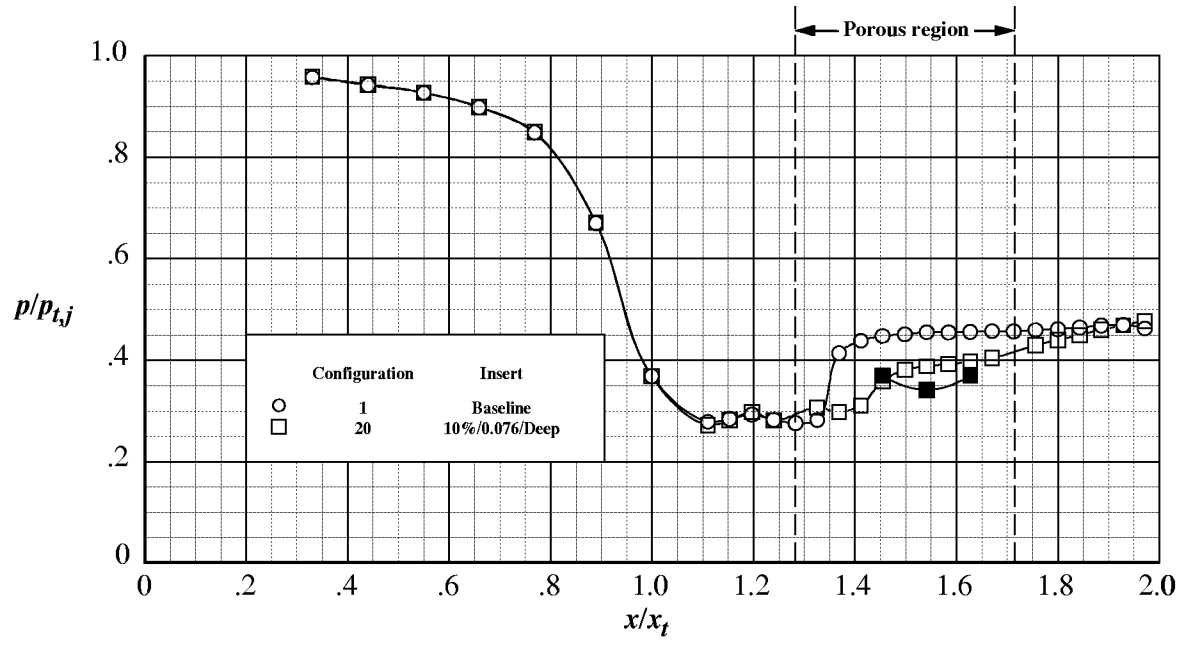


Figure 28. Comparison of surface and cavity internal static pressure ratio distributions for configuration 20 at NPRs from 1.26 to 1.81. Open symbols denote centerline (surface) pressures; solid symbols denote cavity pressures.



(a) Nominal NPR of 1.80.



(b) Nominal NPR of 2.00.

Figure 29. Comparison of internal static pressure ratio distributions for the baseline configuration and porous configuration 20 at nominal NPRs of 1.80 and 2.00. Open symbols denote centerline (surface) pressures; solid symbols denote cavity pressures.

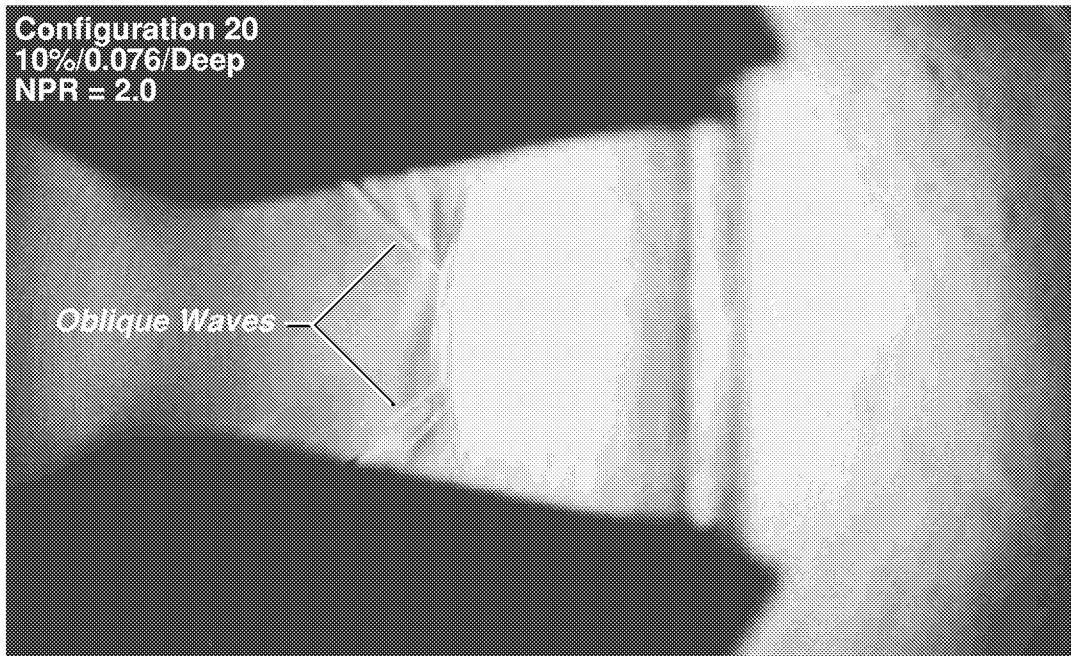
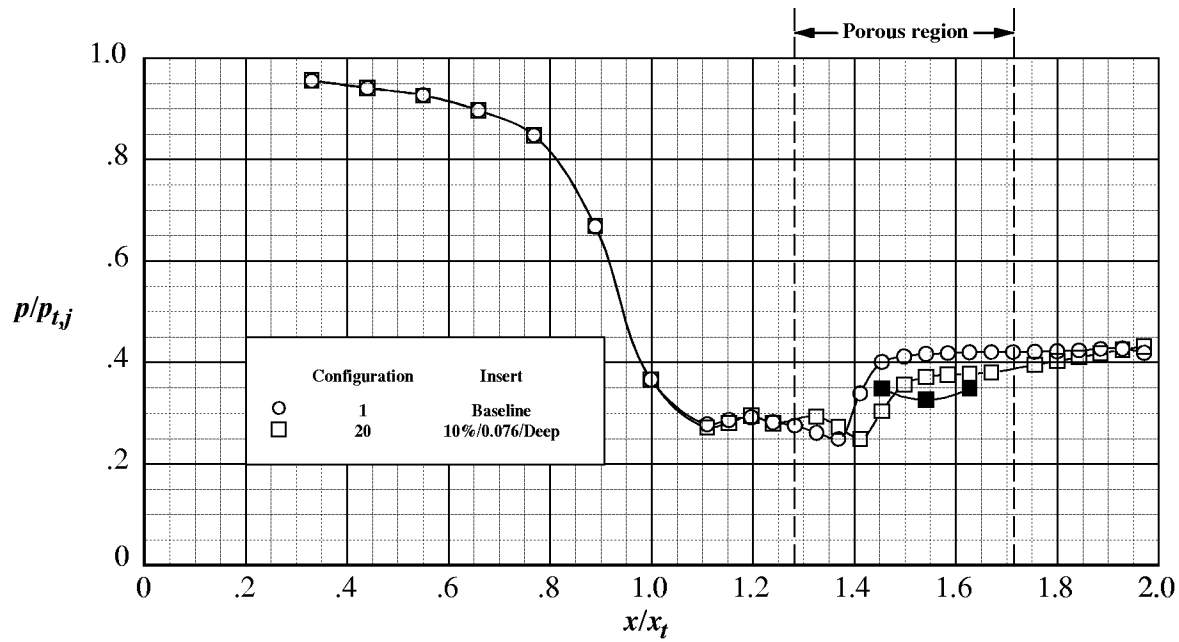
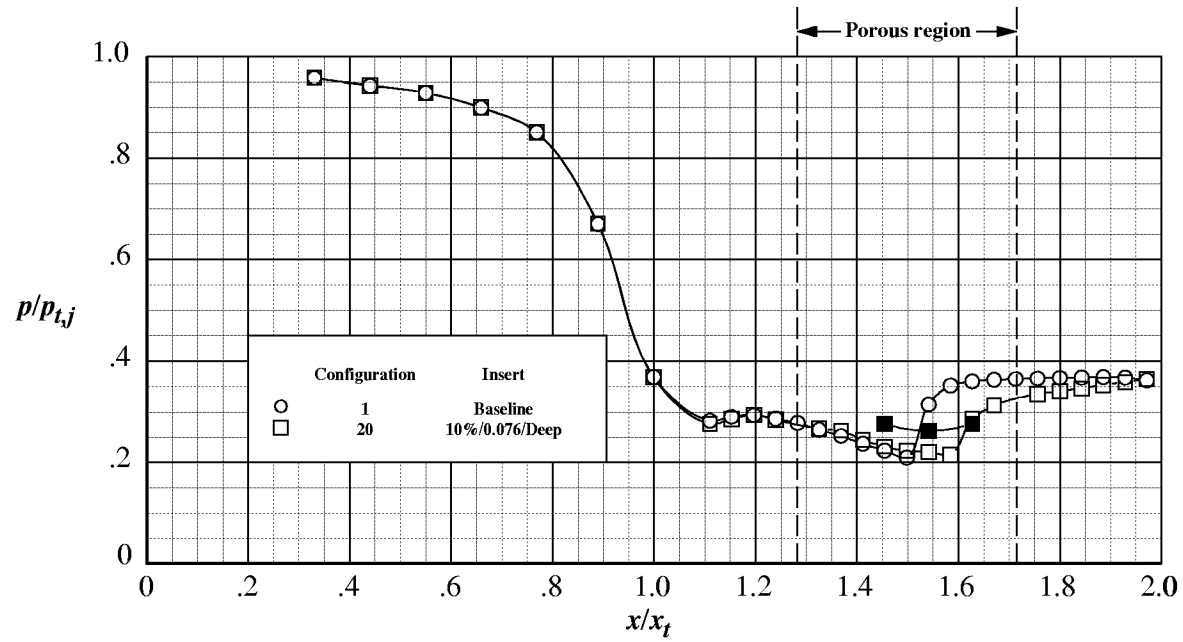


Figure 30. Focusing schlieren flow visualization at $\text{NPR}=2.0$ for configuration 20.

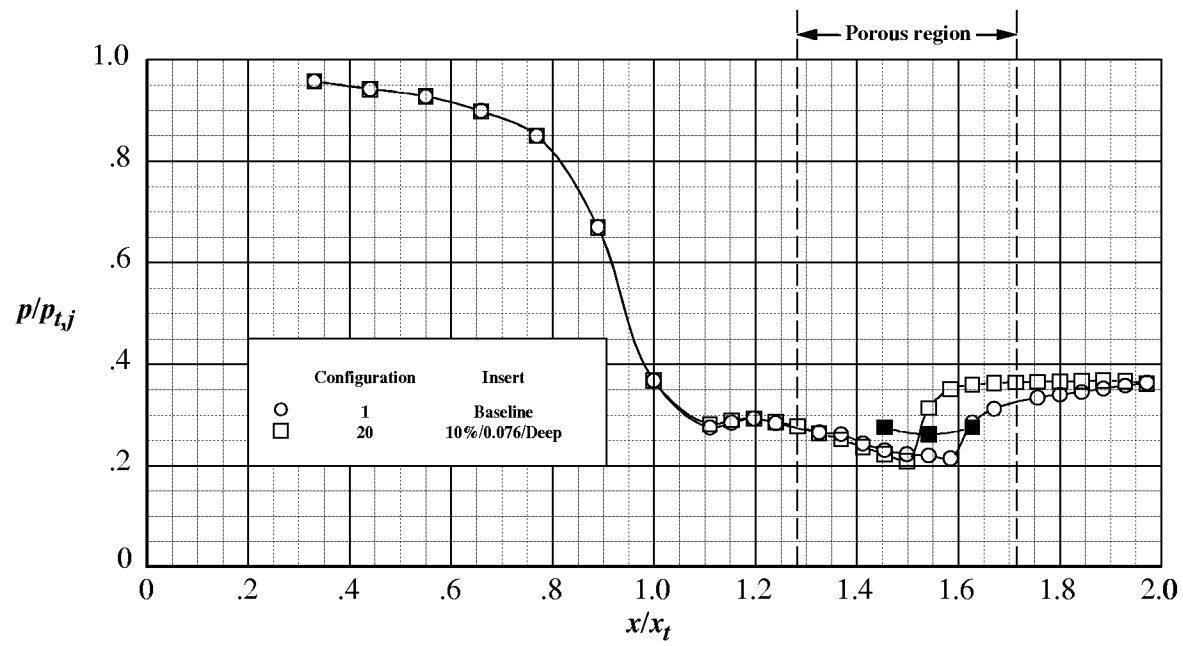


(a) Nominal NPR of 2.20.

Figure 31. Comparison of internal static pressure ratio distributions for the baseline configuration and porous configuration 20 at nominal NPRs from 2.20 to 3.00. Open symbols denote centerline (surface) pressures; solid symbols denote cavity pressures.

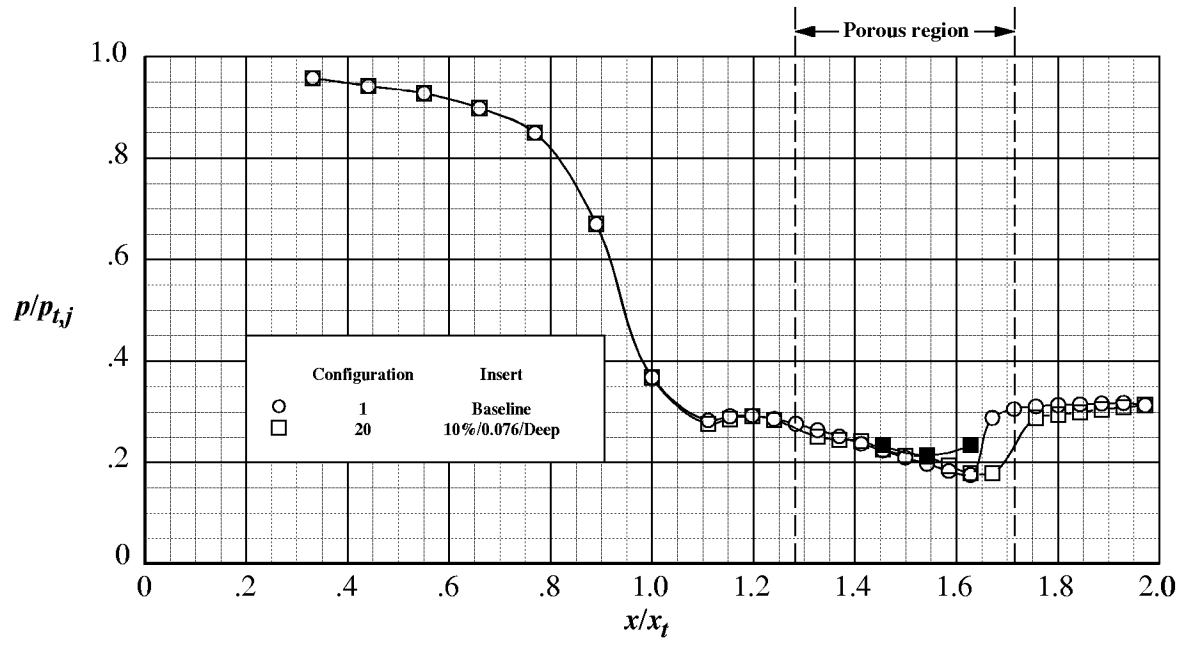


(b) Nominal NPR of 2.40.



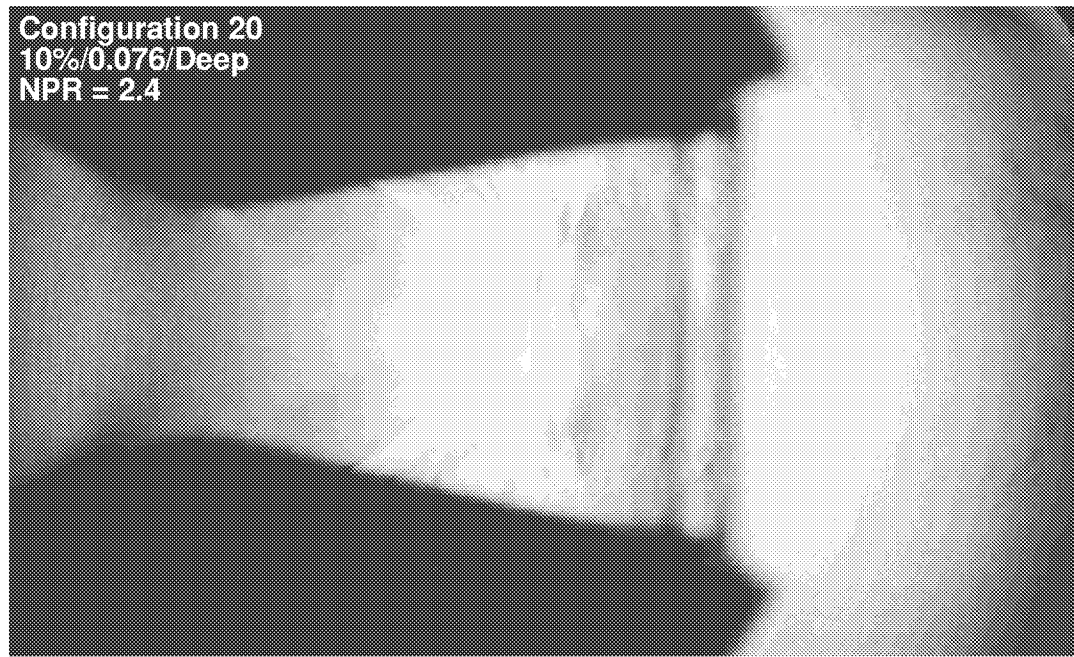
(c) Nominal NPR of 2.60.

Figure 31. Continued.



(d) Nominal NPR of 3.00.

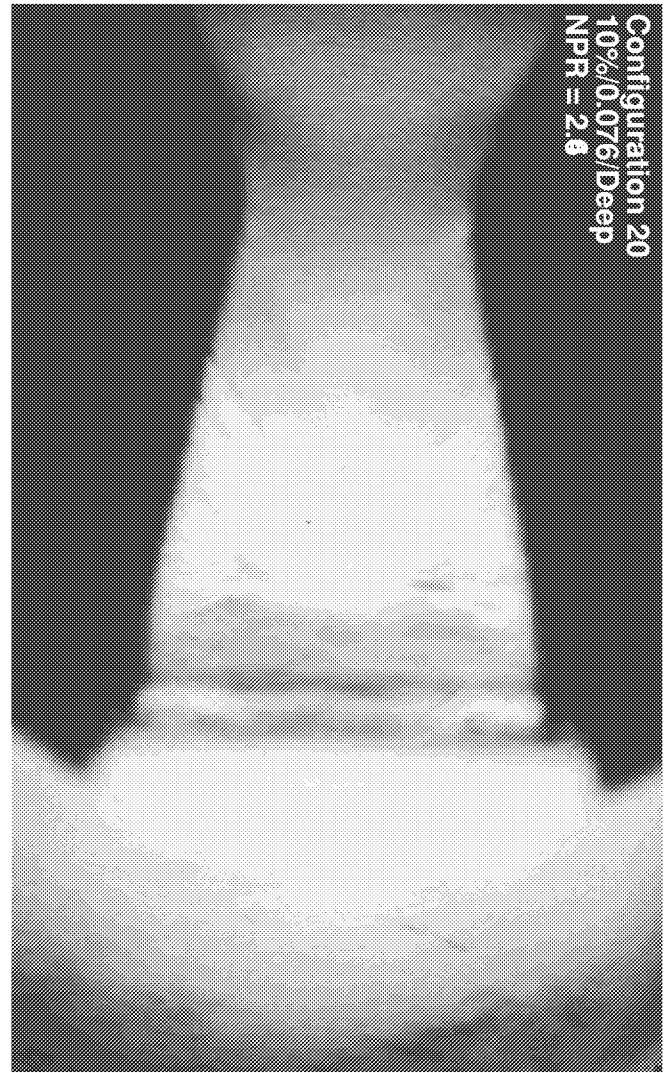
Figure 31. Concluded.



(a) $\text{NPR} = 2.4$.

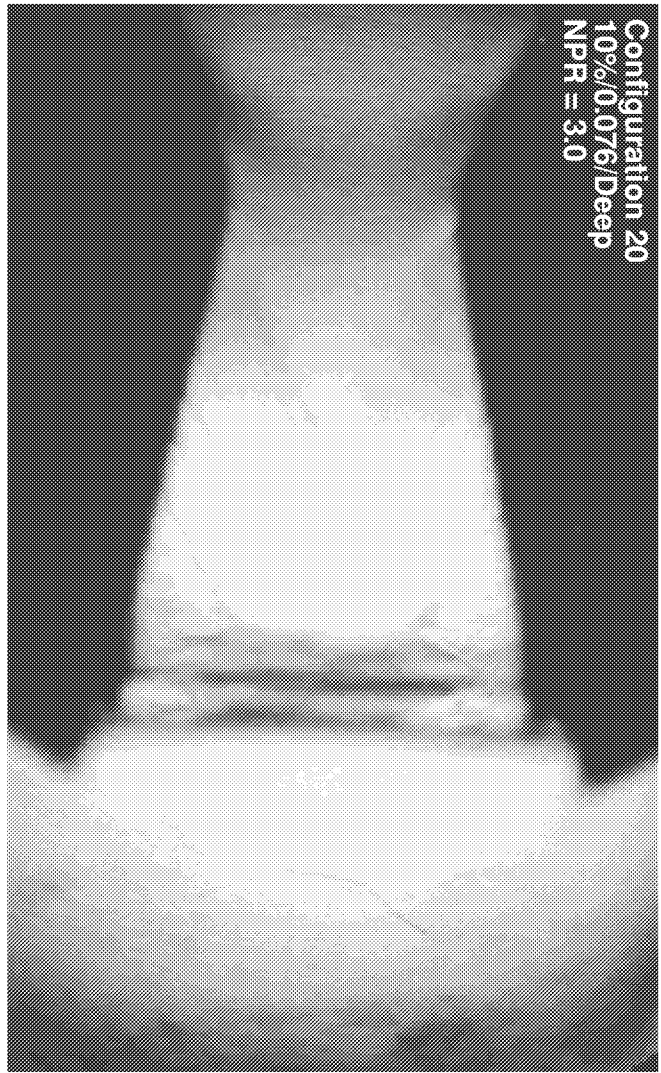
Figure 32. Focusing schlieren flow visualization at NPRs from 2.4 to 3.0 for porous configuration 20.

Configuration 20
10%/0.076 Deep
NPR = 2.6



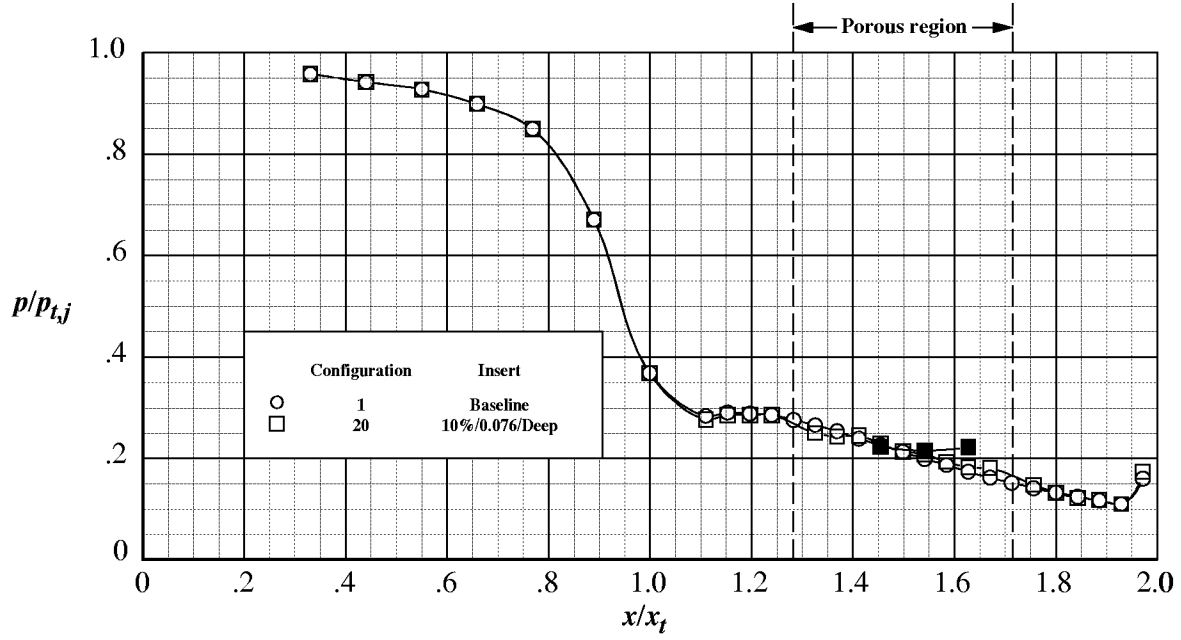
(b) NPR = 2.6.

Configuration 20
10%/0.076 Deep
NPR = 3.0

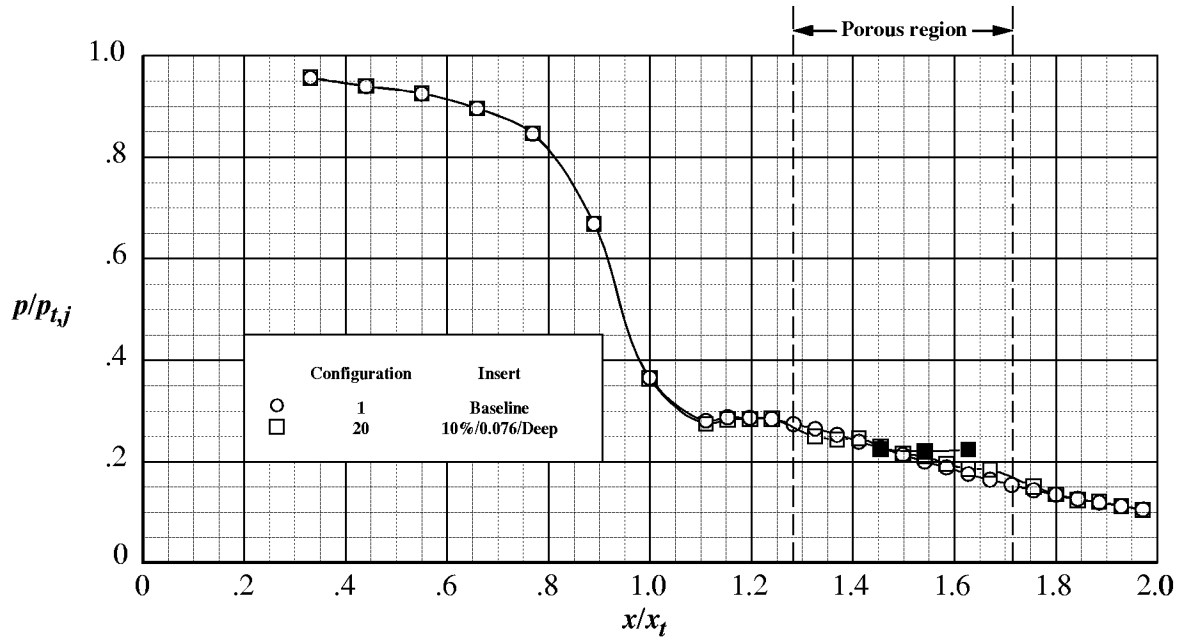


(c) NPR = 3.0.

Figure 32. Concluded.



(a) Nominal NPR of 5.00.



(b) Nominal NPR of 7.00.

Figure 33. Comparison of internal static pressure ratio distributions for the baseline configuration and porous configuration 20 at nominal NPRs of 5.00 and 7.00. Open symbols denote centerline (surface) pressures; solid symbols denote cavity pressures.

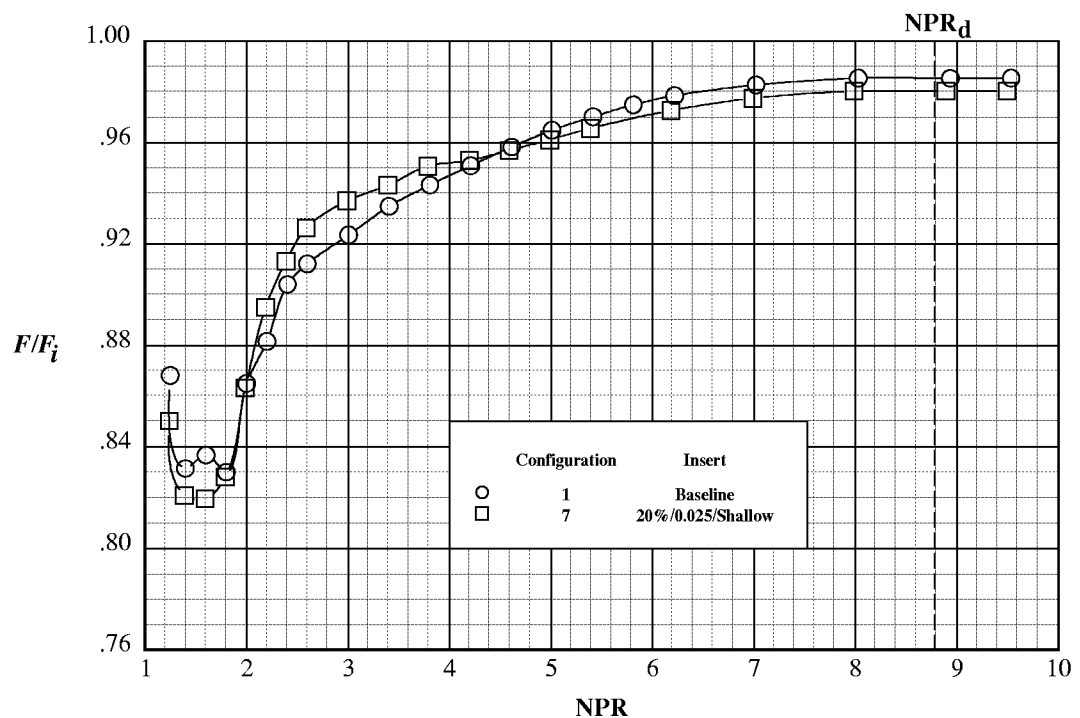


Figure 34. Comparison of nozzle thrust ratio performance for the baseline configuration and porous configuration 7.

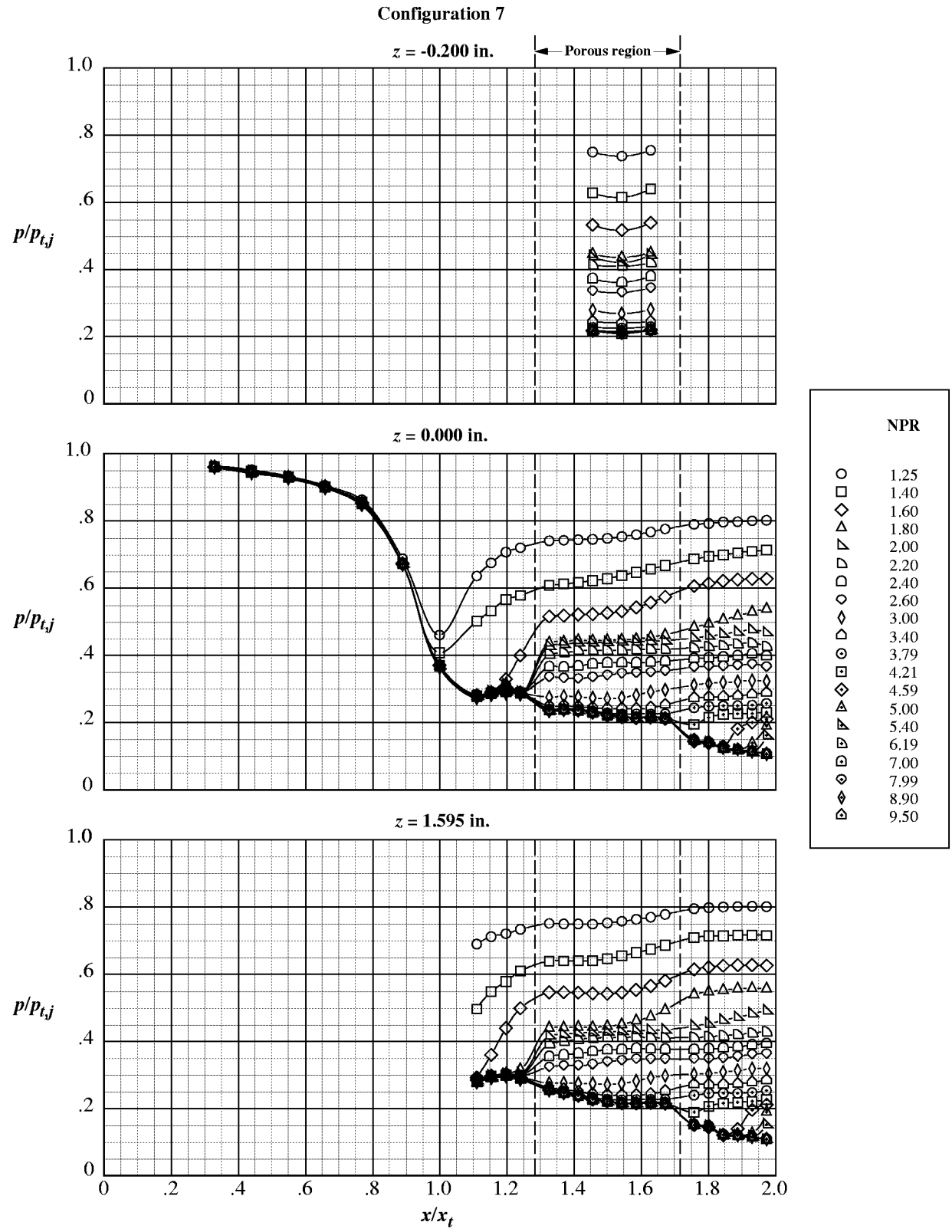
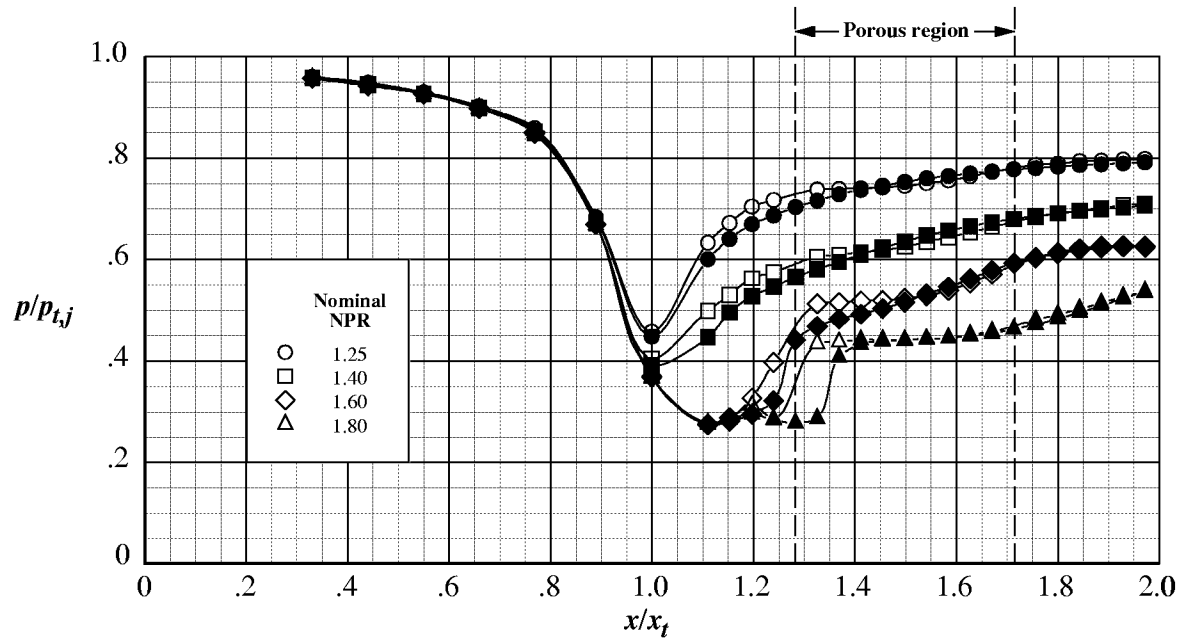
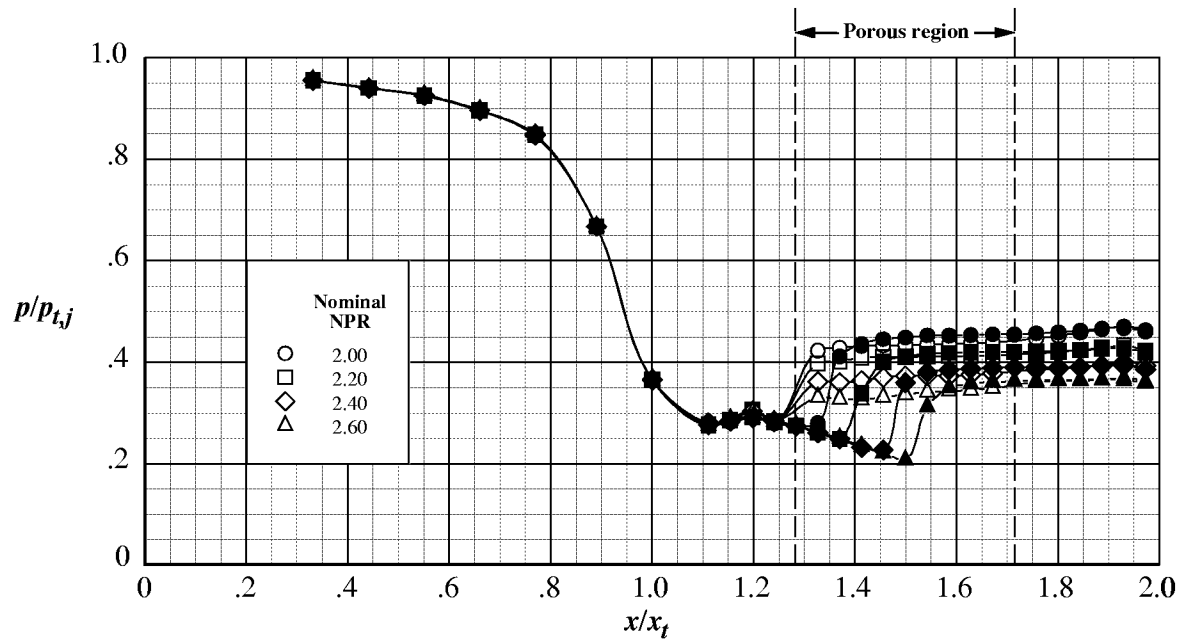


Figure 35. Internal static pressure ratio distributions for porous configuration 7.

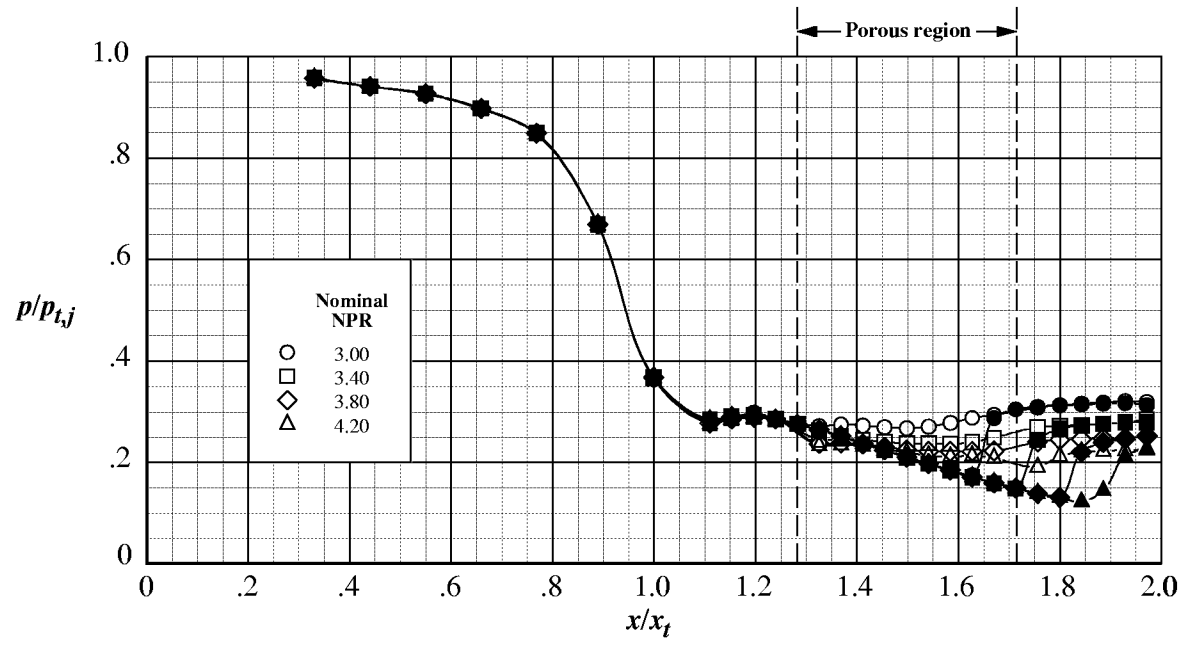


(a) Nominal NPRs from 1.25 to 1.80.

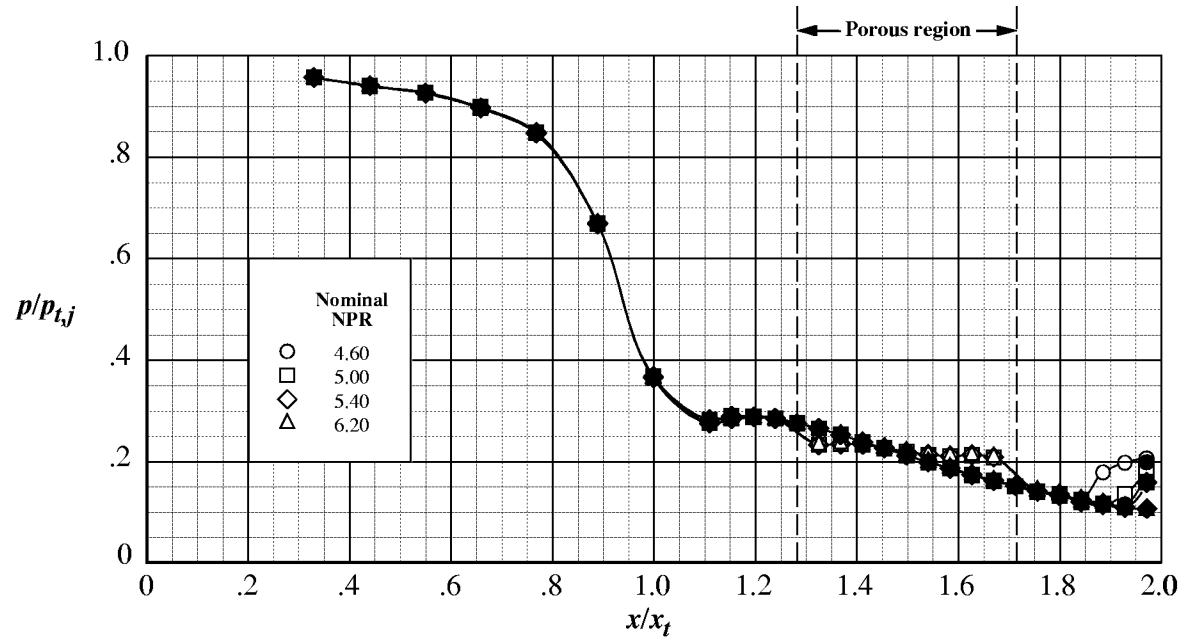


(b) Nominal NPRs from 2.00 to 2.60.

Figure 36. Comparison of centerline internal static pressure ratio distributions between porous configuration 7 (open symbols) and the baseline configuration (solid symbols).

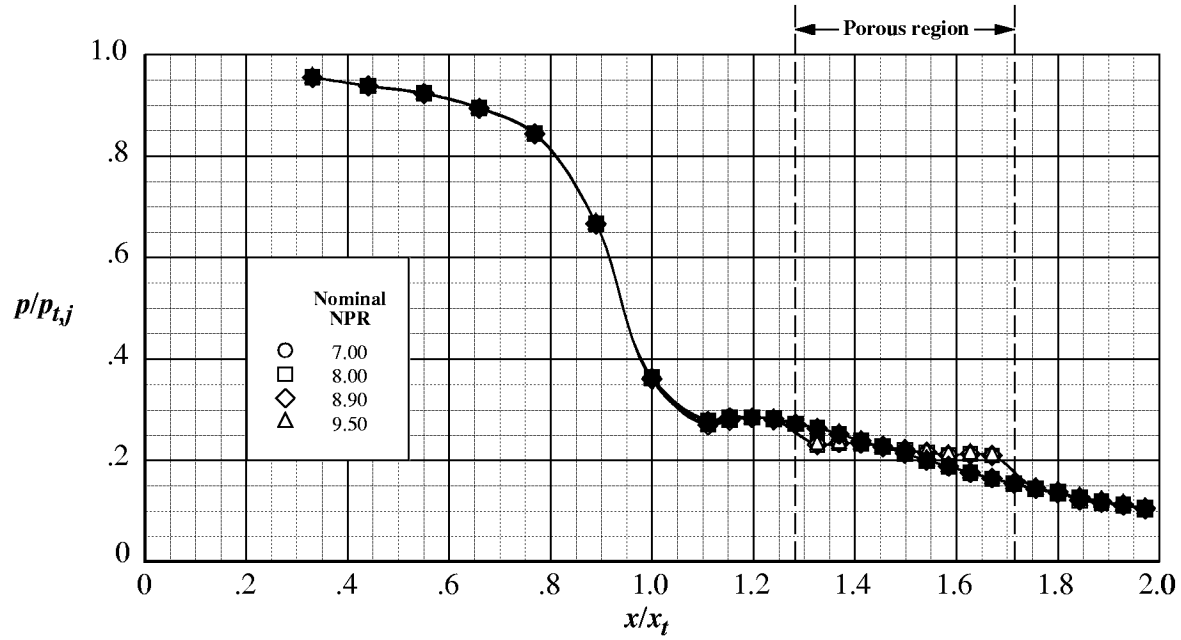


(c) Nominal NPRs from 3.00 to 4.20.



(d) Nominal NPRs from 4.60 to 6.20.

Figure 36. Continued.



(e) Nominal NPRs from 7.00 to 9.50.

Figure 36. Concluded.

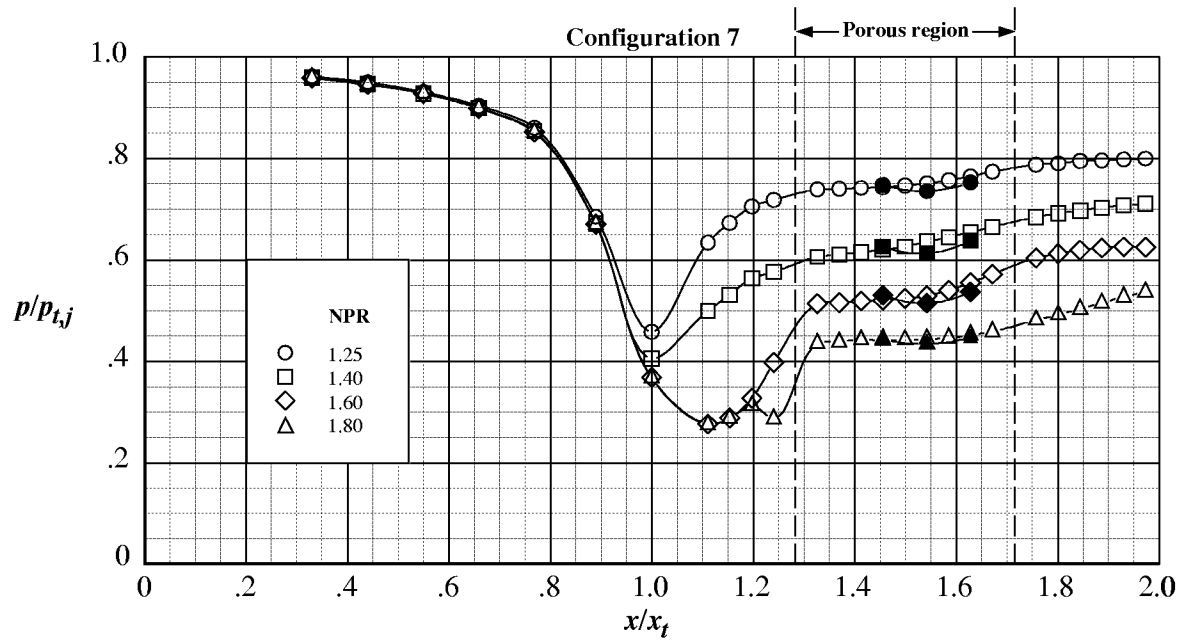
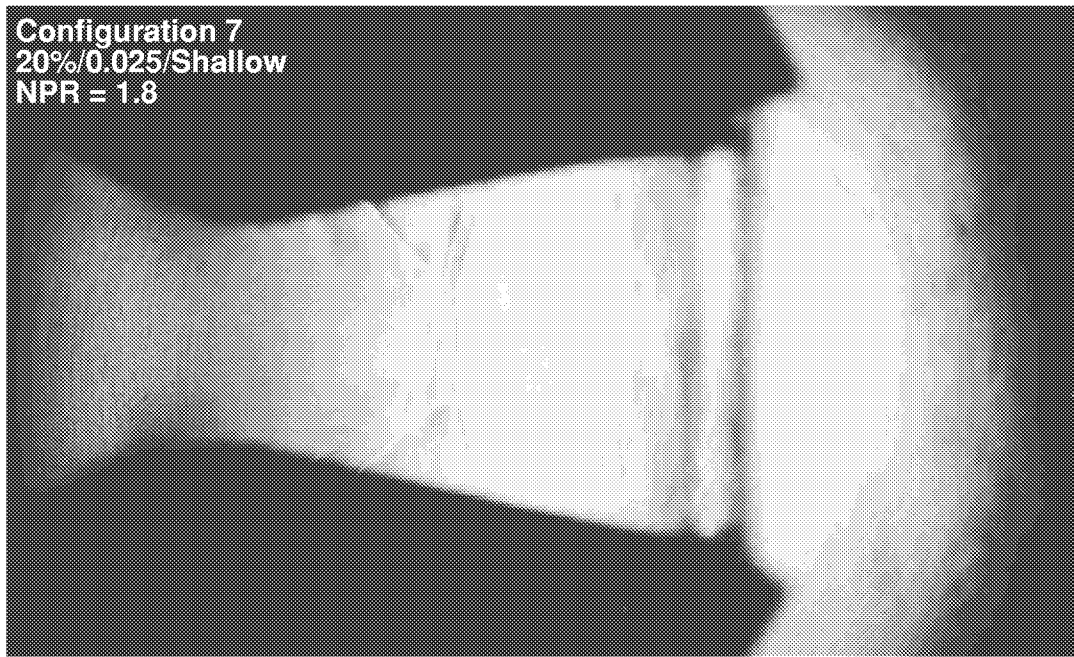
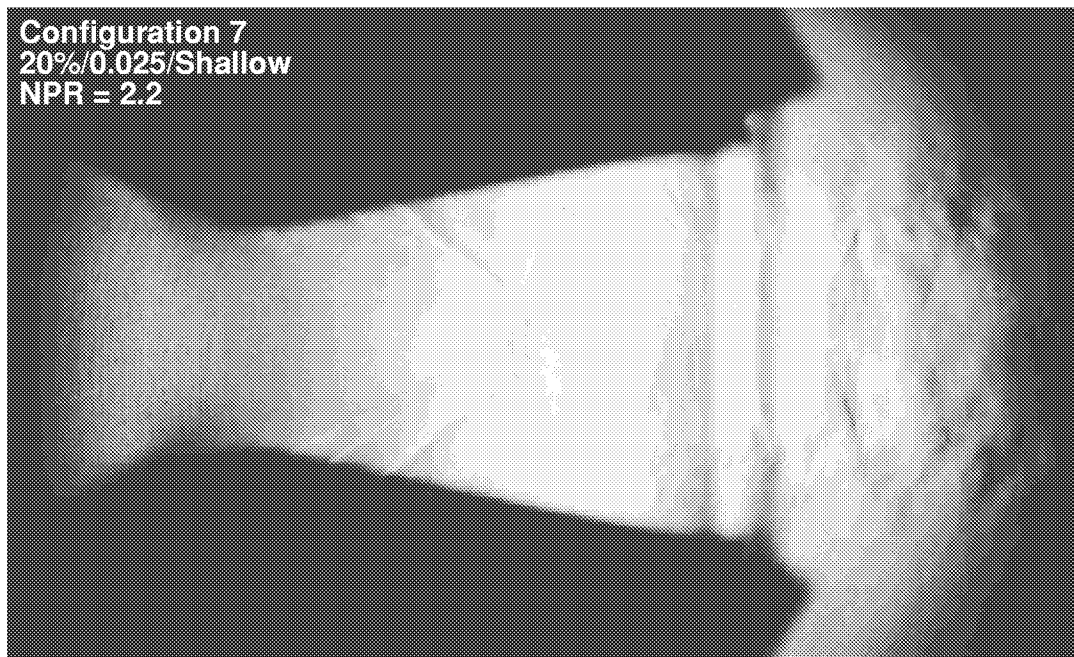


Figure 37. Comparison of surface and cavity internal static pressure ratio distributions for porous configuration 7 at NPRs from 1.25 to 1.80. Open symbols denote centerline (surface) pressures; solid symbols denote cavity pressures.

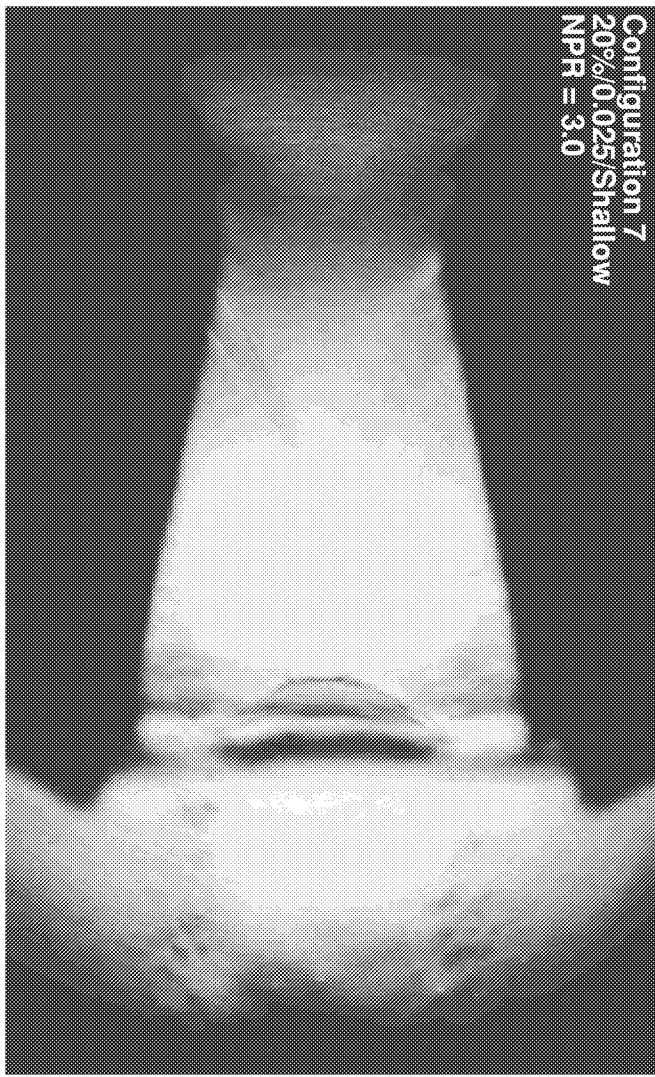


(a) $\text{NPR} = 1.8.$

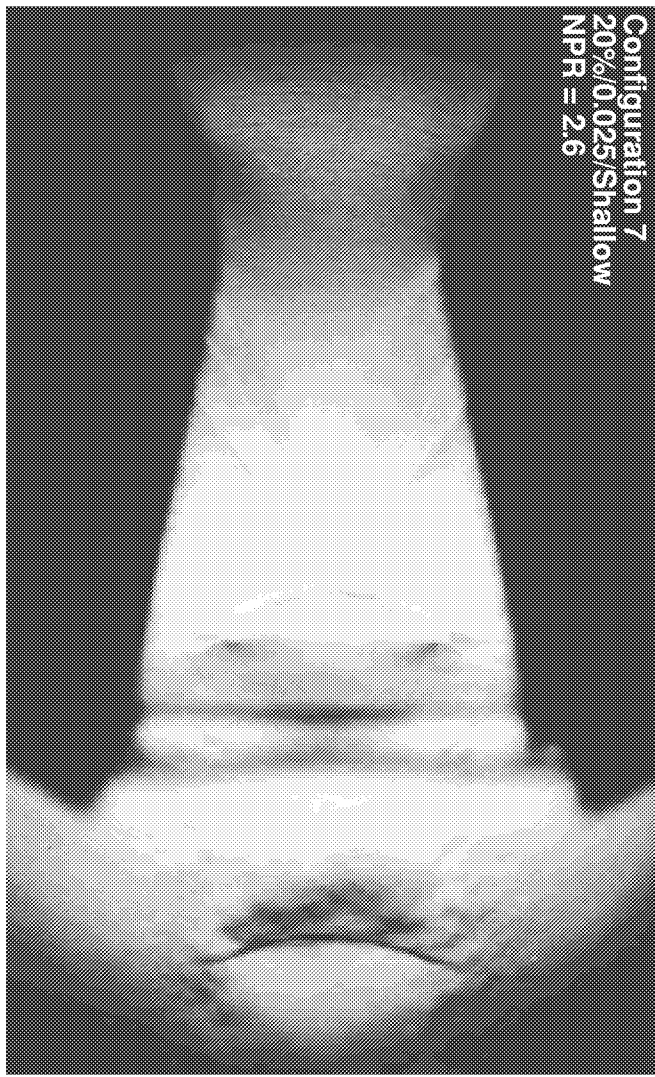


(b) $\text{NPR} = 2.2.$

Figure 38. Focusing schlieren flow visualization for porous configuration 7 at NPRs from 1.8 to 3.0.



(c) $\text{NPR} = 2.6$.



(d) $\text{NPR} = 3.0$.

Figure 38. Concluded.

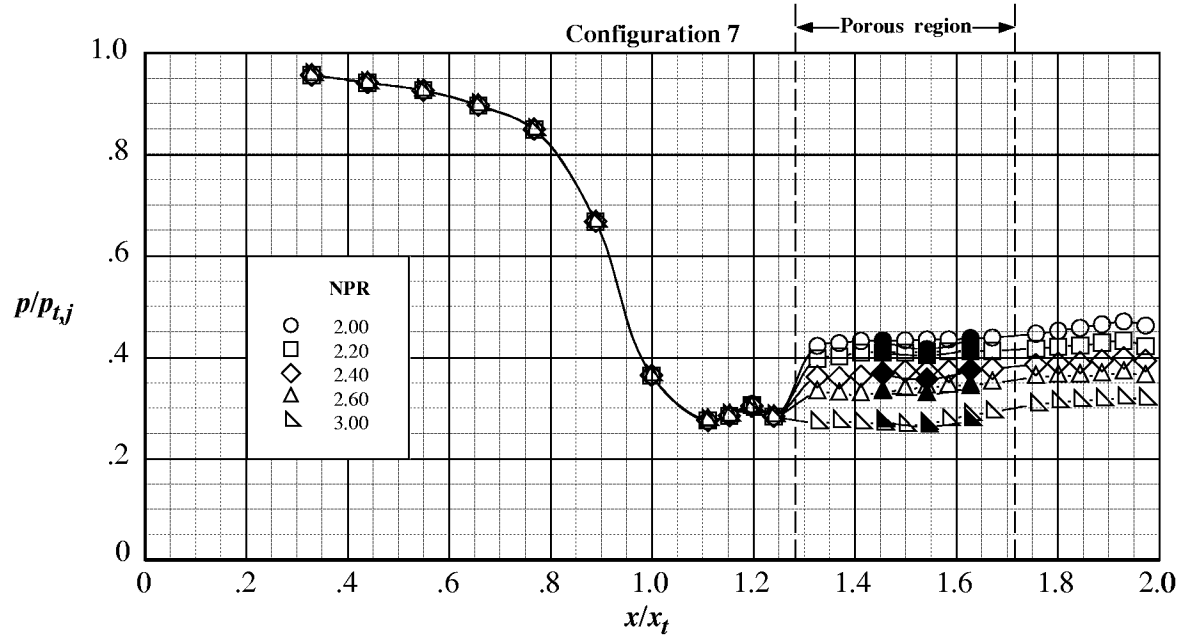


Figure 39. Comparison of surface and cavity internal static pressure distributions for porous configuration 7 at NPR's from 2.00 to 3.00. Open symbols denote centerline (surface) pressures; solid symbols denote cavity pressures.

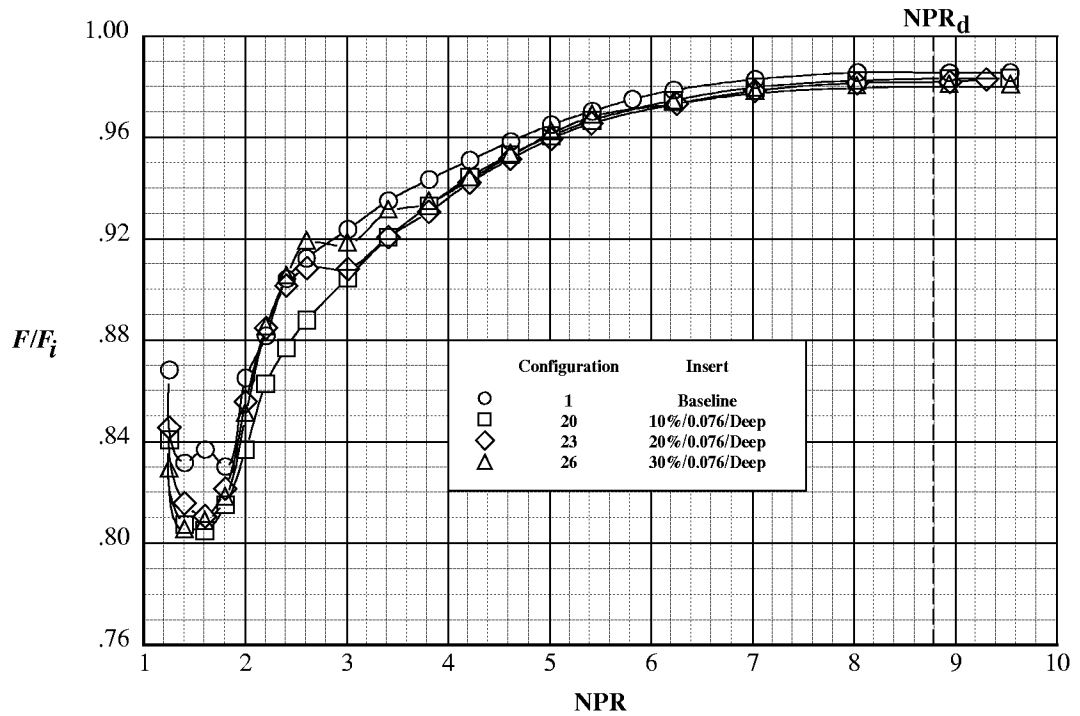


Figure 40. Effect of porosity on nozzle thrust ratio performance for porous configurations 20, 23, and 26.

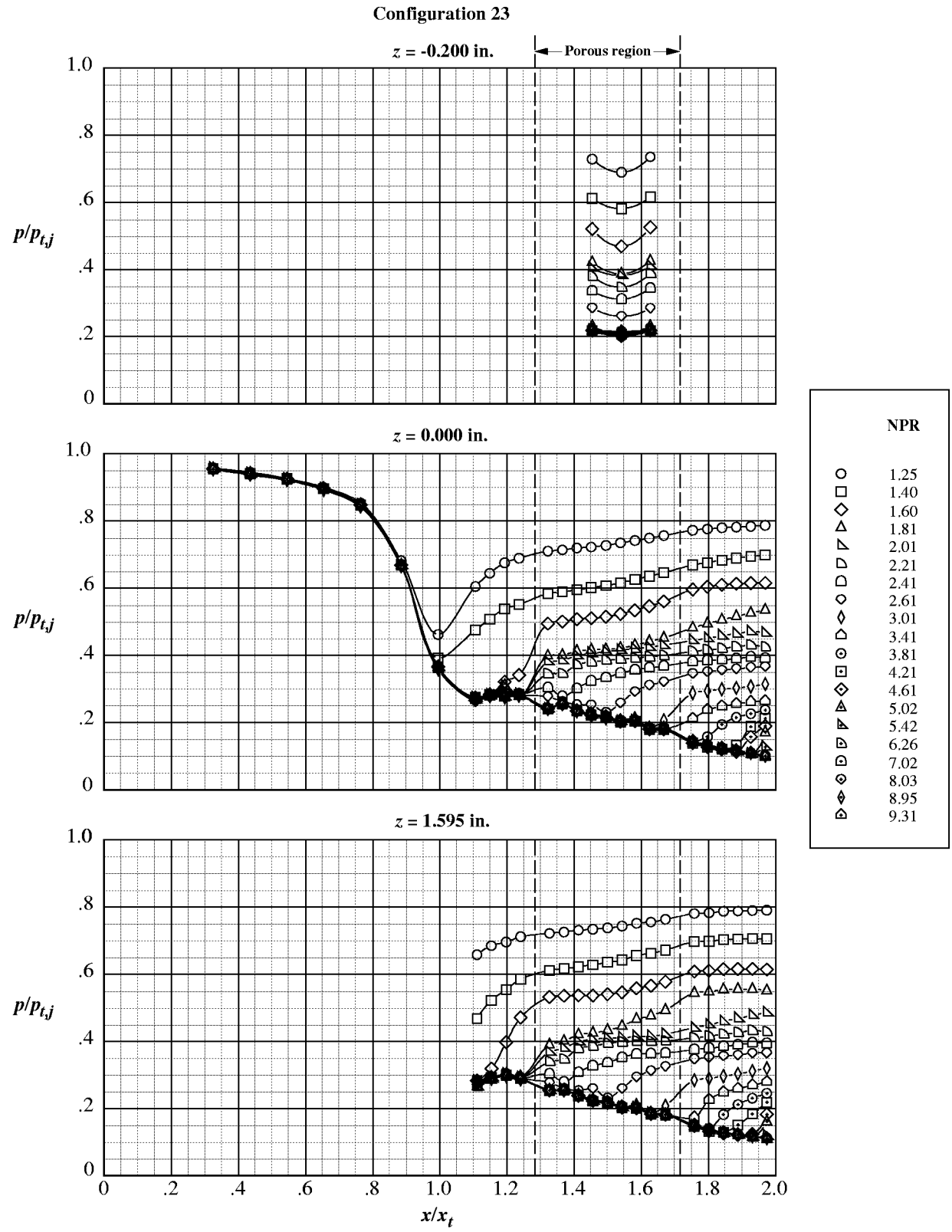


Figure 41. Internal static pressure ratio distributions for porous configuration 23.

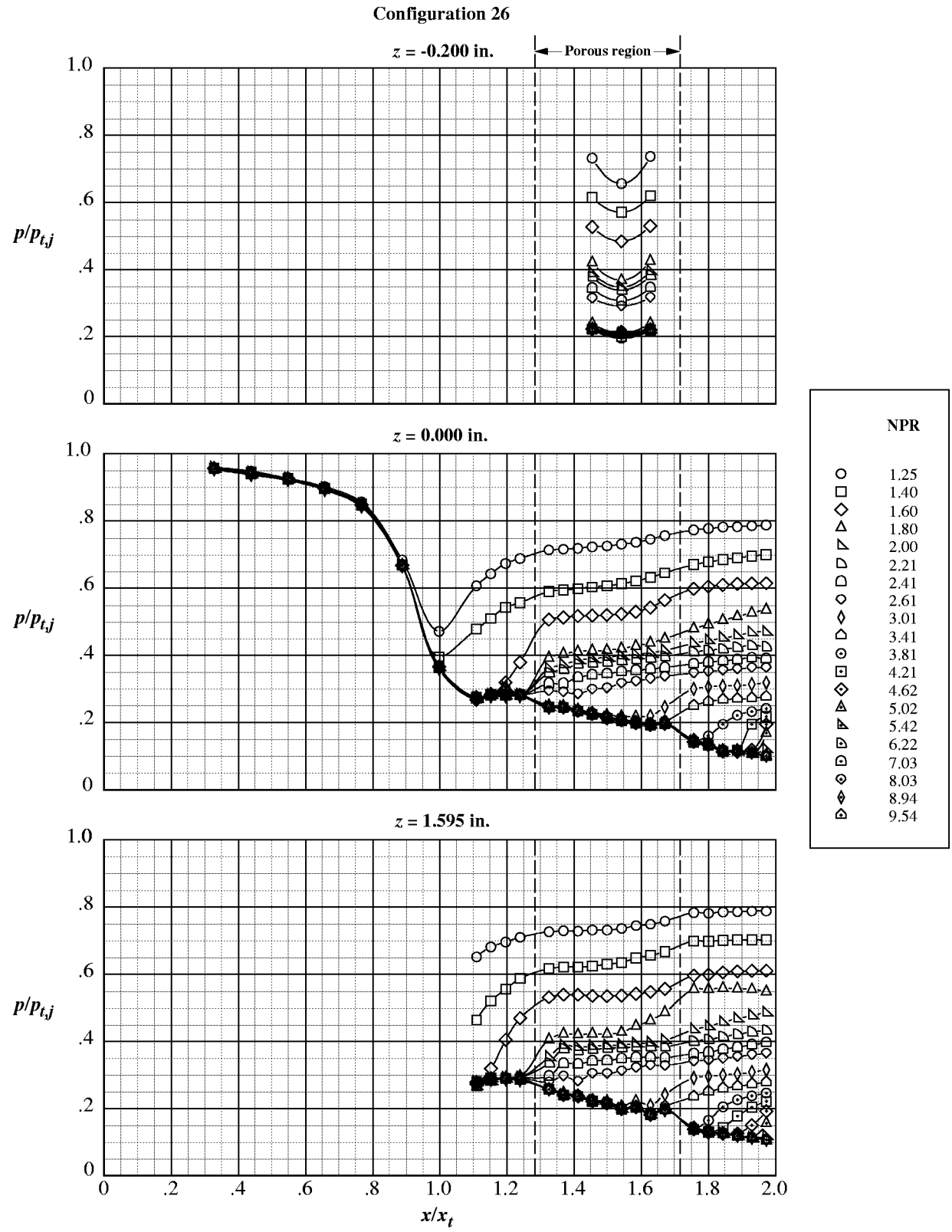


Figure 42. Internal static pressure ratio distributions for porous configuration 26.

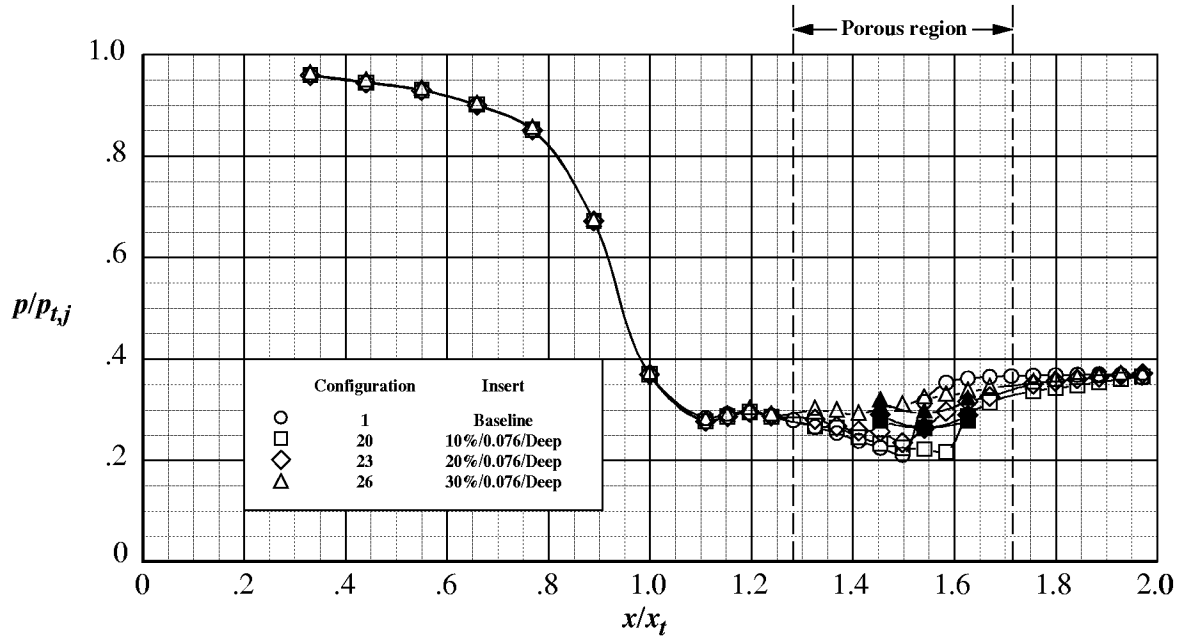
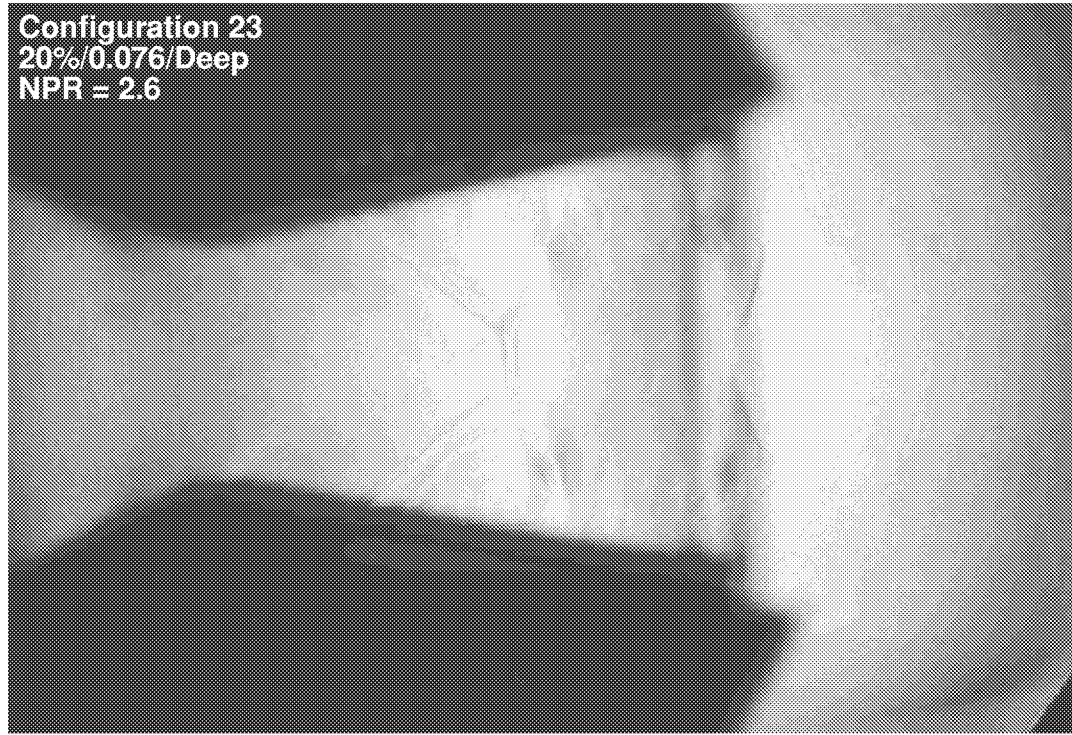
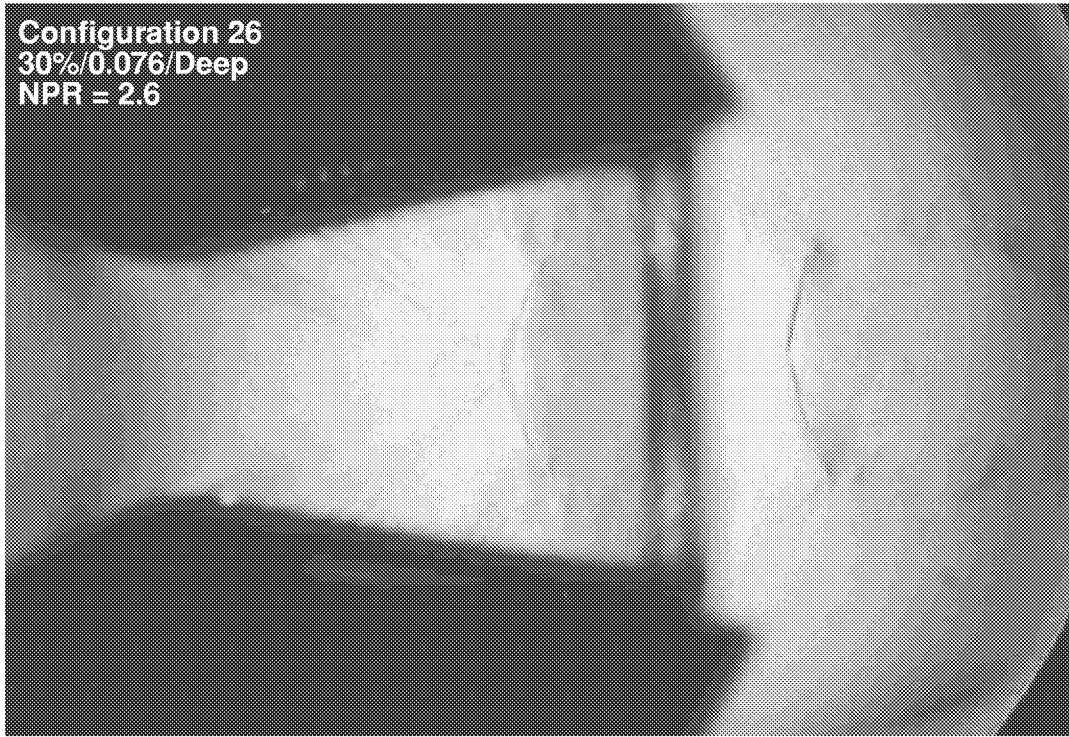


Figure 43. Effect of porosity on internal static pressure ratio distributions for porous configurations 20, 23, and 26 at nominal NPR = 2.60. Open symbols denote centerline (surface) pressures; solid symbols denote cavity pressures.



(a) Configuration 23.

Figure 44. Focusing schlieren flow visualization for porous configurations 23 and 26 at NPR = 2.6.



(b) Configuration 26.

Figure 44. Concluded.

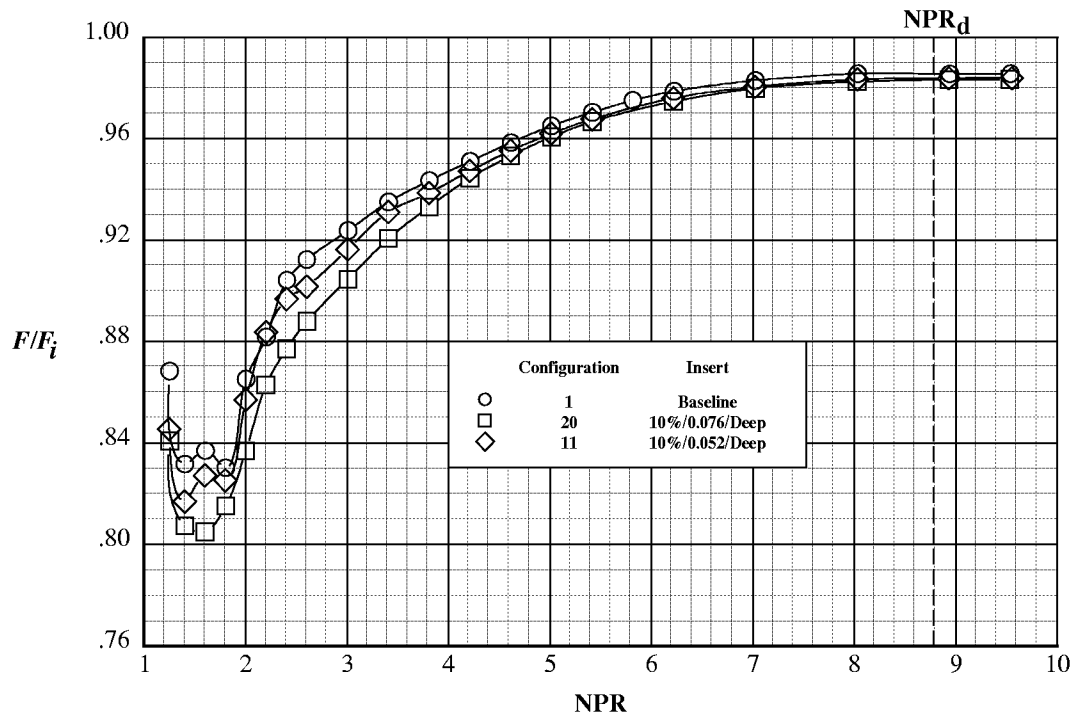


Figure 45. Effect of hole diameter on nozzle thrust ratio performance for porous configurations 20 and 11.

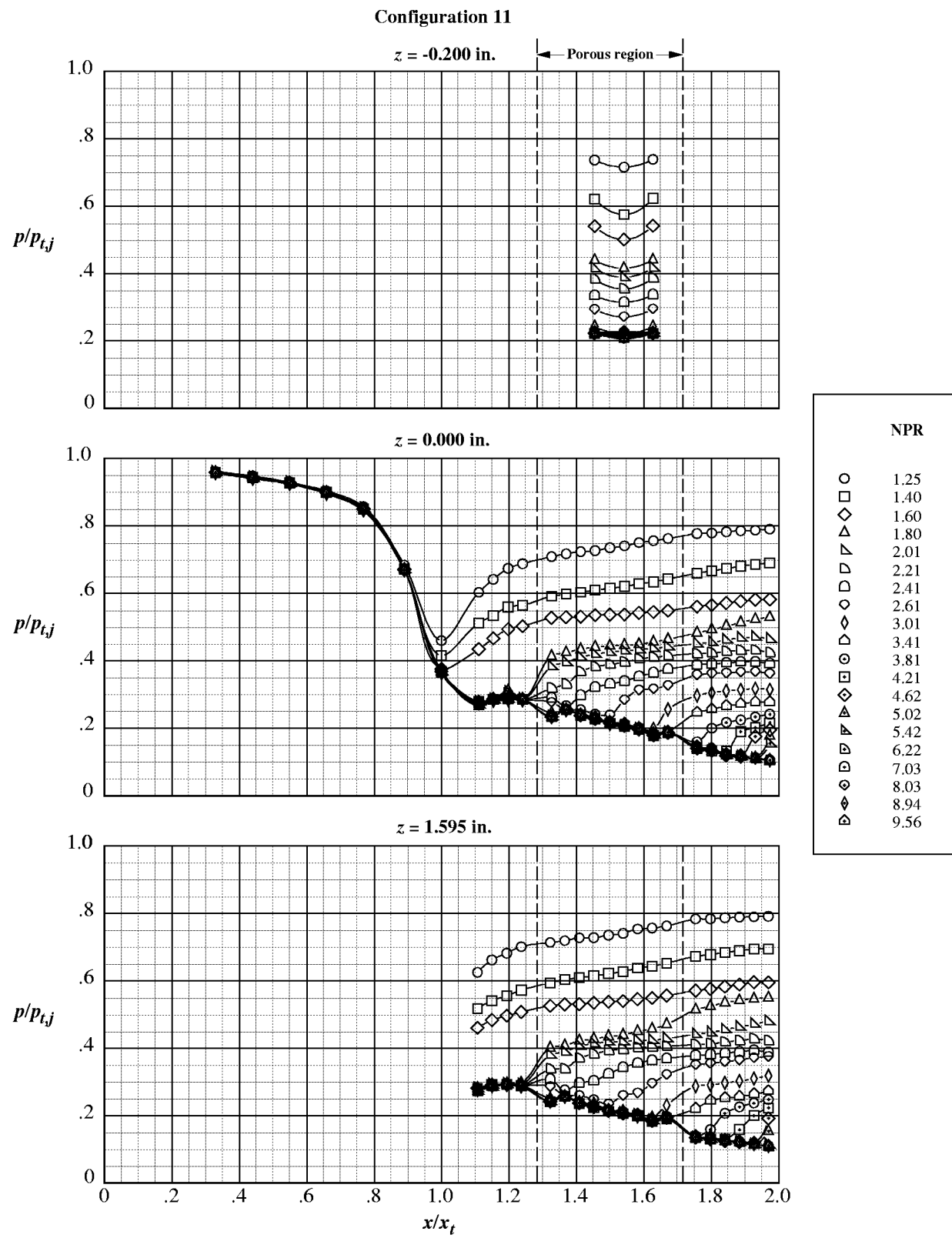


Figure 46. Internal static pressure ratio distributions for porous configuration 11.

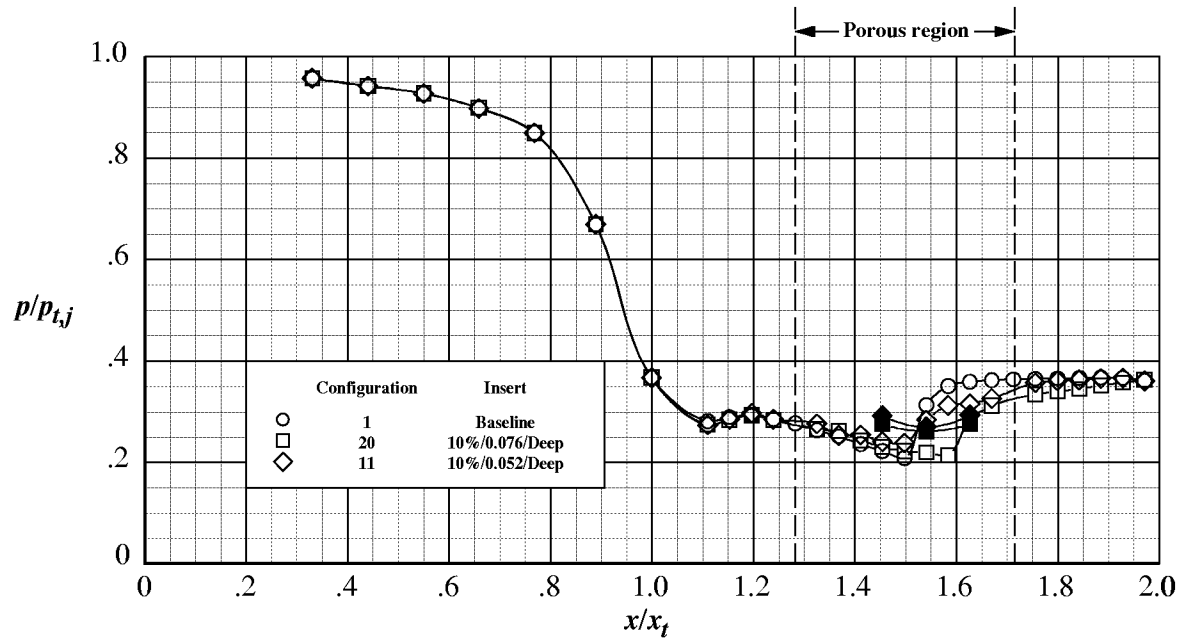


Figure 47. Effect of hole diameter on internal static pressure ratio distributions for porous configurations 20 and 11 at nominal NPR = 2.60. Open symbols denote centerline (surface) pressures; solid symbols denote cavity pressures.

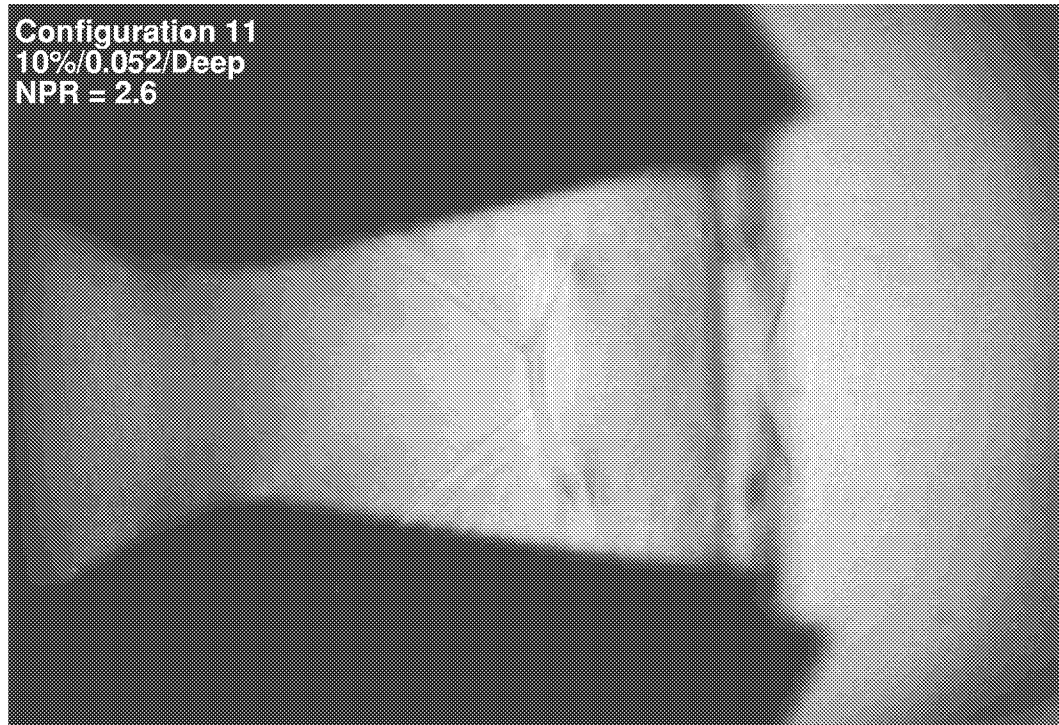


Figure 48. Focusing schlieren flow visualization for porous configuration 11 at NPR = 2.6.

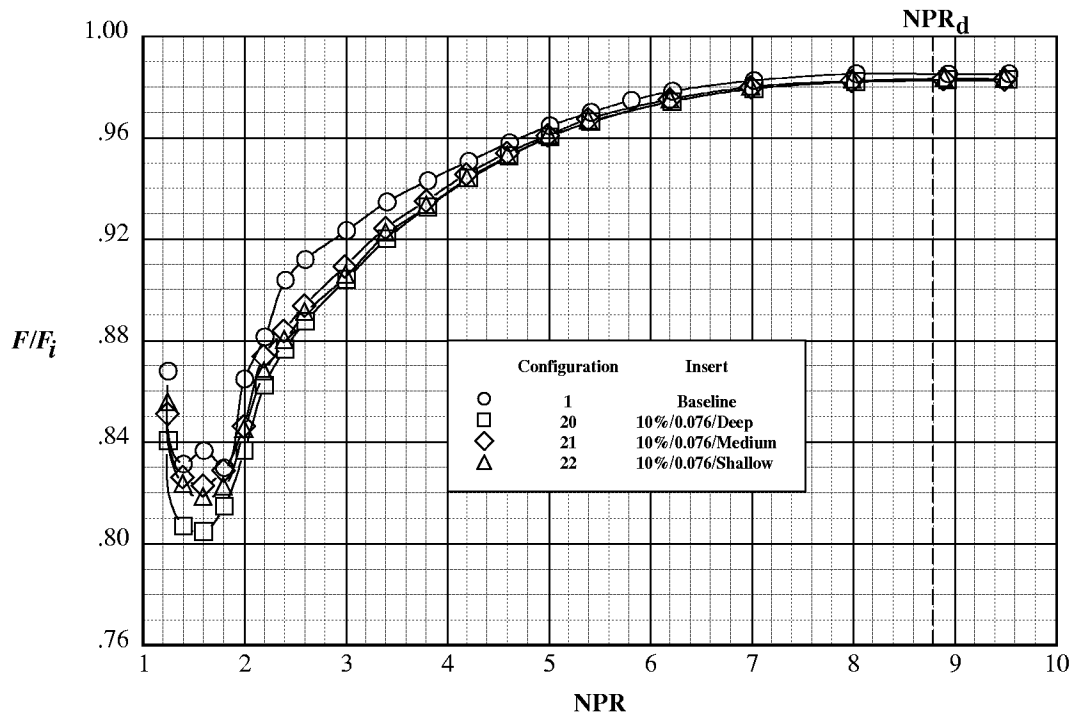


Figure 49. Effect of cavity depth on nozzle thrust ratio performance for porous configurations 20, 21, 22.

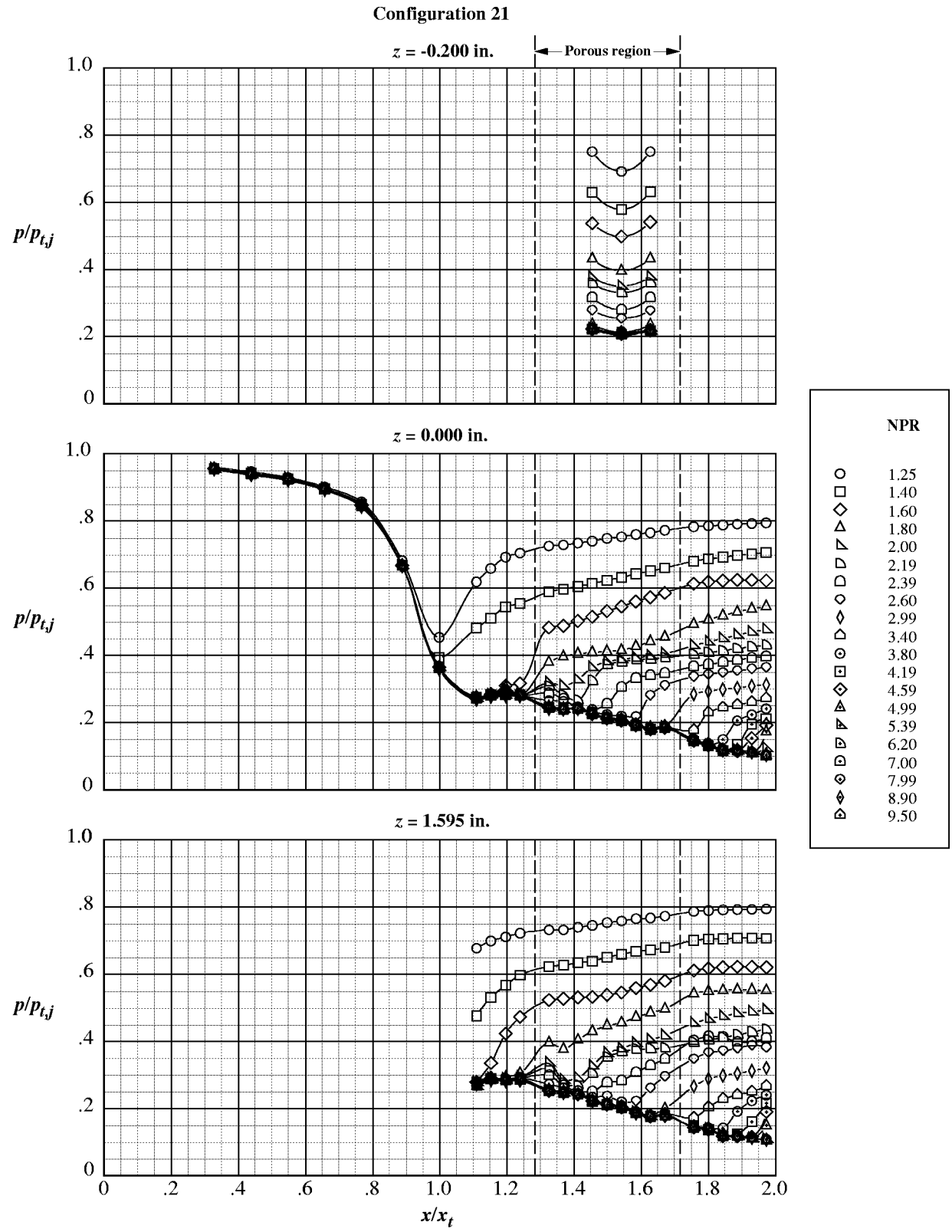


Figure 50. Internal static pressure ratio distributions for porous configuration 21.

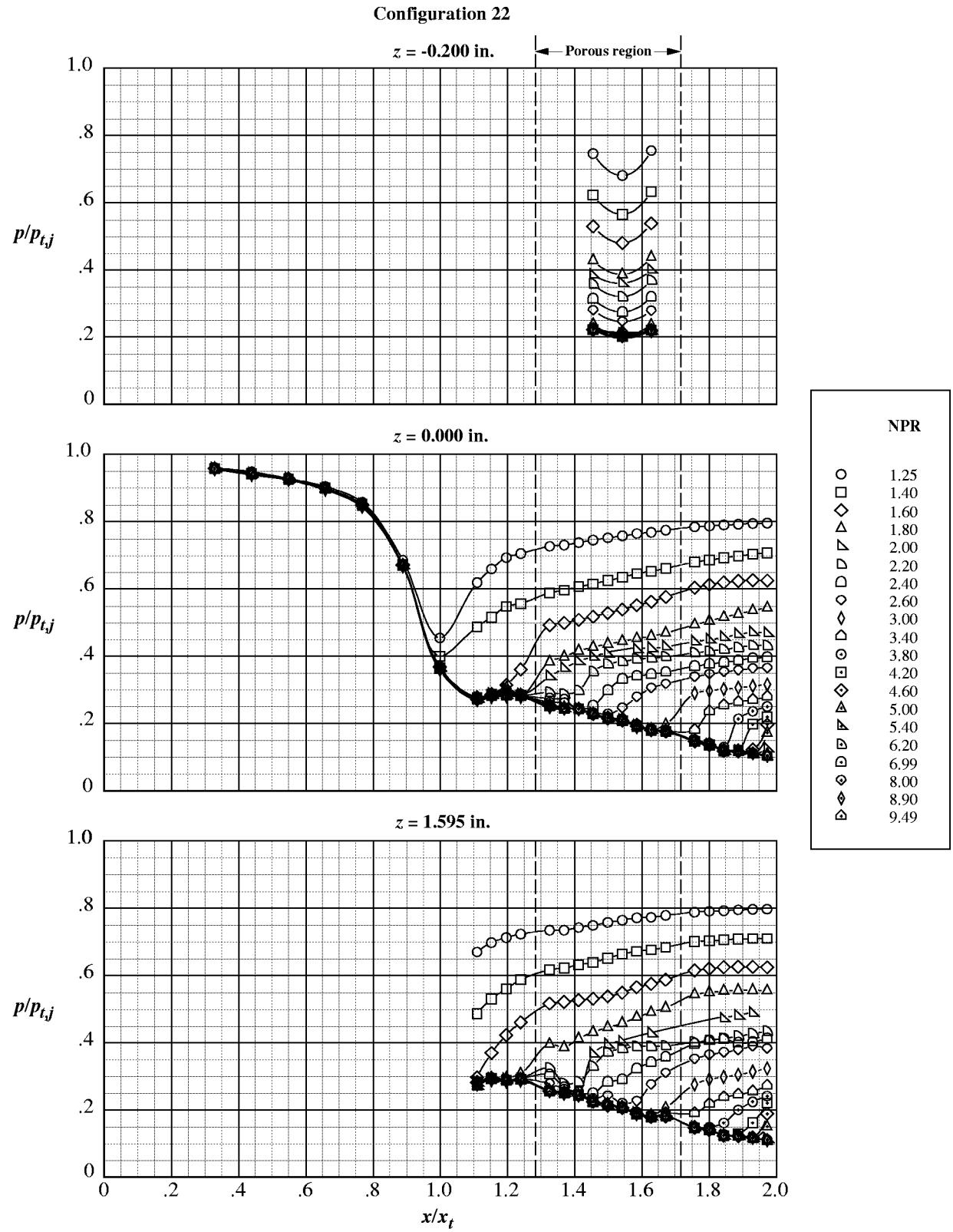


Figure 51. Internal static pressure ratio distributions for porous configuration 22.

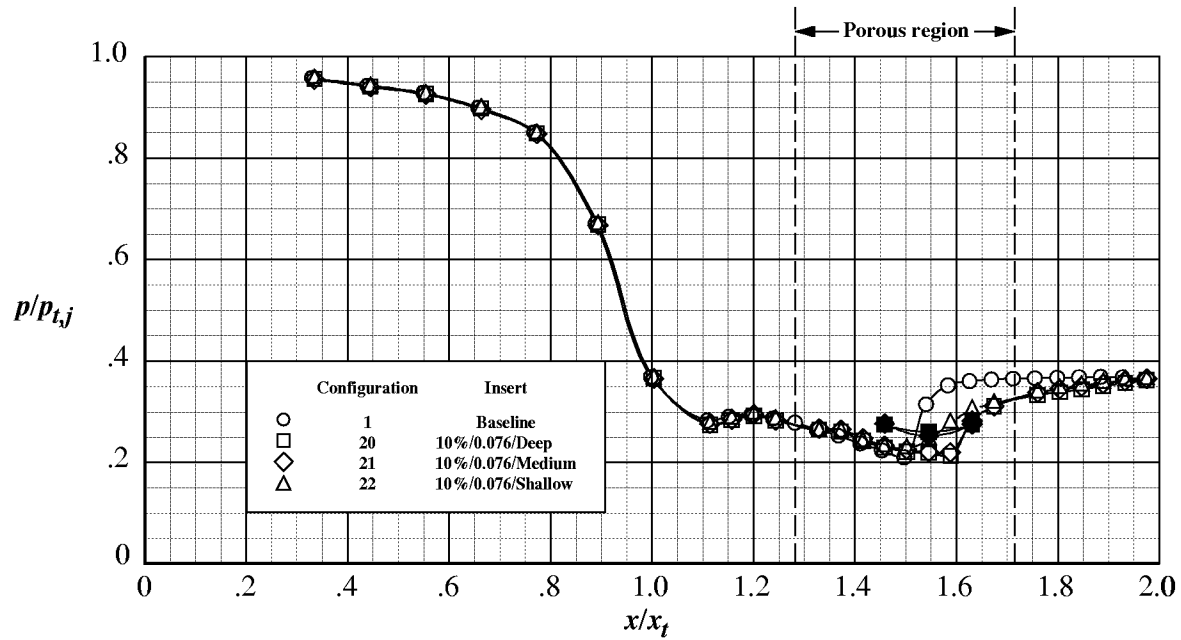
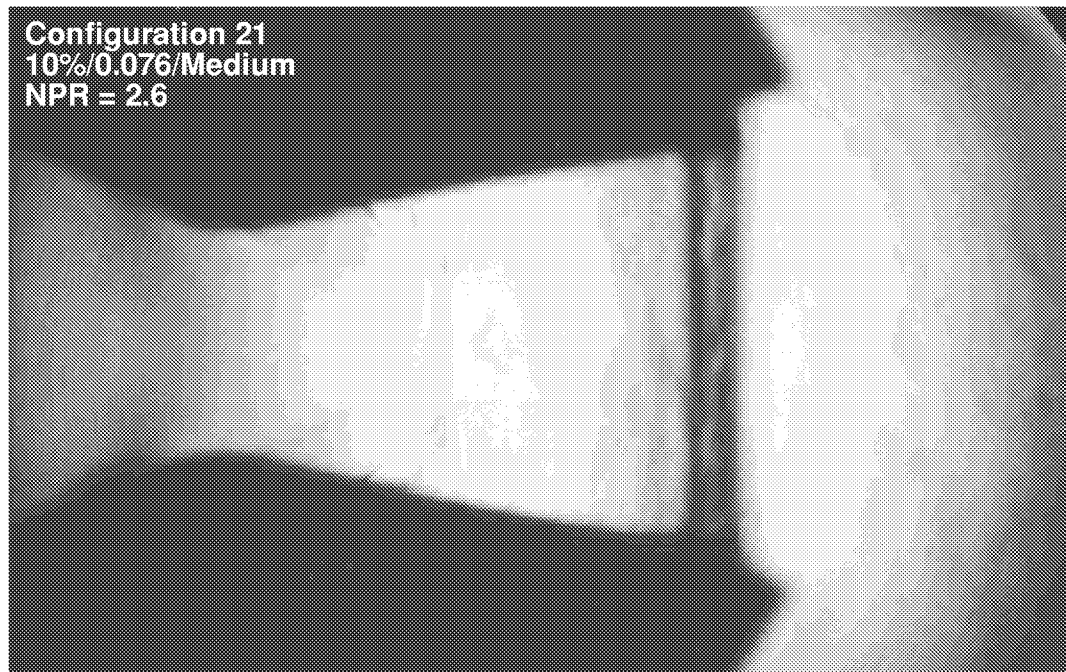
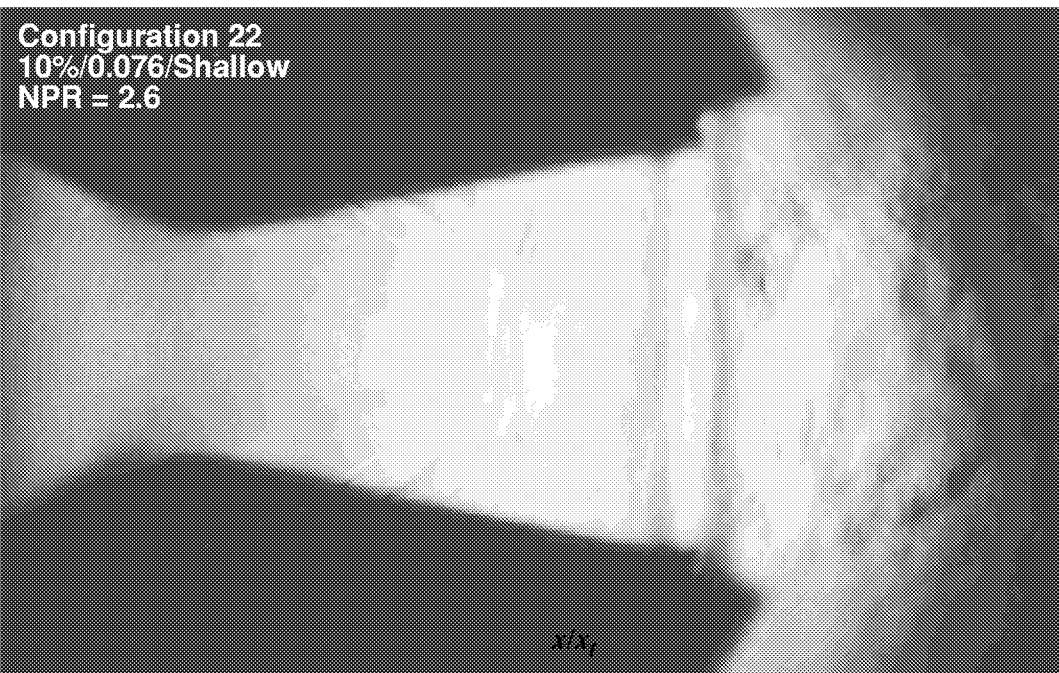


Figure 52. Effect of cavity depth on internal static pressure ratio distributions for porous configurations 20, 21, and 22 at nominal NPR = 2.60. Open symbols denote centerline (surface) pressures; solid symbols denote cavity pressures.



(a) Configuration 21.

Figure 53. Focusing schlieren flow visualization for porous configurations 21 and 22 at NPR = 2.6.



(b) Configuration 22.

Figure 53. Concluded.

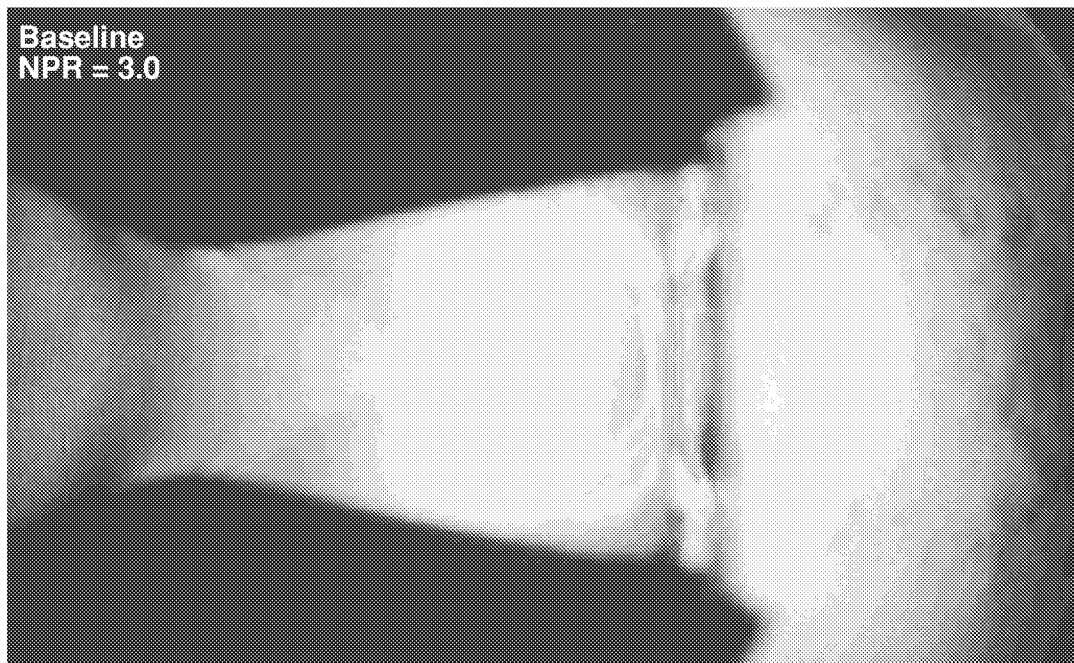


Figure 54. Focusing schlieren flow visualization for the baseline configuration at NPR = 3.0.

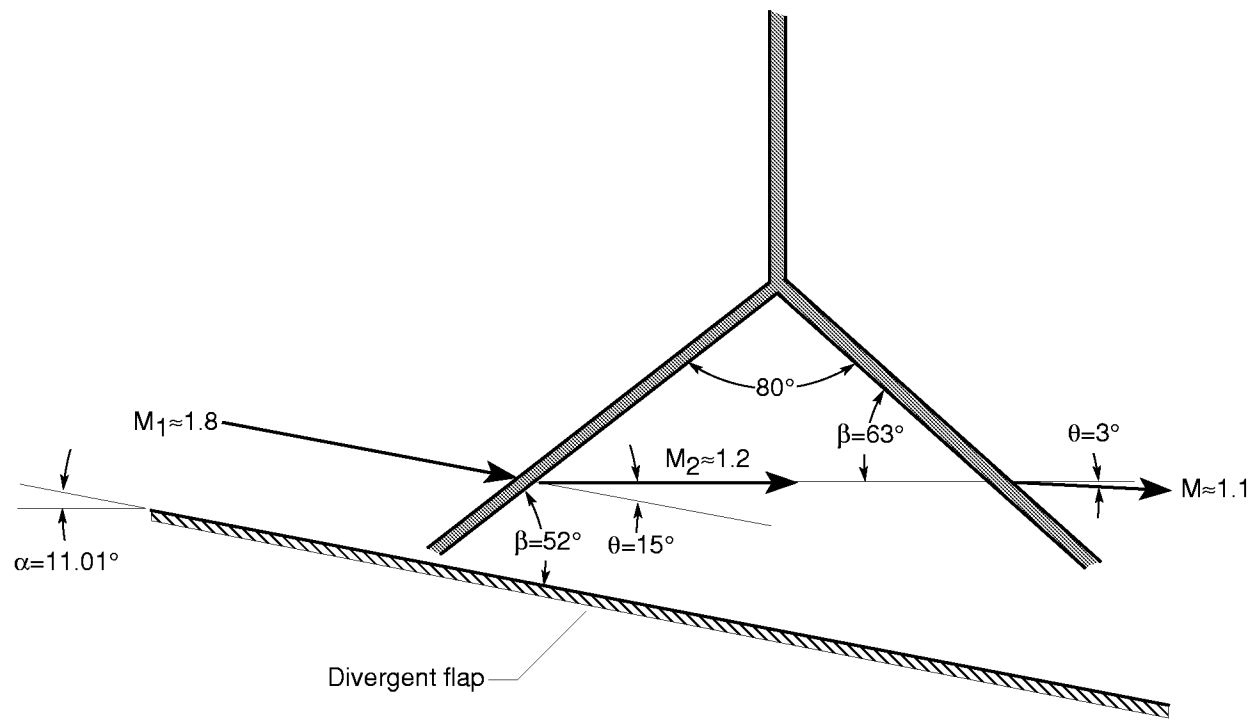


Figure 55. Sketch showing shock-boundary layer interaction lambda foot structure at $NPR = 3.0$ for the baseline configuration.

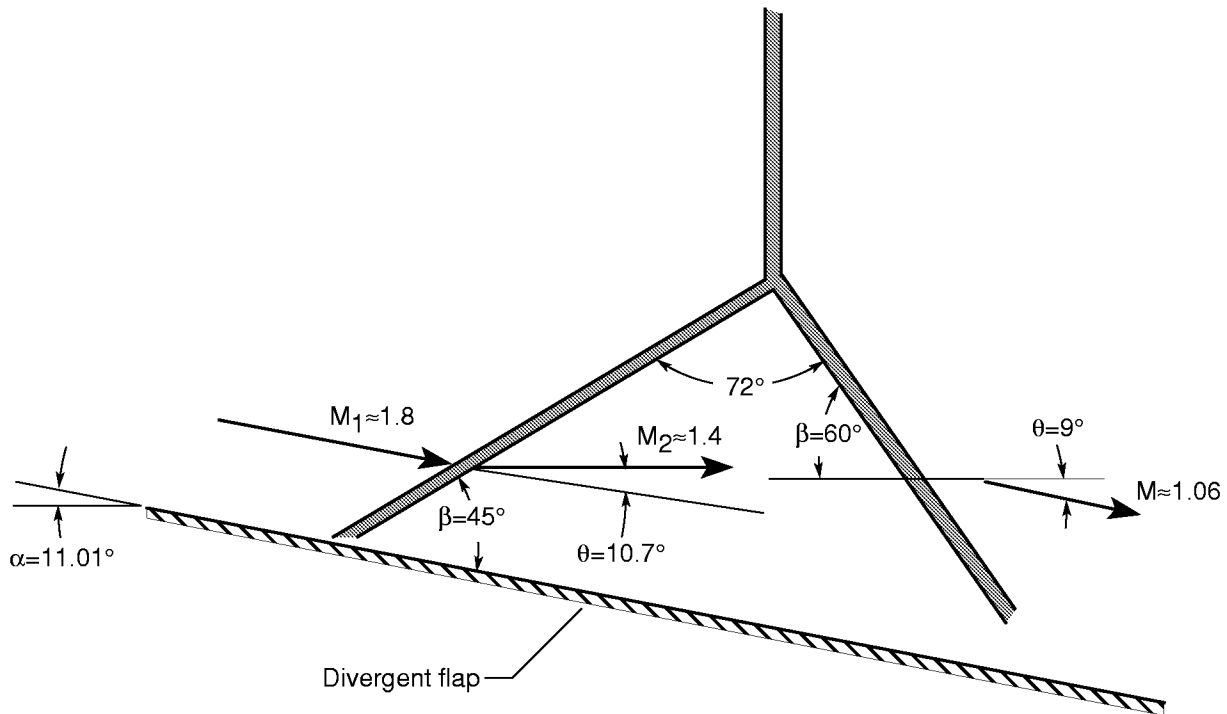


Figure 56. Sketch showing shock-boundary layer interaction lambda foot structure at $NPR = 2.6$ for the configuration 20.

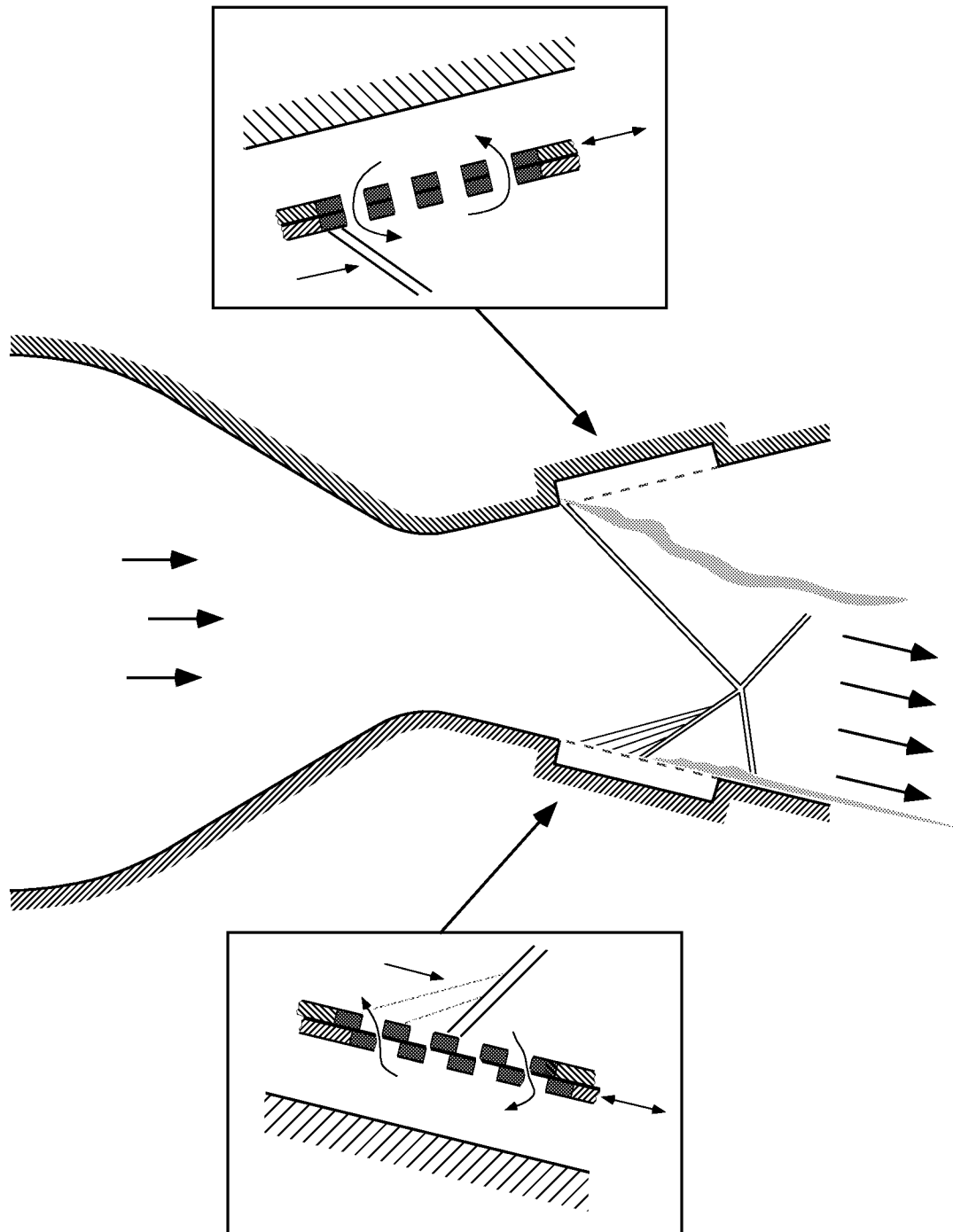


Figure 57. Sketch showing sliding plate variable porosity nozzle concept.

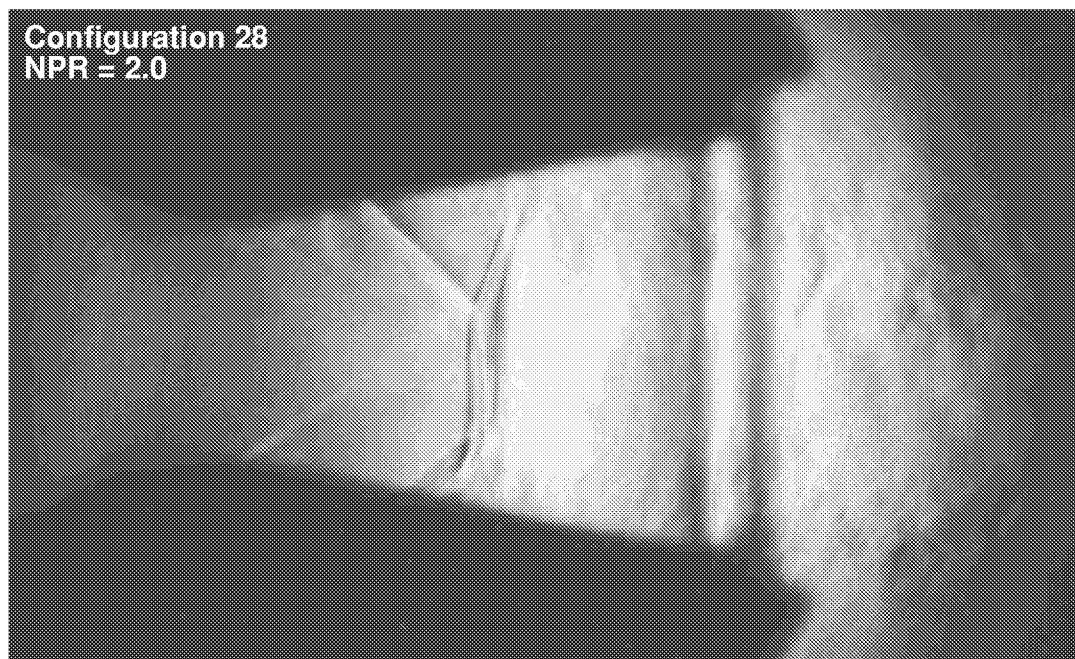
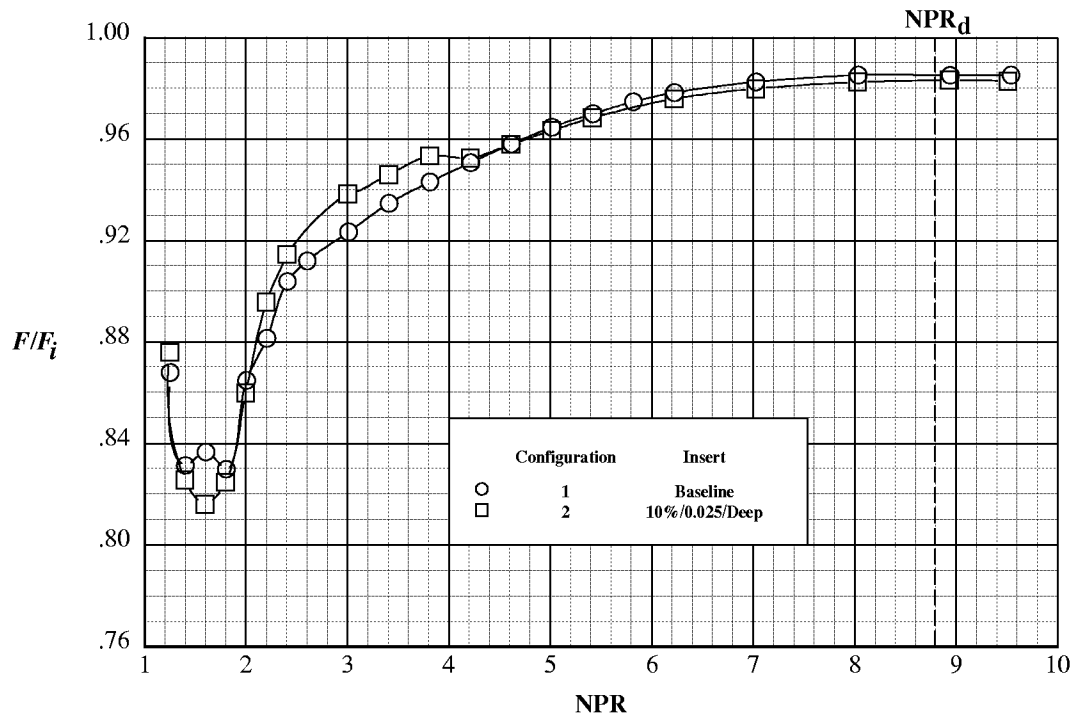
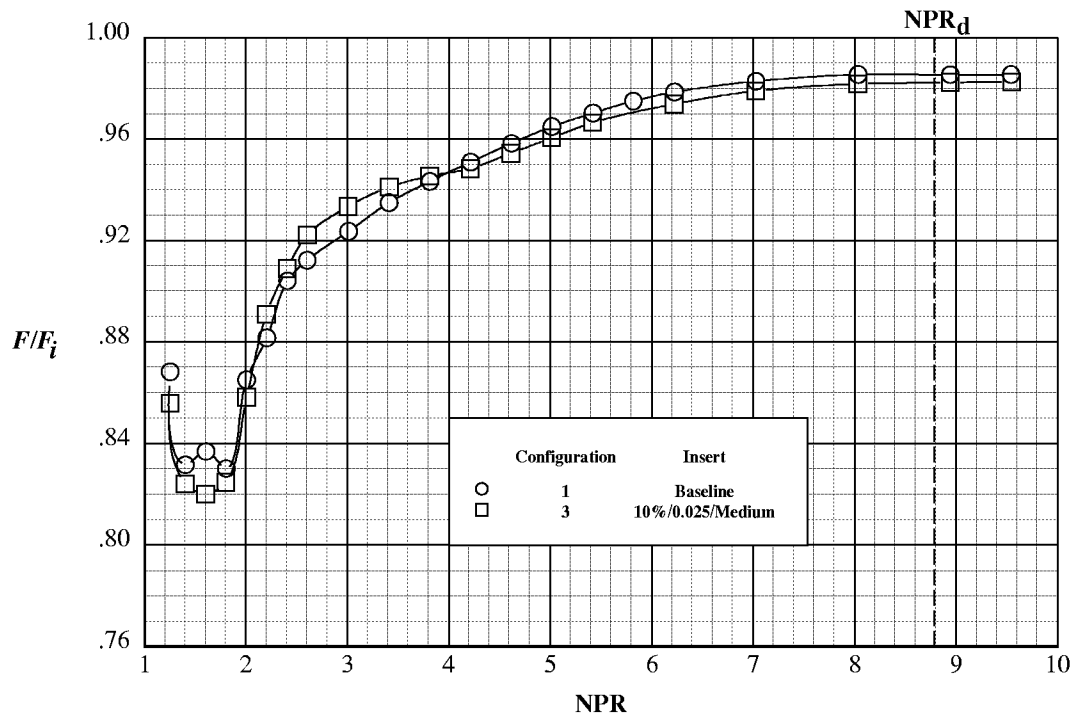


Figure 58. Focusing schlieren flow visualization at $\text{NPR} = 2.0$ showing thrust vectoring capability of the porous nozzle concept.

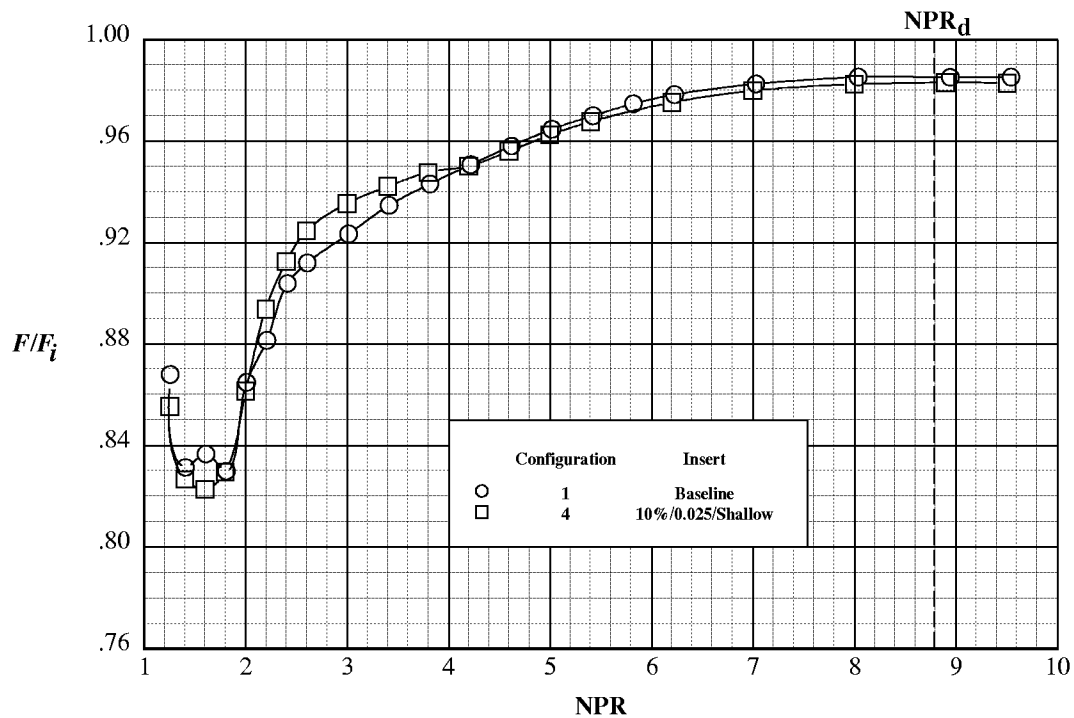


(a) 10% porosity, $d = 0.025$ in., deep cavity.

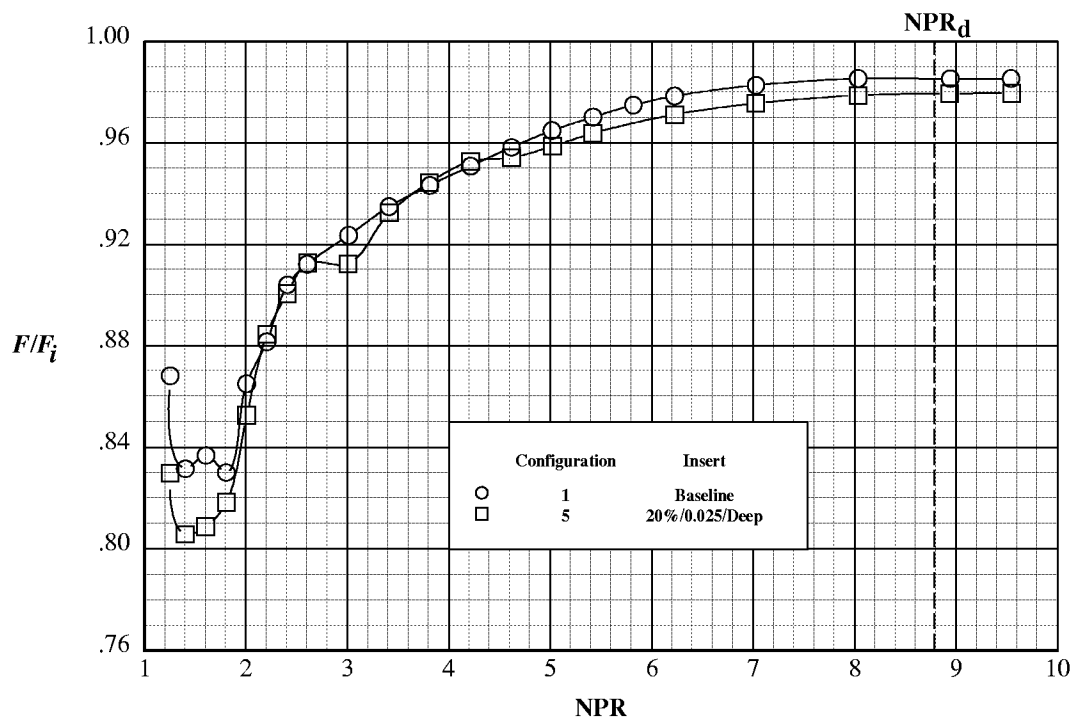


(b) 10% porosity, $d = 0.025$ in., medium cavity.

Figure 59. Comparison of nozzle thrust efficiency performance for baseline and porous configurations.

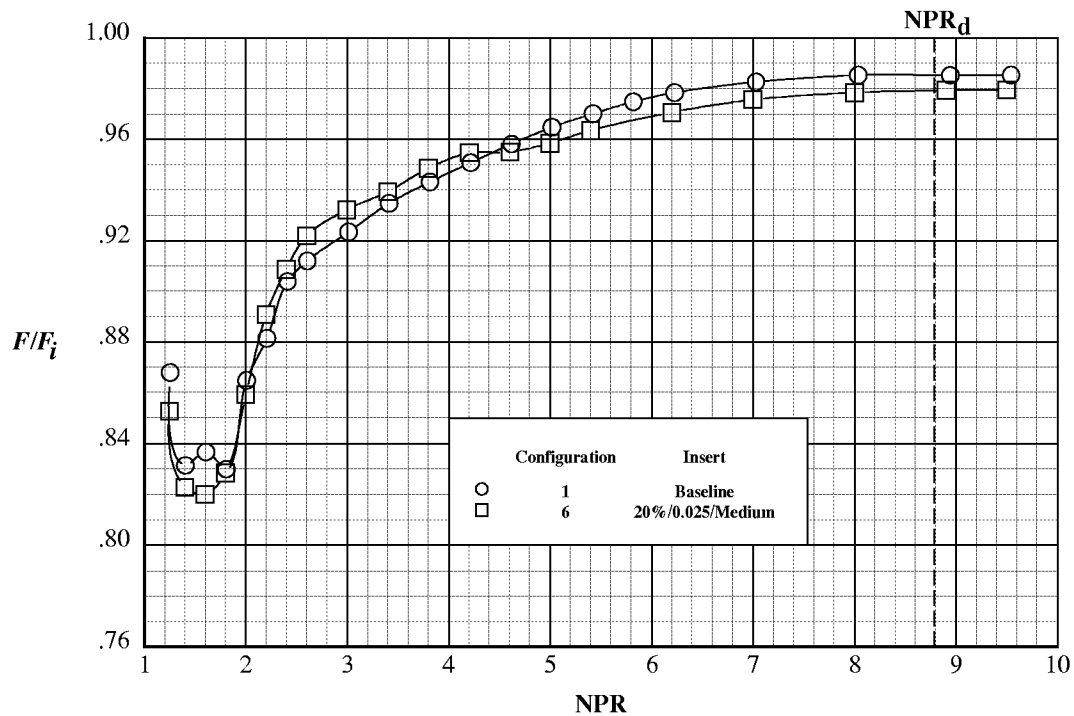


(c) 10% porosity, $d = 0.025$ in., shallow cavity.

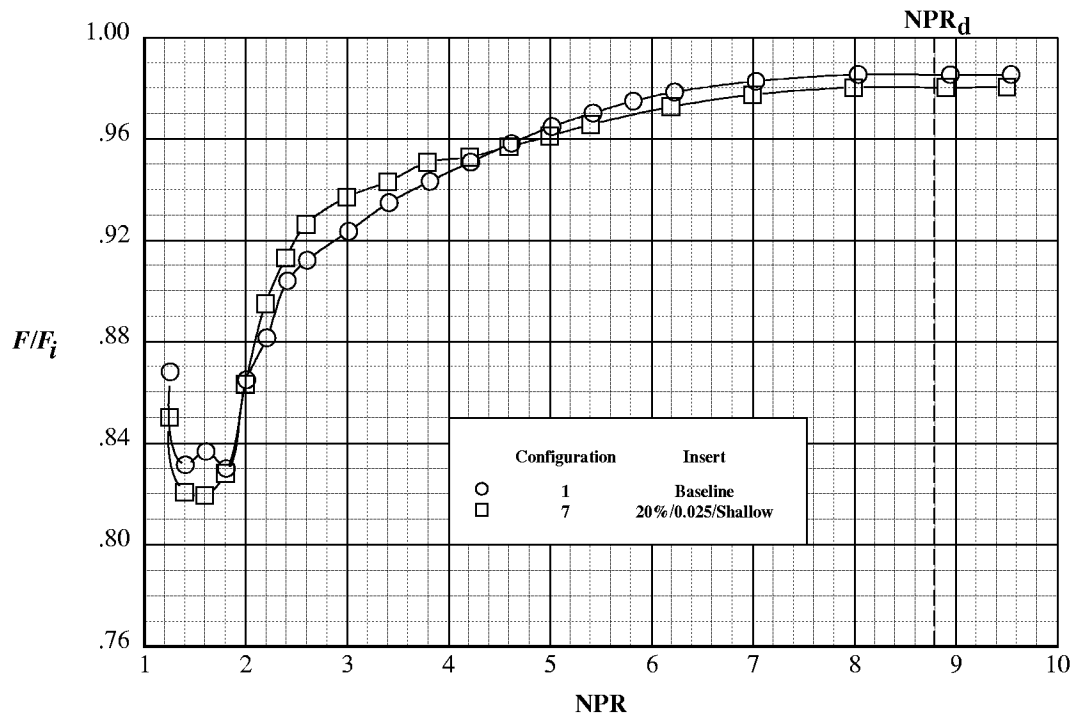


(d) 20% porosity, $d = 0.025$ in., deep cavity.

Figure 59. Continued.

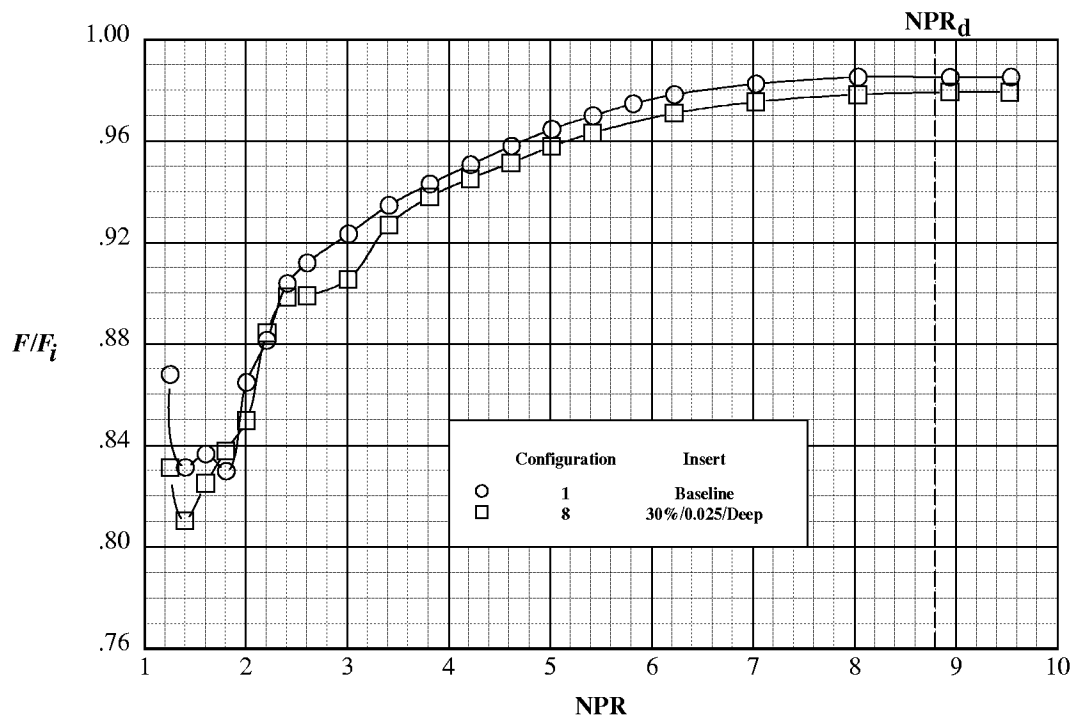


(e) 20% porosity, $d = 0.025$ in., medium cavity.

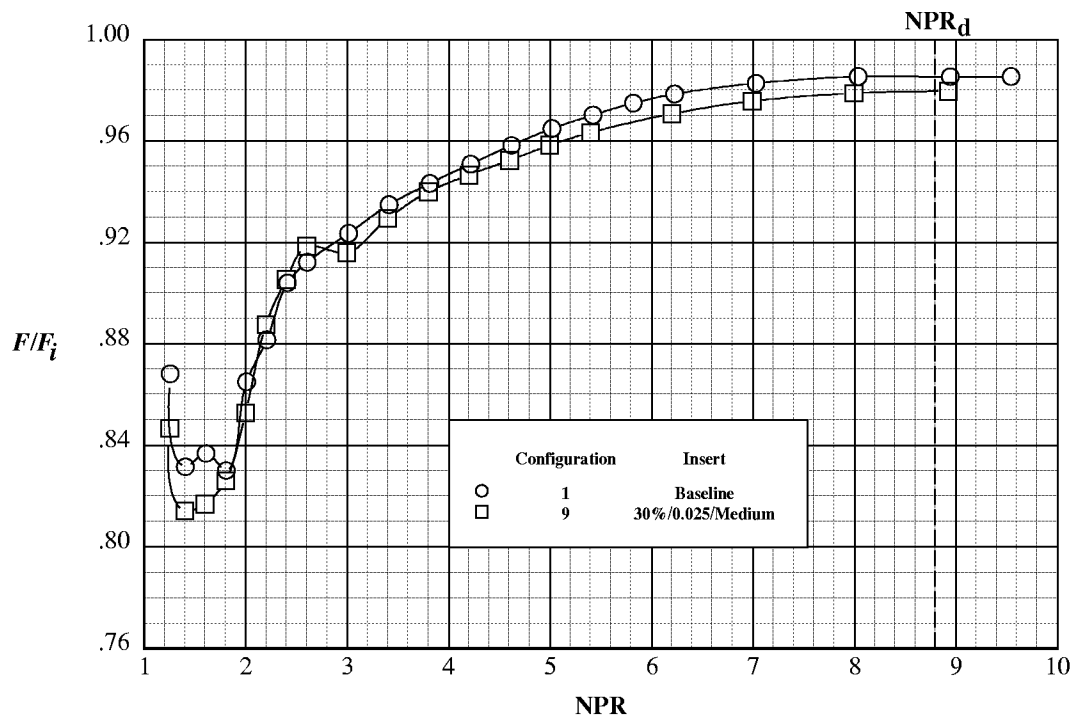


(f) 20% porosity, $d = 0.025$ in., shallow cavity.

Figure 59. Continued.



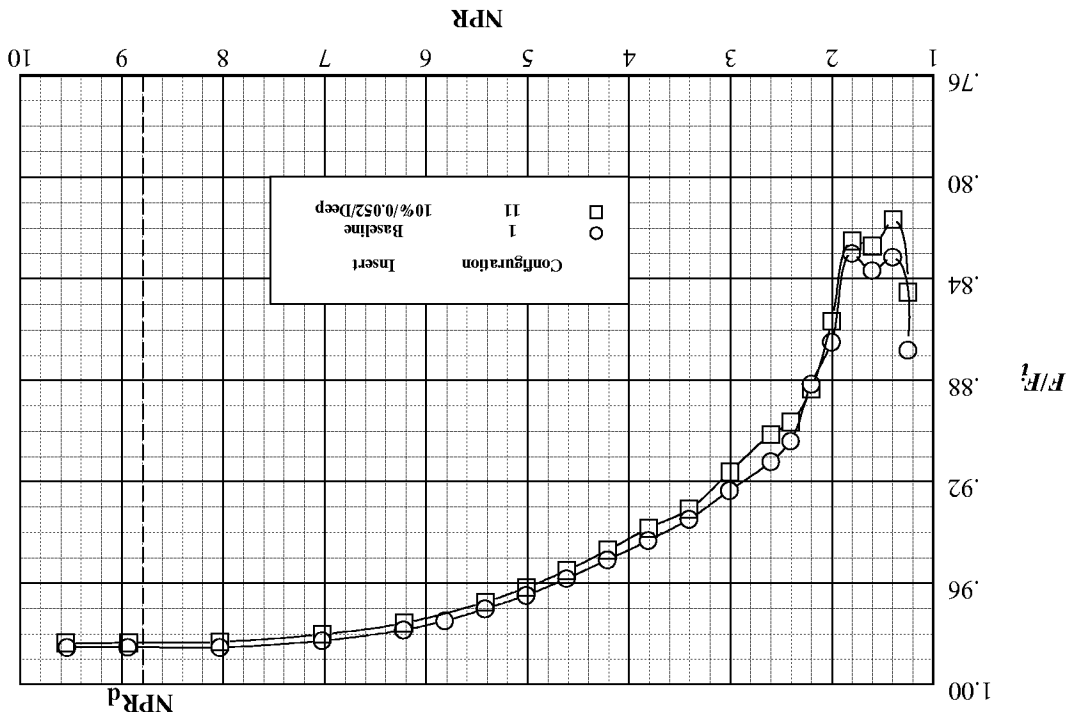
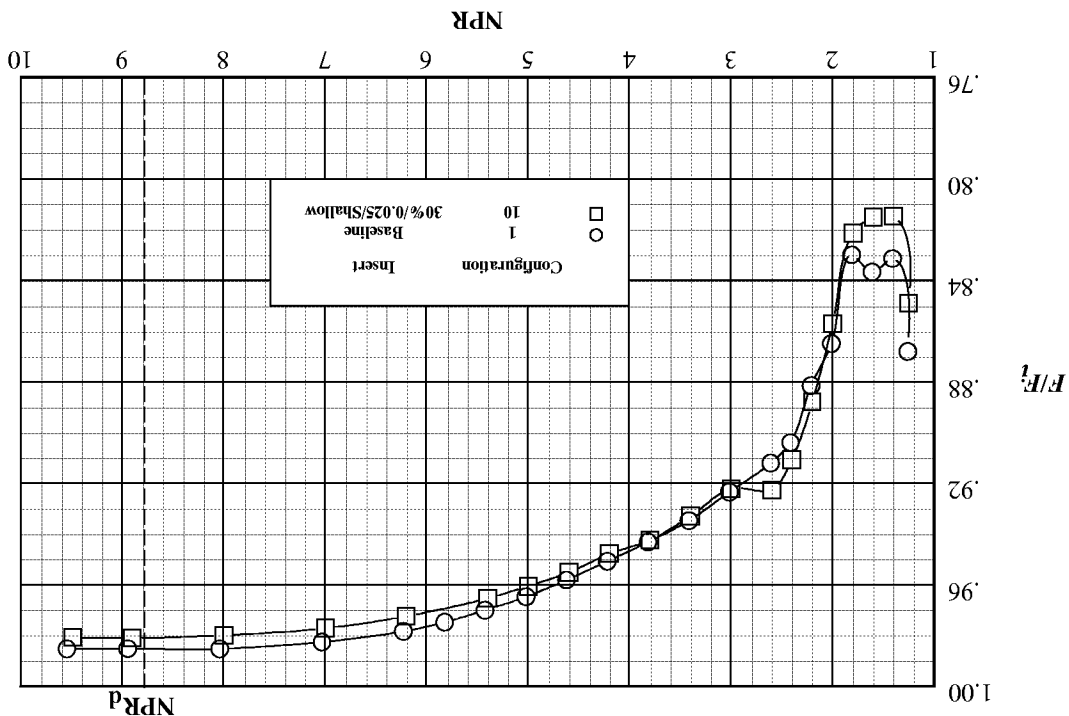
(g) 30% porosity, $d = 0.025$ in., deep cavity.

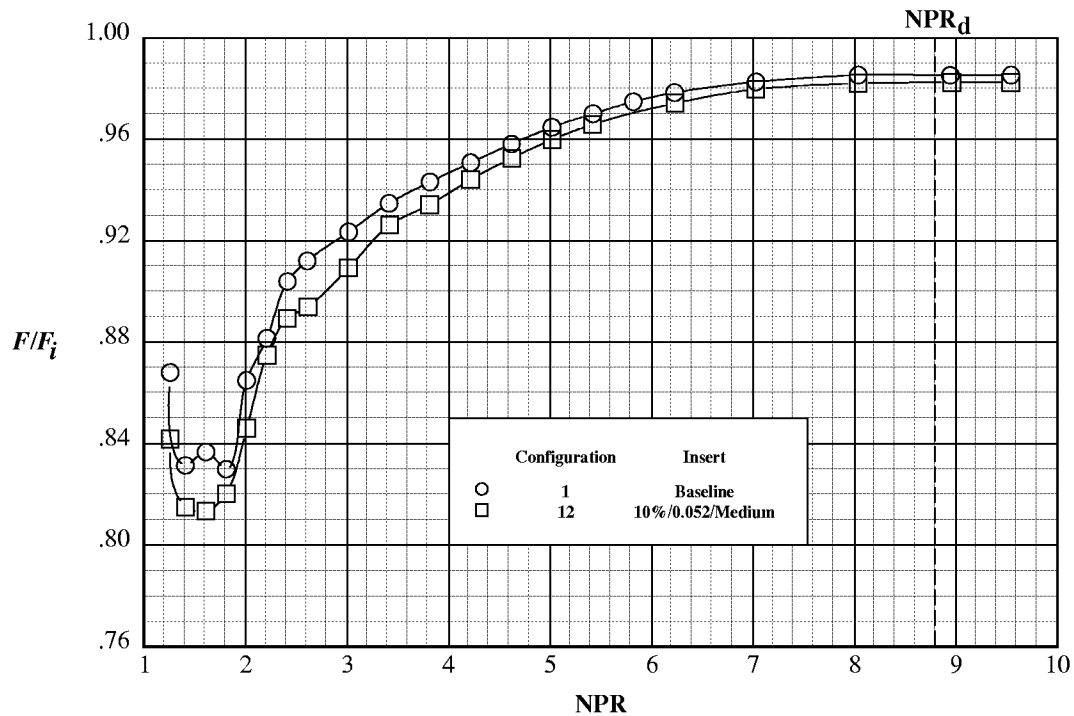


(h) 30% porosity, $d = 0.025$ in., medium cavity.

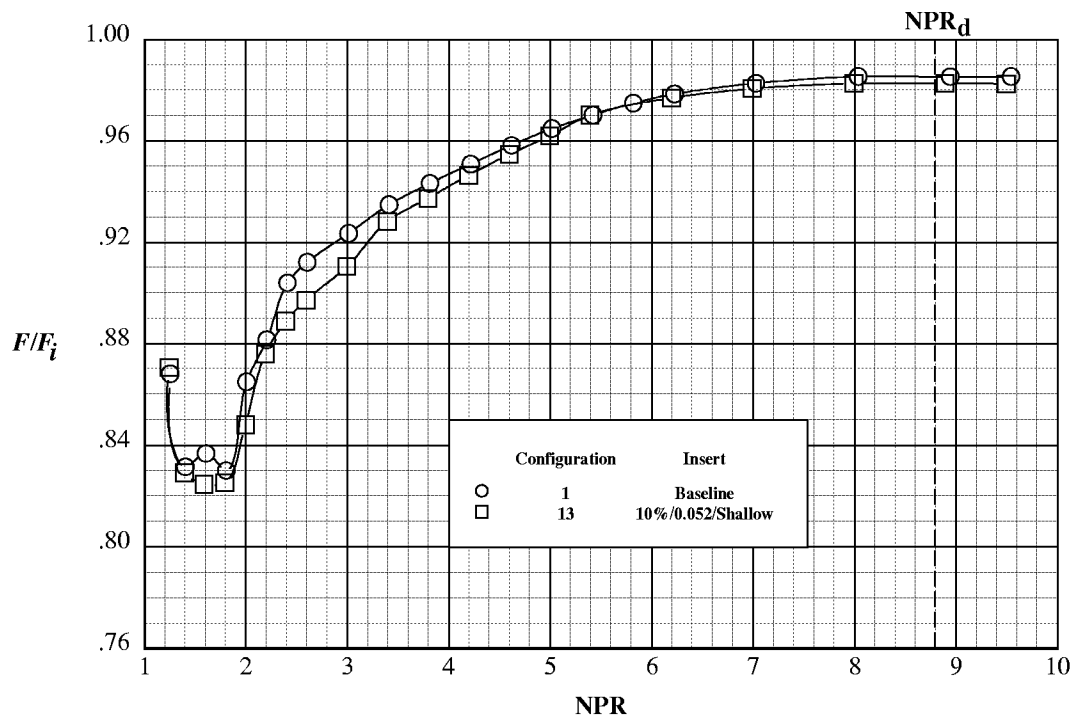
Figure 59. Continued.

Figure 59. Continued.

(j) 10% porosity, $d = 0.052$ m, deep cavity.(i) 30% porosity, $d = 0.025$ m, shallow cavity.

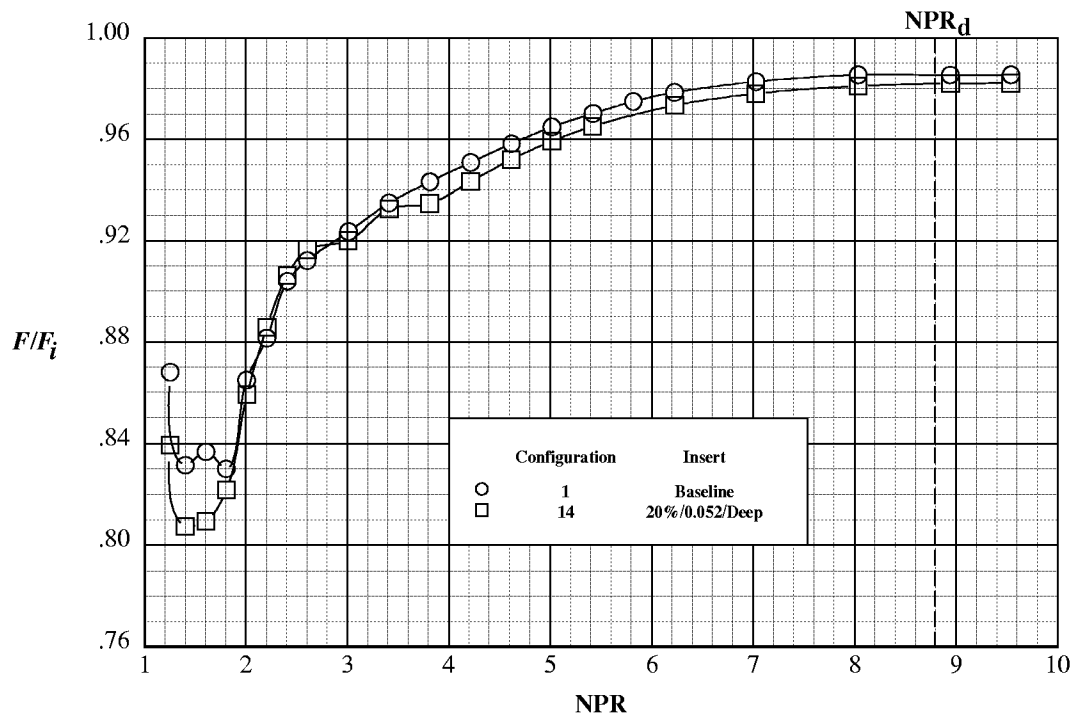


(k) 10% porosity, $d = 0.052$ in., medium cavity.

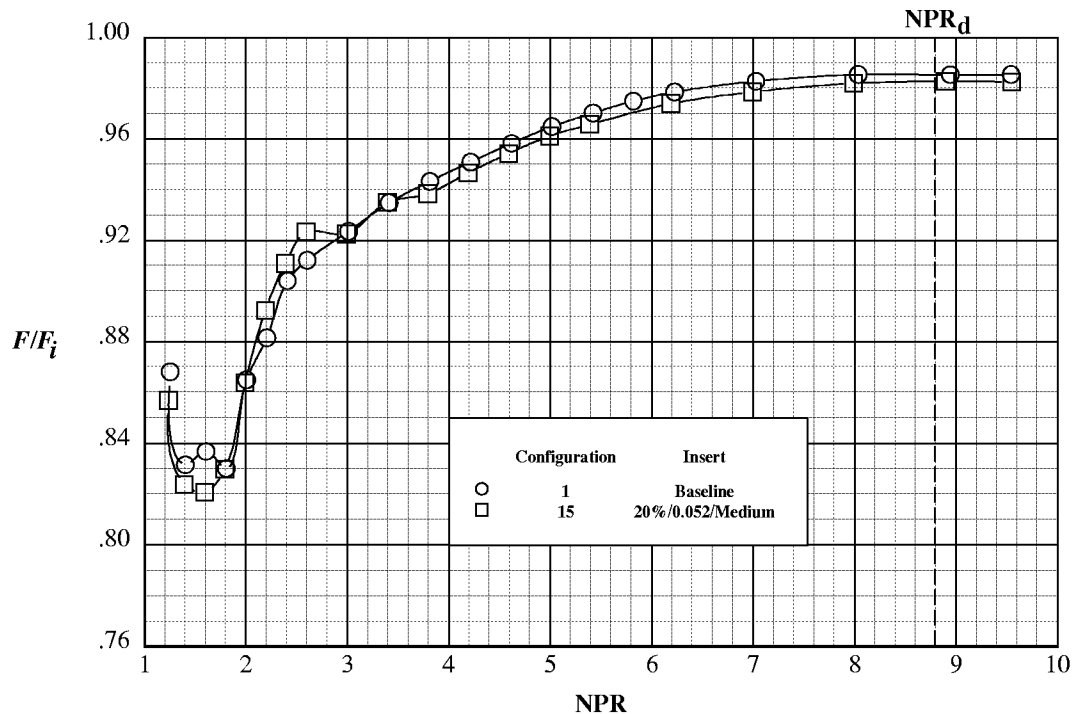


(l) 10% porosity, $d = 0.052$ in., shallow cavity.

Figure 59. Continued.

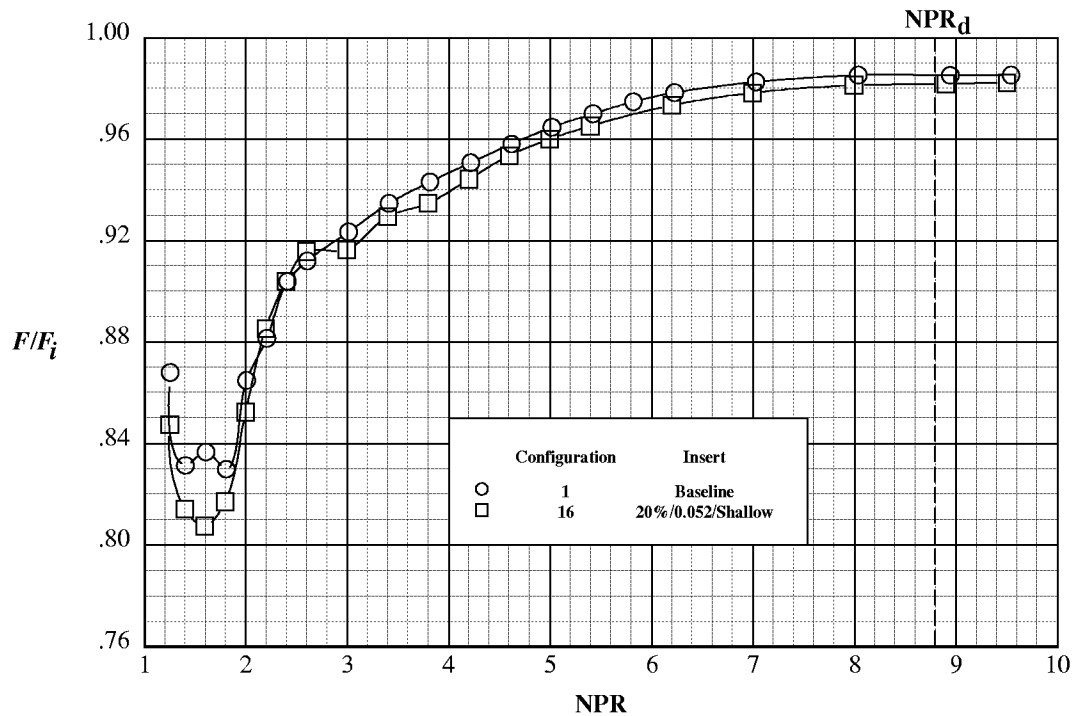


(m) 20% porosity, $d = 0.052$ in., deep cavity.

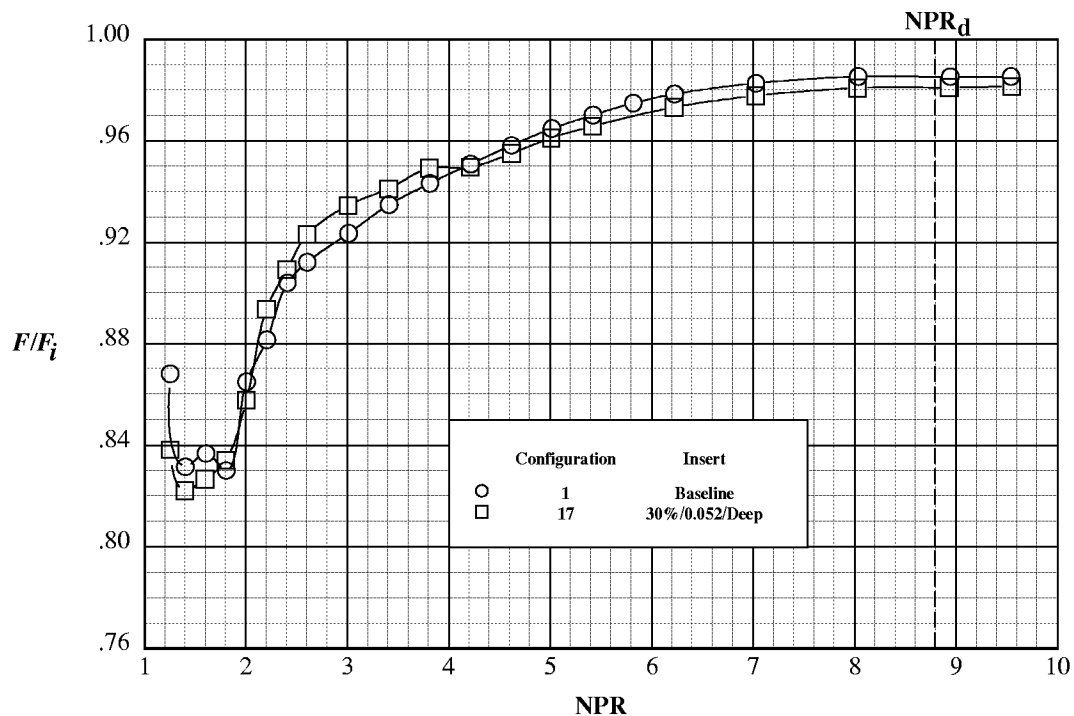


(n) 20% porosity, $d = 0.052$ in., medium cavity.

Figure 59. Continued.

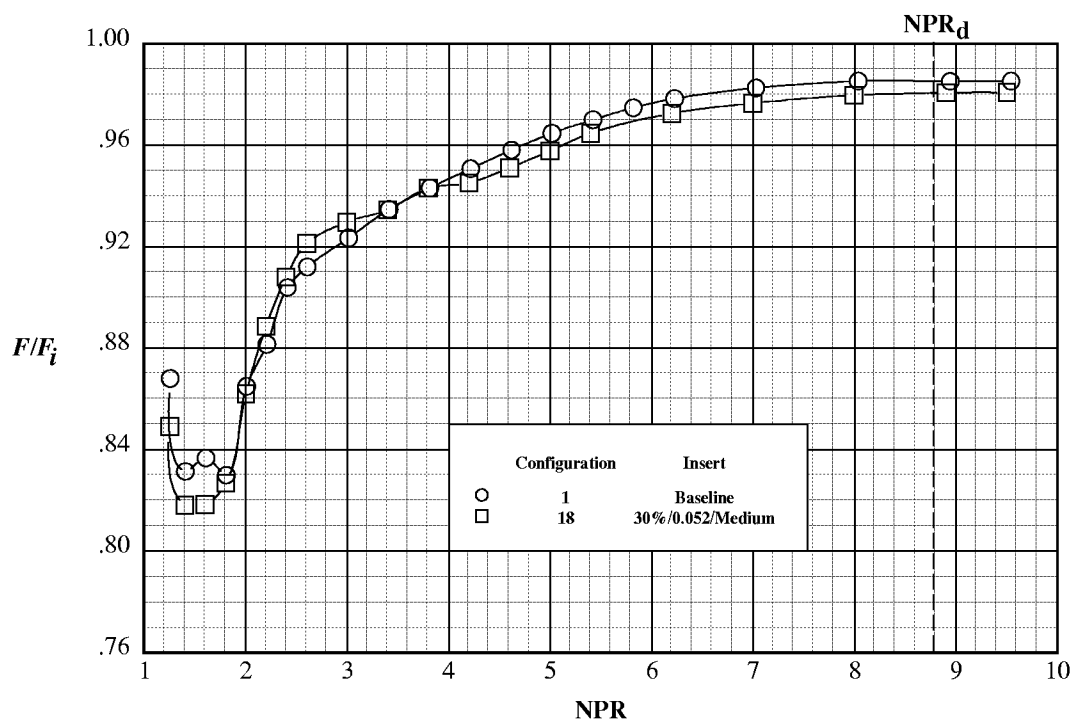


(o) 20% porosity, $d = 0.052$ in., shallow cavity.

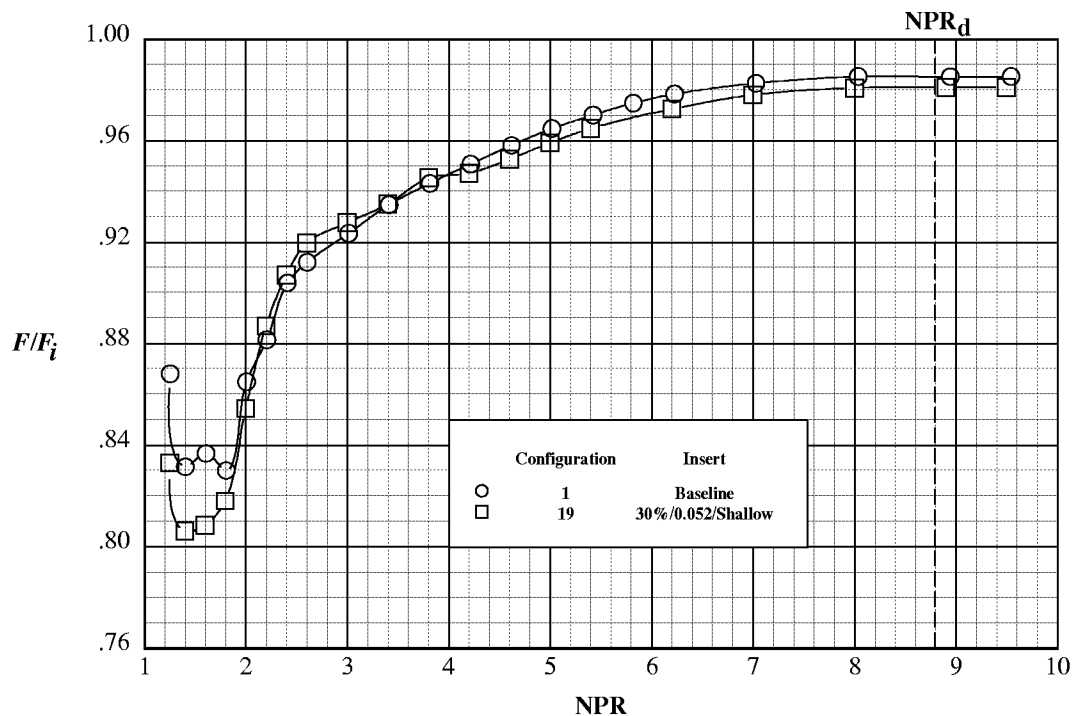


(p) 30% porosity, $d = 0.052$ in., deep cavity.

Figure 59. Continued.

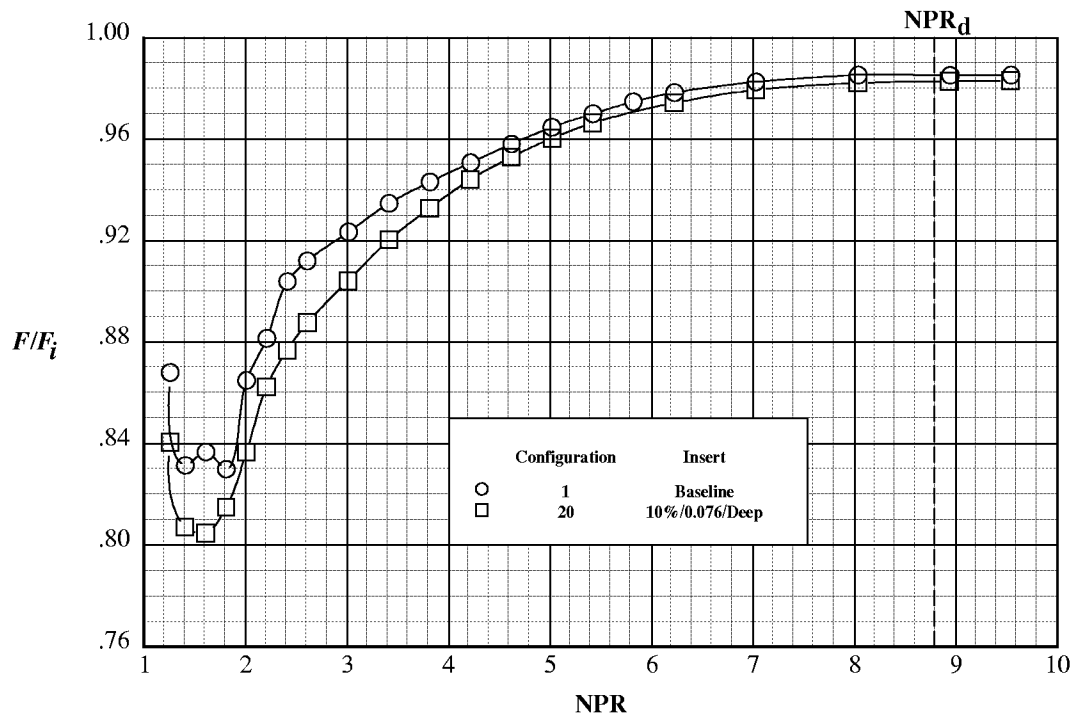


(q) 30% porosity, $d = 0.052$ in., medium cavity.

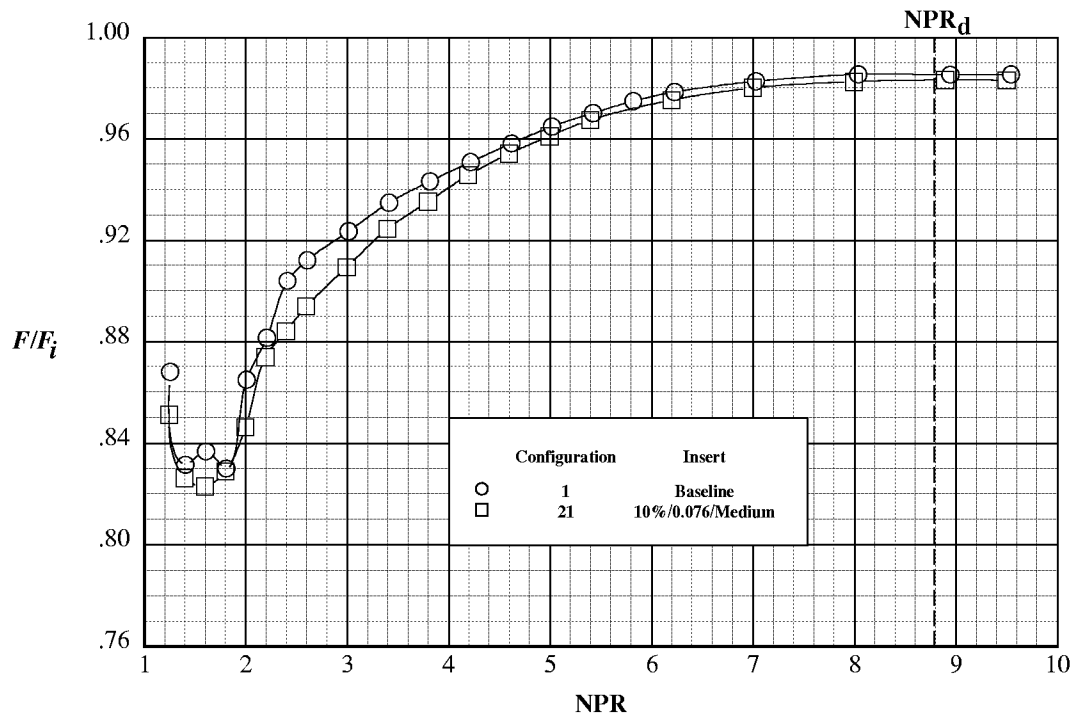


(r) 30% porosity, $d = 0.052$ in., shallow cavity.

Figure 59. Continued.

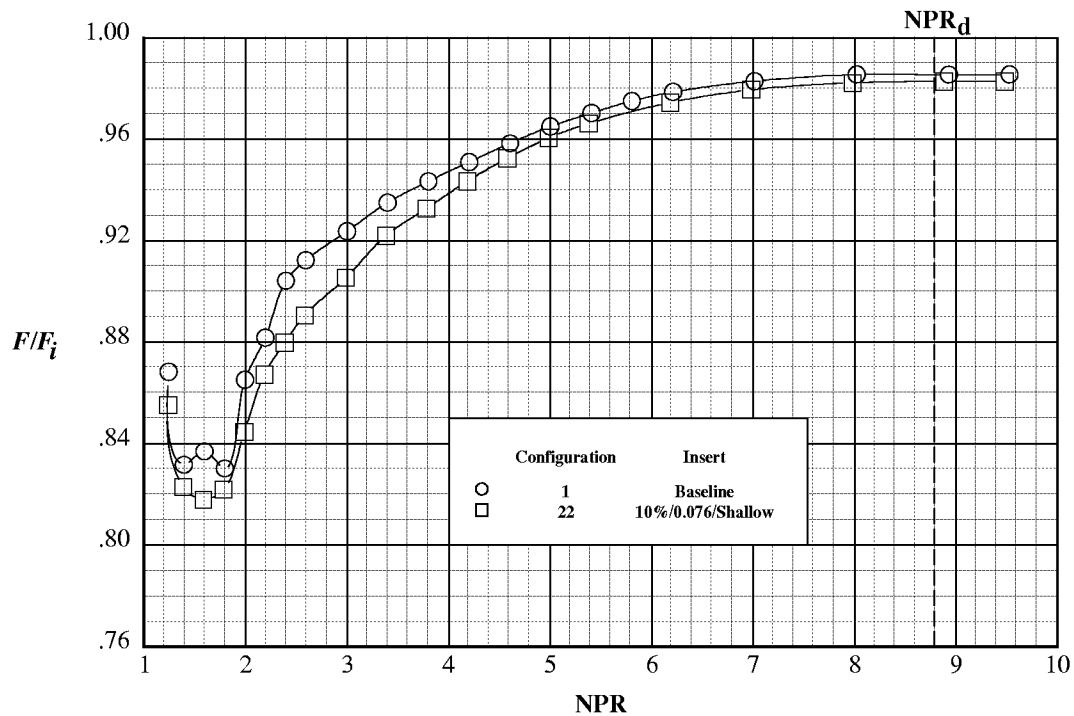


(s) 10% porosity, $d = 0.076$ in., deep cavity.

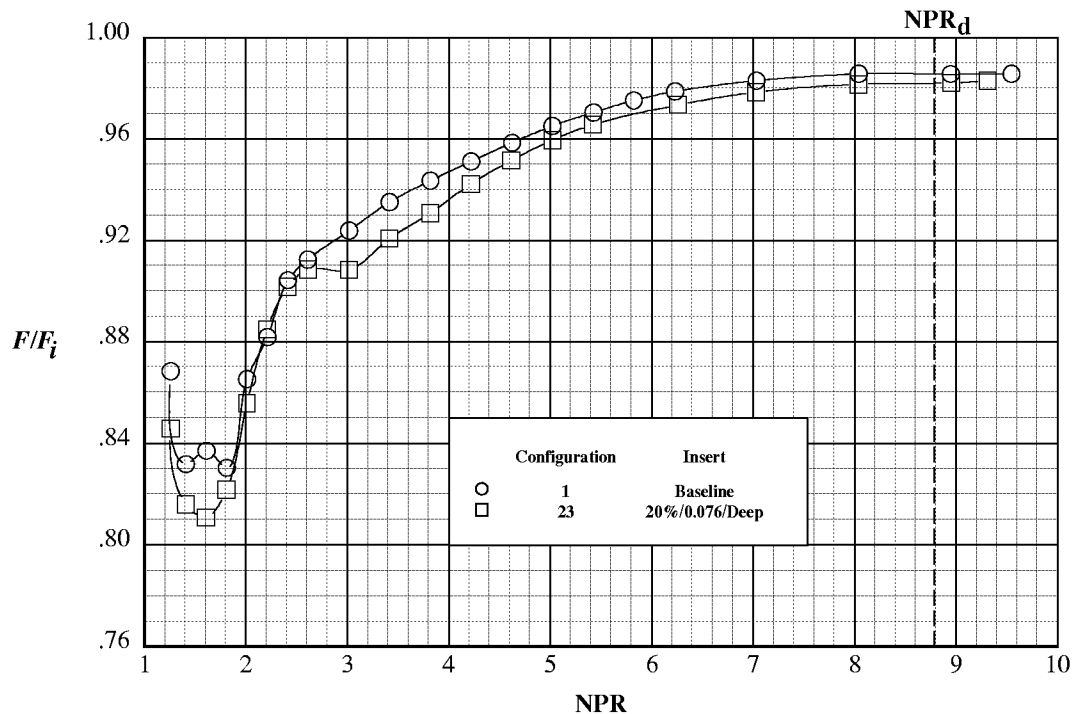


(t) 10% porosity, $d = 0.076$ in., medium cavity.

Figure 59. Continued.

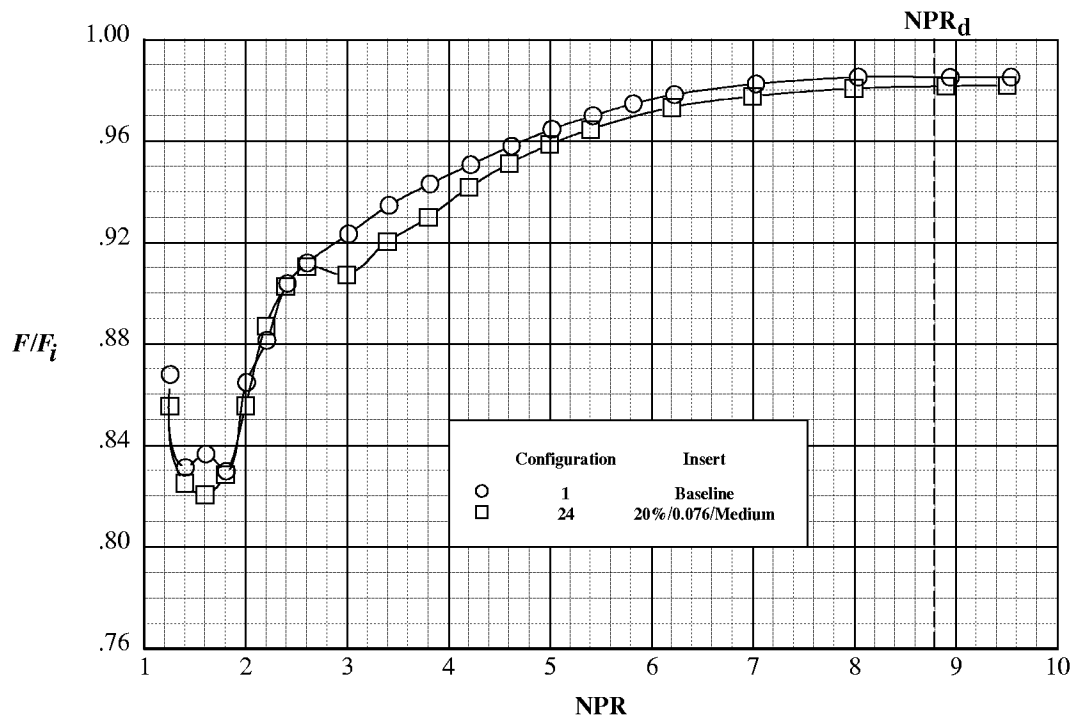


(u) 10% porosity, $d = 0.076$ in., shallow cavity.

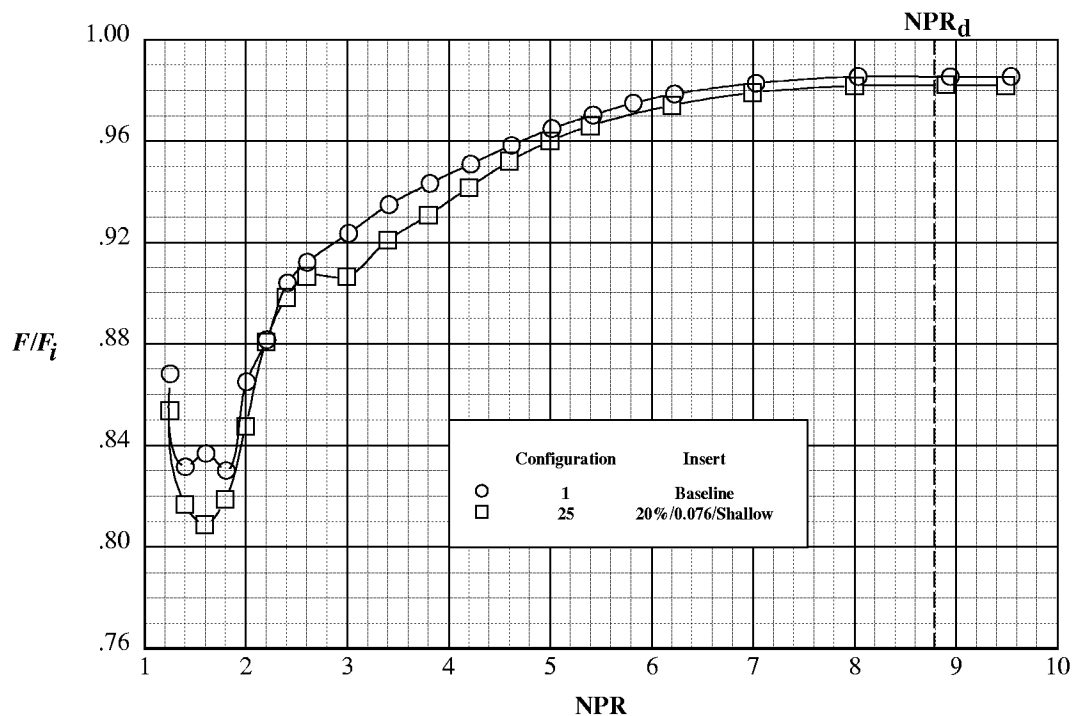


(v) 20% porosity, $d = 0.076$ in., deep cavity.

Figure 59. Continued.

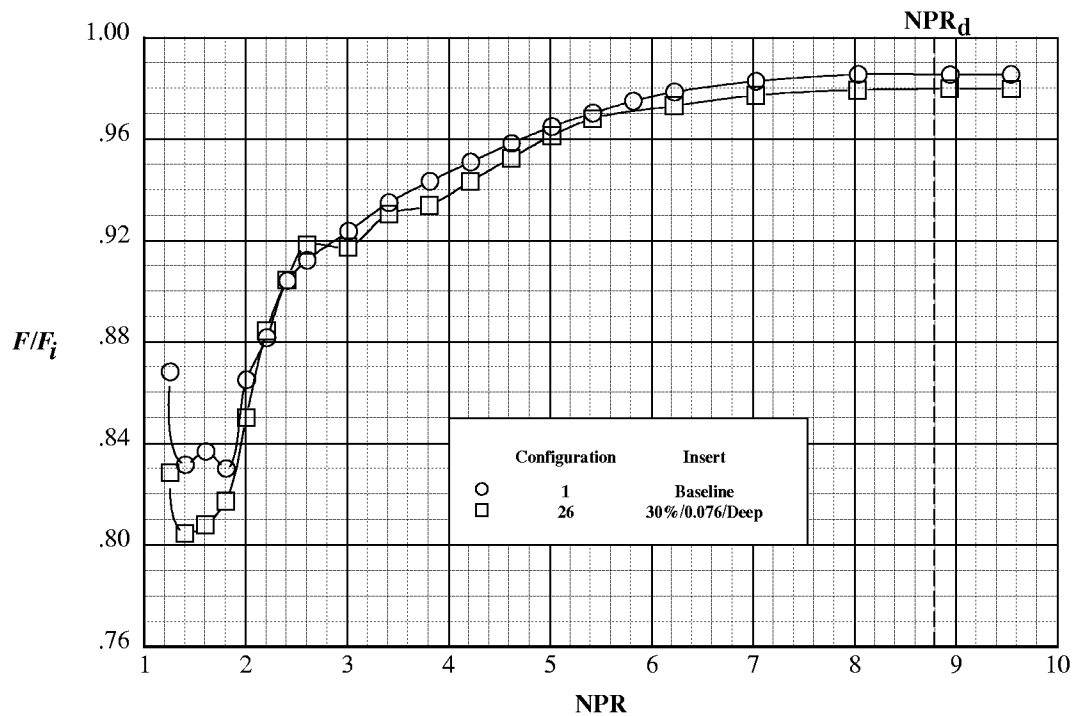


(w) 20% porosity, $d = 0.076$ in., medium cavity.

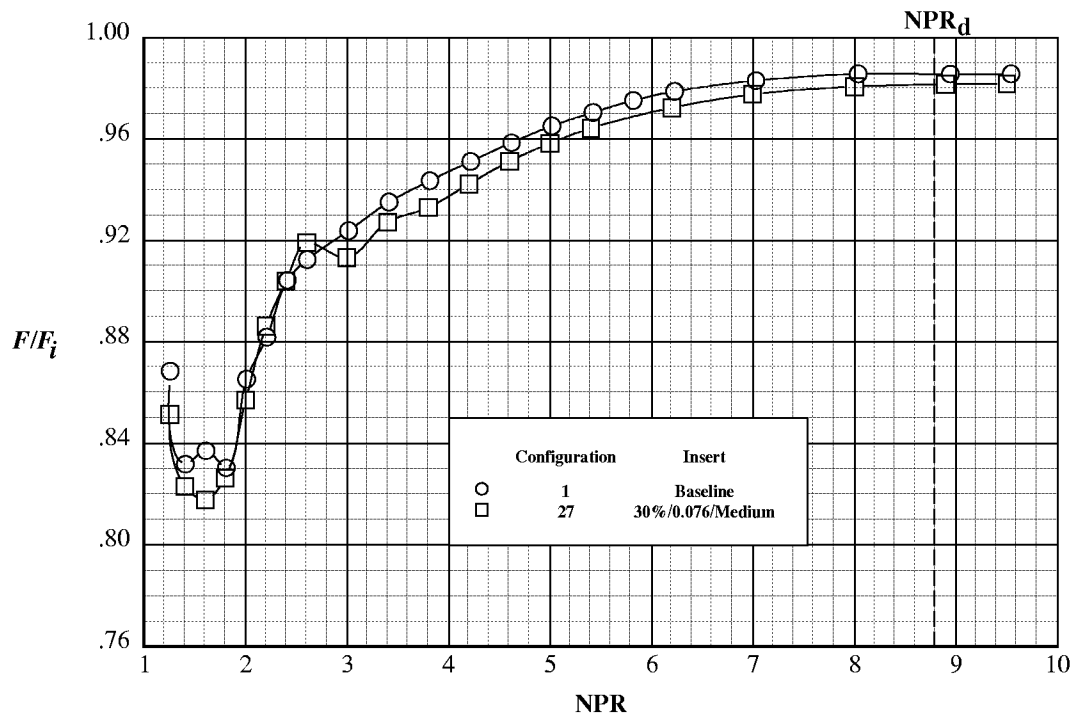


(x) 20% porosity, $d = 0.076$ in., shallow cavity.

Figure 59. Continued.

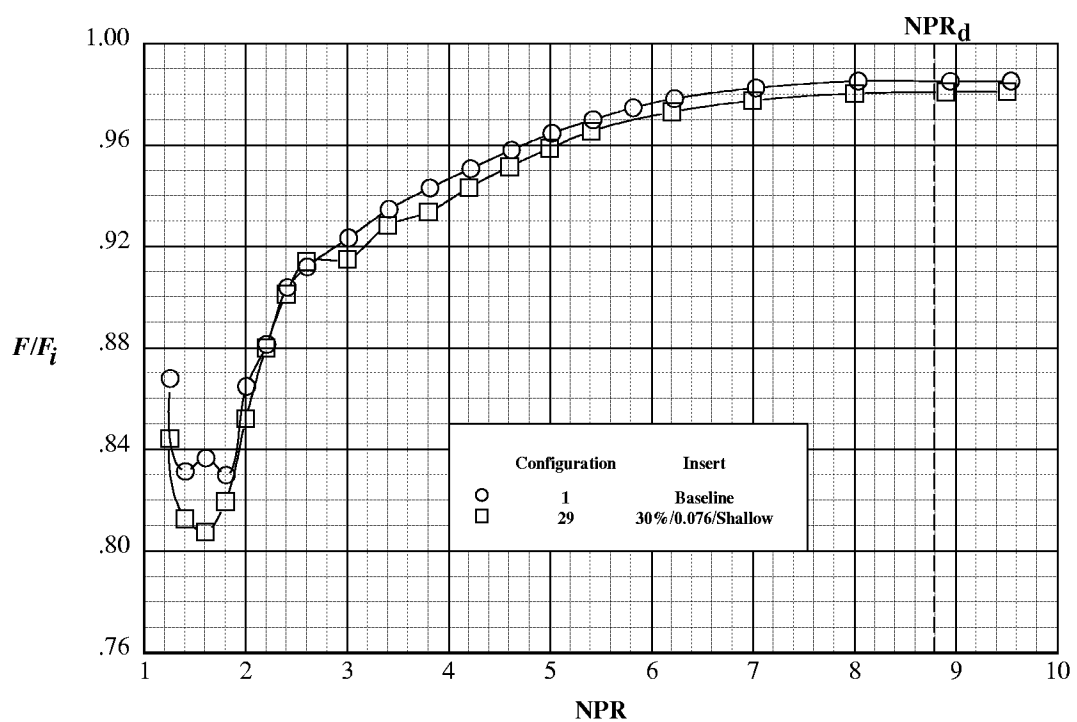


(y) 30% porosity, $d = 0.076$ in., deep cavity.



(z) 30% porosity, $d = 0.076$ in., medium cavity.

Figure 59. Continued.



(aa) 30% porosity, $d = 0.076$ in., shallow cavity.

Figure 59. Concluded.

REPORT DOCUMENTATION PAGE			Form Approved OMB No. 0704-0188
<p>Public reporting burden for this collection of information is estimated to average 1 hour per response, including the time for reviewing instructions, searching existing data sources, gathering and maintaining the data needed, and completing and reviewing the collection of information. Send comments regarding this burden estimate or any other aspect of this collection of information, including suggestions for reducing this burden, to Washington Headquarters Services, Directorate for Information Operations and Reports, 1215 Jefferson Davis Highway, Suite 1204, Arlington, VA 22202-4302, and to the Office of Management and Budget, Paperwork Reduction Project (0704-0188), Washington, DC 20503.</p>			
1. AGENCY USE ONLY (Leave blank)	2. REPORT DATE	3. REPORT TYPE AND DATES COVERED	
	August 1999	Technical Memorandum	
4. TITLE AND SUBTITLE		5. FUNDING NUMBERS	
Static Performance of a Fixed-Geometry Exhaust Nozzle Incorporating Porous Cavities for Shock-Boundary Layer Interaction Control		WU 538-14-12-01	
6. AUTHOR(S)			
Scott C. Asbury and Craig A. Hunter			
7. PERFORMING ORGANIZATION NAME(S) AND ADDRESS(ES)		8. PERFORMING ORGANIZATION REPORT NUMBER	
NASA Langley Research Center Hampton, VA 23681-2199		L-17879	
9. SPONSORING/MONITORING AGENCY NAME(S) AND ADDRESS(ES)		10. SPONSORING/MONITORING AGENCY REPORT NUMBER	
National Aeronautics and Space Administration Washington, DC 20546-0001		NASA/TM-1999-209513	
11. SUPPLEMENTARY NOTES			
12a. DISTRIBUTION/AVAILABILITY STATEMENT		12b. DISTRIBUTION CODE	
Unclassified-Unlimited Subject Category 02 Distribution: Standard Availability: NASA CASI (301) 621-0390			
13. ABSTRACT (Maximum 200 words)			
<p>An investigation was conducted in the model preparation area of the Langley 16-Foot Transonic Tunnel to determine the internal performance of a fixed-geometry exhaust nozzle incorporating porous cavities for shock-boundary layer interaction control. Testing was conducted at static conditions using a sub-scale nozzle model with one baseline and 27 porous configurations. For the porous configurations, the effects of percent open porosity, hole diameter, and cavity depth were determined. All tests were conducted with no external flow at nozzle pressure ratios from 1.25 to approximately 9.50. Results indicate that baseline nozzle performance was dominated by unstable, shock-induced, boundary-layer separation at overexpanded conditions. Porous configurations were capable of controlling off-design separation in the nozzle by either alleviating separation or encouraging stable separation of the exhaust flow. The ability of the porous nozzle concept to alternately alleviate separation or encourage stable separation of exhaust flow through shock-boundary layer interaction control offers tremendous off-design performance benefits for fixed-geometry nozzle installations. In addition, the ability to encourage separation on one divergent flap while alleviating it on the other makes it possible to generate thrust vectoring using a fixed-geometry nozzle.</p>			
14. SUBJECT TERMS		15. NUMBER OF PAGES	
Exhaust Nozzles, Nonaxisymmetric Nozzles, Nozzle, Porosity, Thrust Vectoring		139	
		16. PRICE CODE	
		A07	
17. SECURITY CLASSIFICATION OF REPORT	18. SECURITY CLASSIFICATION OF THIS PAGE	19. SECURITY CLASSIFICATION OF ABSTRACT	20. LIMITATION OF ABSTRACT
Unclassified	Unclassified	Unclassified	UL